THE UNIVERSITY OF CHICAGO

PROBING MULTIPLE POPULATIONS IN GLOBULAR CLUSTERS USING STELLAR STREAMS

A DISSERTATION SUBMITTED TO
THE FACULTY OF THE DIVISION OF THE PHYSICAL SCIENCES
IN CANDIDACY FOR THE DEGREE OF
DOCTOR OF PHILOSOPHY

DEPARTMENT OF ASTRONOMY & ASTROPHYSICS

BY

SAMANTHA A. USMAN

CHICAGO, ILLINOIS

AUGUST 2025

Copyright © 2025 by Samantha A. Usman

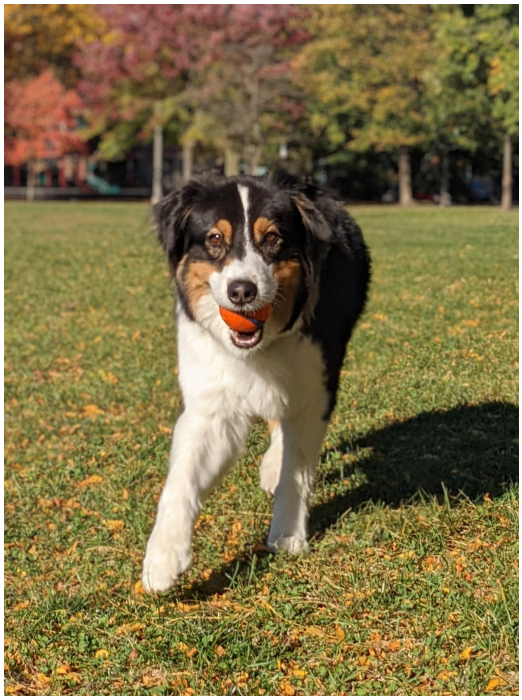

This thesis is dedicated to my dogs, Marble and Burr, who each slept at my feet for many nights while observing.

TABLE OF CONTENTS

LIST OF FIGURES vii

LIST OF TABLES xx

ACKNOWLEDGMENTS xxiv

ABSTRACT xxv

1 INTRODUCTION 1

2 CHEMICAL ABUNDANCES IN THE METAL-POOR GLOBULAR CLUSTER ESO 280-SC06: A FORMERLY MASSIVE, TIDALLY DISRUPTED GLOBULAR CLUSTER 7
2.1 Abstract 7
2.2 Introduction 8
2.3 Observations and Data Reduction 13
2.4 Chemical Abundance Analysis 16
2.4.1 Stellar Parameters 16
2.4.2 Abundance Calculations 20
2.4.3 Measurements 20
2.4.4 nLTE Corrections 24
2.4.5 Abundance Results 26
2.5 Kinematic Analysis 31
2.5.1 Initial Mass Estimate 32
2.6 Discussion 34
2.6.1 Enrichment Fraction vs. Cluster Mass 35
2.6.2 NEMP Star 37
2.6.3 Neutron-Capture Spread 39
2.7 Conclusion 42

3 MULTIPLE POPULATIONS AND A CH STAR FOUND IN THE 300S GLOBULAR CLUSTER STELLAR STREAM 56
3.1 Abstract 56
3.2 Introduction 57
3.3 Observations 61
3.4 Stellar Parameter Determination 63
3.5 Abundance Analysis 66

3.5.1 Abundance Dispersion Analysis . . . 69
3.6 Stream Progenitor Mass Estimate . . . 70
3.7 Results . . . 74
3.8 Discussion . . . 80
3.8.1 Globular Cluster, Not a Dwarf Galaxy . . . 80
3.8.2 Multiple Populations and Initial Mass . . . 85
3.8.3 CH Star and Cluster Dynamics . . . 89
3.9 Conclusion . . . 90

4 MASS-TRANSFER STARS IN DISRUPTING AND FULLY DISRUPTED GLOBULAR CLUSTERS: A BA STAR FOUND IN THE GD-1 STELLAR STREAM . . . 96
4.1 Abstract . . . 96
4.2 Introduction . . . 97
4.3 Observations . . . 99
4.4 Stellar Parameter Determination . . . 103
4.5 Abundance Analysis . . . 103
4.5.1 Measurements . . . 104
4.6 Abundance Results . . . 106
4.6.1 Abundance Dispersion Analysis . . . 106
4.7 Stream Progenitor Mass Estimate . . . 110
4.8 Discussion . . . 112
4.8.1 Multiple Populations in GD-1 . . . 112
4.8.2 Neutron-Capture Range . . . 113
4.8.3 Mass-Transfer Star and Cluster Dynamics . . . 115
4.9 Conclusion . . . 119

5 CHEMICAL ABUNDANCES IN THE LEIPTR STELLAR STREAM: A DISRUPTED ULTRA-FAINT DWARF GALAXY? . . . 124
5.1 Abstract . . . 124
5.2 Introduction . . . 125
5.3 Observations . . . 132
5.4 Abundance Analysis . . . 134
5.4.1 Differential Abundance Analysis . . . 152
5.5 Abundance Results . . . 154
5.5.1 Metallicity Mean and Dispersion . . . 156
5.5.2 C and N . . . 160
5.5.3 α elements (Mg, Ca, Ti) . . . 167

5.5.4 Odd-Z elements (Na, Al, K, Sc) . . . 172
5.5.5 Iron-peak elements (Cr, Mn, Co, Ni, Zn) . . . 173
5.5.6 Neutron-capture elements (Sr, Ba, Eu) . . . 175
5.6 Discussion . . . 177
5.6.1 Extragalactic Origin . . . 179
5.6.2 A Dwarf Galaxy, Not a Globular Cluster . . . 180
5.6.3 Low-Mass, Possibly Ultra-Faint . . . 181
5.6.4 Inhomogeneous Core-Collapse Supernova Enrichment? . . . 183
5.7 Conclusion . . . 185

6 CONCLUSION . . . 188

REFERENCES . . . 198

LIST OF FIGURES

1.1 Properties of globular cluster stellar streams (circles) and dwarf galaxy stellar streams (crosses). The metallicity spread is compared to the velocity dispersion (left), the stream width (center) and the metallicity (right). Graphic from Li et al. [2022]. 2
1.2 The metallicity of a galaxy as a function of mass. Graphic from Kirby et al. [2013]. 3
1.3 Chemical reactions that occur at increased burning temperatures. Figure from Gratton et al. [2019]. 5

2.1 The normalized spectra of the ESO 280-SC06 stars around the measured sodium doublet at 5890 and 5896 Å (top) and the measured aluminum line at 3962 Å (bottom). The thin, dotted vertical lines indicate the precise locations of the sodium lines and aluminum line in their respective panels. Stars 001, 005 and 025 are represented by a gold solid line, a blue dashed line, and a dotted red line, respectively. All stars have a temperature around 5180 K. Despite the similar temperatures, stars 005 and 025 clearly display much weaker sodium and aluminum absorption lines. This demonstrates that both stars are 1P stars, while star 001 is a 2P star. The other stars' spectra are shown as thin gray lines in the background. In the bottom panel, *ISM Na* indicates an absorption feature in the spectrum due to sodium in the interstellar medium. 14
2.2 The color-magnitude diagram for ESO 280-SC06 stars. The dotted line represents a MIST isochrone with log age = 10.15 and metallicity [Fe/H] = −2.5 [Dotter, 2016, Choi et al., 2016]. We shift the isochrone to the red side by 0.08 (as was done in previous analyses such as Simpson 2018). The first-population / 1P stars, AGB star, NEMP star and remaining second-population / 2P stars are denoted to blue hollow circles, a red hollow star, a green hollow square and a yellow hollow plus symbols. . . . 18

2.3 Key abundances for identifying chemical patterns found in multiple populations. The top left plot compares the LTE sodium and aluminum abundances. Directly below this, the bottom left plot adjusts these abundances to incorporate nLTE corrections. The top center, top right and bottom center plots compare the carbon abundances, nitrogen abundances and magnesium abundances, to the nLTE aluminum abundances. Lastly, the bottom right plot compares the nLTE sodium abundances to magnesium abundances. We identify eight stars with chemical enrichment patterns indicative of second-population/2P stars. Stars 005 and and 025 (represented by hollow blue circles) are the only stars that have low sodium and aluminum abundances, and are therefore classified as first-population/1P stars. The AGB star and the NEMP star (identified in Simpson and Martell 2019 are represented by a red hollow star and a green hollow square. The remaining second-population stars are represented by dark yellow plus symbols. For comparison, we also show abundances from M15 [Sobeck et al., 2011], represented by solid green triangles, and M92 [Kirby et al., 2023], represented by solid blue squares with error bars. For nLTE-corrected sodium abundances and magnesium abundances, we overlay a blue region and a light red hatched region to represent the diagnostic thresholds used in Kirby et al. [2023] to classify 1P stars: [Na/Fe] < 0.1 and [Mg/Fe] > 0.45 indicate a star is 1P. 23

2.4 Neutron-capture abundances measured in the ESO 280-SC06 stars. The first-populations/1P stars, the AGB star, the NEMP star, and the remaining second-population/2P stars are represented by blue hollow circles, a red hollow star, a green hollow square and yellow hollow plus symbols, respectively. For comparison, we also compare to abundances from M15 [Sobeck et al., 2011], represented by green triangles, and M92 [Kirby et al., 2023], represented by blue squares with error bars. The NEMP star, 026, has significantly higher *s*-process abundances (strontium, barium, and yttrium) than the other stars. This is consistent with *s*-process enhancement predicted from accretion from an asymptotic giant branch binary companion. Among the other stars, we find no significant spread in neutron-capture abundances, contrary to patterns previously identified in other systems such as M92 [Kirby et al., 2023]. 28

2.5 Three views of the Galactic orbit of ESO 280-SC06. The present position of the cluster is marked with a red pentagon, and its orbit over the past 1 Gyr is shown as a blue line. The high eccentricity and inclination of ESO 280-SC06's orbit mean that it has significant disk crossings at each pericenter passage, roughly every 150 Myr. The position of the Sun is shown with a yellow circle. The Milky Way is represented by the gray circle in the XY plane, and the thick gray line for side-on views in XZ and YZ planes. This orbit was integrated using `gala` with the default `MilkyWayPotential`. 31

2.6 The fraction of 2P stars in GCs as a function of current mass (left) and initial mass (right). The current and initial masses of Milky Way globular clusters (*MW GCs*) are represented by green circles on the left and purple circles on the right, respectively [Milone et al., 2017, Baumgardt et al., 2019]. Globular clusters in the Magellanic Clouds (*MC GCs*), which should not experience significant mass loss, are represented by black stars. (Data for MC GCs are from Mucciarelli et al. 2009, Mateluna et al. 2012, Mucciarelli et al. 2014, Hollyhead et al. 2017, Niederhofer et al. 2017b,a, Martocchia et al. 2017, Hollyhead et al. 2018, Zhang et al. 2018, Martocchia et al. 2018, and Hollyhead et al. 2019 and were compiled by Gratton et al. 2019.) ESO 280-SC06 is represented by the dark gold star. Measurements for the 300S stellar stream are represented by a red cross [Usman et al., 2024]. The dashed and dotted lines represent linear and quadratic fits between the 2P star fraction and cluster mass. 35

3.1 The positions (top panel) and S^5radial velocities (bottom panel) of stars in the region of 300S. Green stars represent 300S stars analyzed in this work. Red crosses represent stars rejected from this work as radial velocity non-members. The four red crosses to the right (at 153 degrees right ascension) represent the multiple radial velocities measured for the most metal-poor star analyzed by Fu et al. [2018]. Blue points represent 300S member stars identified in DECam photometry and S^5 spectroscopy. Gray dots represent other stars observed by S^5. 63

3.2 Isochrones matched to DECam DECaLS DR9 photometry. The blue and orange lines represent the best-fit isochrones found in this article and using parameters from Fu et al. [2018] and Li et al. [2022]. The parameters used for the latter isochrone are: age = 12.5 Gyr, $[\alpha/\mathrm{Fe}] = 0.4$, $[\mathrm{Fe/H}] = -1.27$, d = 17.2 kpc, where [Fe/H] and d were from Li et al. [2022] and the age and $[\alpha/\mathrm{Fe}]$ abundance are obtained from Fu et al. [2018]. Our best-fitting isochrone parameters are: age = 12.5 Gyr, $[\alpha/\mathrm{Fe}] = 0.0$, $[\mathrm{Fe/H}] = -1.35$, d = 17.7 kpc. The green stars, and blue circles represent the dereddened color and magnitude of stars analyzed in this work and other member candidates observed by S^5. The DECam data is a background-subtracted Hess diagram along 300S' sky position. 72
3.3 A comparison of normalized spectra around an O line, two Na lines, and the C-N bands in the top, middle and lower panels, respectively. We highlight the Telluric lines in the top panel. We emphasize here the enriched star J1020+1555 (dashed green line) and the star with most similar stellar parameters, J0956+1603 (red solid line). The former has a higher Na and N enrichment and O depletion as expected of enriched stars in GCs. The spectra of the other stars, which are significantly colder than the highlighted stars, are shown as thin gray lines. The bright red dotted line indicates the wavelength of the measured absorption lines. . . 76
3.4 The abundances of elements characteristic of multiple population enrichment: nitrogen, oxygen, and sodium in the left, middle and right plots, respectively. The purple circles represent the abundances of the ordinary stars. The anomalous stars J1020+1555, J1001+1554, and J1045+1408 are marked with a dark red star, a green cross, and a blue triangle respectively. J1020+1555 has the requisite enrichment in N and Na, and depletion in O. We also measure unusual of Na enrichment in the cool star, J0956+1603. Additionally, in the rightmost plot, the black points represent the NLTE-corrected abundances. However, due to the correlation between T_{eff} and the Na abundance and no depletion in O, we attribute this to an unknown systematic error and do not consider this a second-population star. 77

3.5 Correlated abundances of element Na compared to N and O in the left and right plots, respectively. The purple circles represent the abundances of the ordinary stars. The anomalous stars J1020+1555, J1001+1554, and J1045+1408 are marked with a dark red star, a green cross, and a blue triangle respectively. The black points represent the NLTE-corrected abundances. J1020+1555 has the requisite enrichment in N and Na, and depletion in O. We also measure unusual of Na in the cool star, J0956+1603. However, due to the correlation between $T_{\rm eff}$ (as seen in Fig. 3.4) and the Na abundance and no depletion in O, we attribute this to an unknown systematic error and do not consider this a second-population star. . . . 78
3.6 The abundances of elements characteristic of a CH star: carbon and *s*-process elements strontium, yttrium, and barium. The purple circles represent the abundances of the ordinary stars. The anomalous stars J1020+1555, J1001+1554, and J1045+1408 are marked with a dark red star, a green cross, and a blue triangle respectively. J1001+1554 has clear enrichment in all four of these elements. 79
3.7 Magnesium to iron ratio in stars of Milky Way GCs, the stellar stream 300S, the GSE and GSE GCs. The Milky Way and GSE GCs star abundances are colored points with white and black outlines respectively. The abundances of GSE stars are represented by gray triangles, while our 300S measurements are represented by pink stars with black errorbars. GCs sample the [Mg/Fe] ratio of its host galaxy at its time of formation. The 1P stars for each cluster are the most metal rich at the top of the plot, while 2P stars have depleted Mg and stretch to the bottom of the figure. 300S does not resemble Milky Way GCs, but matches the GSE, indicating it formed *ex situ*. This chemical resemblance further supports the stream's dynamic association with GES given its highly eccentric and retrograde orbit: its energy and angular momenta similarly match that of GES [Fu et al., 2018]. The globular cluster abundances here are data APOGEE data from Mészáros et al. [2020], while the GSE abundances are APOGEE data from Limberg et al. [2021b]. 86

3.8 The current masses (green circles, left) and initial masses (purple circles, right) of intact Milky Way GCs [Milone et al., 2017, Baumgardt et al., 2019]. The measurements for the Magellanic Clouds come from Mucciarelli et al. [2009], Mateluna et al. [2012], Mucciarelli et al. [2014], Hollyhead et al. [2017], Niederhofer et al. [2017b,a], Martocchia et al. [2017], Hollyhead et al. [2018], Zhang et al. [2018], Martocchia et al. [2018], and Hollyhead et al. [2019] and were compiled by Gratton et al. 2019. The lower limit for 300S's mass is its current stream mass, while the upper limit of its mass is calculated from based on a fully dissolved cluster as described in Section 3.6. In the left panel, we see a correlation between the present-day mass of intact Milky Way GCs and the fraction of enriched stars found therein. If we extrapolate a linear relationship, we would expect a system with a mass of $10^{4.5}\,M_\odot$ like 300S would have about half of its stars enriched. Instead, just one of our eight stars exhibited enrichment. In the right panel, we compare the initial masses and the fraction of enriched stars for these same systems. We find a much tighter correlation. If we again assume a linear relationship, 300S still appears underenriched for its mass, but does not appear as significantly displaced. A quadratic relation, however, may be better at representing a critical threshold limit needed to create stellar enrichment. Extrapolating from this relationship (the black, dotted line), 300S appears more closely in line with predictions. In both panels, 300S is marginally more enriched than two other Milky Way globular clusters: Ruprecht 106 and Terzan 8. 95

4.1 The sky location (top panel), radial velocities (bottom panel) of member and member-candidate stars in the GD-1 stellar stream. The gray points represent member candidate stars identified by Ibata et al. [2024]. The black circles and the gold star represent member stars observed in this work, with the latter being the 2P and mass-transfer star. The red crosses represent stars that were observed but were found to be non-members, either due to discrepant radial velocities and/or discrepant metallicities. . 101

4.2 The spectra of three stars around key wavelengths. The yellow, solid line represents the sodium- and barium-enriched star 696*, observed at Lowell Observatory. The purple, dashed line represents a star of most similar temperature, 830*, observed using McDonald Observatory. The red, dotted line represent a star of most similar temperature, 307*, observed with the Magellan Telescopes. The top and bottom panels demonstrate the sodium D lines and a barium line, respectively. Despite 696*'s higher temperature, the star exhibits significantly more absorption, demonstrating its enrichment in both of these elements. 107
4.3 Abundances characteristic of multiple populations. The top left, top right and bottom left panels show the [Al/Fe], [Mg/Fe] and [Na/Fe] with respect to [Fe/H], respectively. The bottom right panel shows [Na/Fe] vs [Fe/H]. Our abundances from stars observed with the McDonald Observatory, Lowell Observatory and the Magellan telescopes are represented by green circles, black crosses, and blue diamonds. For comparison, we also display abundances from ESO 280-SC06 [Usman et al., 2024] and halo stars [Reggiani et al., 2019]. Our analysis assumes local thermodynamic equilibrium, and therefore does not inherently include corrections due to non-local thermodynamic equilibrium. To account for this, we add +0.8 and -0.4 approximate corrections to [Al/Fe] and [Na/Fe] in order to compare to similar datasets presented here. Only one star has high sodium indicative of multiple populations. 108
4.4 Neutron-capture abundances. The top left, top right, bottom left and bottom right panels show the [Ba/Fe], [Y/Fe], [Sr/Fe] and [Eu/Fe] with respect to [Fe/H], respectively. The bottom right panel shows [Na/Fe] vs [Fe/H]. Stars without y-error bars indicate 3σ upper limit measurements. Our abundances from stars observed with McDonald Observatory, Lowell Observatory and the Magellan telescopes are represented by green circles, black crosses, and blue diamonds. For comparison, we also display abundances from Sequoia, Gaia-Sausage-Enceladus (both Aguado et al. 2021a), ESO 280-SC06 [Usman et al., 2024] and halo stars [Reggiani et al., 2019]. One Lowell star demonstrates high enrichment in barium, which is indicative of mass-transfer. 109

4.5 The enriched / 2P star fraction as a function of current mass and initial mass. Intact Milky Way globular clusters' (MW GCs) current masses and initial masses are represented by green circles on the left and purple circles, on the right, respectively. The mass estimates for these clusters come from Globular Cluster Database, V4 [Baumgardt et al., 2023], while the 2P star fraction estimates come from Milone et al. [2017] and Milone et al. [2019]. The GD-1 stellar stream is represented by an orange square in the right panel (and is not in the left panel, since stellar streams are completely unbound and have no current mass). For comparison, we include the cluster ESO 280-SC06 [Usman et al., 2025] and the stellar stream 300S [Usman et al., 2024]. We also include globular clusters in the Magellanic Clouds (*MC GCs*), which are not expected to experience signfican mass loss (black stars). (Data for MC GCs are from Mucciarelli et al. 2009, Mateluna et al. 2012, Mucciarelli et al. 2014, Hollyhead et al. 2017, Niederhofer et al. 2017b,a, Martocchia et al. 2017, Hollyhead et al. 2018, Zhang et al. 2018, Martocchia et al. 2018, and Hollyhead et al. 2019 and were compiled by Gratton et al. 2019.) 114
4.6 The binary fraction (left) and 2P star fraction (center) as a function of core density in Milky Way globular clusters, and as a function of each other (right). We combine catalogs of binary star fraction [Ji and Bregman, 2015], 2P star fraction [Milone et al., 2017, 2019], and mass and densities Baumgardt et al. [2023]. 117
4.7 The binary star fraction as a function of fraction of stellar mass loss experienced by the cluster. We combine catalogs of binary star fraction [Ji and Bregman, 2015] and mass loss calculations derived from Baumgardt et al. [2023]. The dashed, black line represent a linear correlation fitted to the cluster data. 118

5.1 Positions and reflex-corrected radial velocities of Leiptr candidate stars. The members from the `STREAMFINDER` catalog are represented by black circles and four members analyzed in this work are represented by light-blue stars. The non-member, Leiptr-252, is emphasized as a red X. The reflex-corrected proper motions in degrees per Myr are indicated by arrows in the top panel. Any stars in the `STREAMFINDER` catalog without confirmed radial velocities were omitted. 133

5.2 Spectra around the Ba II line at 4554.0 Å; Mg I b triplet; and the Sr II line at 4077.7 Å. The stars are ordered top to bottom from coolest to hottest. The shaded region around the spectra shows the uncertainty in normalized flux. Leiptr-252 is a clear outlier with stronger and broader lines. 135
5.3 A comparison of normalized spectra of stars with similar stellar parameters around the Hβ line at 4861 Å. Additional absorption lines are shown adjacent to the central line. The top plot has the stars Leiptr-186 (purple dashed line) and Leiptr-342 (gold solid line), both with $T_{\rm eff}$ around 4650 K. The bottom plot has stars Leiptr-208 (blue dot-dashed line) and Leiptr-321 (red solid line), both with $T_{\rm eff}$ around 5050 K. The similarity of the hydrogen line profiles suggest each pair of stars has very similar temperatures; but Leiptr-321 and Leiptr-342 have stronger metal lines than Leiptr-208 and Leiptr-186, respectively, indicating their metallicities must differ. 142
5.4 A comparison of normalized spectra of stars with similar stellar parameters around the Hα line at 6563 Å. Additional absorption lines are shown adjacent to the central line. The top plot has the stars Leiptr-186 (purple dashed line) and Leiptr-342 (gold solid line), both with $T_{\rm eff}$ around 4650 K. The bottom plot has stars Leiptr-208 (blue dot-dashed line) and Leiptr-321 (red solid line), both with $T_{\rm eff}$ around 5050 K. The similarity of the hydrogen line profiles suggest each pair of stars has very similar temperatures; but Leiptr-321 and Leiptr-342 have stronger metal lines than Leiptr-208 and Leiptr-186, respectively, indicating their metallicities must differ. 143
5.5 A comparison of normalized rest-frame spectra of Leiptr-321 and Leiptr-208 that have similar stellar parameters, centered around the Mg I b triplet; Ca I line at 4454.8 Å; Ti II line at 4395.0 Å; Na I line at 5895.9 Å; K I line at 7664.9 Å; and Sc II line at 5526.8 Å. Additional absorption lines are shown adjacent to the central line, including interstellar medium and telluric features in the sodium and potassium panels, respectively. The telluric features around K I are offset because the stars are shifted to rest frame. The plots have stars Leiptr-208 (blue dot-dashed line) and Leiptr-321 (red solid line), both with $T_{\rm eff}$ around 5050 K. It is clear that Leiptr-321 has overall higher metallicity, as well as much higher abundances of sodium, potassium, and scandium. 144

5.6 Abundance differences between matched pairs of stars with similar temperatures. The top panel shows the difference between the cooler pair, Leiptr-342 and Leiptr-186, indicated by light-blue squares in this and future figures. The bottom panel shows the difference between the warmer pair, Leiptr-321 and Leiptr-208, indicated by light-blue circles in this and future figures. The longer error bars with smaller cap sizes show the standard deviation. The shorter error bars with larger cap sizes show the standard error. No error bar is shown if just one line is used. A horizontal dashed line is shown corresponding to $\Delta \log \epsilon(\mathrm{Fe})$; differences of other elements relative to this line indicate Δ[X/Fe]. 145
5.7 Comparison of Leiptr-208 and Leiptr-321 (light-blue circles) and Leiptr-186 and Leiptr-342 (light-blue squares) nitrogen abundances against carbon on the leftmost plot. The other two plots to the right illustrate carbon and nitrogen abundance in relation to effective temperature. The non-member Leiptr-252 is shown as a red X. Total uncertainty is shown in black for accuracy and abundance uncertainty without additional systematic errors is shown in the same color as the stars for statistical precision as described in Section 5.4. [X/Fe] = 0 is plotted as a bold black line. Abundances of metal-poor Milky Way halo stars appear as gray plus signs and abundances from the M15 globular cluster appear as dark-red upside-down triangles. 156
5.8 Comparison of Leiptr-208 and Leiptr-321 (light-blue circles) and Leiptr-186 and Leiptr-342 (light-blue squares) α abundances with other stellar populations. The non-member Leiptr-252 is shown as a red X. uncertainty is shown in black for accuracy and abundance uncertainty without additional systematic errors is shown in the same color as the stars for statistical precision as described in Section 5.4. [X/Fe] = 0 is plotted as a bold black line. Metal-poor Milky Way halo stars appear as gray plus signs and GSE stars appear as dark-blue plus signs. Abundances of stars from massive dwarf galaxies, intermediate-mass dwarf galaxies, and ultra-faint dwarf galaxies appear as yellow triangles, pink triangles, and purple triangles, respectively. Abundances of stars from the M92 and NGC 2419 Milky Way globular clusters appear as dark-red upside-down triangles. Abundances from dwarf galaxy stream stars appear as pink stars and abundances from globular cluster stream stars appear as dark-red stars. . 166

5.9 Comparison of Leiptr-208 and Leiptr-321 (light-blue circles) and Leiptr-186 and Leiptr-342 (light-blue squares) odd-z abundances with other stellar populations. The non-member Leiptr-252 is shown as a red X. Total uncertainty is shown in black for accuracy and abundance uncertainty without additional systematic errors is shown in the same color as the stars for statistical precision as described in Section 5.4. [X/Fe] = 0 is plotted as a bold black line. Metal-poor Milky Way halo stars appear as gray plus signs and GSE stars appear as dark-blue plus signs. Abundances of stars from massive dwarf galaxies, intermediate-mass dwarf galaxies, and ultra-faint dwarf galaxies appear as yellow triangles, pink triangles, and purple triangles, respectively. Abundances of stars from the M92 and NGC 2419 Milky Way globular clusters appear as dark-red upside-down triangles. Abundances from dwarf galaxy stream stars appear as pink stars and abundances from globular cluster stream stars appear as dark-red stars. Leiptr-208 and Leiptr-321 (blue circles) and Leiptr-186 and Leiptr-342 (blue squares) abundances for sodium, aluminum, and potassium are additionally plotted to correct for especially significant NLTE effects. *approximate NLTE corrections are calculated as an average for aluminum and independently for sodium and potassium (see text for details) 168

5.10 Comparison of Leiptr-208 and Leiptr-321 (light-blue circles) and Leiptr-186 and Leiptr-342 (light-blue squares) iron-peak abundances with other stellar populations. The non-member Leiptr-252 is shown as a red X. Total uncertainty is shown in black for accuracy and abundance uncertainty without additional systematic errors is shown in the same color as the stars for statistical precision as described in Section 5.4. [X/Fe] = 0 is plotted as a bold black line. Metal-poor Milky Way halo stars appear as gray plus signs and GSE stars appear as dark-blue plus signs. Abundances of stars from massive dwarf galaxies, intermediate-mass dwarf galaxies, and ultra-faint dwarf galaxies appear as yellow triangles, pink triangles, and purple triangles, respectively. Abundances of stars from the M92 Milky Way globular cluster appear as dark-red upside-down triangles. Abundances from dwarf galaxy stream stars appear as pink stars and abundances from globular cluster stream stars appear as dark-red stars. Leiptr-208 and Leiptr-321 (blue circles) and Leiptr-186 and Leiptr-342 (blue squares) abundances for manganese are additionally plotted to correct for especially significant NLTE effects. *approximate NLTE corrections are calculated independently for manganese (see text for details) . . 171

5.11 Comparison of Leiptr-208 and Leiptr-321 (light-blue circles) and Leiptr-186 and Leiptr-342 (light-blue squares) neutron-capture abundances with other stellar populations. The non-member Leiptr-252 is shown as a red X. Total uncertainty is shown in black for accuracy and abundance uncertainty without additional systematic errors is shown in the same color as the stars for statistical precision as described in Section 5.4. [X/Fe] = 0 is plotted as a bold black line. Metal-poor Milky Way halo stars appear as gray plus signs and GSE stars appear as dark-blue plus signs. Abundances of stars from massive dwarf galaxies, intermediate-mass dwarf galaxies, and ultra-faint dwarf galaxies appear as yellow triangles, pink triangles, and purple triangles, respectively. Abundances of stars from the M15, M22, M92, and NGC 2419 Milky Way globular clusters appear as dark-red upside-down triangles. Abundances from dwarf galaxy stream stars appear as pink stars and abundances from globular cluster stream stars appear as dark-red stars. 174

5.12 [Mg/Fe] and [Ba/Fe] for known dwarf galaxies compared to Leiptr-208 and Leiptr-321 (light-blue circles) and Leiptr-186 and Leiptr-342 (light-blue squares). Total uncertainty is shown in black for accuracy and abundance uncertainty without additional systematic errors is shown in the same color as the stars for statistical precision as described in Section 5.4. [X/Fe] = 0 is plotted as a bold black line. In order from highest to lowest mass using LOESS smoothing, abundances are plotted for GSE (thick blue line), Fornax (purple line), Sculptor (dotted purple line), Sextans (thin gray line), Draco (dashed gray line), Boötes I (thin green line), and Carina II (dot-dashed green line). Solar masses are given in the legend. Abundances are also plotted for the dwarf galaxy streams Chenab (yellow square), Elqui (orange diamond), Indus (pink triangle), and Jhelum (dark-orange star). Leiptr's low-α abundances are most similar to dwarf galaxies of mass $M_\star \lesssim 10^6 M_\odot$. It's neutron-capture abundances are even lower, only consistent with dwarf galaxies of mass $M_\star \lesssim 10^5 M_\odot$. Unlike Elqui, the previous lowest-mass dwarf galaxy stream, Leiptr's neutron-capture abundances are constant or declining with increasing metallicity which suggests that it is even lower-mass. 178

6.1 Contributions to the Milky Way from *in-situ* and *ex-situ* sources. Both figures from Naidu et al. [2020]. The top row shows the energy-momentum plot for stars in our Milky Way, with the right panel specifically highlighting the stars' origins. The bottom row shows the proportional contribution of stars from different sources as a function of radial distance (left panel) and distance out of the plane of the disk Z (right panel). 189
6.2 Palomar 5 is famous for its impressive tidal tails, spanning 20° across the sky. The tails were first discovered in SDSS data by Odenkirchen et al. [2003]. Gieles et al. [2021] argues an inherent population of stellar-mass black holes would account for the clusters' unusual dynamical properties. However, a black hole population could cause a different distribution of enriched stars than a disruption model caused by tidal forces. Figures adapted from SDSS [2003] (inset) and Gieles et al. [2021]. 190
6.3 A visual representation of the location of enriched stars in a globular cluster stream disrupted via tidal dissipation (left) or black hole ejection (right). 192
6.4 Potential formation mechanisms of binary black hole systems. Figure from Mapelli [2020]. 193
6.5 Representation of projects that will be reduced and or canceled due to proposed budget cuts. Red crosses represent programs that will be canceled. Blue crosses represent programs in which the NASA contribution will be canceled, but which are lead by another organization, e.g. the European Space Agency. The yellow exclamation point represent programs which will lose more than half of their funding relative to the previous year. Figure from Grayson [2025], adapted from NASA Goddard Space Flight Center. 196

LIST OF TABLES

2.1 Summary of ESO 280-SC06 Properties. The distance, proper motions, radial velocity, current mass $M_{\rm fin}$ and radius measurements are from literature sources. We discuss our measured metallicity and 2P star fraction in Section 2.4, Subsection 2.4.3. The orbital parameters are discussed in Section 2.5 and we calculate the initial mass in Subsection 2.5.1. 15

2.2 The stellar parameters of observed stars in this analysis. All stars are red giant branch stars, with the probable exception of star 184 (denoted by *), which appears to be an asymptotic branch star. The effective temperatures $T_{\rm eff}$ are calculated using the relations described in Mucciarelli et al. [2021]. Star 184 returns three extremely different temperatures from these relations, depending on which color is used for the calculation. log g is calculated using the relation in Ji et al. [2020b]. The microturbulence velocity and metallicity are calculated in our spectroscopic analysis. Stars 005 and 025 (denoted with †) are the identified 1P stars. Star 026 (denoted with ‡) is the NEMP star identified in Simpson and Martell [2019]. 17

2.3 Example Line Table, Star 576. This table is available in its entirety in machine-readable form as part of the arXiv source. expot is excitation potential; loggf is oscillator strength; log ϵ is the absolute stellar abundance to H; e_{stat} is the statistical abundance uncertainty due to the equivalent width uncertainty; eqw is equivalent width; e_{eqw} is uncertainty in equivalent width; FWHM is the full width of the line at half maximum; $e_{T_{\rm eff}}$ is the difference on the abundance due to 1σ uncertainties on effective temperature, and similarly for e_g for the surface gravity, e_v for the microturbulence, and e_M for the metallicity. Elements with no listed equivalent width were measured using synthesis. The wavelengths of synthesized lines have been rounded to the nearest whole wavelength. Elements marked with the less-than symbol, $<$, are 3σ upper limits. . . . 19

2.4 nLTE Corrections for aluminum and sodium. For the two coldest stars (marked with an asterisk *), the calculated surface gravity was less than one, log $g < 1$. The nLTE calculators leverage sets of grids of stellar atmospheres which span a wide range of stellar parameters. The grids do not extensively cover surface gravities below log $g < 1$. We therefore round the surface gravity of the stars 184 and 576 up to log g =1. The calculated Al correction for stars 008 and 184 (denoted with a dagger †) are higher than 1; however, Nordlander and Lind [2017] suggests Al corrections above 1 are not reliable, and should instead be capped at 1. Despite using these reduced corrections, both stars have very high Al abundances and are therefore still classified as 2P stars. 25
2.5 Cluster Abundance Means & Dispersions. Estimated abundance means and dispersions for ESO 280-SC06. The error bars represent 1σ confidence limits. Stars which have upper limits for a given abundance are excluded from its mean and dispersion calculation. Star 184 is excluded for elements which can be enriched in NEMP stars (denoted with †). If a dispersion cannot be measured, we give an upper limit at 95% confidence. If the two 1P stars, 005 and 025 are excluded from the analysis, we measure no dispersion in aluminum. We find an upper limit of 0.38. . 27
2.6 Star 001 Abundances 46
2.7 Star 003 Abundances 47
2.8 Star 005 Abundances 48
2.9 Star 008 Abundances 49
2.10 Star 016 Abundances 50
2.11 Star 025 Abundances 51
2.12 Star 026 Abundances 52
2.13 Star 033 Abundances 53
2.14 Star 184 Abundances 54
2.15 Star 576 Abundances 55

3.1 The coordinates and exposure time for each star observed in this study. The distances were calculated using the relationship in Fu et al. [2018]. The Source column refers to the catalog or paper from which the star was chosen: S^5 were stars observed by the S^5 collaboration using AAT, Gaia stars were astrometrically selected from the Gaia catalog, and the Fu et al. [2018] star was the most metal-poor star in their sample. 58

3.2 Stellar parameters. [Fe/H] NLTE corrections were found using an online calculator based on Bergemann et al. [2012c] and Lind et al. [2012]. As this tool only covers parameter ranges $4000 < T_{\rm eff} < 8000$, $1.0 < \log g < 5.0$, $1.0 < \nu_t < 2.0$, for stars with parameters outside of these ranges we fix the respective inputs to $T_{\rm eff} = 4000$ K, $\log g = 1.0$, and $\nu_t = 2$. . . . 64
3.3 The measured element abundance for each star for our measured elements. We were unable to measure N in the cool star, J1045+1408. We also include Na abundances which have had NLTE corrections been applied, though we are unable to calculate error for the corrected abundances as our analysis is fully LTE. 81
3.4 The most probable mean abundance and dispersion of 300S as inferred from the element abundances measured in all eight stars. The error bars and upper limits shown here represent one standard deviation confidence. We constrain the metallicity dispersion to less than < 0.09 with 95% confidence. Since our analysis was performed with the assumption of local thermodynamic equilibrium, we are unable to estimate the error for NLTE-corrected Na abundances, and therefore cannot measure 300's mean abundance and dispersion for the corrected abundances. 82
3.5 A comparison of the abundances of elements typically enriched or depleted in second-population globular cluster stars. The 1st-Pop Mean abundances are the most probable mean abundances for the first-population stars in 300S, as inferred from five typical stars in our sample (excluding the three anomalous stars). We compare this to the abundance found in our enriched star J1020+1555 and give the significance of the star's abundances with respect to the normal star population. 83
3.6 A comparison of the abundances of elements typically enriched in CH stars. The 1st-Pop Mean abundances are the most probable mean abundances for the first-population stars in 300S, as inferred from five typical stars in our sample (excluding the three anomalous stars). We compare this to the abundance found in our CH star J1001+1554 and give the significance of the star's abundances with respect to the normal star population. 83
3.7 The following is a sample table of data for the star 0956+1603. Full data tables are available online. 94

4.1 Observed stars and their parameters. Stars are labeled with the first four digits of their *Gaia* IDs. 100

4.2 Stellar parameters of observed stars. Effective temperatures and surface gravities are estimated using photometry. The stars observed with Magellan, 306* and 307*, have surface gravities, metallicity, and microturbulence uncertainties of 0.15, 0.2, and 0.2 km s^{-1}. Due to higher SNR, we use uncertainties 0.2, 0.3 and 0.3 km $s^{-1}$for stars observed with McDonald and Lowell. 102
4.3 Cluster Mean Abundances and Dispersions. N denotes the number of measurements incorporated into the mean abundance and dispersion. . . 110
4.4 Abundances measured in star 165. 120
4.5 Abundances measured in star 693. 120
4.6 Abundances measured in star 696. 121
4.7 Abundances measured in star 805. 121
4.8 Abundances measured in star 830. 122
4.9 Abundances measured in star 7962. 122
4.10 Abundances measured in star 7965. 123

5.1 SNR 4500 Å and 6500 Å is the signal-to-noise per pixel at 4500 Å and 6500 Å. RV is the heliocentric radial velocity with 1 km s^{-1} uncertainty. (* indicates the non-member star.) 130
5.2 Leiptr Candidate Stellar Parameters and Uncertainties 138
5.3 Leiptr Candidate Line List 147
5.4 Leiptr-186 Abundances 148
5.4 Leiptr-186 Abundances 149
5.4 Leiptr-186 Abundances 150
5.5 Leiptr-208 Abundances 150
5.5 Leiptr-208 Abundances 151
5.5 Leiptr-208 Abundances 152
5.6 Leiptr-252* Abundances 157
5.6 Leiptr-252* Abundances 158
5.6 Leiptr-252* Abundances 159
5.7 Leiptr-321 Abundances 161
5.7 Leiptr-321 Abundances 162
5.7 Leiptr-321 Abundances 163
5.8 Leiptr-342 Abundances 163
5.8 Leiptr-342 Abundances 164
5.8 Leiptr-342 Abundances 165

6.1 Globular Cluster Tidal Tails. Table is supplemented by the Globular Cluster Database [Baumgardt et al., 2023]. 191

ACKNOWLEDGMENTS

I acknowledge the support of the American Association of University Women through their American Dissertation Fellowship.

ABSTRACT

Just like the moon causes tides on the Earth, the Milky Way causes tides on star systems dropped into our galaxy. Globular clusters and dwarf galaxies that fall into the Milky Way's gravitational potential are slowly stripped of their stars until they fully disrupt into stellar streams. By spectroscopically observing stars in these streams, we can learn more about the environment in which these star clusters and dwarf galaxies formed. In this thesis, we explore for disrupting and fully disrupted stellar systems:

- ESO 280-SC06, the most metal-poor intact globular cluster in the Milky Way with a surprisingly high fraction of enriched stars;
- 300S, a globular cluster stream whose initial mass straddled the critical threshold for creating enriched stars;
- GD-1, a globular cluster stream that contains a star enriched by a binary companion, a rare find in globular clusters; and
- Leiptr, an ultra-faint dwarf galaxy stellar stream, the least massive disrupted dwarf galaxy identified to-date.

Through the chemical analysis of these four systems, we learn more about the environment needed to form enriched stars in globular clusters, how the disruption of a globular cluster can impact the survival of binary stars, and the formation of dwarf galaxies on the smallest scales.

CHAPTER 1

INTRODUCTION

When galaxies and star clusters fall into the Milky Way (or the proto-Milky Way), our galaxy's gravitational potential can slowly tear them apart. This occurs in stages: initially, the star systems slowly have mass stripped away in the form of tidal tails. Next, the stars become completely gravitationally unbound, and it continues its orbit as a stellar stream. Lastly, the star system becomes fully mixed into the galaxy, sometimes becoming almost indistinguishable from the stars that formed *in-situ*.

However, we can find stars in these intermediate stages of disruption to learn more about how they formed and their journey over their lifetime. Stellar streams are of particular interest due to their many uses in other areas of astronomy. For example, globular cluster stellar streams can serve as sensitive probes to the Milky Way's gravitational potential, giving us insight into the galactic dark matter halo. Smaller dark matter halos can also interact with stellar streams directly, causing changes to the spatial distribution of stars and allowing us to constrain properties of dark matter. Streams whose progenitors were dwarf galaxies, however, can tell us about the galactic merger history and unique chemical evolution in small dark matter halos.

Globular clusters and dwarf galaxies often look very similar after they have been fully disrupted. There can be some indicators of the stream's origin, such as the width of the stream or its velocity dispersion. Figure 1.1 (from Li et al. 2022) demonstrates the different stream properties that can be used to classify a cluster's progenitor.

Sometimes, the most sure-fire way to confirm a stream's origin is to look at its

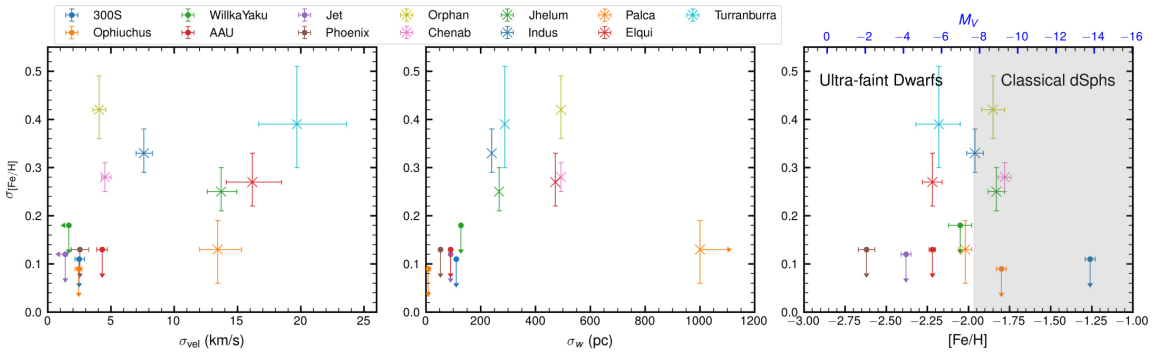

Figure 1.1 Properties of globular cluster stellar streams (circles) and dwarf galaxy stellar streams (crosses). The metallicity spread is compared to the velocity dispersion (left), the stream width (center) and the metallicity (right). Graphic from Li et al. [2022].

chemical composition. We can use spectroscopy to identify elements in the stars of a stellar stream. Because globular clusters and dwarf galaxies look different *chemically*, we expect their disrupted remnants to look different, too. Metallicity, in particular, is a great way to differentiate the two. Globular clusters generally have uniform metallicity, with a few oddballs like ω Cetauri (which may be a nuclear star cluster anyway, an entirely different can of chemical worms). Galaxies, on the other hand, consistently have a wide range of metallicities in their stars, relating back to how the dark matter halos they form in trap metals to enrich later generations of stars. In fact, you can use the metallicity of a dwarf galaxy to infer its original mass. Figure 1.2 from Kirby et al. [2013] demonstrates how closely linked the metallicity of a cluster is linked to its mass. Detecting a metallicity dispersion is a clear indicator that a stream is a dwarf galaxy.

Globular clusters, too, have a unique chemical fingerprint: most globular clusters in the Milky Way have a distinct, correlated abundance pattern unique to globu-

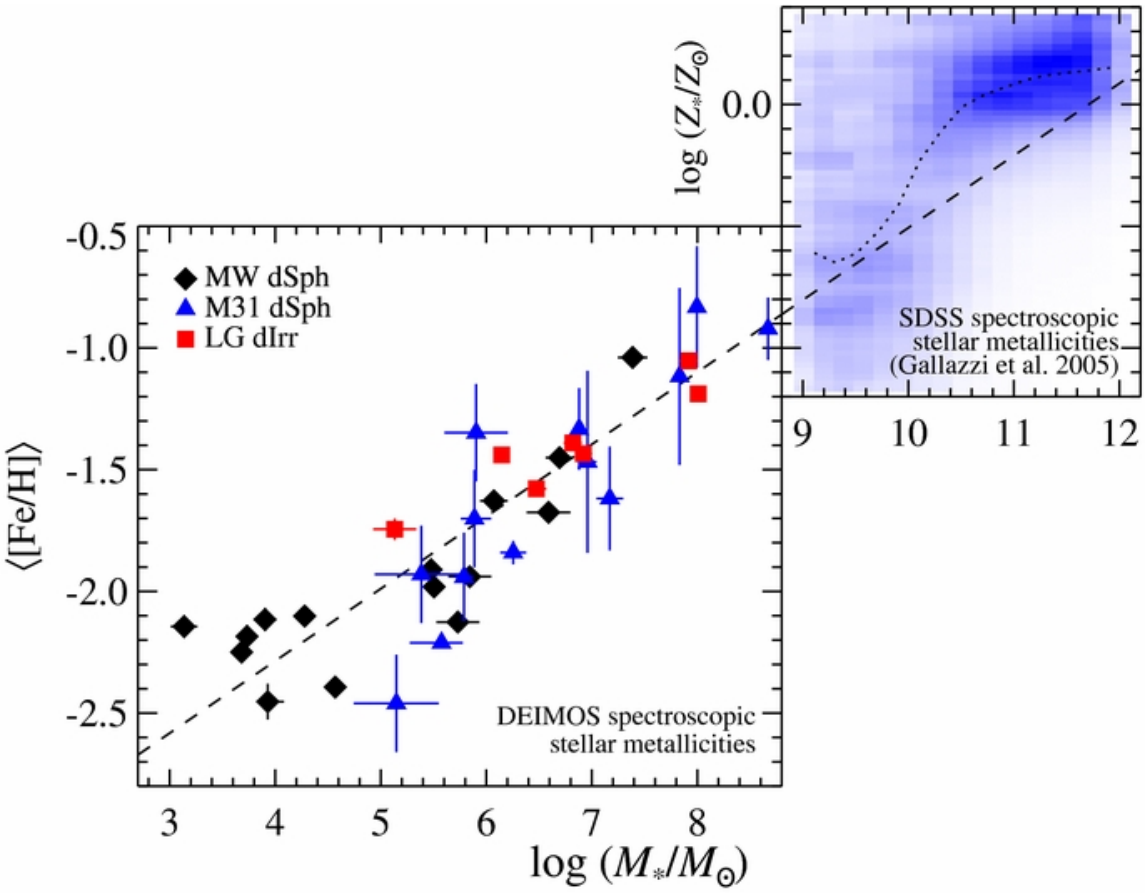

Figure 1.2 The metallicity of a galaxy as a function of mass. Graphic from Kirby et al. [2013].

lar clusters. This essentially consists of a base population stars, whose chemistry is similar to solar abundances (when scaled for metallicity) and open clusters, and a population of enriched stars, which have high abundances of sodium, aluminum, and nitrogen and low abundances of magnesium and oxygen. These are sometimes referred to as first-population (1P) and second-population (2P), or first-generation (1G) and second-generation (2G) stars, with the former being seemingly more common. However, it is not *totally* clear if there is a time component to the generations.

So far, there have been no successful attempt to fit isochrones of different ages, as the chemistry of the populations are too different and the ages are too similar to be able to properly constrain an age difference. I sometimes refer to the stars with high sodium as "enriched" stars (see Chapter 3), and sometimes "2P" stars (see Chapter 2). However, I truly prefer to call them what they are: salty stars. (Upon hearing this, Oleg Gnedin suggested at a conference that we call 1P/1G/unenriched stars "sweet" stars, since their higher carbon and oxygen abundances was more similar to sucrose.)

Salty stars are only found in globular clusters and their remnants. It's not totally clear what causes them to form, though it has something to do with the temperature at which the previous generation of stars were burning: higher temperatures produce the element correlations we see in salty stars. Figure 1.3 shows the the CNO-cycle, the Ne-Na cycle, and the Mg-Al cycle, and the relative temperatures at which they occur.

This process is occurring at some point in the globular cluster's formation, but we don't know the exact mechanism. There's lots of ideas, some relating to asymptotic giant branch stars and their enriched solar winds, massive rotating stars, or the separation of chemicals in the proto-cluster prior to star formation. My favorite is related to runaway stellar collisions, leading to massive stars a thousand times the mass of our sun [Bastian and Lardo, 2018].

No matter the exact mechanism, we know that the mass of the cluster is a factor. There's a clear relationship between the mass of a cluster and the fraction of salty stars it contains: really massive globular clusters have extremely high fractions of

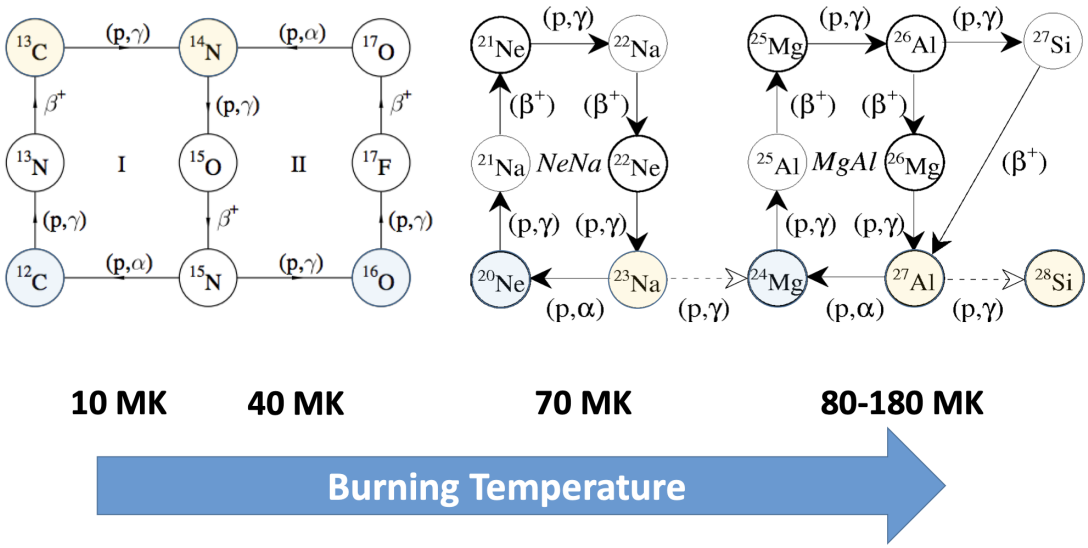

Figure 1.3 Chemical reactions that occur at increased burning temperatures. Figure from Gratton et al. [2019].

salty stars, with the biggest cluster ω Centauri, being comprised of more than 90% salty stars. Globular cluster stellar streams, however, are usually much, much smaller than this. After all, these are the clusters that fought the galactic potential and lost. They often teeter on the bring of being massive enough to have salty stars, and indeed both of the streams I share here in Chapters 3 and 4 have just one salty star out of eight. Even still, the detection of any salty stars is a clear indication that the stream's progenitor is a globular cluster. By observing and chemically tagging these disrupting and disrupted stellar systems, we can learn more about the environments in which they formed.

In this thesis, I will review four disrupting or fully disrupted star systems. In Chapter 2, I will discuss the most metal-poor intact globular cluster, ESO 280-SC06. We find the cluster has a surprisingly high fraction of salty stars, unexpected in

a cluster of this mass. We suggest this augmented salty star fraction is due to unenriched stars being preferentially stripped from the cluster due to tidal stripping from the Milky Way.

In Chapters 3 and 4, I discuss the fully disrupted globular cluster stellar streams 300S and GD-1. The progenitors of these streams both straddle a critical mass threshold for the formation of salty stars. They also each contain a star enhanced with *s*-process elements such as barium and yttrium, indicating these stars have been enriched by a binary companion. We explore the relationship between mass loss and the long-term survival of binary systems in globular clusters.

Lastly, in Chapter 5, I discuss Leiptr, the lowest mass dwarf galaxy stream identified to-date. Leiptr's progenitor was an ultra-faint dwarf galaxy, the least massive type of galaxy that has been identified. It was thought that disrupted ultra-faint galaxies would not be identifiable in the Milky Way, due to the large range of metallicities and velocities found in dwarf galaxy streams (see again Figure 1.1).

CHAPTER 2

CHEMICAL ABUNDANCES IN THE METAL-POOR GLOBULAR CLUSTER ESO 280-SC06: A FORMERLY MASSIVE, TIDALLY DISRUPTED GLOBULAR CLUSTER

This paper has been accepted for publication in the Open Journal of Astrophysics and is available on arXiv.org. Usman et al. [2025]

2.1 Abstract

We present the first high-resolution abundance study of ESO 280-SC06, one of the least luminous and most metal-poor gravitationally bound Milky Way globular clusters. Using Magellan/MIKE spectroscopy for ten stars, we confirm the cluster's low metallicity as [Fe/H] = -2.54 ± 0.06 and the presence of a nitrogen-enhanced star enriched by binary mass transfer. We determine abundances or abundance upper limits for 21 additional elements from the light, alpha, odd-Z, iron peak, and neutron-capture groups for all ten stars. We find no spread in neutron-capture elements, unlike previous trends identified in some metal-poor globular clusters such as M15 and M92. Eight of the ten stars have light-element abundance patterns consistent with second-population globular cluster stars, which is a significantly larger second-population fraction than would be expected from the low present-day mass of $10^{4.1}$ $M_\odot$. We estimate the initial mass of the cluster as $10^{5.4\breve{}5.7}$ $M_\odot$ based on its orbit in the Milky Way. A preferential loss of first-population stars could explain the high fraction of second-population stars at the present time. Our results emphasize

the importance of considering mass loss when studying globular clusters and their enrichment patterns.

2.2 Introduction

Globular clusters (GCs) were once thought to each be comprised of a simple stellar population where all stars had the same age and chemical abundance. However, chemical analyses starting in the 1970s have identified unexpected, correlated abundance patterns within these clusters [Osborn, 1971]. Generally in GCs, we find stars with light element abundances similar to solar abundances when scaled to the correct metallicity (the *first population*, or *1P*) and stars with correlated enhancements in nitrogen, sodium and aluminum, and depletions in carbon, oxygen and magnesium (the *second population*, or *2P*). Carretta et al. [2009b] and Mészáros et al. [2015] are both broad studies that spectroscopically map out this phenomenon in the Milky Way. There are a small number of GCs for which no 2P stars have been identified, including Ruprecht 106 and E3 in the Milky Way (Villanova et al. 2013; Salinas and Strader 2015) and NGC 419 in the Small Magellanic Cloud [Martocchia et al., 2017]. Although this abundance signature is both ubiquitous and unique in GCs, none of the mechanisms proposed for its origin are able to explain all of the observed properties of GCs (e.g. Bastian and Lardo 2018, Gratton et al. 2019, Milone and Marino 2022).

One clue to the origin of these systems is the relationship between the mass of the cluster and the fraction of 2P stars found therein. Previous work has found that more massive clusters contain a higher fraction of 2P stars than smaller clusters (e.g.

Bastian and Lardo 2018, using 2P star fractions from Milone et al. 2017 and masses from Baumgardt and Hilker 2018). This correlation is even more apparent when comparing the 2P star fraction to the calculated *initial mass* of a globular cluster, instead of comparing to the present-day mass [Gratton et al., 2019, Usman et al., 2024]. There appears to be an initial mass threshold, in the range $10^{4.7-5.0}\,M_\odot$, that a globular cluster must achieve in order to contain 2P stars. Once the initial mass passes this critical mass, clusters can achieve much higher enriched star fractions: GCs with initial masses around $10^{5.5}\,M_\odot$ and $10^{6.2}\,M_\odot$ contain 2P star fractions of approximately 50% and 75% respectively.

We can probe the low-mass end of this relation and further constrain the initial mass threshold by observing and analyzing the chemistry of low-mass, disrupting clusters, or that of fully disrupted clusters in the form of stellar streams. The S^5collaboration has done one such analysis on the stellar stream 300S [Usman et al., 2024]. This globular cluster remnant had an estimated stream mass of about $10^{4.5}\,M_\odot$, and one star in eight with an enrichment pattern consistent with 2P stars, significantly lower than the 2P fraction in intact Milky Way GCs of comparable current mass. However, the upper limit for the initial mass of the system was calculated to be $10^{4.9}\,M_\odot$. The enrichment of the stream agreed well with systems of comparable initial mass when compared using the stream progenitor's initial mass.

The exact mechanism that links the mass of a cluster and its enriched star fraction is obfuscated because of the complexities in calculating initial mass. Current calculations of globular cluster mass loss rely on relations inferred from N-body simulations, e.g. those performed in Baumgardt and Makino [2003], Lamers et al. [2005]

and Baumgardt and Hilker [2018]. In addition to this, the spatial distribution of 1P and 2P stars could impact the measured star fraction. For example, Lardo et al. [2011] found the clusters M2, M3, M5, M13, M15, M92 and M53 have more 2P stars towards their centers, though more recent surveys suggest M5 [Lee, 2017] and M15 [Nardiello et al., 2018] are more mixed than previously thought. A few clusters have shown evidence of dynamical mixing, with unenriched and enriched populations becoming spatially distributed throughout the cluster (e.g. NGC 6752, by Milone et al. 2013; NGC 6362, by Dalessandro et al. 2014). If a cluster is not sufficiently mixed prior to experiencing mass loss, 1P stars may be preferentially stripped from the cluster [Vesperini et al., 2021]. The resulting cluster would have a heightened enriched star fraction relative to its current mass.

While GCs can have large fractions of 2P stars, which are moderately enriched in nitrogen and depleted in carbon, there exists a distinct category of stars which are highly enriched in nitrogen, referred to as *nitrogen-enriched metal-poor* (NEMP) stars. NEMP stars are defined by Johnson et al. [2007] as having [N/Fe] $> +0.5$ and [C/N] < -0.5, while at low metallicity, [Fe/H] < -2.0. Unlike 2P stars, NEMP stars are thought to be enriched via accretion from a companion star on the asymptotic giant branch (AGB, Aoki et al. 2007, Pols et al. 2012). Evidence for this enrichment mechanism is supported by the common co-identification of *s*-process elements, such as barium, strontium and yttrium which are synthesized by AGB stars [Luck and Bond, 1991, Izzard et al., 2009]. Stars with similar nitrogen and *s*-process enhancement can sometimes be referred to as barium-enhanced or Ba stars (e.g. Luck and Bond 1991, D'Orazi et al. 2010) and carbon-enhanced or CH stars (e.g. Côté et al.

1997).

Since NEMP/Ba/CH stars are thought to form in binaries, GCs may not be an ideal location for the evolution of these stars, as the high density of stars in GCs causes binary systems to be disrupted [Côté et al., 1997]. Indeed, D'Orazi et al. [2010] observed 1,205 red giant branch stars in GCs and identified just five Ba stars, a rate of 0.4%, compared to the 2% rate of Ba stars among field stars [Luck and Bond, 1991]. The authors also suggest the higher rate of Ba stars among 1P stars relative to 2P stars is indicative of the environment in which 2P stars form: a denser environment would both allow for 2P stars to form and disrupt binary systems, causing the rates of 2P stars and Ba stars to be anti-correlated.

Similarly, a Ba-enriched star has been identified in the aforementioned globular cluster stellar stream 300S [Usman et al., 2024]. The identification of a mass-transfer star in a stellar stream could indicate a disrupting or fully disrupted system could be a more hospitable environment for the long-term survival of binary stars. By exploring and chemically tagging stars in such systems, we can further probe the relationship between these GCs and their enriched star populations.

ESO 280-SC06 is one of the faintest and most metal-poor GCs in the Milky Way currently known. ESO 280-SC06 was discovered by the ESO/Uppsala survey of the southern sky and was originally identified as an open cluster [Holmberg et al., 1977, Lauberts, 1982]. The cluster was classified as a GC several decades later by Ortolani et al. [2000], and was found to have a metallicity of $[\mathrm{Fe/H}] = -1.8$ and a distance of 21.9 kpc. The metallicity of the cluster was re-measured as part of a survey of 153 clusters observed by Bica et al. [2006] and was found using photometry from La Silla

telescope to have a metallicity of [Fe/H] = −2.00 and a distance of 21.7 kpc from the sun. The cluster was studied again using 2MASS photometry by Bonatto and Bica [2008] and found to have a metallicity of [Fe/H] = −1.8 and a total magnitude of $M_V = -4.9$. The authors suggest this total magnitude should be treated as a lower limit, as the analysis does not take into account different spectral types of stars and ESO 280-SC06 is particularly far at a distance of ∼22 kpc. The magnitude was later remeasured by Baumgardt et al. [2020] using the Hubble Space Telescope and ground-based photometry and was indeed found to be brighter than the previous estimate, at a magnitude $M_V = -4.28$.

Simpson [2018] observed ESO 280-SC06 using the 2dF/AAOmega spectrograph on the Anglo-Australian Telescope and identified 13 red giant branch member stars. The author used calcium triplet line strengths to infer a cluster metallicity of [Fe/H] $= -2.48^{+0.06}_{-0.11}$ and measured a mass of $10^{4.1\pm0.1}\,M_\odot$. These cluster parameters were later revised again by Simpson and Martell [2019], who observed and identified 23 member stars in the cluster. The authors measured a metallicity of [Fe/H] = −2.47, found the cluster's distance to be 20.6 kpc from the Sun and identified an NEMP star. The distance to the cluster was later revisited by Baumgardt and Vasiliev [2021], who found the distance to be 20.95 ± 0.66 kpc, in agreement with Simpson and Martell [2019]. Massari et al. [2019] combined kinematic data from *Gaia* with estimated cluster ages for Milky Way GCs and analyzed their integrals of motion in order to identify common origins. The authors suggest that ESO 280-SC06 originally formed in the Gaia-Sausage-Enceladus (*GSE*, Belokurov et al. 2018, Helmi et al. 2018), and fell into the Milky Way with its host galaxy. There are currently no estimates of

multiple population fractions in ESO 280-SC06.

In this paper, we observe and analyze 10 red giant branch stars in the cluster to estimate its 2P star fraction. Here we present the chemical abundances of these 10 stars with high-resolution spectroscopy using the Magellan telescopes. In Section 2.3, we detail our observations. Section 2.4 describes our chemical abundance analysis methods and results. In Section 2.5, we report a kinematic analysis of ESO 280-SC06. We discuss our results in Section 2.6 and conclude in Section 2.7.

2.3 Observations and Data Reduction

We selected ten of the brightest member stars of ESO 280-SC06 from Simpson [2018] and Simpson and Martell [2019] to observe with Magellan/MIKE [Bernstein et al., 2003]. Observations were conducted on March 9, June 23-24, and July 25-27 in 2017. Data from adjacent nights were reduced together with CarPy [Kelson, 2003]. All 10 stars were observed with a $0.7'' \times 5.0''$ slit, with 2×2 on-chip binning to reduce read noise. The slit yields a spectral resolution of $\sim$28,000 and $\sim$35,000 in the red and blue, respectively. We can see an example of these spectra in Figure 2.1, which shows the measured sodium doublet and aluminum line. Each order of each reduced spectrum was normalized using a third degree natural spline. Radial velocities are measured by cross-correlating the Mg b region with a high signal-to-noise spectrum of HD122563. After correcting for the radial velocities, data from different runs are combined order-by-order using an inverse-variance weighted average of the individu-

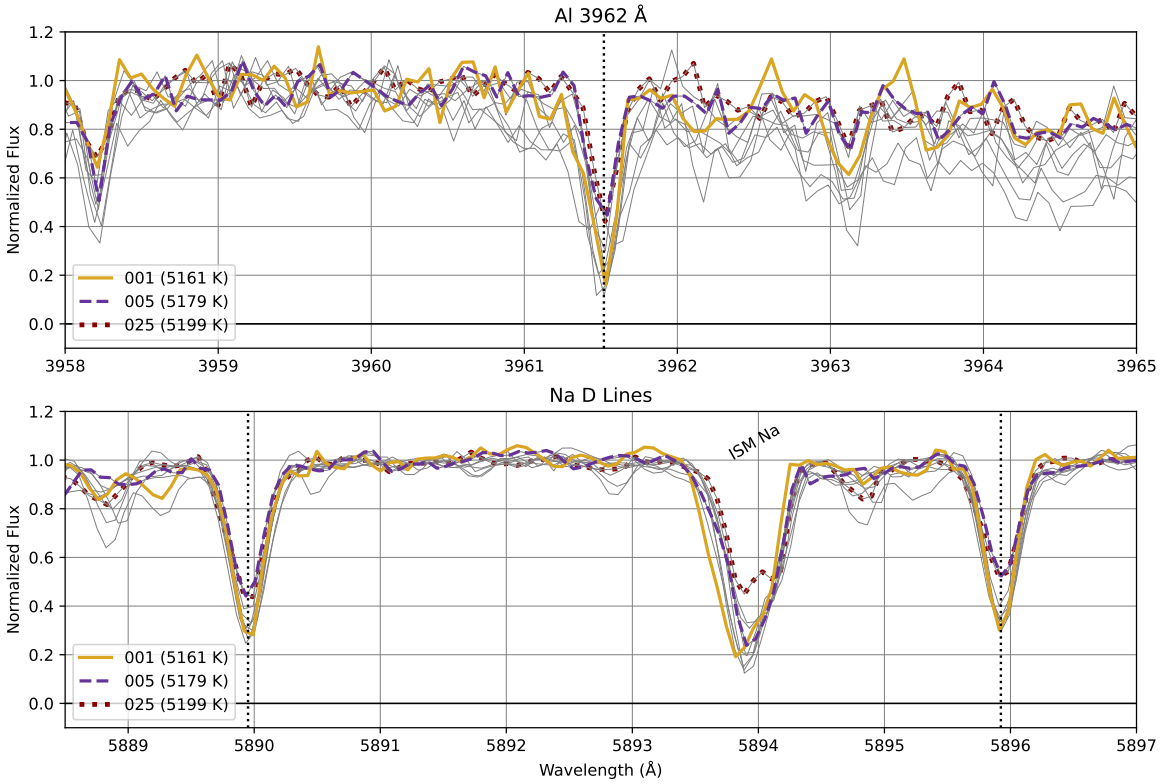

Figure 2.1 The normalized spectra of the ESO 280-SC06 stars around the measured sodium doublet at 5890 and 5896 Å (top) and the measured aluminum line at 3962 Å (bottom). The thin, dotted vertical lines indicate the precise locations of the sodium lines and aluminum line in their respective panels. Stars 001, 005 and 025 are represented by a gold solid line, a blue dashed line, and a dotted red line, respectively. All stars have a temperature around 5180 K. Despite the similar temperatures, stars 005 and 025 clearly display much weaker sodium and aluminum absorption lines. This demonstrates that both stars are 1P stars, while star 001 is a 2P star. The other stars' spectra are shown as thin gray lines in the background. In the bottom panel, *ISM Na* indicates an absorption feature in the spectrum due to sodium in the interstellar medium.

Variables		Values	Source
RA	(h:m:s)	18:09:06.0	Harris [1996]
Dec	(d:m:s)	−46:25:23	Harris [1996]
Distance	(kpc)	20.95 ± 0.66	Baumgardt and Vasiliev [2021]
Proper Motion RA	($\mathrm{mas\,yr^{-1}}$)	−0.55	Simpson and Martell [2019]
Proper Motion Dec	($\mathrm{mas\,yr^{-1}}$)	−2.69	Simpson and Martell [2019]
Radial Velocity	($\mathrm{km\ s^{-1}}$)	94.9 ± 0.5	Simpson and Martell [2019]
M_V		-2.48	Baumgardt et al. [2020]
Core Radius	(pc)	1.5 ±0.0	Simpson [2018]
Tidal Radius	(pc)	53.1 ± 15.0	Simpson [2018]
M_{fin}	($\mathrm{M_\odot}$)	$10^{4.0-4.2}$	Simpson [2018]
M_{ini}	($\mathrm{M_\odot}$)	$10^{5.4-5.7}$	
Apocenter	(kpc)	13.8	
Pericenter	(kpc)	1.23	
Eccentricity		0.84	
[Fe/H]		-2.54 ± 0.06	
2P Fraction		$0.80^{+0.07}_{-0.18}$	

Table 2.1 Summary of ESO 280-SC06 Properties. The distance, proper motions, radial velocity, current mass M_{fin} and radius measurements are from literature sources. We discuss our measured metallicity and 2P star fraction in Section 2.4, Subsection 2.4.3. The orbital parameters are discussed in Section 2.5 and we calculate the initial mass in Subsection 2.5.1.

ally normalized spectra, then stitched into a single spectrum[1]. Table 2.1 details the cluster parameters and Table 2.2 details each star's observations.

2.4 Chemical Abundance Analysis

2.4.1 Stellar Parameters

For our analysis, we estimate the stellar parameters using *Gaia* photometry. First, we dereddened using Equation 1 from Collaboration et al. [2018]. We used reddening data from Schlegel et al. [1998] with corrections from Schlafly and Finkbeiner [2011]. We accessed the E(B–V) from the online database IRSA.[2] We then used the dereddened photometric data to estimate the $T_{\rm eff}$ and log g using Equation (1) from Mucciarelli et al. [2021] for BP−RP and Equation (3) from Ji et al. [2020b], respectively.

We note that the photometric temperature for star 184 was more sensitive than the other stars to the choice of color used in the photometric relation from Mucciarelli et al. [2021]. We suspect this star is an AGB, and therefore does not exactly follow predicted temperatures for RGB stars described in the relations. We subsequently chose to use the temperature resulting from BP−RP, as this was both the median photometric temperature and was consistent with the color relation used for the other observed stars. To account for our uncertainty on temperatures in AGB stars relative to predictions for RGB stars, we use an increased uncertainty of 200 K for

1. Code available at https://github.com/alexji/alexmods/blob/master/alexmods/specutils/continuum.py

2. https://irsa.ipac.caltech.edu/applications/DUST/

Star	Gaia ID	*Gaia* G (mag)	t_{exp} (min)	SNR 4500Å	SNR 6500Å	$v_{\rm hel}$ (km s^{-1})	$T_{\rm eff}$ (K)	log g (dex)	ν_t (km s^{-1})	[Fe/H] (dex)
001	6719598998858700032	17.22	120	16	34	95.0	5161 ± 75	2.19 ± 0.15	1.48 ± 0.2	-2.50 ± 0.2
003	6719599101937916544	16.58	171	16	43	93.0	4988 ± 75	1.86 ± 0.15	2.27 ± 0.2	-2.68 ± 0.2
005†	6719599209329902720	16.48	100	20	44	93.1	5179 ± 75	1.90 ± 0.15	1.82 ± 0.2	-2.48 ± 0.2
008	6719598998858703744	15.98	70	18	42	90.9	4967 ± 75	1.60 ± 0.15	2.08 ± 0.2	-2.47 ± 0.2
016	6719599174970284928	15.86	60	21	47	93.4	4900 ± 75	1.54 ± 0.15	1.89 ± 0.2	-2.50 ± 0.2
025†	6719599170657398400	16.39	134	19	44	92.6	5199 ± 75	1.87 ± 0.15	2.39 ± 0.2	-2.54 ± 0.2
026‡	6719598900092253184	16.51	139	20	50	91.9	4907 ± 75	1.79 ± 0.15	1.83 ± 0.2	-2.38 ± 0.2
033	6719598174224943104	16.07	75	19	46	91.9	4783 ± 75	1.57 ± 0.15	2.16 ± 0.2	-2.59 ± 0.2
184*	6719599003157597184	14.16	15	20	58	89.0	4441 ± 200	0.65 ± 0.15	2.13 ± 0.2	-2.58 ± 0.2
576	6719598075458648576	14.64	40	28	70	93.0	4506 ± 75	0.86 ± 0.15	2.83 ± 0.2	-2.69 ± 0.2

Table 2.2 The stellar parameters of observed stars in this analysis. All stars are red giant branch stars, with the probable exception of star 184 (denoted by *), which appears to be an asymptotic branch star. The effective temperatures $T_{\rm eff}$ are calculated using the relations described in Mucciarelli et al. [2021]. Star 184 returns three extremely different temperatures from these relations, depending on which color is used for the calculation. log g is calculated using the relation in Ji et al. [2020b]. The microturbulence velocity and metallicity are calculated in our spectroscopic analysis. Stars 005 and 025 (denoted with †) are the identified 1P stars. Star 026 (denoted with ‡) is the NEMP star identified in Simpson and Martell [2019].

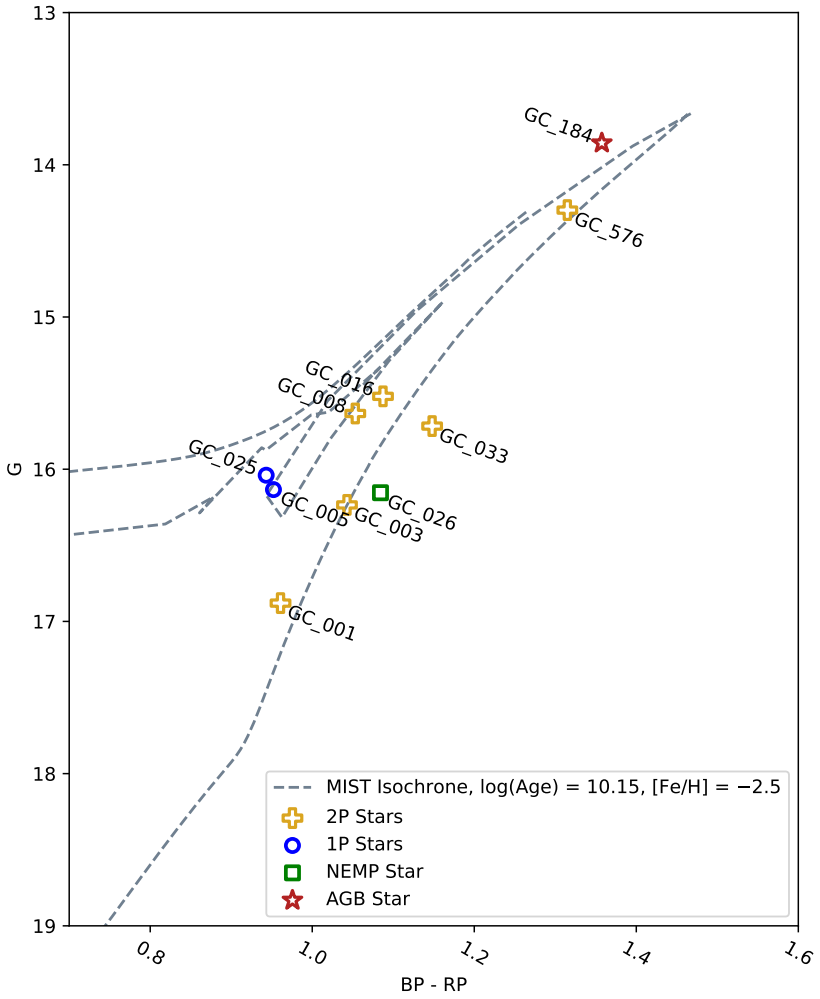

Figure 2.2 The color-magnitude diagram for ESO 280-SC06 stars. The dotted line represents a MIST isochrone with log age = 10.15 and metallicity [Fe/H] = −2.5 [Dotter, 2016, Choi et al., 2016]. We shift the isochrone to the red side by 0.08 (as was done in previous analyses such as Simpson 2018). The first-population / 1P stars, AGB star, NEMP star and remaining second-population / 2P stars are denoted to blue hollow circles, a red hollow star, a green hollow square and a yellow hollow plus symbols.

Element	Wavelength (Å)	expot	loggf		log ϵ	$e_{\rm stat}$	eqw	$e_{\rm eqw}$	FWHM	$e_{\rm Teff}$	$e_{\log g}$	$e_{\nu t}$	$e_{\rm MH}$	$e_{\rm tot}$
...	...	...	...	...		...	...	...	...	...	...	...	...	...
O I	6300.0	0.0	−9.82	<	7.069	–	–	–	–	–	–	–	–	–
Fe I	6400.001	3.603	−0.27		5.073	0.071	43.463	4.569	0.385	0.058	−0.006	−0.015	0.003	0.14
Fe I	6430.846	2.174	−1.95		5.124	0.082	39.666	5.224	0.325	0.081	−0.004	−0.013	0.003	0.15
Ca I	6439.075	2.524	0.47		4.248	0.081	72.584	5.399	0.443	0.041	−0.013	−0.037	0.002	0.14
K I	7664.911	0.0	0.125		3.279	0.047	66.39	3.393	0.365	0.049	−0.012	−0.032	0.002	0.123
K I	7698.974	0.0	−0.178		3.292	0.064	46.477	4.298	0.444	0.052	−0.008	−0.018	−0.001	0.13
Sc II	5030.0	–	–		0.684	0.294	–	–	0.188	0.04	0.054	−0.005	0.006	0.32
Sc II	4669.0	–	–		0.843	0.139	–	–	0.148	0.031	0.053	−0.006	0.006	0.18
...	...	...	...	...		...	...	...	...	...	...	...	...	...

Table 2.3 Example Line Table, Star 576. This table is available in its entirety in machine-readable form as part of the arXiv source. expot is excitation potential; loggf is oscillator strength; log ϵ is the absolute stellar abundance to H; e_{stat} is the statistical abundance uncertainty due to the equivalent width uncertainty; eqw is equivalent width; e_{eqw} is uncertainty in equivalent width; FWHM is the full width of the line at half maximum; $e_{T_{\rm eff}}$ is the difference on the abundance due to 1σ uncertainties on effective temperature, and similarly for e_g for the surface gravity, e_v for the microturbulence, and e_M for the metallicity. Elements with no listed equivalent width were measured using synthesis. The wavelengths of synthesized lines have been rounded to the nearest whole wavelength. Elements marked with the less-than symbol, <, are 3σ upper limits.

star 184, as is reflected in Table 2.2.

2.4.2 Abundance Calculations

The overall analysis steps follow the method performed in Atzberger et al. [2025]. The majority of the analysis was conducted using the code `SMHR` (first described in Casey 2014, most recently in Casey et al. 2025), which provides a graphical user interface to fit equivalent widths, synthesize more complex absorption regions, interpolate ATLAS model atmospheres [Castelli and Kurucz, 2003], run MOOG to determine chemical abundances through curves of growth [Sneden, 1973, Sobeck et al., 2011], and calculate stellar parameter and chemical abundance uncertainties [Ji et al., 2020b, Atzberger et al., 2025]. The uncertainty for each individual measurement is calculated by propagating uncertainties in the stellar parameters and in the equivalent width measurements through the abundance inference. An example of a line list and measured uncertainties are presented in Table 2.3 The overall abundance uncertainty for a star combines these individual uncertainties through a weighted average. For more details, see Atzberger et al. [2025]. The analysis is performed assuming local thermodynamic equilibrium (*LTE*), though for two elements we calculate additional corrections to account for non-LTE effects at the end of the analysis.

2.4.3 Measurements

Chemical abundances are measured using a combination of equivalent widths and synthesis. Our results are detailed in Tables 2.6–2.14. We include nLTE abundances

for Na and Al in these tables.

Metallicity. Metallicity was determined using Fe I lines, which are measured using equivalent widths. We use the nested sampling algorithm `dynesty` to calculate Bayesian posteriors for the cluster's mean metallicity and metallicity dispersion [Speagle, 2020, Higson et al., 2019, Koposov et al., 2022]. This method is identical to the method used for the abundance dispersion analysis in Usman et al. [2024] (Section 4.1), including the likelihood function (Equation 4). We find a mean metallicity for the entire cluster of [Fe I/H] $= -2.54 \pm 0.06$, with an upper limit dispersion of 0.09. Similarly, the mean metallicity for the entire cluster with Fe II is [Fe II/H] $= -2.55 \pm 0.05$, with an upper limit dispersion of 0.08. This metallicity is consistent with previous work, such as Simpson and Martell [2019].

Carbon and Nitrogen. Carbon and nitrogen are measured through synthesis of CH and CN molecular bands, respectively. For the CH bands, we measure the regions around 4310 Å and 4323 Å. For the CN bands, we measure the region around 3877 Å. These bands have significant absorption that are too complex to be modeled with an equivalent width, so we therefore synthesize these regions. For a few stars, there is no significant observable enrichment, and we instead estimate upper limits.

α elements. The α elements measured here are magnesium, silicon, calcium and titanium. Magnesium was measured using equivalent widths of five lines between 4500 and 5600 Å. Silicon was measured using an equivalent width at the wavelength 4102 Å and with a synthesis at 3906 Å. Calcium was measured using equivalent widths of a dozen absorption lines between 4200 and 6500 Å. Titanium I was measured using equivalent widths of six lines between 4500 and 5100 Å. Titanium II was

measured using equivalent widths of about 20 lines between 4000 and 4800 Å.

odd-Z elements. The odd-Z elements measured here are sodium, potassium and aluminum. Sodium was measured by synthesizing the sodium D lines at 5890 and 5896 Å. Aluminum was measured by synthesizing the absorption line at 3962 Å. We also synthesize a large hydrogen line located in the spectrum next to 3962 Å to ensure the aluminum line is accurately measured. While these abundances are measured assuming LTE, we also estimate nLTE corrections for sodium and aluminum, as discussed in Section 2.4.4. Potassium is measured using equivalent widths of the lines at 7664 and 7698 Å.

Iron-peak elements. Iron-peak elements measured here are chromium, manganese, nickel and zinc. Chromium was measured using equivalent widths at the lines 4652 and 5409 Å. Manganese was measured by synthesizing three lines at wavelengths 4824, 4782, and 4753 Å. Note that we exclude the manganese triplet around $4031-4033$ Å, as we expect that there are unaccounted uncertainties, perhaps due to nLTE effects. Nickel is measured using two equivalent widths at 4401 and 4714 Å, while the line at 5476 Å is synthesized. Lastly, zinc is measured using a synthesized line at 4811 Å.

Neutron-capture elements. The neutron-capture elements measured are strontium, yttrium, zirconium, barium, lanthanum, europium and dysprosium. Strontium II is measured by synthesizing 4078 and 4215 Å. Yttrium is measured by synthesizing lines at 4900, 4884 and 4397 Å. Zirconium is measured by synthesizing the line at 4208 Å. Barium is measured by synthesizing five lines between 4500 and 6500 Å. Lanthanum is measured by synthesizing four lines between 4000 and 5000 Å. Eu-

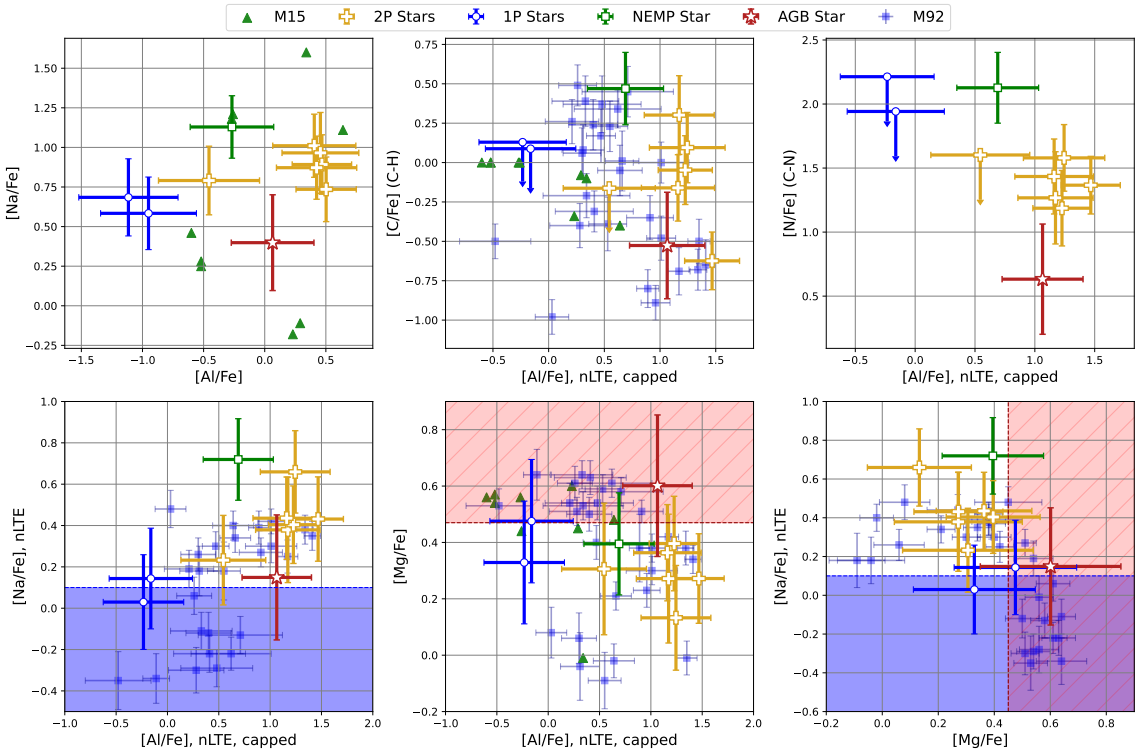

Figure 2.3 Key abundances for identifying chemical patterns found in multiple populations. The top left plot compares the LTE sodium and aluminum abundances. Directly below this, the bottom left plot adjusts these abundances to incorporate nLTE corrections. The top center, top right and bottom center plots compare the carbon abundances, nitrogen abundances and magnesium abundances, to the nLTE aluminum abundances. Lastly, the bottom right plot compares the nLTE sodium abundances to magnesium abundances. We identify eight stars with chemical enrichment patterns indicative of second-population/2P stars. Stars 005 and and 025 (represented by hollow blue circles) are the only stars that have low sodium and aluminum abundances, and are therefore classified as first-population/1P stars. The AGB star and the NEMP star (identified in Simpson and Martell 2019 are represented by a red hollow star and a green hollow square. The remaining second-population stars are represented by dark yellow plus symbols. For comparison, we also show abundances from M15 [Sobeck et al., 2011], represented by solid green triangles, and M92 [Kirby et al., 2023], represented by solid blue squares with error bars. For nLTE-corrected sodium abundances and magnesium abundances, we overlay a blue region and a light red hatched region to represent the diagnostic thresholds used in Kirby et al. [2023] to classify 1P stars: [Na/Fe] < 0.1 and [Mg/Fe] > 0.45 indicate a star is 1P.

ropium is generally too low to be measured using the line at 6645 Å, so in some stars, we synthesize up to three bluer lines between 4100 and 4450 Å.

2.4.4 nLTE Corrections

In the bulk of our analysis, we assume our stars are in local thermodynamic equilibrium, *LTE*. However, this assumption is often violated in massive stars. Some inferred abundances can therefore be over- or underestimated, and therefore we apply non-LTE (*nLTE)* corrections to account for this discrepancy.

The abundances of two key elements characteristic of multiple populations, aluminum and sodium, can often be misestimated due to nLTE effects. We determined nLTE abundance corrections for our stars from Lind et al. [2011] for sodium and Nordlander and Lind [2017] for aluminum. Table 2.4 provides aluminum and sodium corrections for each star. For sodium we used the average correction between lines 5890 and 5896 Å with a range of -0.6 to -0.2.

We used the line at 3961 Å for aluminum, which had a correction range of $+0.7$ to $+1.2$. However, Nordlander and Lind [2017] suggests that nLTE corrections may reach only as large as $+1$ dex. Corrections above that range may not be reliable above $+1$ dex, due to limitations in the grid models [Nordlander, 2019]. For this reason, we cap nLTE aluminum abundances to $+1$ dex if that limit was exceeded, as was the case for stars 008 and 184. Despite these capped corrections, both stars are very aluminum rich and are still classified as 2P stars.

We note that for some stars, the stellar parameters needed to be adjusted slightly to fit within the target parameter range to estimate the nLTE corrections. Stars

Star	Na	Al
001	−0.3510	+0.839
003	−0.5865	+0.717
005	−0.5540	+0.717
008	−0.5585	+1.131†
016	−0.4880	+0.759
025	−0.5410	+0.953
026	−0.4095	+0.958
033	−0.4365	+0.737
184	−0.2495*	+1.187*†
576	−0.3040*	+0.965*

Table 2.4 nLTE Corrections for aluminum and sodium. For the two coldest stars (marked with an asterisk *), the calculated surface gravity was less than one, log $g <$ 1. The nLTE calculators leverage sets of grids of stellar atmospheres which span a wide range of stellar parameters. The grids do not extensively cover surface gravities below log $g < 1$. We therefore round the surface gravity of the stars 184 and 576 up to log g =1. The calculated Al correction for stars 008 and 184 (denoted with a dagger †) are higher than 1; however, Nordlander and Lind [2017] suggests Al corrections above 1 are not reliable, and should instead be capped at 1. Despite using these reduced corrections, both stars have very high Al abundances and are therefore still classified as 2P stars.

184 and 576 were estimated using a log g of 1, instead of their true value. These adjustments may lead to a small error in these stars' corrections.

2.4.5 Abundance Results

Multiple Populations

In our analysis, we classify eight of the ten observed stars as 2P stars. The 1P stars are 005 and 025, which show relatively less sodium and aluminum relative to the remaining stars. In Figure 2.1, we compare the spectra of 1P stars 005 and 025 (represented by purple dashed and red dotted lines, respectively) to the spectrum of 2P star 001 (represented by a dark yellow solid line) in the region of the sodium D lines and the aluminum line at 3962 Å. All three stars have similar effective temperatures, $T_{\rm eff} \approx 5180$ K. Despite the similar stellar parameters, the stars 005 and 025 clearly exhibit significantly less absorption at the wavelengths of the aluminum and sodium lines relative to 001, indicating that the former are 1P stars while the latter is a 2P star.

We also compare our measured abundances to those of M92 [Kirby et al., 2023] in Figure 2.3. In Kirby et al. [2023], the authors define two thresholds for classifying 1P or 2P stars: stars with nLTE-corrected [Na/Fe] > 0.1 and/or [Mg/Fe] < 0.45 are considered 2P stars, though they specify that the constraint on sodium seems to be a more robust classifier. In our system, stars 005 and 025 show little enrichment in sodium or aluminum, with nLTE-corrected abundances [Na/Fe] $= 0.03$ and 0.14 and [Al/Fe] $= -0.23$ and -0.16, respectively. Star 025 additionally has high magnesium,

Element	Mean Abundance	Dispersion
[Fe/H]	-2.54 ± 0.06	<0.11
[Fe II/H]	-2.55 ± 0.05	<0.10
[C/Fe I]†	-0.17 ± 0.14	$0.20^{+0.20}_{-0.15}$
[N/Fe I]†	$0.95^{+0.04}_{-0.11}$	$0.29^{+0.27}_{-0.23}$
[Na/Fe I]	0.84 ± 0.07	<0.18
[Na/Fe I]$_{\rm nLTE}$	0.39 ± 0.07	<0.21
[Mg/Fe I]	0.34 ± 0.06	<0.13
[Al/Fe I]	0.03 ± 0.19	$0.44^{+0.22}_{-0.19}$
[Al/Fe I]$_{\rm nLTE}$	$0.84^{+0.11}_{-0.17}$	$0.41^{+0.21}_{-0.19}$
[Si/Fe I]	0.59 ± 0.09	<0.14
[K/Fe I]	0.70 ± 0.07	<0.12
[Ca/Fe I]	0.38 ± 0.06	<0.11
[Sc/Fe II]	0.10 ± 0.06	<0.12
[Ti/Fe I]	0.28 ± 0.07	<0.13
[Ti II/Fe II]	0.38 ± 0.07	<0.12
[V/Fe I]	0.11 ± 0.10	<0.19
[Cr/Fe I]	-0.17 ± 0.07	<0.15
[Mn/Fe I]	-0.38 ± 0.08	<0.14
[Co/Fe I]	0.16 ± 0.08	<0.14
[Ni/Fe I]	0.07 ± 0.07	<0.14
[Zn/Fe I]	0.20 ± 0.10	<0.17
[Sr/Fe II]†	0.21 ± 0.10	<0.25
[Y/Fe II]†	-0.12 ± 0.08	<0.14
[Zr/Fe II]	0.28 ± 0.09	<0.17
[Ba/Fe II]†	-0.34 ± 0.06	<0.12
[La/Fe II]†	-0.00 ± 0.12	<0.31
[Eu/Fe II]	0.38 ± 0.08	<0.18

Table 2.5 Cluster Abundance Means & Dispersions. Estimated abundance means and dispersions for ESO 280-SC06. The error bars represent 1σ confidence limits. Stars which have upper limits for a given abundance are excluded from its mean and dispersion calculation. Star 184 is excluded for elements which can be enriched in NEMP stars (denoted with †). If a dispersion cannot be measured, we give an upper limit at 95% confidence. If the two 1P stars, 005 and 025 are excluded from the analysis, we measure no dispersion in aluminum. We find an upper limit of 0.38.

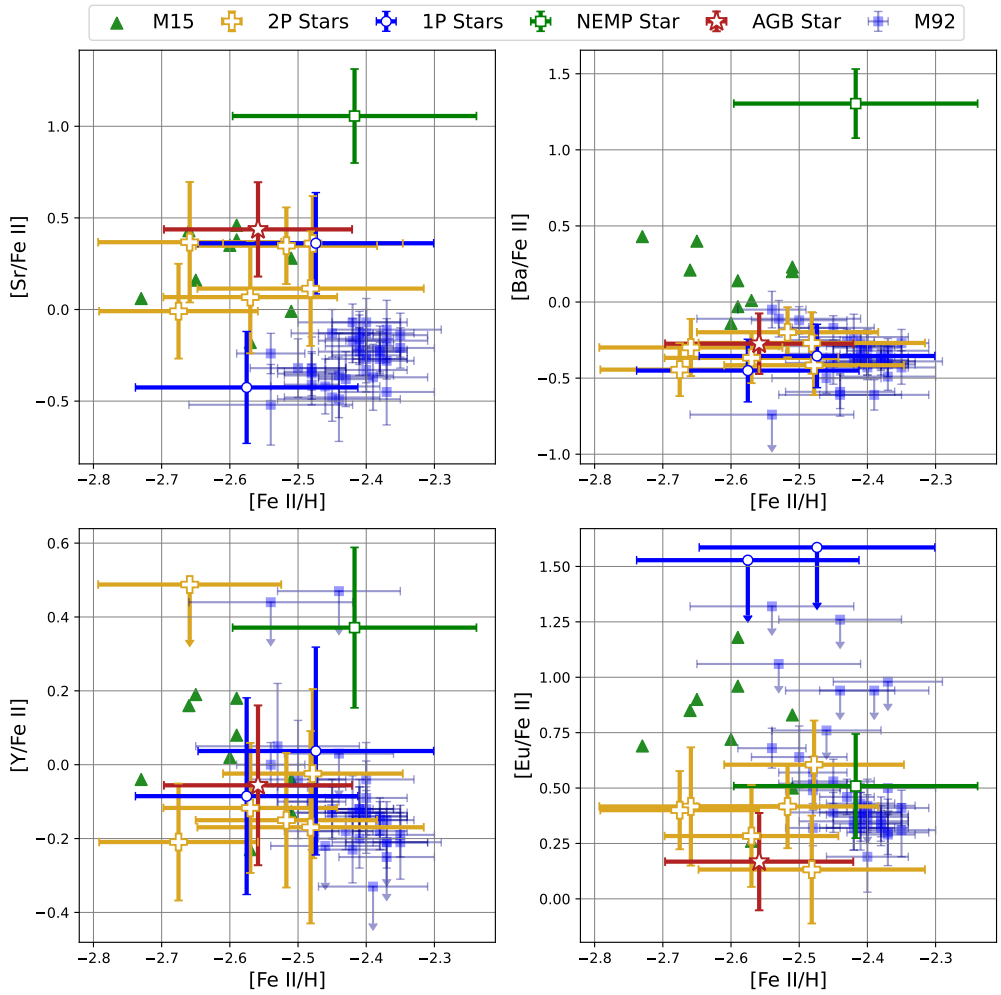

Figure 2.4 Neutron-capture abundances measured in the ESO 280-SC06 stars. The first-populations/1P stars, the AGB star, the NEMP star, and the remaining second-population/2P stars are represented by blue hollow circles, a red hollow star, a green hollow square and yellow hollow plus symbols, respectively. For comparison, we also compare to abundances from M15 [Sobeck et al., 2011], represented by green triangles, and M92 [Kirby et al., 2023], represented by blue squares with error bars. The NEMP star, 026, has significantly higher *s*-process abundances (strontium, barium, and yttrium) than the other stars. This is consistent with *s*-process enhancement predicted from accretion from an asymptotic giant branch binary companion. Among the other stars, we find no significant spread in neutron-capture abundances, contrary to patterns previously identified in other systems such as M92 [Kirby et al., 2023].

further conforming to expected chemical patterns.

A key feature of the multiple population phenomenon is the relative ratios of 1P to 2P stars in clusters, with more massive clusters having higher fractions of 2P stars. Specifically, we define the fraction of enriched stars as $f_{\rm enrich} = \frac{\rm 2P}{\rm 1P+2P}$. We therefore estimate ESO 280-SC06 has an 80% enrichment fraction, as eight of our ten stars are 2P stars. We can estimate error bars by assuming the cluster is comprised of two populations with some inherent fraction of enriched stars. Since there exists no known correlation between a star's magnitude and whether it is a 1P or 2P star [see the color magnitude diagrams from Piotto et al., 2015], we assume our sample of stars is a random draw from a binomial distribution with this endemic enrichment fraction. We therefore can infer the cluster's enrichment fraction to be $f_{\rm enrich} = 0.80^{+0.07}_{-0.18}$ using Bayesian statistics. We discuss further implications of this enrichment fraction with respect to the cluster's mass in Section 2.6, Subsection 2.6.1.

NEMP Star

Our analysis also confirms the nitrogen and *s*-process enrichment in star 026, as initially identified by Simpson and Martell [2019]. Figure 2.4 demonstrates star 026's enrichment in strontium, barium and yttrium relative to the other observed stars. We also demonstrate that star 026 does *not* present any enrichment in europium, indicating that the star is enriched specifically in *s*-process elements and not *r*-process elements. This enrichment pattern is consistent with mass transfer from an AGB companion, similar to stars identified in the 300S stream by Usman et al. [2024] and most recently in M55 by Da Costa and Nordlander [2025].

Although some of the surface abundances of star 026 have been altered by mass transfer, we are confident in our identification of it as a 2P star based on the Na, Mg and Al abundances. The lower-mass AGB stars that are the site of s-process nucleosynthesis are not a major site of the hot hydrogen burning that produces the O-Na and Mg-Al anticorrelations. We further discuss the implications of the mass-transfer star in Section 2.6, Subsection 2.6.2.

Neutron-Capture Spread

If we exclude the NEMP-s star, 026, from our analysis, we identify no significant neutron-capture spread in ESO 280-SC06. This contradicts previous expectations, as similarly metal-poor GCs M15 and M92 have been found to exhibit spreads in these elements [Sobeck et al., 2011, Kirby et al., 2023]. Since our abundance uncertainties conservatively include all propagated uncertainties from stellar parameters, our uncertainties may be too large to constrain these element dispersions. For example, Kirby et al. [2023] constrains a barium dispersion of $0.09^{+0.06}_{-0.05}$. Among our stars with our conservative uncertainty estimates, we are only able to constrain a dispersion of less than < 0.12 at 95% confidence. We therefore cannot achieve the same level of precision presented in Kirby et al. [2023].

We further discuss the implications of these neutron-capture element spreads in GCs in Section 2.6, Subsection 2.6.3.

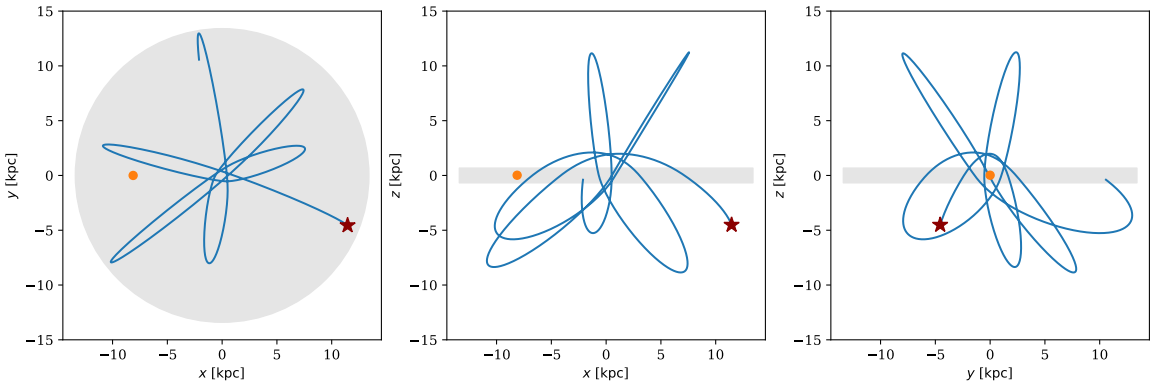

Figure 2.5 Three views of the Galactic orbit of ESO 280-SC06. The present position of the cluster is marked with a red pentagon, and its orbit over the past 1 Gyr is shown as a blue line. The high eccentricity and inclination of ESO 280-SC06's orbit mean that it has significant disk crossings at each pericenter passage, roughly every 150 Myr. The position of the Sun is shown with a yellow circle. The Milky Way is represented by the gray circle in the XY plane, and the thick gray line for side-on views in XZ and YZ planes. This orbit was integrated using `gala` with the default `MilkyWayPotential`.

2.5 Kinematic Analysis

We used `gala` [Price-Whelan, 2017, Price-Whelan et al., 2020] to integrate the Galactic orbit and calculate kinematic properties of ESO 280-SC06, using the built-in `MilkyWayPotential`. The coordinates, proper motion components, and distance are adopted from Simpson and Martell [2019] and summarized in Table 2.1. We used a time step of 0.1 Myr and integrated backwards for 1 Gyr.

The orbit is shown in Figure 2.5. ESO 280-SC06 is currently located on the far side of the Milky Way disk from the Sun. Its orbit has an apocenter of 13.7 kpc, pericenter of 1.2 kpc, and eccentricity of 0.83. The ESO 280-SC06 orbit intercepts the Milky Way disk many times. This tight orbit could cause the cluster to lose a

significant amount of mass over its lifetime.

2.5.1 Initial Mass Estimate

Based on the orbital parameters, we estimate the mass loss of ESO 280-SC06 in order to estimate the cluster's mass at formation. We estimate this initial mass using two separate methods:

Method 1: The first method accounts for mass loss due to stellar evolution and tidal dissolution.We model the globular cluster using a Kroupa initial mass function (*IMF*, Kroupa 2001). We use the parameters for a system with metallicity fraction Z = 0.004 from Table 1 of Kruijssen and Lamers [2008]. A metallicity of [Fe/H] = −2.5 is approximately equivalent to a metallicity of (Z = 0.003), so this approximation is accurate for our purposes. Given this IMF, the fractional mass loss from stellar evolution q, given in Equation 2 in Lamers et al. [2005] as a function of time t is:

$$\log q(t) = (\log t - 6.9)^{0.256} - 1.696. \tag{2.1}$$

We then use this to estimate the amount of mass still bound in the cluster by Equation 3 of the same paper:

$$\mu(t) = 1 - q(t) \tag{2.2}$$

We additionally account for the dissolution due to two-body relaxation, as de-

scribed with Equation 7 of Kruijssen and Mieske [2009]:

$$t_0 = t_{0,\odot} \left(\frac{r_{apo}}{8.5\text{kpc}} \right) \left(\frac{V_c}{220 \frac{km}{s}} \right)^{-1} (1 - \epsilon) \tag{2.3}$$

where t_0 and $t_{0,\odot}$ are the dissolution times of our system and a system at the Galactocentric distance of the Sun, r_{apo} is the distance at the orbit's apocenter, V_c is the circular velocity at r_{apo} and ϵ is the orbital eccentricity.

These are used to calculate the initial mass M_i using Equation 7 of Lamers et al. [2005]:

$$M_i \approx \frac{1}{\mu(t)} \times \left(\frac{M}{M_\odot} + \left(\frac{\gamma t}{t_0} \right)^{\frac{1}{\gamma}} \right) \tag{2.4}$$

where γ is the index describing mass loss, and is set to 0.7 for clusters [Lamers et al., 2010].

We use the current mass $10^{4.1}\,\mathrm{M}_\odot$ (as determined by Simpson 2018) and the orbital parameters described in Section 2.5. Through this method, we find an initial mass of $10^{5.4} M_\odot$.

Method 2: We also calculate the initial mass, assuming mass loss driven by internal dynamical interactions and tidal stripping, as quantified in Baumgardt et al. [2019]. The current mass of a cluster can be calculated by:

$$M(t) = \frac{M_{\text{ini}}}{2} \left(1 - \frac{t}{T_{\text{diss}}} \right) \tag{2.5}$$

where M_{ini} is the cluster's initial mass and T_{diss} is the cluster's dissolution time in

Myr. The latter can be calculated with Equation 5 of Baumgardt et al. [2019]:

$$T_{\rm diss} = 1.35 \times \left(\frac{M_{\rm ini}}{\ln(0.02 N_{\rm ini})} \right)^{0.75} \times \frac{r_{\rm apo}}{V_c} \times (1 - \epsilon) \tag{2.6}$$

where $N_{\rm ini}$, is the initial number of stars, which is estimated by $N_{\rm ini} = M_{\rm ini}/0.65$ with the assumption that the average star's mass is 0.65 $M_\odot$, using the same Kroupa [2001] IMF as in Baumgardt et al. [2019]. We use the same parameters as in Method 1, as seen in Table 2.1. For this method, we additionally calculate the initial mass given a range of disruption times, $11-14$ Gyr, as we do not know exactly when the cluster was accreted onto the Milky Way.

We set the current mass equal to the mass estimate from Simpson and Martell [2019], $10^{4.1}\,M_\odot$, and solved for an initial mass which could disrupt to its current mass. We find the initial mass is between $10^{5.5-5.7}\,M_\odot$. The uncertainties in mass loss are large enough that this mass estimate is relatively consistent with the estimate from the previous method. We therefore estimate that the initial mass is in the range $10^{5.4-5.7}\,M_\odot$. ESO 280-SC06 has therefore lost between 95 and 98% of its initial mass.

2.6 Discussion

ESO 280-SC06 is a distinctly low-metallicity and low-mass globular cluster. By spectroscopically identifying multiple populations in this system, we can probe one of the lowest-mass gravitationally bound systems to improve our understanding of the relationship between the mass of a cluster and the chemical enrichment found

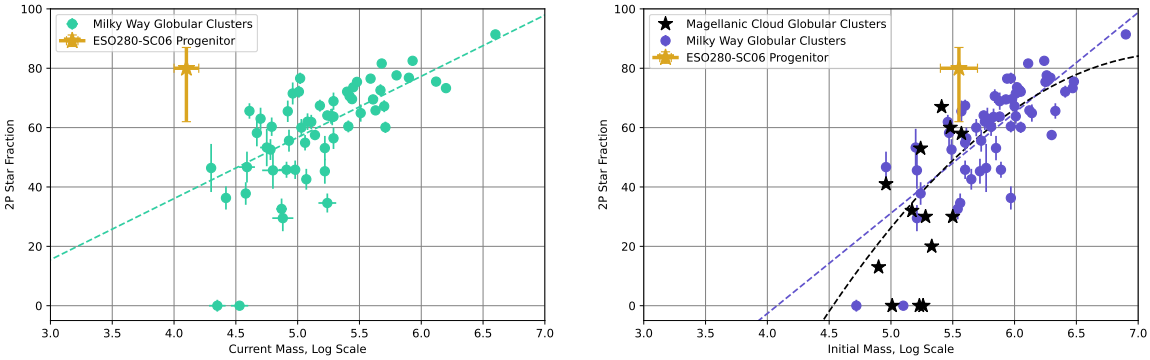

Figure 2.6 The fraction of 2P stars in GCs as a function of current mass (left) and initial mass (right). The current and initial masses of Milky Way globular clusters (*MW GCs*) are represented by green circles on the left and purple circles on the right, respectively [Milone et al., 2017, Baumgardt et al., 2019]. Globular clusters in the Magellanic Clouds (*MC GCs*), which should not experience significant mass loss, are represented by black stars. (Data for MC GCs are from Mucciarelli et al. 2009, Mateluna et al. 2012, Mucciarelli et al. 2014, Hollyhead et al. 2017, Niederhofer et al. 2017b,a, Martocchia et al. 2017, Hollyhead et al. 2018, Zhang et al. 2018, Martocchia et al. 2018, and Hollyhead et al. 2019 and were compiled by Gratton et al. 2019.) ESO 280-SC06 is represented by the dark gold star. Measurements for the 300S stellar stream are represented by a red cross [Usman et al., 2024]. The dashed and dotted lines represent linear and quadratic fits between the 2P star fraction and cluster mass.

therein.

2.6.1 Enrichment Fraction vs. Cluster Mass

The current mass of ESO 280-SC06 is $10^{4.1\pm0.1}$ $M_\odot$ [Simpson, 2018]. When compared to gravitationally bound clusters of comparable mass, the cluster appears to have a significantly high fraction of multiple population stars. Clusters of similar current mass generally have a 2P star fraction of 40%, as can be observed in the left panel of Figure 2.6.

Given the primordial nature of GC abundance anticorrelations, one might expect that initial mass is a better predictor for the fraction of 2P stars [e.g., Bastian and Lardo, 2018, Usman et al., 2024]. When comparing our fraction of 2P stars relative to our estimated initial mass of $10^{5.55\pm0.15}$, our enrichment of 80% still appears high relative to comparable systems, but is within error bars of the general trend. This relationship is demonstrated in the right panel of Figure 2.6.

It is possible that our sample of ten stars has an unusually high fraction of 2P stars and is not an accurate representation of the cluster. However, we do not anticipate any selection effects that favor 2P stars over 1P stars. We chose the brightest stars available to follow up in our sample, and there is not any known correlation between 1P / 2P status and the brightness of the star [Bastian and Lardo, 2018]. We must also consider that the high fraction of 2P stars relative to initial mass could indicate that our initial mass estimate is too low. This would indicate that current models for mass loss may not fully encapsulate losses in extreme cases like ESO 280-SC06, for which the orbit never strays farther than 14 kpc from the Galactic center and crosses the plane of the disk relatively frequently.

Alternatively, ESO 280-SC06's high enrichment fraction may indicate preferential stripping of 1P stars. Vesperini et al. [2021] carried out simulations of the impact of stellar dynamics in clusters on the spatial distribution of the 2P stars. The authors find that clusters will preferentially have 2P stars towards the center, and 1P stars are more likely to be stripped away by external influences. In these simulations, the clusters will dynamically mix over time, causing a higher proportion of 2P stars to be lost at later times. If ESO 280-SC06 experienced significant mass loss very

early in its lifetime, it may have preferentially lost a higher proportion of 1P stars because that dynamical mixing had not yet occurred. Observing and chemically tagging stars that have been tidally stripped from ESO 280-SC06 could confirm or contradict this theory, because a much higher fraction of 1P stars would be expected in the population of tidally stripped stars. Other clusters with low present-day masses may have more time to spatially homogenize prior to losing a significant portion of their stars, causing them to have an overall lower fraction of 2P stars observed today relative to ESO 280-SC06.

2.6.2 NEMP Star

In the previous work of Simpson and Martell [2019], a nitrogen-enriched metal poor star (NEMP) was identified using medium-resolution spectroscopy on 3.9-m Anglo-Australian Telescope using its AAOmega spectrograph. We re-observe this star using high-resolution spectroscopy using Magellan/MIKE. We find, in addition to nitrogen enhancement, the star is enhanced in *s*-process elements including strontium, yttrium, barium and lanthanum. Stars with this type of abundance anomaly are sometimes referred to as CEMP-s stars, CH stars or Ba stars, depending on the context (e.g. Luck and Bond 1991, D'Orazi et al. 2010, Côté et al. 1997).

This particular combination of chemical enrichment is indicative of mass transfer from a binary companion. These stars are unusual in GCs, e.g. a previous study by D'Orazi et al. [2010] of 1,205 red giant branch stars in GCs found just five stars of this type. Of the five post-mass transfer stars identified in that study, just one was classified as a 2P star. The authors suggest that high-density environments

which give rise to 2P globular cluster stars are significantly more likely to disrupt binary star systems before any type of mass transfer can occur. Dynamical studies of stellar multiplicity in cluster environments [e.g., Ferraro et al., 2023] find correlations between cluster density and binary evolution outcomes. Therefore, the presence of these *s*-process enhanced stars could potentially be used as a probe of dynamical interactions within a proto-globular cluster environment.

While dense GC environments may disrupt the long-term survival of binary systems, it remains unclear whether a disrupted globular cluster would provide a more suitable environment for the survival of binary systems. A similar post-mass transfer star was also identified in the 300S globular cluster stellar stream [Usman et al., 2024]. The detection of a post-mass transfer star in both a low-mass cluster that has undergone significant mass loss and the fully disrupted globular cluster stellar stream 300S could indicate that the same mechanism that aids the creation of these mass-transfer stars also impacts the cluster's ability to retain stars. After all, the rate of mass-transfer stars among the globular cluster stars in D'Orazi et al. [2010] is 0.4% and in field stars is 2% [Luck and Bond, 1991]. Even if star 026 is the *only* mass-transfer star out of the 45 members of ESO 280-SC06 identified in Simpson and Martell [2019], ESO 280 would still have a rate of mass-transfer stars five times higher than D'Orazi et al. [2010] found in GCs and comparable to the rate in the field. Perhaps this increased rate of post-mass transfer stars hints that the weakening of the gravitational potential of a cluster both inhibits the destruction of binary star formation, and enhances the mass loss rate and subsequent dissolution of the cluster. Further exploration into the dynamics of binary systems in GCs during periods of

significant mass loss is planned as future work as these systems could shed light on preferential natal environments for mass-transfer binaries.

2.6.3 Neutron-Capture Spread

In addition to light-element variations, some GCs have variations in neutron-capture elements. These variation patterns were first identified in M15 by Sneden et al. [1997], which found correlated abundances of barium and europium. These neutron-capture variations were later confirmed by Sneden et al. [2000], Otsuki et al. [2006], Sobeck et al. [2011], Worley et al. [2013] and Cabrera Garcia et al. [2024]. The correlation of barium and europium indicates that these elements were created through an r-process nucleosynthetic event (or events), instead of by the s-process. This substantially complicates the chemical evolution of GCs, because while both light element and s-process element variations can be created in AGB stars, they are not expected to create significant amounts of r-process elements. Thus, additional nucleosynthetic processes are required to account for the r-process enrichment. Additionally, the r-process elements in M15 have no apparent correlation with light-element abundances, i.e. there is no relationship between r-process enrichment and 1P or 2P populations. The lack of relationship between r-process and multiple stellar populations indicates that these processes did not develop concurrently in M15.

Similarly, the globular cluster M92 was found to have a significant spread in r-process elements such as yttrium, zirconium, lanthanum and europium, which again were uncorrelated with the light element enrichment patterns indicative of multiple stellar populations in Roederer and Sneden [2011]. The authors found evidence of

similar r-process dispersions in M5 and NGC 3201. In her study of 12 red giant branch stars in M92 using high-resolution spectra from Keck, Cohen [2011] is unable to replicate a spread in r-process elements. The author demonstrates that the correlation between absorption line strength and the stellar parameters of the observed stars, and suggests that the previously identified r-process dispersion was a result of previously unidentified systematic uncertainties. Roederer and Thompson [2015] followed up on these results by analyzing 15 red giant branch stars in NGC 4833 using Magellan/MIKE and found similar heavy element spreads that could be attributed to systematics. The authors concluded the metallicity dispersions in Roederer and Sneden [2011], with the exception of M15, were likely due to these systematic uncertainties.

More recently, Kirby et al. [2023] found the r-process spread in M92 to have an interesting relationship with the cluster's multiple stellar populations: 1P stars exhibited a strong dispersion in r-process enrichment, while 2P exhibited very little spread. For example, the authors find that barium, lanthanum, and europium have dispersions of $0.09^{+0.06}_{-0.05}$, $0.18^{+0.10}_{-0.06}$, and $0.14^{+0.08}_{-0.06}$ in M92's 1P stars, respectively. In the 2P stars, however, they constrain the dispersions to < 0.02, < 0.08, and < 0.03, respectively The authors suggest that an r-process nucleosynthetic event occurred as the first stars began to form, inhomogeneously enriching the gas which formed into 1P stars and resulting in these early stars. By the time the 2P stars formed, the star-forming gas was sufficiently mixed such that the later generation of stars had consistent r-process enrichment. Both of these clusters with confirmed r-process enrichment are relatively low-metallicity, with measured [Fe/H] $\simeq -2.4$.

Kirby et al. [2023] suggested that, at higher metallicities, variations in r-process enrichment would look insignificant relative to high levels of inherent iron enrichment in the cluster's natal gas.

We expect ESO 280-SC06 to be a good probe of r-process dispersion, as it is the lowest-metallicity intact globular cluster in the Milky Way at our measured metallicity of [Fe/H] $\simeq -2.54$. The initial observations of ESO 280-SC06 presented here were intended to measure the dispersion of neutron-capture elements. However, we are unable to measure a spread in any of our measured neutron-capture elements. Excluding stars with upper limit measurements and the NEMP-s star, which is enriched in s-process, we constrain barium, lanthanum and europium dispersions to < 0.12, < 0.31 and < 0.18, respectively at 95% confidence, as shown in Table 2.5. We may be unable to constrain these dispersions as strongly as Kirby et al. [2023] due to our conservative abundance uncertainties, which include propagated uncertainties due to stellar parameter uncertainties. Alternatively, this may simply mean that any r-process nucleosynthetic process in ESO 280-SC06 occurred significantly earlier than the cluster's period of star formation, allowing for sufficient gas mixing to create a relatively uniform enrichment pattern within the cluster.

Lastly, the lack of spread may be due to ESO 280-SC06's high 2P star fraction. Kirby et al. [2023] specifically identifies abundance dispersions in M92's 1P stars. Since our sample contains just two 1P stars, we may not have a high enough fraction of 1P stars to measure similar abundance spreads. Identifying more 1P stars in ESO 280-SC06, or 1P stars that were stripped from the cluster during its orbit, may allow for a stronger constraint on neutron-capture abundance spreads.

2.7 Conclusion

In this paper, we have constrained the fraction of 2P stars in the low-mass, metal-poor globular cluster ESO 280-SC06. We find it to be surprisingly enriched, with a 2P star fraction of $\sim 80\%$. GCs of comparable current mass generally have a 2P star fraction of 40% or less.

However, recent work suggests initial mass is a more accurate predictor of 2P star fraction than current mass [Gratton et al., 2019, Usman et al., 2024]. We use two different methods to calculate the initial mass, and conclude that ESO 280-SC06 formed with a mass in the range of $10^{5.4-5.7}\,M_\odot$. The cluster has therefore lost approximately 95 to 98% of its initial mass, significantly higher than the typical cluster. In N-body simulations over various orbits, globular clusters lose on average 80% of their initial mass [Baumgardt et al., 2019].

Even when comparing the initial mass of the clusters, ESO 280-SC06 still appears more enriched in 2P stars relative to other Milky Way clusters. While this could be explained by a potentially unrepresentative sample, overenrichment could indicate that current mass loss models cannot fully describe the disruption caused along extreme orbits. ESO 280-SC06's orbit varies between 1 kpc and 14 kpc from the Galactic center, and crosses the disk every ~ 150 Myr. This eccentric and tight orbit may experience stronger interactions and disruption than is currently modeled with simplified mass loss estimates.

Another possibility for the high enrichment fraction could be the preferential stripping of 1P stars in the cluster. 2P stars in GCs tend to be more centrally located than 1P stars at the time of formation, then mix over their lifetimes. If

ESO 280-SC06 experienced significant mass loss early in its lifetime, it may have not been dynamically mixed prior to experiencing tidal stripping. This uneven spatial distribution would result in 1P stars being stripped first from the cluster, leaving a higher fraction of 2P stars relative to clusters that were fully mixed prior to experiencing significant tidal disruption.

We re-observe a nitrogen-enriched star initially identified in Simpson and Martell [2019]. We identify significant enrichment in *s*-process elements, and therefore classify it as a post-mass transfer star. Sometimes called CEMP-s stars, CH stars or Ba stars, post-mass transfer stars are not usually identified in GCs, as they require close binary systems that long enough for a $3 - 8$ $M_\odot$ star to evolve onto the AGB, and we expect these to be disrupted in dense cluster environments. A similar post-mass transfer star was identified in the 300S globular cluster stellar stream by Usman et al. [2024]. This may indicate that disrupting or disrupted system may provide a more hospitable environment for binary systems than dense, stable GCs.

Lastly, we find no detectable spread in neutron-capture elements in ESO 280-SC06. Previous studies of metal-poor GCs M15 and M92 found detectable spreads of neutron-capture elements among the 1P stars [Sobeck et al., 2011, Kirby et al., 2023]. It has been suggested that metal-poor clusters may more clearly demonstrate these dispersions than their metal-rich counterparts due to enrichment mechanisms which increase enrichment in both metallicity and neutron-capture elements. ESO 280-SC06 may contradict this trend; however, our conservative abundance uncertainties may simply not allow for dispersions to be constrained as tightly as they have been in analyses such as Kirby et al. [2023]. Further study could confirm ESO 280-SC06's

uniform enrichment in neutron-capture elements.

Acknowledgments:

This paper includes data gathered with the 6.5 meter Magellan Telescopes located at Las Campanas Observatory, Chile.

SAU acknowledges the support of the American Association of University Women through their American Dissertation Fellowship.

JR acknowledged the support from the Carnegie Observatory Internship and to the mentors throughout the project.

APJ acknowledges support from a Carnegie Fellowship, the Thacher Research Award in Astronomy, and the Alfred P. Sloan Research Fellowship. APJ and SAU were supported by the National Science Foundation grant AST-2206264.

SLM and JDS acknowledge support from the Australian Research Council through Discovery Project grant DP180101791 and from the UNSW Scientia Fellowship programme. This research has been supported in part by the Australian Research Council Centre of Excellence for All Sky Astrophysics in 3 Dimensions (ASTRO 3D), through project number CE170100013. SLM also acknowledges funding from ARC DP220102254.

T.S.L. acknowledge financial support from Natural Sciences and Engineering Research Council of Canada (NSERC) through grant RGPIN-2022-04794.

This research has made use of NASA's Astrophysics Data System Bibliographic Services; the arXiv preprint server operated by Cornell University; and the SIMBAD databases hosted by the Strasbourg Astronomical Data Center.

This work has made use of data from the European Space Agency (ESA) mission *Gaia* (https://www.cosmos.esa.int/gaia), processed by the *Gaia* Data Processing and Analysis Consortium (DPAC, https://www.cosmos.esa.int/web/gaia/dpac/consortium). Funding for the DPAC has been provided by national institutions, in particular the institutions participating in the *Gaia* Multilateral Agreement.

Software: `numpy` [van der Walt et al., 2011], `matplotlib` [Hunter, 2007], `astropy` [Price-Whelan et al., 2018], `dynesty` [Koposov et al., 2022],

Table 2.6 Star 001 Abundances

Element	Species	N	$\log \epsilon$	[X/H]	$e_{[X/H]}$	[X/Fe]	$e_{[X/Fe]}$
Fe I	26.0	25	5.12	−2.38	0.17	–	–
Fe II	26.1	7	5.02	−2.48	0.13	–	–
Na I	11.0	2	4.87	−1.37	0.18	1.01	0.2
Na, nLTE						0.66	
Mg I	12.0	5	5.35	−2.25	0.14	0.13	0.19
Al I	13.0	1	4.48	−1.97	0.31	0.41	0.34
Al, nLTE						1.24	
Si I	14.0	2	5.91	−1.6	0.24	0.78	0.26
K I	19.0	2	3.23	−1.8	0.2	0.58	0.23
Ca I	20.0	7	4.26	−2.08	0.14	0.29	0.18
Sc II	21.1	6	0.86	−2.29	0.17	0.19	0.2
Ti I	22.0	6	2.85	−2.1	0.15	0.28	0.19
Ti II	22.1	13	2.89	−2.06	0.18	0.42	0.2
V II	23.1	1	1.62	−2.31	0.28	0.17	0.31
Cr I	24.0	1	3.2	−2.44	0.19	−0.07	0.23
Mn I	25.0	1	2.61	−2.82	0.26	−0.44	0.29
Co I	27.0	4	2.85	−2.14	0.17	0.24	0.22
Ni I	28.0	2	4.04	−2.18	0.18	0.2	0.21
Zn I	30.0	1	2.42	−2.14	0.24	0.23	0.28
Sr II	38.1	2	0.75	−2.12	0.25	0.36	0.26
Y II	39.1	3	−0.29	−2.5	0.2	−0.02	0.23
Zr II	40.1	1	0.35	−2.23	0.26	0.25	0.28
Ba II	56.1	5	−0.71	−2.89	0.17	−0.42	0.2
Eu II	63.1	2	−1.35	−1.87	0.16	0.61	0.2
C−H	106.0	2	6.15	−2.28	0.22	0.09	0.22
C−N	607.0	1	7.03	−0.8	0.27	1.58	0.26
O I	8.0	1	–	−0.64	–	1.73	–
V I	23.0	1	–	−2.05	–	0.33	–
La II	57.1	4	–	−1.16	–	1.32	–
Dy II	66.1	3	–	−0.62	–	1.86	–

Table 2.7 Star 003 Abundances

Element	Species	N	$\log \epsilon$	[X/H]	$e_{[X/H]}$	[X/Fe]	$e_{[X/Fe]}$
Fe I	26.0	41	4.9	−2.6	0.21	–	–
Fe II	26.1	12	4.84	−2.66	0.13	–	–
Na I	11.0	2	4.61	−1.63	0.21	0.97	0.26
Na, nLTE						0.38	
Mg I	12.0	4	5.27	−2.33	0.14	0.27	0.23
Al I	13.0	1	4.31	−2.14	0.27	0.46	0.31
Al, nLTE						1.17	
Si I	14.0	2	5.5	−2.01	0.25	0.59	0.3
K I	19.0	2	3.16	−1.87	0.14	0.73	0.23
Ca I	20.0	14	4.17	−2.17	0.14	0.43	0.23
Sc II	21.1	6	0.61	−2.54	0.16	0.11	0.19
Ti I	22.0	6	2.67	−2.28	0.24	0.31	0.29
Ti II	22.1	17	2.7	−2.25	0.19	0.41	0.22
Cr I	24.0	1	3.0	−2.64	0.18	−0.04	0.25
Cr II	24.1	1	3.16	−2.48	0.18	0.18	0.21
Mn I	25.0	1	2.71	−2.72	0.3	−0.12	0.35
Co I	27.0	4	2.59	−2.4	0.26	0.2	0.3
Ni I	28.0	2	3.65	−2.57	0.17	0.03	0.25
Sr II	38.1	2	0.58	−2.29	0.32	0.37	0.33
Ba II	56.1	5	−0.78	−2.96	0.15	−0.3	0.19
Eu II	63.1	1	−1.72	−2.24	0.24	0.42	0.27
C−H	106.0	2	6.13	−2.3	0.21	0.3	0.25
C−N	607.0	1	6.5	−1.33	0.35	1.27	0.36
O I	8.0	1	–	−0.99	–	1.61	–
V I	23.0	1	–	−2.15	–	0.45	–
V II	23.1	2	–	−1.47	–	1.19	–
Zn I	30.0	1	–	−2.26	–	0.34	–
Y II	39.1	2	–	−2.17	–	0.49	–
Zr II	40.1	1	–	−1.95	–	0.71	–
La II	57.1	3	–	−1.47	–	1.18	–
Dy II	66.1	2	–	−1.11	–	1.55	–

Table 2.8 Star 005 Abundances

Element	Species	N	$\log \epsilon$	[X/H]	$e_{[X/H]}$	[X/Fe]	$e_{[X/Fe]}$
Fe I	26.0	57	4.97	−2.53	0.2	–	–
Fe II	26.1	16	5.03	−2.47	0.17	–	–
Na I	11.0	2	4.3	−1.94	0.19	0.58	0.23
Na, nLTE						0.03	
Mg I	12.0	5	5.4	−2.2	0.15	0.33	0.22
Al I	13.0	1	2.97	−3.48	0.35	−0.95	0.39
Al, nLTE						−0.23	
Si I	14.0	2	5.5	−2.01	0.26	0.51	0.31
K I	19.0	2	3.11	−1.92	0.14	0.6	0.22
Ca I	20.0	11	4.19	−2.15	0.12	0.38	0.21
Sc II	21.1	5	0.69	−2.46	0.14	0.01	0.21
Ti I	22.0	6	2.74	−2.21	0.23	0.31	0.27
Ti II	22.1	20	2.83	−2.12	0.16	0.36	0.21
V II	23.1	1	1.62	−2.31	0.2	0.16	0.26
Cr I	24.0	1	3.03	−2.61	0.18	−0.09	0.24
Cr II	24.1	2	3.16	−2.48	0.15	−0.0	0.22
Mn I	25.0	2	2.53	−2.9	0.19	−0.37	0.26
Co I	27.0	4	2.62	−2.37	0.17	0.15	0.24
Ni I	28.0	2	3.81	−2.41	0.18	0.12	0.24
Sr II	38.1	2	0.76	−2.11	0.25	0.36	0.28
Y II	39.1	2	−0.23	−2.44	0.23	0.04	0.28
Zr II	40.1	1	0.63	−1.95	0.34	0.52	0.37
Ba II	56.1	4	−0.65	−2.83	0.15	−0.35	0.21
La II	57.1	2	−0.97	−2.07	0.22	0.4	0.27
O I	8.0	1	–	−1.08	–	1.45	–
V I	23.0	1	–	−2.23	–	0.29	–
Zn I	30.0	1	–	−1.93	–	0.6	–
Eu II	63.1	3	–	−0.89	–	1.59	–
Dy II	66.1	3	–	−1.09	–	1.38	–
C−H	106.0	2	–	−2.4	–	0.13	–
C−N	607.0	1	–	−0.31	–	2.21	–

Table 2.9 Star 008 Abundances

Element	Species	N	$\log \epsilon$	[X/H]	$e_{[X/H]}$	[X/Fe]	$e_{[X/Fe]}$
Fe I	26.0	44	4.9	−2.6	0.18	–	–
Fe II	26.1	13	5.02	−2.48	0.17	–	–
Na I	11.0	2	4.43	−1.81	0.19	0.79	0.22
Na, nLTE						0.23	
Mg I	12.0	5	5.31	−2.29	0.18	0.31	0.23
Al I	13.0	1	3.4	−3.05	0.38	−0.46	0.41
Al, nLTE						0.54	
Si I	14.0	2	5.54	−1.97	0.26	0.63	0.28
K I	19.0	2	3.11	−1.92	0.14	0.67	0.2
Ca I	20.0	14	4.13	−2.21	0.13	0.38	0.19
Sc II	21.1	7	0.67	−2.48	0.18	0.01	0.23
Ti I	22.0	6	2.74	−2.21	0.17	0.38	0.21
Ti II	22.1	25	2.76	−2.19	0.18	0.29	0.22
V I	23.0	1	1.58	−2.35	0.21	0.25	0.25
V II	23.1	1	1.52	−2.41	0.39	0.08	0.42
Cr I	24.0	1	2.88	−2.76	0.18	−0.16	0.23
Cr II	24.1	1	2.98	−2.66	0.18	−0.18	0.23
Mn I	25.0	3	2.47	−2.96	0.18	−0.36	0.24
Co I	27.0	4	2.39	−2.6	0.29	−0.0	0.33
Ni I	28.0	2	3.52	−2.7	0.18	−0.1	0.23
Zn I	30.0	1	2.08	−2.47	0.22	0.12	0.27
Sr II	38.1	2	0.5	−2.37	0.29	0.11	0.31
Y II	39.1	1	−0.44	−2.65	0.21	−0.17	0.26
Zr II	40.1	1	0.42	−2.16	0.27	0.32	0.31
Ba II	56.1	4	−0.57	−2.75	0.15	−0.27	0.2
La II	57.1	1	−1.35	−2.45	0.28	0.03	0.32
Eu II	63.1	2	−1.83	−2.35	0.19	0.13	0.24
O I	8.0	1	–	−1.17	–	1.42	–
Dy II	66.1	2	–	−1.19	–	1.29	–
C−H	106.0	2	–	−2.76	–	−0.16	–
C−N	607.0	1	–	−1.0	–	1.6	–

Table 2.10 Star 016 Abundances

Element	Species	N	$\log \epsilon$	[X/H]	$e_{[X/H]}$	[X/Fe]	$e_{[X/Fe]}$
Fe I	26.0	43	5.06	−2.44	0.15	–	–
Fe II	26.1	11	4.98	−2.52	0.13	–	–
Na I	11.0	2	4.69	−1.55	0.19	0.89	0.19
Na, nLTE						0.40	
Mg I	12.0	6	5.56	−2.04	0.14	0.4	0.17
Al I	13.0	1	4.48	−1.97	0.21	0.47	0.24
Al, nLTE						1.23	
Si I	14.0	1	5.64	−1.87	0.24	0.57	0.25
K I	19.0	2	3.32	−1.71	0.15	0.73	0.18
Ca I	20.0	16	4.21	−2.13	0.16	0.31	0.19
Sc II	21.1	7	0.84	−2.31	0.14	0.2	0.16
Ti I	22.0	10	2.77	−2.18	0.22	0.25	0.23
Ti II	22.1	27	2.85	−2.1	0.17	0.41	0.18
V I	23.0	1	1.46	−2.47	0.31	−0.03	0.33
V II	23.1	2	1.49	−2.44	0.19	0.07	0.22
Cr I	24.0	1	2.76	−2.88	0.2	−0.44	0.22
Cr II	24.1	1	2.93	−2.71	0.2	−0.19	0.23
Mn I	25.0	4	2.53	−2.9	0.15	−0.46	0.19
Co I	27.0	5	2.77	−2.22	0.19	0.22	0.21
Ni I	28.0	4	3.79	−2.43	0.16	0.01	0.18
Zn I	30.0	1	2.19	−2.36	0.34	0.07	0.36
Sr II	38.1	2	0.7	−2.17	0.21	0.35	0.21
Y II	39.1	4	−0.46	−2.67	0.15	−0.15	0.18
Zr II	40.1	1	0.17	−2.41	0.2	0.11	0.23
Ba II	56.1	5	−0.54	−2.72	0.15	−0.2	0.16
La II	57.1	1	−1.64	−2.74	0.3	−0.22	0.32
Eu II	63.1	2	−1.58	−2.1	0.16	0.42	0.19
Dy II	66.1	2	−0.78	−1.88	0.26	0.64	0.28
C−H	106.0	2	5.94	−2.49	0.22	−0.05	0.22
C−N	607.0	1	6.58	−1.25	0.31	1.19	0.29
O I	8.0	1	–	−1.1	–	1.34	–

Table 2.11 Star 025 Abundances

Element	Species	N	$\log \epsilon$	[X/H]	$e_{[X/H]}$	[X/Fe]	$e_{[X/Fe]}$
Fe I	26.0	28	4.9	−2.6	0.2	–	–
Fe II	26.1	15	4.92	−2.58	0.16	–	–
Na I	11.0	2	4.32	−1.92	0.19	0.68	0.24
Na, nLTE						0.14	
Mg I	12.0	5	5.47	−2.13	0.14	0.48	0.22
Al I	13.0	1	2.73	−3.72	0.36	−1.12	0.41
Al, nLTE						−0.16	
Si I	14.0	2	5.52	−1.99	0.19	0.61	0.25
K I	19.0	2	3.29	−1.74	0.14	0.86	0.23
Ca I	20.0	11	4.18	−2.16	0.12	0.45	0.21
Sc II	21.1	6	0.78	−2.37	0.14	0.21	0.2
Ti I	22.0	5	2.73	−2.22	0.18	0.38	0.24
Ti II	22.1	20	2.77	−2.18	0.16	0.4	0.21
V I	23.0	1	1.66	−2.27	0.23	0.33	0.28
V II	23.1	2	1.74	−2.19	0.23	0.38	0.27
Cr I	24.0	2	2.98	−2.66	0.26	−0.05	0.31
Mn I	25.0	3	2.73	−2.7	0.21	−0.1	0.27
Co I	27.0	2	2.55	−2.44	0.22	0.16	0.27
Ni I	28.0	2	3.67	−2.55	0.16	0.06	0.23
Zn I	30.0	1	2.38	−2.18	0.2	0.42	0.27
Sr II	38.1	2	−0.13	−3.0	0.28	−0.43	0.31
Y II	39.1	2	−0.45	−2.66	0.23	−0.09	0.27
Zr II	40.1	1	0.12	−2.46	0.25	0.12	0.29
Ba II	56.1	4	−0.85	−3.03	0.15	−0.45	0.21
La II	57.1	1	−1.41	−2.51	0.36	0.07	0.39
O I	8.0	1	–	−1.13	–	1.47	–
Eu II	63.1	3	–	−1.05	–	1.53	–
Dy II	66.1	3	–	−1.05	–	1.52	–
C−H	106.0	2	–	−2.51	–	0.09	–
C−N	607.0	1	–	−0.66	–	1.94	–

Table 2.12 Star 026 Abundances

Element	Species	N	$\log \epsilon$	[X/H]	$e_{[X/H]}$	[X/Fe]	$e_{[X/Fe]}$
Fe I	26.0	55	4.98	−2.52	0.17	–	–
Fe II	26.1	14	5.08	−2.42	0.18	–	–
Na I	11.0	2	4.85	−1.39	0.19	1.13	0.2
Na, nLTE						0.72	
Mg I	12.0	5	5.47	−2.13	0.14	0.39	0.18
Al I	13.0	1	3.66	−2.79	0.32	−0.27	0.34
Al, nLTE						0.69	
Si I	14.0	2	5.78	−1.73	0.46	0.79	0.47
K I	19.0	2	3.11	−1.92	0.2	0.6	0.23
Ca I	20.0	14	4.23	−2.11	0.13	0.42	0.18
Sc II	21.1	5	0.73	−2.42	0.18	−0.0	0.23
Ti I	22.0	7	2.78	−2.17	0.21	0.35	0.23
Ti II	22.1	13	2.78	−2.17	0.14	0.25	0.2
V I	23.0	1	1.49	−2.44	0.2	0.08	0.26
V II	23.1	1	1.78	−2.15	0.22	0.27	0.28
Cr I	24.0	1	2.72	−2.92	0.19	−0.4	0.22
Cr II	24.1	1	3.22	−2.42	0.18	−0.01	0.24
Mn I	25.0	1	2.5	−2.93	0.2	−0.41	0.24
Co I	27.0	3	2.52	−2.47	0.21	0.05	0.23
Ni I	28.0	3	3.64	−2.58	0.18	−0.06	0.21
Zn I	30.0	1	2.14	−2.41	0.2	0.11	0.25
Sr II	38.1	2	1.51	−1.36	0.2	1.06	0.26
Y II	39.1	5	0.16	−2.05	0.15	0.37	0.22
Zr II	40.1	1	0.61	−1.97	0.22	0.45	0.27
Ba II	56.1	5	1.07	−1.11	0.18	1.3	0.23
La II	57.1	5	−0.22	−1.32	0.15	1.09	0.22
Eu II	63.1	2	−1.39	−1.91	0.18	0.51	0.24
C−H	106.0	2	6.38	−2.05	0.22	0.47	0.23
C−N	607.0	1	7.44	−0.4	0.29	2.13	0.28
O I	8.0	1	–	−1.1	–	1.42	–
Dy II	66.1	1	–	−0.97	–	1.44	–

Table 2.13 Star 033 Abundances

Element	Species	N	$\log \epsilon$	[X/H]	$e_{[X/H]}$	[X/Fe]	$e_{[X/Fe]}$
Fe I	26.0	45	4.87	−2.63	0.15	–	–
Fe II	26.1	15	4.93	−2.57	0.13	–	–
Na I	11.0	2	4.48	−1.76	0.21	0.87	0.2
Na, nLTE						0.44	
Mg I	12.0	5	5.34	−2.26	0.15	0.36	0.17
Al I	13.0	1	4.25	−2.2	0.32	0.42	0.33
Al, nLTE						1.16	
Si I	14.0	2	5.46	−2.05	0.21	0.58	0.22
K I	19.0	2	3.09	−1.94	0.16	0.69	0.19
Ca I	20.0	17	4.11	−2.23	0.17	0.39	0.2
Sc II	21.1	8	0.6	−2.55	0.17	0.02	0.19
Ti I	22.0	11	2.55	−2.4	0.18	0.23	0.19
Ti II	22.1	28	2.71	−2.24	0.17	0.33	0.19
V I	23.0	2	1.45	−2.48	0.16	0.15	0.2
V II	23.1	2	1.65	−2.28	0.19	0.29	0.21
Cr I	24.0	6	2.99	−2.65	0.21	−0.02	0.23
Cr II	24.1	1	3.08	−2.56	0.19	0.01	0.21
Mn I	25.0	4	2.35	−3.08	0.16	−0.45	0.19
Co I	27.0	3	2.5	−2.49	0.24	0.14	0.26
Ni I	28.0	3	3.88	−2.34	0.16	0.29	0.18
Zn I	30.0	1	2.26	−2.3	0.19	0.33	0.24
Sr II	38.1	2	0.37	−2.5	0.29	0.07	0.31
Y II	39.1	5	−0.48	−2.69	0.15	−0.12	0.18
Zr II	40.1	1	0.25	−2.33	0.21	0.24	0.23
Ba II	56.1	5	−0.76	−2.94	0.14	−0.37	0.17
Eu II	63.1	2	−1.77	−2.29	0.21	0.28	0.23
C−H	106.0	2	5.64	−2.79	0.21	−0.16	0.21
C−N	607.0	1	6.64	−1.19	0.33	1.43	0.29
O I	8.0	1	–	−1.95	–	0.68	–
La II	57.1	3	–	−1.79	–	0.78	–
Dy II	66.1	1	–	−1.7	–	0.87	–

Table 2.14 Star 184 Abundances

Element	Species	N	$\log \epsilon$	[X/H]	$e_{[X/H]}$	[X/Fe]	$e_{[X/Fe]}$
Fe I	26.0	62	5.08	−2.42	0.31	–	–
Fe II	26.1	21	4.94	−2.56	0.14	–	–
Na I	11.0	2	4.22	−2.02	0.45	0.4	0.3
Na, nLTE						0.15	
Mg I	12.0	5	5.78	−1.82	0.27	0.6	0.25
Al I	13.0	1	4.09	−2.36	0.39	0.06	0.34
Al, nLTE						1.06	
Si I	14.0	2	5.43	−2.08	0.37	0.34	0.31
K I	19.0	2	3.5	−1.53	0.33	0.89	0.26
Ca I	20.0	20	4.33	−2.01	0.23	0.41	0.25
Sc II	21.1	8	0.81	−2.34	0.19	0.22	0.22
Ti I	22.0	26	2.84	−2.11	0.35	0.31	0.26
Ti II	22.1	26	2.99	−1.96	0.19	0.59	0.22
V I	23.0	1	1.5	−2.43	0.31	−0.01	0.28
V II	23.1	1	1.69	−2.24	0.23	0.32	0.27
Cr I	24.0	12	3.11	−2.53	0.32	−0.11	0.23
Cr II	24.1	2	3.2	−2.44	0.16	0.12	0.19
Mn I	25.0	3	2.53	−2.9	0.25	−0.48	0.24
Co I	27.0	4	2.92	−2.07	0.33	0.35	0.28
Ni I	28.0	14	3.82	−2.4	0.31	0.02	0.27
Zn I	30.0	2	2.2	−2.36	0.16	0.06	0.31
Sr II	38.1	2	0.75	−2.12	0.22	0.44	0.26
Y II	39.1	7	−0.4	−2.61	0.18	−0.06	0.22
Zr II	40.1	1	0.49	−2.09	0.27	0.47	0.27
Ba II	56.1	5	−0.65	−2.83	0.17	−0.27	0.2
La II	57.1	4	−1.74	−2.84	0.19	−0.28	0.23
Eu II	63.1	3	−1.87	−2.39	0.17	0.17	0.22
Dy II	66.1	1	−1.28	−2.38	0.29	0.18	0.31
C−H	106.0	1	5.48	−2.95	0.47	−0.53	0.34
C−N	607.0	1	6.04	−1.79	0.58	0.63	0.43
O I	8.0	1	–	−1.52	–	0.9	–

Table 2.15 Star 576 Abundances

Element	Species	N	$\log \epsilon$	[X/H]	$e_{[X/H]}$	[X/Fe]	$e_{[X/Fe]}$
Fe I	26.0	35	4.89	−2.61	0.14	–	–
Fe II	26.1	16	4.82	−2.68	0.12	–	–
Na I	11.0	2	4.36	−1.88	0.24	0.74	0.2
Na, nLTE						0.43	
Mg I	12.0	5	5.26	−2.34	0.16	0.27	0.16
Al I	13.0	1	4.34	−2.11	0.24	0.5	0.25
Al, nLTE						1.47	
Si I	14.0	2	5.47	−2.04	0.2	0.57	0.19
K I	19.0	2	3.12	−1.91	0.16	0.7	0.16
Ca I	20.0	21	4.08	−2.26	0.15	0.35	0.17
Sc II	21.1	7	0.49	−2.66	0.13	0.02	0.15
Ti I	22.0	20	2.49	−2.46	0.17	0.15	0.16
Ti II	22.1	34	2.63	−2.32	0.18	0.35	0.2
V I	23.0	1	1.34	−2.59	0.18	0.02	0.19
V II	23.1	2	1.5	−2.43	0.17	0.24	0.19
Cr I	24.0	12	2.84	−2.8	0.17	−0.19	0.16
Cr II	24.1	3	3.04	−2.6	0.13	0.08	0.16
Mn I	25.0	4	2.46	−2.97	0.15	−0.36	0.16
Co I	27.0	4	2.42	−2.57	0.23	0.05	0.22
Ni I	28.0	16	3.71	−2.51	0.23	0.1	0.23
Zn I	30.0	3	2.15	−2.41	0.13	0.2	0.18
Sr II	38.1	2	0.19	−2.68	0.25	−0.01	0.26
Y II	39.1	6	−0.67	−2.88	0.13	−0.21	0.16
Zr II	40.1	1	0.17	−2.41	0.19	0.27	0.21
Ba II	56.1	5	−0.94	−3.12	0.15	−0.44	0.17
La II	57.1	4	−1.56	−2.66	0.14	0.02	0.17
Eu II	63.1	2	−1.76	−2.28	0.15	0.4	0.18
Dy II	66.1	1	−1.14	−2.24	0.26	0.43	0.27
C−H	106.0	2	5.2	−3.23	0.19	−0.62	0.18
C−N	607.0	1	6.59	−1.24	0.26	1.37	0.22
O I	8.0	1	–	−1.62	–	0.99	–

CHAPTER 3

MULTIPLE POPULATIONS AND A CH STAR FOUND IN THE 300S GLOBULAR CLUSTER STELLAR STREAM

This paper was published in April 2024 in the Monthly Notices of the Royal Astronomical Society, Volume 529, Issue 3, pages 2413-2427. Usman et al. [2024]

3.1 Abstract

Milky Way globular clusters (GCs) display chemical enrichment in a phenomenon called multiple stellar populations (MSPs). While the enrichment mechanism is not fully understood, there is a correlation between a cluster's mass and the fraction of enriched stars found therein. However, present-day GC masses are often smaller than their masses at the time of formation due to dynamical mass loss. In this work, we explore the relationship between mass and MSPs using the stellar stream 300S. We present the chemical abundances of eight red giant branch member stars in 300S with high-resolution spectroscopy from Magellan/MIKE. We identify one enriched star characteristic of MSPs and no detectable metallicity dispersion, confirming that the progenitor of 300S was a globular cluster. The fraction of enriched stars (12.5%) observed in our 300S stars is less than the 50% of stars found enriched in Milky Way GCs of comparable present-day mass ($\sim 10^{4.5}\,M_{\odot}$). We calculate the mass of 300S's progenitor and compare it to the initial masses of intact GCs, finding that 300S aligns well with the trend between the system mass at formation and enrichment. 300S's progenitor may straddle the critical mass threshold for the formation of MSPs and

can therefore serve as a benchmark for the stellar enrichment process. Additionally, we identify a CH star, with high abundances of *s*-process elements, probably accreted from a binary companion. The rarity of such binaries in intact GCs may imply stellar streams permit the survival of binaries that would otherwise be disrupted.

3.2 Introduction

The Milky Way's history of mergers with stellar systems can be traced through the remnants of dwarf galaxies and globular clusters (GCs) long ago disrupted by the galaxy's gravity [Li et al., 2019, 2022]. These systems are tidally disrupted first into stellar streams, before eventually becoming fully mixed into the Milky Way halo. For example, the remnants of GCs can be seen by nitrogen-enriched stars distributed throughout the outer reaches of the Galaxy [e.g., Martell et al., 2011, 2016, Schiavon et al., 2017, Fernández-Trincado et al., 2020]. Stellar streams from GCs can act as a clue to understand the dynamics and enrichment of their intact progenitors. For example, outside of GCs, stars can be found to have unusual element enrichment due to accretion from a binary companion such as CH stars [e.g., McClure et al., 1980, McClure and Woodsworth, 1990, Luck and Bond, 1991, Lucatello et al., 2003, Hansen et al., 2016], but GCs tend to disrupt binary systems well before mass transfer can occur due to their high density [Côté et al., 1997]. Spectroscopic observations of GCs or their resulting stellar streams could shed light on their stellar dynamics.

Perhaps the most interesting aspect of GCs is that most have multiple stellar populations (MSPs): groups of stars with correlated enrichment in elements such as N, Na, and Al and depletion in elements such as C, O and Mg [Osborn, 1971,

Table 3.1 The coordinates and exposure time for each star observed in this study. The distances were calculated using the relationship in Fu et al. [2018]. The Source column refers to the catalog or paper from which the star was chosen: S^5 were stars observed by the S^5 collaboration using AAT, Gaia stars were astrometrically selected from the Gaia catalog, and the Fu et al. [2018] star was the most metal-poor star in their sample.

Gaia ID	**RA** (°)	**Dec** (°)	**Name**	$\mathbf{G_0}$ (mag, dered)	**Distance** (kpc)	**BP−RP** (mag, dered)	**Radial Velocity** (km s^{-1})	**MJD**	**Exposure Time** (s)	**Source**	**Notes**
3885023078597531520	161.382227	14.149791	J1045+1408	12.69	15.4	1.80	295.1 ±0.8 297.0 ± 1.0 (GDR3)	59342.0	600	Gaia	Cool Star
3885197802162705152	162.428814	15.014678	J1049+1500	13.10	15.2	1.59	289.8 ±0.8 291.1 ± 1.9 (GDR3)	59342.0	900	Gaia	
621582446059931264	151.605717	15.153214	J1006+1509	13.99	17.4	1.50	307.1 ±0.5 305.1 ± 0.7 (S^5) 307.0 ± 3.9 (GDR3)	59351.0 58907.5	1200	S^5	
622629352928532480	150.462821	15.900839	J1001+1554	14.16	17.7	1.42	307.7 ±1.0 309.7 ± 0.8 (S^5) 306.4 ± 2.6 (GDR3)	59351.0 58907.5	1200	S^5	CH Star
622077466810856960	153.138229	15.908147	J1012+1554	14.38	17.1	1.37	301.5 ±0.8 301.3 ± 0.7 (S^5) 302.4 ± 3.6 (GDR3)	59342.0 59232.6	1200	S^5	
621871205301503488	150.588462	15.691547	J1002+1541	15.11	17.6	1.27	305.1 ±0.5 303.1 ± 0.9 (S^5)	59342.0 58907.5	2500	S^5	
3888560349238428928	155.183933	15.925786	J1020+1555	15.29	16.7	1.20	299.8 ±0.7 297.7 ± 1.0 (S^5)	59342.0 58900.7	5300	S^5	Enriched Star
616868118157193344	149.225325	16.062778	J0956+1603	15.65	17.9	1.18	304.3 ±0.9 302.8 ± 0.7 (S^5)	59351.0 58908.5	3000	S^5	
622146628669531008	153.057089	16.394690	J1012+1623	17.80			261.5 ±1.7 (MIKE) 263.2 ± 2.1 (MIKE) 275.7 ± 2.2 (S^5) 297.5 ± 6.0 (SEGUE)	59342 59650.0 59232.6 54174	1800 900	Fu18	Non-member Binary
3884319807767821312	157.492922	13.904273	J1029+1354	13.34			238.3 ±0.5 233.8 ± 1.9 (GDR3)	59342	900	Gaia	Non-member

Bell and Dickens, 1980, Cottrell and Da Costa, 1981, Norris et al., 1981].[1] MSPs are thought to develop only during the formation of dense star clusters, though the exact mechanism is not well understood [e.g., Carretta, 2006, Carretta et al., 2009b, Bastian and Lardo, 2018]. The majority of globular clusters exhibit this unique correlated enrichment, though some unusual globular clusters like Ruprecht 106 have had no detected enriched stars [Villanova et al., 2013]. One clue to the nature of this phenomenon is the clear correlation between the mass of a globular cluster and its fraction of enriched stars [e.g., Milone et al., 2017, Bastian and Lardo, 2018, Gratton et al., 2019]. The most massive intact Milky Way GCs contain higher fractions of enriched stars, with clusters of mass $>10^{4.5}$ $M_{\odot}$ generally having at least half of their stars enriched [Milone et al., 2017]. The trend is not perfect, however: even the lowest-mass globular clusters can contain MSPs, contrary to expectations [Simpson et al., 2017]. The relationship between the fraction of enriched stars and the mass can be clarified when instead looking at the *initial* mass of the systems instead of their present-day mas. Gratton et al. [2019] suggested that a globular cluster needs to achieve a minimum mass *at its time of formation* in order to create MSPs.

Determining the initial mass of a globular cluster is not as straightforward as measuring the mass we see today, since the masses of GCs are not static [e.g., Gnedin and Ostriker, 1997]. Intact Milky Way GCs have typically lost 80% of their initial mass due to tidal stripping, though the respective mass loss depends on each cluster's unique orbit [Baumgardt et al., 2019]. The critical mass for the formation of MSPs therefore appears lower when looking solely at current mass measurements of intact

1. For the remainder of this paper, we refer to second-population stars as "enriched", despite being unusually *depleted* in some elements.

Milky Way GCs. We can more closely examine the dependence of MSPs on initial mass by examining GCs accreted onto the Milky Way. Additionally, comparisons of the fraction of enriched stars between Milky Way GCs and Magellanic Cloud GCs have found that the disruption of GCs via tidal forces may impact our understanding of mass and the enrichment of stars in GCs [Milone et al., 2020]. Stellar streams from disrupted GCs remain a useful and novel way to examine the relationship between the initial mass of a system and its enrichment. Previous research on identifying MSPs in GCs have been performed on the GD-1 and Phoenix streams [Wan et al., 2020, Casey et al., 2021, Balbinot et al., 2022]. We turn to another ideal candidate for analysis, the 300S stellar stream.

The 300S stream was first found unintentionally by Geha et al. [2009] while studying the dwarf galaxy Segue 1, which overlaps 300S on the sky. Its stars have since been re-observed spectroscopically by the Southern Stellar Stream Spectroscopic Survey, S^5 [Li et al., 2019, 2022]. From its highly eccentric and retrograde orbit, it is clear the stream's progenitor was accreted onto the Milky Way from another galaxy [Fu et al., 2018]. 300S's progenitor may have formed in the galaxy Gaia-Sausage-Enceladus (*GSE*, Belokurov et al. 2018, Helmi et al. 2018) prior to its merger with the Milky Way [Fu et al., 2018, Li et al., 2022].

In addition to its origin, the nature of the progenitor itself has also been debated over the past decade. The stream has low abundances of α elements and has previously been found to have a metallicity dispersion, indicating that its progenitor was likely a dwarf galaxy [Frebel et al., 2013b, Fu et al., 2018]. However, Li et al. [2022] used the Ca triplet to measure the metallicity, finding no detectable metallicity

dispersion and concluding the progenitor of 300S was a globular cluster.

In this paper, we present a chemical abundance analysis of stars in 300S. We show 300S is a globular cluster by identifying MSPs and finding no dispersion in metallicity. Further, we detect a star enriched in carbon and *s*-process elements, which we will refer to as a CH star. In Section 3.3, we describe the target selection and observations. Section 3.4 describes the determination of stellar parameters. Section 3.5 describes the abundance analysis, including how the abundance dispersion was calculated. The current stream mass and the initial mass of its progenitor are calculated in Section 3.6. The results are shown in Section 3.7. We summarize our interpretations in Section 3.8. Lastly, we discuss the broader implications for MSPs and future work in Section 3.9.

3.3 Observations

We selected ten of the brightest candidate member stars of 300S in three ways (Table 3.1). First, we chose the six brightest 300S member stars found by S^5 in Li et al. [2022]. We refer readers to Li et al. [2022] for more details on the initial S^5 data reduction and analysis, as well as the member star selection. As S^5 limited the targets to $G > 14$ for 300S stream to avoid cross-talk between the brightest and faintest targets, we further selected three possible stars using Gaia DR3 [Gaia Collaboration et al., 2016, 2023a] at a brighter magnitude (or beyond the S^5 footprint) which could be potentially missed by S^5, guided by the locations in the proper motion space and color-magnitude diagram of the previously identified 300S member stars from Li et al. [2022]. Finally, we also included the most metal-poor star from Fu et al. [2018], as

this star is the main driver of the metallicity dispersion revealed by Fu et al. [2018].

These ten stars were observed using the Magellan/MIKE high-resolution spectrograph on May 5th and 16th, 2021, using a $0.7''$ slit and 2×2 on-chip binning [Bernstein et al., 2003]. We achieve a resolution of R $\sim$ 28,000 on the blue echelle orders and R $\sim$ 22,000 on the red echelle orders. The data were reduced using `CarPy` [Kelson, 2003]. Details about the observations, including heliocentric radial velocities and exposure times, can be found in Table 3.1. The star J1020+1555 was also observed on April 13th, 2023 to increase the SNR, and the star J1012+1623 was observed on March 12th, 2022 to obtain an additional radial velocity. We achieve SNRs measured per pixel ranging from 60 to 100 for red wavelengths around 8,000 Å and 35 to 50 for blue wavelengths around 4,500 Å.

Fig. 3.1 depicts the position and velocities of stars in the same region of sky as 300S. We calculate the radial velocity by cross-correlating each echelle order with HD122563. We take a weighted average of the orders' velocities to find the radial velocity of the star, down-weighting orders with high uncertainty. The standard deviation of these velocities are taken to be the overall uncertainty of the star's radial velocity. We also include radial velocities of stars obtained with S^5[Li et al., 2019] and Gaia DR3 [Katz et al., 2023]. Of the ten stars observed with MIKE, two were found to have radial velocities inconsistent with the stream track, indicating they are not members of 300S and were therefore rejected from this study. In particular, there are four radial velocities for the most metal-poor candidate member star analyzed by Fu et al. [2018] (J1012+1623), showing clear velocity variations consistent with being in a close binary. We observed this star twice with MIKE to confirm its binarity.

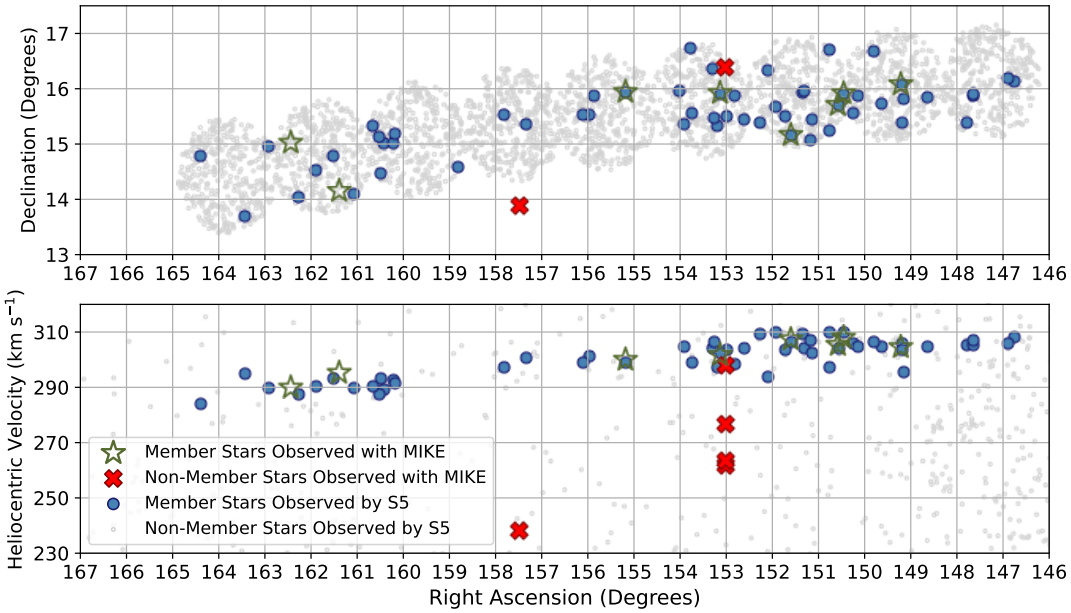

Figure 3.1 The positions (top panel) and S^5radial velocities (bottom panel) of stars in the region of 300S. Green stars represent 300S stars analyzed in this work. Red crosses represent stars rejected from this work as radial velocity non-members. The four red crosses to the right (at 153 degrees right ascension) represent the multiple radial velocities measured for the most metal-poor star analyzed by Fu et al. [2018]. Blue points represent 300S member stars identified in DECam photometry and S^5 spectroscopy. Gray dots represent other stars observed by S^5.

Though more velocities would be needed to robustly obtain a systemic velocity, the current data suggest that the SEGUE velocity was obtained at an unlucky phase of the binary orbit. Thus, we now classify this star as a radial velocity non-member.

3.4 Stellar Parameter Determination

Four stellar parameters are needed to estimate stellar abundances: effective temperature T_{eff}, surface gravity log g, metallicity [Fe/H], and the microturbulence ν_t. The

Table 3.2 Stellar parameters. [Fe/H] NLTE corrections were found using an online calculator based on Bergemann et al. [2012c] and Lind et al. [2012]. As this tool only covers parameter ranges $4000 < T_{\rm eff} < 8000$, $1.0 < \log g < 5.0$, $1.0 < \nu_t < 2.0$, for stars with parameters outside of these ranges we fix the respective inputs to $T_{\rm eff} = 4000$ K, $\log g = 1.0$, and $\nu_t = 2$.

Star Name	$T_{\rm eff}$ (K)	$\log g$	ν_t km s^{-1}	[Fe/H]	$\Delta_{\rm [Fe/H] - [Fe/H]_{NLTE}}$	$\rm [Fe/H]_{NLTE}$
J1045+1408	3880	0.20	2.39	−1.48	0.004	−1.47
J1049+1500	4120	0.55	1.99	−1.38	0.027	−1.35
J1006+1509	4230	0.85	2.06	−1.46	0.036	−1.43
J1001+1554	4350	1.00	1.95	−1.38	0.024	−1.36
J1012+1554	4420	1.13	2.06	−1.43	0.048	−1.39
J1002+1541	4580	1.50	1.52	−1.27	0.046	−1.22
J1020+1555	4710	1.68	1.86	−1.31	0.045	−1.27
J0956+1603	4740	1.78	1.66	−1.32	0.029	−1.29

first two are determined using using Gaia DR3 data, which we dereddened using Equation 1 from Collaboration et al. [2018] and reddening data from Schlegel et al. [1998] with applied corrections from Schlafly and Finkbeiner [2011], specifically from the online database IRSA.[2] $T_{\rm eff}$ is calculated using Equation (1) from Mucciarelli et al. [2021], using the coefficients for red giant branch stars:

$$\begin{aligned}\frac{5040}{T_{\rm eff}} = 0.5472 + 0.5914 \times C + 0.2347 \times C^2 - \\ 0.0119 \times \rm [Fe/H] - 0.0012 \times [Fe/H]^2 - \\ 0.0012 \times \rm [Fe/H] \times C\end{aligned} \tag{3.1}$$

Here, C is the Gaia color $(\rm G\text{-}RP)_0$ of the star. We use [Fe/H] as measured spectroscopically for each star as given in Table 3.2. We assume the star is in local ther-

2. https://irsa.ipac.caltech.edu/applications/DUST/

modynamic equilibrium (LTE) and do not calculate non-LTE corrections (nLTE). Most of our stars are in the range of 4000 K to 4800 K. The most luminous star, J1045+1408, is slightly below this range at 3880 K.

Uncertainties in $T_{\rm eff}$ and $\log g$ were estimated by propagating color and magnitude uncertainty. The uncertainties for the $T_{\rm eff}$ equation from Mucciarelli et al. [2021] estimates an uncertainty of 71 K. Each star had a unique color uncertainty based on the minimum and maximum estimates of reddening as calculated using dust maps from Schlegel et al. [1998] with corrections as applied by Schlafly and Finkbeiner [2011]. We find these color uncertainties are 0.02 mag or less for all stars. When propagating reddening uncertainties, the resulting $T_{\rm eff}$ error does not exceed 15 K. For this reason, we conservatively round to a total uncertainty of 100 K for all of our stars.

The surface gravity $\log g$ is calculated using Equation 3 from Venn et al. [2017]:

$$\log g = 4.44 + \log M + 4 \log \left(\frac{T_{\rm eff}}{5780{\rm K}} \right) + \\ 0.4 \times (g_0 - \mu + {\rm BC}(M_g) - 4.75), \tag{3.2}$$

where μ is the distance modulus, BC(M_g) is the bolometric correction, and all constants are values for the Sun. M is the mass of the star, as interpolated from the best-fit isochrone. The mass for all stars is found to be about 0.8 $M_\odot$, which is typical of old red giant stars. We calculate μ from the distance gradient found by Fu

et al. [2018]:

$$d\ (\mathrm{kpc}) = 48.9952 - 0.2083 \times \alpha \tag{3.3}$$

where α is the right ascension in degrees. The bolometric corrections, BC, were interpolated from MARCS grids [Casagrande and VandenBerg, 2018] as a function of various stellar parameters.[3] We used the maximum and minimum T_{eff} and reddening estimates to find the range of potential log g values and used the extrema as estimates for our uncertainty. Through this propagation of error, we found the uncertainty in log g to be < 0.11 in all stars. We propagate the uncertainty in distance to find an additional uncertainty of < 0.06 in all stars. We adopt a total uncertainty of 0.2 for log g.

The remaining stellar parameters used in the abundance analysis, microturbulence ν_t and metallicity [Fe/H], were found using our spectroscopic measurements, as described in the next section. Specifically, ν_t is found by balancing line strength versus Fe I abundance, while [Fe/H] is manually set to match the spectroscopically measured [Fe I/H] metallicity. The [Fe/H] error is the standard deviation found from the spectroscopic analysis.

3.5 Abundance Analysis

The spectra were analyzed using `SMHR`, a flexible interface for high-resolution spectral analysis [Casey, 2014]. We performed a standard analysis assuming local thermo-

3. https://github.com/casaluca/bolometric-corrections/blob/master/bcutil.py

dynamic equilibrium (LTE) using the radiative transfer code `MOOG` [Sneden, 1973, Sobeck et al., 2011] and 1D ATLAS stellar atmosphere models [Castelli and Kurucz, 2003]. We used `SMHR` to normalize and stitch together orders of the spectra, calculate and correct for radial velocities, fit equivalent widths, synthesize complex absorption regions, interpolate stellar atmospheres, and use curves-of-growth to determine abundances from absorption features. To analyze the cool star, we used the further extended ATLAS catalog [Mészáros et al., 2012], which covers stellar atmospheres down to effective temperatures of 3500 K. We adopted the line list used in Naidu et al. [2022], which works well for red giants with [Fe/H] ≈ -1. We used the line selection by Jönsson et al. [2017], Lomaeva et al. [2019], Forsberg et al. [2019] supplemented by Roederer et al. [2018b]. The atomic data for the Fe, O, Mg, Ca, and Ti I lines was adopted from Jönsson et al. [2017], and other elements were from `linemake`, [Placco et al., 2021]. For a more thorough description of how `SMHR` works, see Casey [2014] and Ji et al. [2020b].

Metallicity. Metallicity was determined from Fe I lines. Our analysis in LTE returned an average metallicity of [Fe/H] $= -1.39 \pm 0.03$. The assumption of LTE is generally violated in metal-poor red giants, requiring non-LTE (NLTE) calculations. We estimated corrections to the measured abundances to improve accuracy using calculations from Bergemann et al. [2019] using an online NLTE calculator.[4] This tool takes stellar parameters $T_{\rm eff}$, ν_t, and $\log g$ (as well as [Fe/H] for non-Fe elements) and combines it with measured equivalent widths for specific lines to return corrections for each absorption line. We calculate the correction for each line that is

4. http://www.inspect-stars.com/cp/application.py/

both measured in our analysis and available through the online calculator and apply it to our abundance measurements. We then take the unweighted average for the corrected abundances and use this value as our NLTE-corrected measurements. The calculator does not return uncertainties for the NLTE corrections, nor are we able to account for NLTE changes in our uncertainty measurements as our analysis pipeline assumes LTE. We therefore do not include uncertainty for abundances after NLTE corrections have been applied. We found the average NLTE-corrected abundance is [Fe/H] $= -1.35$, with a larger correction for cooler stars.

C, N, O. Carbon abundances were inferred by fitting the spectral data with synthesized models in the range of 4300-4325 Å. When available, nitrogen abundances were measured using synthesized models in the 3860-3890 Å CN band. These bands are too complex to measure with equivalent widths, unlike many other elements, including some of the iron-peak and neutron-capture elements. O was measured using the forbidden line at 6300 Å. Telluric lines in the same region were fortunately moved when correcting to rest frame such that they are clearly identifiable at 6298/6299 and 6302/6303 Å, far away from the forbidden O line.

α-elements: Mg, Si, Ca. Magnesium, silicon, and calcium were measured using equivalent widths in all eight stars. Mg I was measured using four to seven absorption lines between 4500 and 5800 Å. Si I had up to six lines used, all between 5600 and 6000 Å. Ca I had up to seven lines in the range of 5800 and 6500 Å.

Odd-Z Elements: Na, K. Sodium and potassium were measured using equivalent widths. Na was measured using two lines at 5682 and 5688 Å. K abundances were measured using equivalent widths of lines at 7699 and 7665 Å.

Fe-Peak Elements: Ti, Mn, Ni, Zn. Titanium, manganese, nickel, and zinc were measured using a combination of synthesis and equivalent widths. While Ti was not measurable in all stars, it could be measured in a few stars using equivalent widths of lines at 6091 and 6336 Å. Mn was measured using synthesis to allow for hyperfine splitting, primarily in the range of 4700-4900 Å and 6023 Å. Ni was mostly measured using equivalent widths between 6000 and 6400 Å, but was also synthesized at 5476 Ådue to a blend. Zn was measured at 4722 and 4810 Å using equivalent widths.

Neutron-Capture Elements: Sr, Y, Ba, Eu. Strontium, yttrium, barium, and europium were measured using a combination of synthesis and equivalent widths. Sr and Eu were synthesized at 4215 Å and 6645 Å, respectively. Five lines were used to measure Ba at wavelengths from 4554 Å to 6496 Å. Since Ba has complex hyperfine and isotopic structure, we synthesize a range of absorption features for each line to properly measure the abundance [Gallagher et al., 2012]. For seven of the stars, we use an r-process isotopic mixture, but for the CH star, J1001+1554, we use an s-process isotopic mixture, as s-process enrichment would be expected from accretion from a binary partner. Four lines were used to measure Y at wavelengths from 4854 Å to 5200 Å.

The measured abundances described here are shown in Table 3.3.

3.5.1 Abundance Dispersion Analysis

We calculate the intrinsic dispersion of all measured elements in the stars analyzed here. We calculate the mean abundance and dispersion of the stream μ, σ given our measurements, $\vec{x}$ using Eqn. 3.4. $\sigma^2_{\rm int}$ and σ^2_i represent the intrinsic dispersion

and the individual error measurements, respectively, while μ is the mean abundance value. The log likelihood is:

$$\mathcal{L}(\mu, \sigma|\vec{x}) = \frac{-1}{2}\Sigma_{i=1}^{N}\left[\ln\left(2\pi(\sigma_{\rm int}^2 + \sigma_i^2)\right) + \frac{(x_i-\mu)^2}{(\sigma_{\rm int}^2+\sigma_i^2)}\right] \tag{3.4}$$

We then perform nested sampling over a range of combinations for the dispersion $\sigma_{\rm int}^2$ and the mean μ. We use the nested sampling algorithm `dynesty` [Speagle, 2020, Higson et al., 2019, Koposov et al., 2022] to calculate Bayesian posteriors for the cluster's abundance means and dispersions. We include abundances and dispersions of the stream with and without anomalous stars to better demonstrate the significance of their exceptional abundances. Results are given in Table 3.4. Most importantly, we find no significant dispersion in metallicity, indicating it is unlikely to be a dwarf galaxy. A few elements such as Na and C have a measurable spread in abundances, mainly due to the anomalous stars such as the enriched star and the CH star, as will be discussed in Section 3.7. We compare those stars to the main stellar population in Tables 3.5 and 3.6, respectively.

3.6 Stream Progenitor Mass Estimate

We estimated the stellar mass of the 300S stream by comparing the number of confirmed red giant branch member stars to that of theoretical isochrones and their luminosity functions. We did this for all eight stars analyzed in this work, as well as the remaining 34 300S member stars from S^5[Li et al., 2022]. The S^5 observations are sufficiently complete within its observation footprint to a *Gaia* G magnitude of 17.2,

as confirmed by matching the stream's observations with the theoretical luminosity function.

We used the Dartmouth Stellar Evolution Database [Dotter et al., 2008][5] to generate isochrones and visually fit them to our data. The best-fit isochrone and the isochrone using stream parameters as measured by Fu et al. [2018] and Li et al. [2022] are shown in Fig. 3.2. We fit DECam DECaLs DR9 photometry for all 300S member stars observed by S^5[Dey et al., 2019]. We created a background-subtracted Hess diagram to best match the isochrones to the main sequence turn-off. From the isochrones, we find the cluster to be at a distance $d = 18.2 \pm 1$ kpc, have an age of 12.5 ± 1.5 Gyr, [Fe/H] $= -1.35^{+0.15}_{-0.05}$, and [α/Fe] $= 0.0$.

We estimate that S5/AAT observations are complete for stars brighter than a Gaia G magnitude of 17.2, as this is when our total number of observed stars falls below the predicted distribution from the luminosity functions.

We compare the proportion of stars we observe above our magnitude limit to the total mass of stars for the luminosity function. We use a luminosity function using a Salpeter initial mass function [Salpeter, 1955] and a 0.1 $M_\odot$ mass cutoff. This may likely be an overestimate for the current stream mass, as these low-mass stars may be preferentially stripped before others in the system due to mass segregation. However, we are most interested in the stream's mass as a lower limit on the mass of the cluster at the time of formation. The mass estimate with these assumptions may therefore more accurately reflect the mass of the system before tidal stripping occurred, though may be inflated compared to the present mass.

5. http://stellar.dartmouth.edu/models/

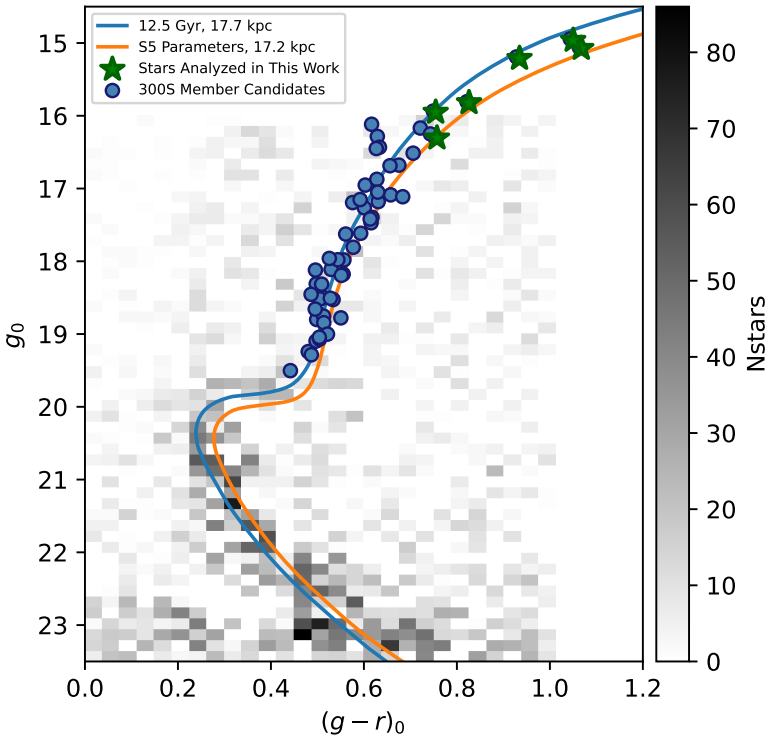

Figure 3.2 Isochrones matched to DECam DECaLS DR9 photometry. The blue and orange lines represent the best-fit isochrones found in this article and using parameters from Fu et al. [2018] and Li et al. [2022]. The parameters used for the latter isochrone are: age = 12.5 Gyr, [α/Fe] = 0.4, [Fe/H] = -1.27, d = 17.2 kpc, where [Fe/H] and d were from Li et al. [2022] and the age and [α/Fe] abundance are obtained from Fu et al. [2018]. Our best-fitting isochrone parameters are: age = 12.5 Gyr, [α/Fe] = 0.0, [Fe/H] = -1.35, d = 17.7 kpc. The green stars, and blue circles represent the dereddened color and magnitude of stars analyzed in this work and other member candidates observed by S^5. The DECam data is a background-subtracted Hess diagram along 300S' sky position.

We then use the number of observed stars to solve for the total mass of the stellar stream in our system.

$$\frac{N_{\text{observable, lum func}}}{M_{\text{tot, lum func}}} = \frac{N_{\text{observable, 300S}}}{M_{\text{tot, 300S}}} \tag{3.5}$$

Since we are observing red giant branch stars, the number of observable stars has stochastic error due to the short period of time the stars stay in this evolutionary stage. We use the 1 σ Poisson error as our upper and lower limits for the current mass for each isochrone. The fixed magnitude detection limit means that the estimated mass depends on the distance, so we also use the highest and lowest distance estimates to estimate an error on the expected detection fraction. We solve for the mass of the system with each isochrone with the predicted, upper and lower estimates for the mass, as well as our upper and lower distance measurements. We choose the resulting extrema from these various combinations of parameters to use as limits on the mass of our system.

From this calculation, we find that the current mass of 300S is $10^{4.6^{+0.3}_{-0.1}}$ $M_\odot$. However, we did not include stars which extend beyond S^5's footprint for the stream. $10^{4.6}$ $M_\odot$ is therefore a lower limit for the progenitor mass. More sophisticated methods of calculating masses could be used in future investigations [e.g., Martin et al., 2008, 2016].

We use a different method to estimate an upper limit on the stream mass: Eqn. 5 from Baumgardt and Makino [2003] gives the dissolution time T_{Diss}, the amount of time it would take for a globular cluster to completely disrupt given its initial mass M_{Ini}, initial number of stars N_{Ini}, and its orbital parameters assuming an isothermal

mass distribution for the Milky Way:

$$T_{\rm Diss} = 1.35 \times \left(\frac{M_{\rm Ini}}{\ln(0.02 N_{\rm Ini})} \right)^{0.75} \times \frac{R_{\rm Apo}}{V_G} \times (1 - \epsilon) \tag{3.6}$$

Here, $R_{\rm Apo}$, V_G, and ϵ are the distance at apocenter in kpc, the circular velocity of the Milky Way (assumed to be 240 km s^{-1}) and the eccentricity of the system's orbit, respectively. Since 300S is completely dissolved and we can find no intact cluster, we use known orbital parameters and possible dissolution times to see the highest and lowest possible initial masses that would be disrupted by now. We use the cluster's lower age limit and the age of the universe as minimum and maximum dissolution times respectively. The cluster can disrupt any time after forming, so this is essentially a range for the upper limit of the dissolution time. We used 300S's orbital parameters found in Li et al. [2022] and the best-fit age we found using isochrones. We find the maximum initial mass of 300S to be $\rm M_{Ini} = 10^{4.8 \pm 0.1}$ $\rm M_\odot$.

In conclusion, we find the progenitor mass of 300S is likely to be in the range of $10^{4.5-4.9}$ $\rm M_\odot$. We note, however, that models of mass loss are under development and constraints on the initial mass may improve significantly with time.

3.7 Results

We analyzed ten red giant branch member candidates of the 300S stream. We found two of the stars to be inconsistent with stream members (including the most metal-poor star analyzed in Fu et al. 2018), due to discrepant radial velocities. The eight analyzed stars had a mean LTE metallicity of [Fe/H] = −1.38 with an in-

trinsic dispersion of less than 0.09 at 95% confidence level. Abundances measured for each star can be found in Table 3.3. Mean element abundances and dispersions are listed in Table 3.4. Of the eight stars, we highlight three in particular: the enriched J1020+1555, the CH star J1001+1554, and the cool star J1045+1408.

Enriched star: J1020+1555. The second-warmest star of the group, J1020+1555, has the characteristic abundances of enriched stars found in GCs. Specifically: J1020+1555 has enrichment in N and Na, and depletion in O. We can see the differences in the absorption lines by comparing J1020+1555 to the 300S candidate with the most similar stellar parameters: J0956+1603. In Fig. 3.3, we can see that J1020+1555 (the dashed green line) has visually obvious differences in the absorption at key wavelengths compared to J0956+1603 (the solid red line). The abundances as a function of $T_{\rm eff}$ in Fig. 3.4 and the abundance anti-correlations can be seen in Fig. 3.5. Fig. 3.4 demonstrates that J1020+1555's anomalous abundances are prominent when compared to stars with similar $T_{\rm eff}$. The abundances are therefore not due to something like unusual stellar parameters, as could be the case in the cool star as we discuss later. Fig. 3.5 demonstrates that the abundances follow predicted correlations as observed in intact globular clusters. Lastly we compare the data numerically and show the significance of the Na abundance scatter in Table 3.5.

The CH star: J1001+1554. This star has a significant amount of C and *s*-process elements; specifically Sr, Y, and Ba have high abundances. We can visually see the difference in the carbon and *s*-process elements in Fig. 3.6 and numerically in Table 3.6. This enrichment indicates that J1001+1554 is a part of a binary star

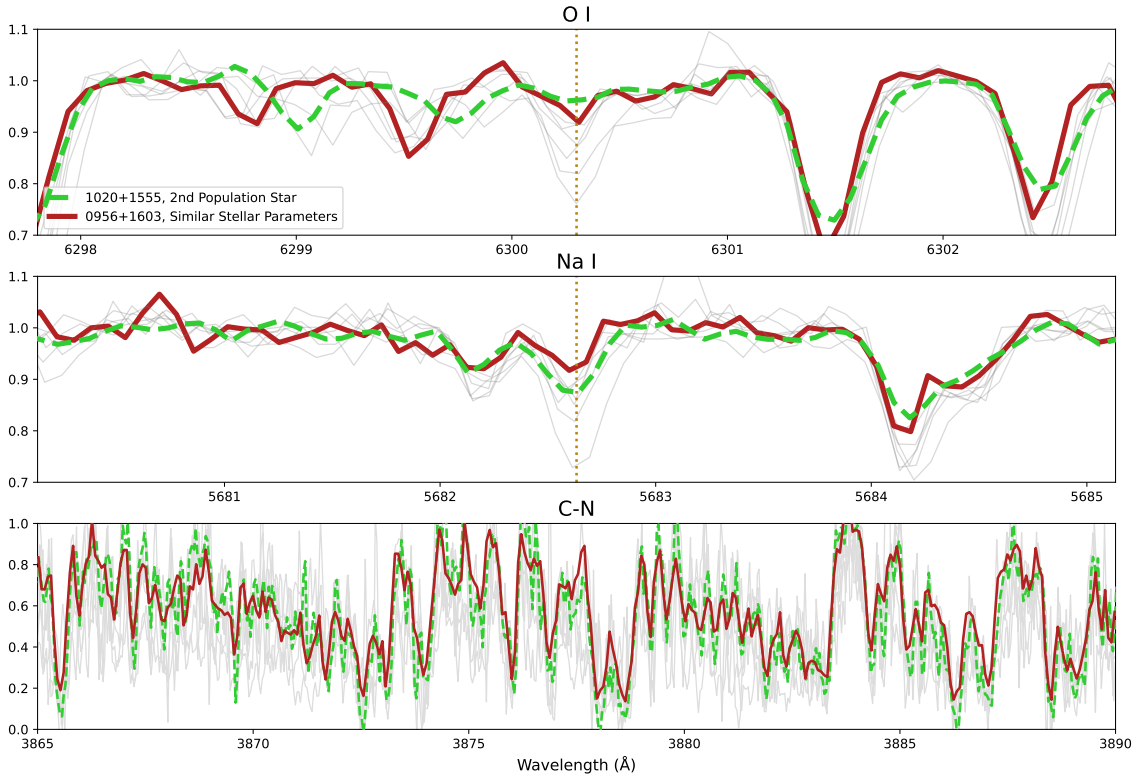

Figure 3.3 A comparison of normalized spectra around an O line, two Na lines, and the C-N bands in the top, middle and lower panels, respectively. We highlight the Telluric lines in the top panel. We emphasize here the enriched star J1020+1555 (dashed green line) and the star with most similar stellar parameters, J0956+1603 (red solid line). The former has a higher Na and N enrichment and O depletion as expected of enriched stars in GCs. The spectra of the other stars, which are significantly colder than the highlighted stars, are shown as thin gray lines. The bright red dotted line indicates the wavelength of the measured absorption lines.

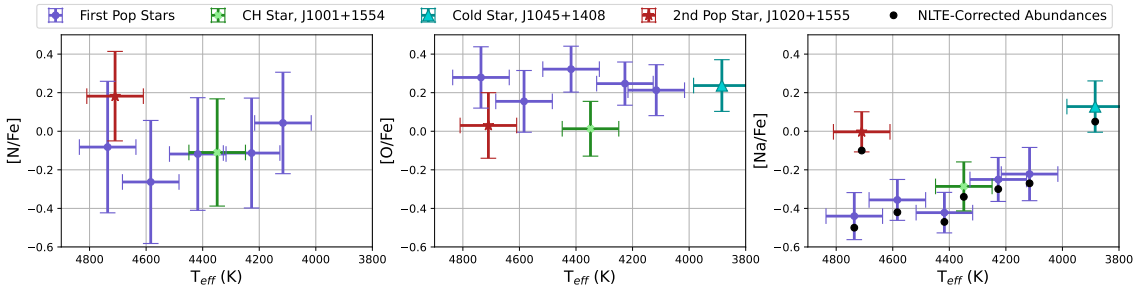

Figure 3.4 The abundances of elements characteristic of multiple population enrichment: nitrogen, oxygen, and sodium in the left, middle and right plots, respectively. The purple circles represent the abundances of the ordinary stars. The anomalous stars J1020+1555, J1001+1554, and J1045+1408 are marked with a dark red star, a green cross, and a blue triangle respectively. J1020+1555 has the requisite enrichment in N and Na, and depletion in O. We also measure unusual of Na enrichment in the cool star, J0956+1603. Additionally, in the rightmost plot, the black points represent the NLTE-corrected abundances. However, due to the correlation between $T_{\rm eff}$ and the Na abundance and no depletion in O, we attribute this to an unknown systematic error and do not consider this a second-population star.

system, and its carbon and *s*-process material were accreted from an AGB companion star [e.g., McClure and Woodsworth, 1990, Lucatello et al., 2003, Hansen et al., 2016]. No significant radial velocity variations were detected from the three velocity measurements in Table 3.1, though future more precise velocity measurements could potentially see a companion. The enrichment found in this star is similar to that of CEMP-s stars or Ba stars [e.g., Beers and Christlieb, 2005]; these stars may all have a similar enrichment mechanism involving mass transfer from a binary companion. CH stars such as this one are uncommon in GCs, probably because the high density of the systems tend to disrupt binaries before they can reach the mass transfer phase [Côté et al., 1997, D'Orazi et al., 2010]. We note that evolutionary mixing leads to changes in C abundances, which requires corrections to obtain the natal C abundance

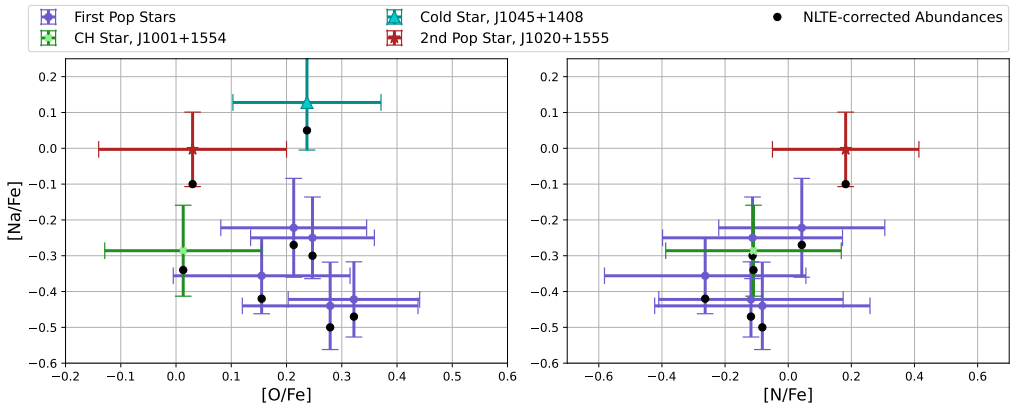

Figure 3.5 Correlated abundances of element Na compared to N and O in the left and right plots, respectively. The purple circles represent the abundances of the ordinary stars. The anomalous stars J1020+1555, J1001+1554, and J1045+1408 are marked with a dark red star, a green cross, and a blue triangle respectively. The black points represent the NLTE-corrected abundances. J1020+1555 has the requisite enrichment in N and Na, and depletion in O. We also measure unusual of Na in the cool star, J0956+1603. However, due to the correlation between $T_{\rm eff}$ (as seen in Fig. 3.4) and the Na abundance and no depletion in O, we attribute this to an unknown systematic error and do not consider this a second-population star.

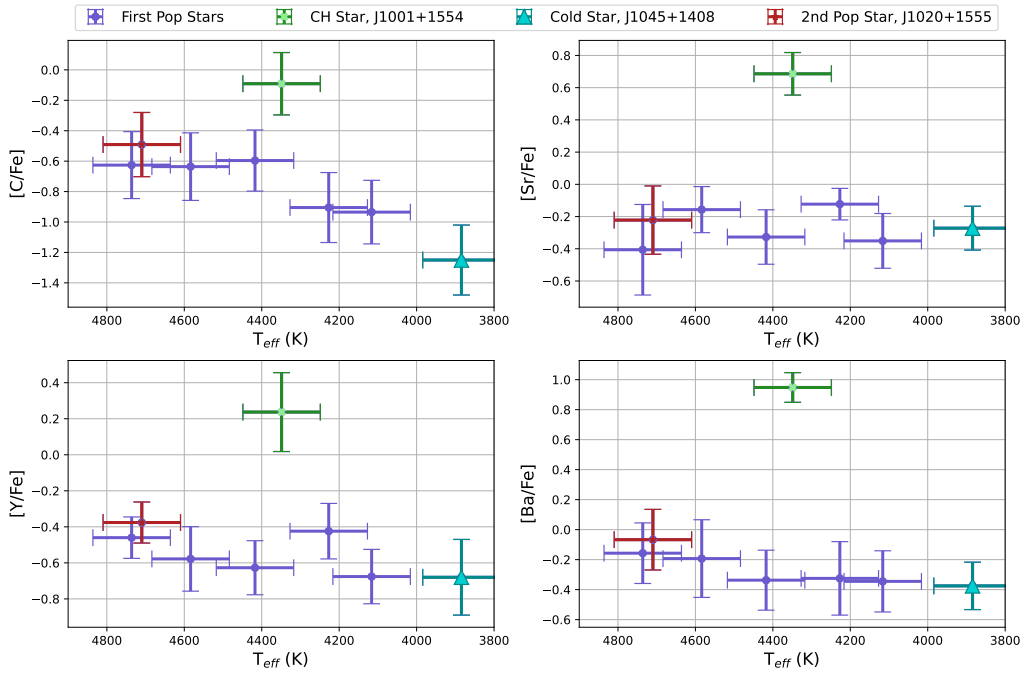

Figure 3.6 The abundances of elements characteristic of a CH star: carbon and *s*-process elements strontium, yttrium, and barium. The purple circles represent the abundances of the ordinary stars. The anomalous stars J1020+1555, J1001+1554, and J1045+1408 are marked with a dark red star, a green cross, and a blue triangle respectively. J1001+1554 has clear enrichment in all four of these elements.

[Placco et al., 2014]. Though the abundances we present here do not include mixing corrections, the corrections would *increase* C for the CH star, as C-enhanced stars have a larger corrections than stars with less carbon.

The cool star: J1045+1408. This star is the most luminous of the group, with an absolute Gaia G magnitude of about -3.25 and effective temperature $T_{\rm eff}$ of 3880 K. This star has a higher Na abundance than the other stars. There is a systematic correlating the Na abundance to $T_{\rm eff}$, as can be seen in Fig. 3.4. Since this star is the coolest and has the lowest surface gravity of our stars, we expected larger

NLTE effects than in our other stars. We calculated NLTE corrections for the Na abundances for all stars using an online NLTE calculator based on Lind et al. [2011].[6] The NLTE corrections to the Na abundances (derived using the 5682/5688Å doublet) are about 0.05 to 0.10 dex and the resulting abundances can be seen in Fig. 3.4. The cool star's Na abundance still appears higher than those of the other stars, even when accounting for NLTE effects and the apparent $T_{\rm eff}$ systematic. However, the cool star shows no O depletion as is found in the enriched star, and N was not measurable, so we have no further evidence it is an enriched star. We conclude that the anomalous Na abundance is probably not a reflection of stellar enrichment, though we cannot rule it out.

3.8 Discussion

3.8.1 Globular Cluster, Not a Dwarf Galaxy

Previous studies of 300S struggled to determine whether the progenitor of the stellar stream was a dwarf galaxy or a globular cluster. The stream was found by Fu et al. [2018] to have a metallicity dispersion. Li et al. [2022], however, measured no metallicity dispersion. To settle the contradicting results, we re-observed the most metal-poor star in Fu et al. [2018] with MIKE twice to verify its membership. The star's measured radial velocity is inconsistent with the stream moving at 300 km s^{-1}; further, the star shows significant variations in its radial velocities over time: on the two occasions the star was observed with MIKE, the observed radial velocity was

6. http://www.inspect-stars.com/cp/application.py/

Table 3.3 The measured element abundance for each star for our measured elements. We were unable to measure N in the cool star, J1045+1408. We also include Na abundances which have had NLTE corrections been applied, though we are unable to calculate error for the corrected abundances as our analysis is fully LTE.

Star	**[Fe I/H]**	$\sigma_{\mathrm{Fe\ I}}$	**[Fe II/H]**	$\sigma_{\mathrm{Fe\ II}}$	**[C/Fe]**	σ_{C}	**[N/Fe]**	σ_{N}	**[O/Fe]**	σ_{O}	**[Na/Fe]**	NLTE	σ_{Na}
J1045+1408	−1.48	0.06	−1.23	0.15	−1.25	0.23	-	-	+0.24	0.13	+0.13	0.05	0.13
J1049+1500	−1.38	0.06	−1.24	0.15	−0.94	0.21	0.04	0.26	+0.21	0.13	−0.22	−0.27	0.14
J1006+1509	−1.46	0.07	−1.45	0.14	−0.91	0.23	−0.11	0.29	+0.25	0.11	−0.25	−0.30	0.11
J1001+1554	−1.38	0.06	−1.44	0.10	−0.09	0.21	−0.11	0.28	+0.01	0.14	−0.29	−0.34	0.13
J1012+1554	−1.43	0.07	−1.31	0.09	−0.60	0.20	−0.12	0.29	+0.32	0.12	−0.42	−0.47	0.11
J1002+1541	−1.27	0.09	−1.22	0.09	−0.64	0.22	−0.27	0.32	+0.15	0.16	−0.36	−0.42	0.11
J1020+1555	−1.31	0.07	−1.38	0.11	−0.49	0.21	0.18	0.23	+0.03	0.17	−0.00	−0.10	0.10
J0956+1603	−1.32	0.11	−1.34	0.12	−0.63	0.22	−0.08	0.34	+0.28	0.16	−0.44	−0.50	0.12

Star	**[Mg/Fe]**	σ_{Mg}	**[Si/Fe]**	σ_{Si}	**[Ca/Fe]**	σ_{Ca}	**[Sc/Fe]**	σ_{Sc}	**[Ti/Fe]**	σ_{Ti}	**[Mn/Fe]**	σ_{Mn}
J1045+1408	+0.16	0.11	+0.40	0.08	+0.04	0.12	−0.53	0.14	−0.20	0.19	−0.51	0.18
J1049+1500	+0.22	0.22	+0.26	0.09	+0.16	0.17	−0.30	0.14	+0.03	0.21	−0.37	0.18
J1006+1509	+0.11	0.11	+0.29	0.09	+0.16	0.15	−0.19	0.13	+0.11	0.19	−0.42	0.14
J1001+1554	+0.19	0.22	+0.26	0.08	+0.15	0.11	−0.08	0.13	+0.18	0.13	−0.31	0.14
J1012+1554	+0.04	0.11	+0.24	0.07	+0.18	0.09	−0.21	0.13	+0.12	0.15	−0.40	0.14
J1002+1541	−0.00	0.12	+0.13	0.10	+0.19	0.16	−0.31	0.14	−0.21	0.20	−0.37	0.15
J1020+1555	+0.07	0.09	+0.17	0.08	+0.13	0.15	−0.10	0.12	−0.18	0.16	−0.33	0.16
J0956+1603	−0.04	0.13	+0.17	0.12	+0.20	0.14	−0.13	0.13	+0.47	0.32	−0.37	0.19

Star	**[Ni/Fe]**	σ_{Ni}	**[Zn/Fe]**	σ_{Zn}	**[Sr/Fe]**	σ_{Sr}	**[Y/Fe]**	σ_{Y}	**[Ba/Fe]**	σ_{Ba}	**[Eu/Fe]**	σ_{Eu}
J1045+1408	−0.14	0.24	−0.09	0.17	−0.27	0.14	−0.68	0.21	−0.38	0.16	+0.13	0.10
J1049+1500	−0.13	0.11	−0.41	0.11	−0.35	0.17	−0.68	0.15	−0.34	0.20	+0.12	0.10
J1006+1509	−0.06	0.11	−0.25	0.12	−0.12	0.10	−0.42	0.15	−0.33	0.25	+0.37	0.10
J1001+1554	−0.23	0.18	−0.41	0.11	+0.69	0.13	+0.24	0.22	+0.98	0.11	+0.48	0.08
J1012+1554	−0.08	0.13	−0.20	0.11	−0.33	0.17	−0.63	0.15	−0.34	0.20	+0.31	0.09
J1002+1541	−0.03	0.15	+0.01	0.16	−0.16	0.14	−0.58	0.18	−0.19	0.26	+0.12	0.14
J1020+1555	−0.12	0.14	−0.15	0.13	−0.22	0.21	−0.38	0.11	−0.07	0.20	+0.47	0.08
J0956+1603	−0.17	0.22	−0.25	0.15	−0.41	0.28	−0.46	0.12	−0.16	0.20	+0.14	0.16

Table 3.4 The most probable mean abundance and dispersion of 300S as inferred from the element abundances measured in all eight stars. The error bars and upper limits shown here represent one standard deviation confidence. We constrain the metallicity dispersion to less than < 0.09 with 95% confidence. Since our analysis was performed with the assumption of local thermodynamic equilibrium, we are unable to estimate the error for NLTE-corrected Na abundances, and therefore cannot measure 300's mean abundance and dispersion for the corrected abundances.

Element	Mean	Dispersion
[Fe/H]	-1.39 ± 0.03	< 0.06
[C/Fe]	-0.68 ± 0.11	$0.22^{+0.15}_{-0.16}$
[N/Fe]	-0.04 ± 0.13	$0.04^{+0.08}_{-0.02}$
[O/Fe]	0.20 ± 0.05	$0.03^{+0.05}_{-0.02}$
[Na/Fe]	-0.24 ± 0.07	$0.14^{+0.08}_{-0.07}$
[Mg/Fe]	0.08 ± 0.05	$0.03^{+0.03}_{-0.02}$
[Si/Fe]	0.25 ± 0.04	$0.03^{+0.03}_{-0.02}$
[K/Fe]	0.51 ± 0.11	$0.04^{+0.08}_{-0.02}$
[Ca/Fe]	0.15 ± 0.05	$0.03^{+0.03}_{-0.02}$
[Ti/Fe]	0.02 ± 0.07	$0.05^{+0.08}_{-0.03}$
[Mn/Fe]	-0.38 ± 0.06	$0.03^{+0.04}_{-0.02}$
[Ni/Fe]	-0.11 ± 0.06	$0.03^{+0.04}_{-0.02}$
[Zn/Fe]	-0.24 ± 0.06	$0.04^{+0.07}_{-0.02}$
[Sr/Fe]	-0.13 ± 0.14	$0.34^{+0.13}_{-0.10}$
[Y/Fe]	-0.47 ± 0.07	$0.08^{+0.13}_{-0.06}$
[Ba/Fe]	-0.08 ± 0.19	$0.46^{+0.18}_{-0.11}$
[Eu/Fe]	0.30 ± 0.06	$0.12^{+0.07}_{-0.06}$

Table 3.5 A comparison of the abundances of elements typically enriched or depleted in second-population globular cluster stars. The 1st-Pop Mean abundances are the most probable mean abundances for the first-population stars in 300S, as inferred from five typical stars in our sample (excluding the three anomalous stars). We compare this to the abundance found in our enriched star J1020+1555 and give the significance of the star's abundances with respect to the normal star population.

Element	1st-Pop Mean	J1020+1555 Abundance	Significance
[Fe/H]	-1.39 ± 0.04	-1.31 ± 0.07	0.95
[C/Fe]	-0.74 ± 0.11	-0.49 ± 0.21	1.04
[N/Fe]	-0.10 ± 0.14	0.18 ± 0.23	1.04
[O/Fe]	0.25 ± 0.06	0.03 ± 0.17	1.22
[Na/Fe]	-0.35 ± 0.06	0.00 ± 0.10	2.91
[Mg/Fe]	0.05 ± 0.06	0.07 ± 0.09	0.18

Table 3.6 A comparison of the abundances of elements typically enriched in CH stars. The 1st-Pop Mean abundances are the most probable mean abundances for the first-population stars in 300S, as inferred from five typical stars in our sample (excluding the three anomalous stars). We compare this to the abundance found in our CH star J1001+1554 and give the significance of the star's abundances with respect to the normal star population.

Element	1st-Pop Mean	J1001+1554 Abundance	Significance
[Fe/H]	-1.39 ± 0.04	-1.38 ± 0.06	0.16
[C/Fe]	-0.74 ± 0.11	-0.09 ± 0.20	2.80
[Sr/Fe]	-0.22 ± 0.08	0.69 ± 0.13	6.06
[Ba/Fe]	-0.27 ± 0.11	0.98 ± 0.11	8.47
[Eu/Fe]	0.24 ± 0.06	0.48 ± 0.08	2.50

measured to be ∼260 km s^{-1}. S^5measured a velocity of ∼275 km s^{-1}. Lastly, the SEGUE data used by Fu et al. [2018] indicates a velocity of ∼297 km s^{-1}. These large variations in radial velocity (>50 km s^{-1}) measured over several years imply the star is a part of a binary system. The average velocity is not similar enough to the stellar stream to be considered a member, as can be observed in Figure 3.1. Excluding this star from the analysis, the 300S stars have an insignificant metallicity spread.

Frebel et al. [2013b] also suggested the progenitor of 300S was a dwarf galaxy due to its low magnesium. We confirm the low [Mg/Fe] abundance, though we disagree with the interpretation. The GCs that formed *in situ* essentially sample the [Mg/Fe] ratio at different ages of the Milky Way. Low [Mg/Fe] abundance can simply indicate that a stellar system formed *ex situ*, such as the low Mg abundance of the S2 stream which may be a part of the Helmi stream [Aguado et al., 2021b]. The progenitor of 300S likely formed *ex situ*. The stream's trajectory is most similar to that of the GSE and its associated remnant GCs [Myeong et al., 2018, Massari et al., 2019, Forbes et al., 2020, Callingham et al., 2022, Limberg et al., 2022]. Fu et al. 2018 found an orbit similar to the Virgo Overdensity, which has since been determined to be debris from the GSE merger, e.g., Simon 2019, Iorio and Belokurov 2019, Naidu et al. 2021, Perottoni et al. 2022. Similarly, Li et al. [2022] calls attention to 300S's high eccentricity and its position close to GSE in the $E_{\rm tot} - L_Z$ plane to further suggest their association. These matching orbits indicate that it could have formed in GSE prior to the latter's merger with the Milky Way.

Indeed, the [Mg/Fe] observed in 300S matches the abundances found in GSE. In

Fig. 3.7, we compare the magnesium abundances of stars in 300S (represented by pink stars with black errorbars) to abundances in other systems. The gray semi-transparent triangles and symbols with dark outlines are APOGEE abundances for GSE stars and GSE GC stars, as identified by Limberg et al. [2021b]. The symbols with white outlines are APOGEE abundances for Milky Way GC stars identified by Mészáros et al. [2020], though we adopt the APOGEE DR17 abundances due to a significant zero-point offset. The most Mg-rich stars from each cluster represent the 1P stars for the respective system, as enriched stars in MSPs become depleted of Mg. We define the 1P stars using a cut in [Al/Fe]; since enriched stars exhibit high aluminum abundances, we make a cut at [Al/Fe] < 0.25 to determine which stars are unenriched. For the Milky Way GC stars, the resulting Mg-rich 1P stars hover around [Mg/Fe] $= 0.35$. The most Mg-rich stars of 300S fall alongside the Mg abundances of GSE and GSE cluster stars with an average [Mg/Fe] ≈ 0.2 [Belokurov and Kravtsov, 2023]. 300S abundances more closely aligns with the Mg content found in GSE and its clusters, further indicating along with the similar orbital properties that they may have a common origin, or that the former formed inside of the latter.

3.8.2 Multiple Populations and Initial Mass

We further confirm that the progenitor of 300S was a globular cluster by detecting a second-population star, J1020+1555. However, the stream does not contain as many enriched stars as we had initially expected. A correlation exists between the mass of intact Milky Way GCs and the fraction of enriched stars found therein, as seen in the left panel of Fig. 3.8. Assuming a binomial distribution, we infer that for just

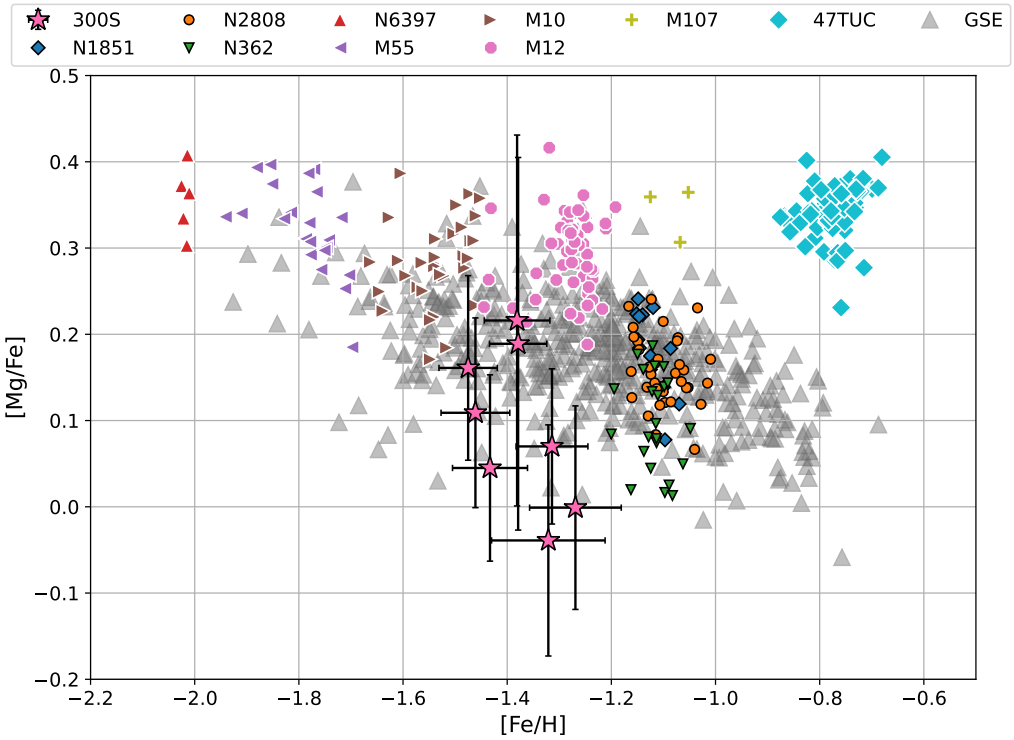

Figure 3.7 Magnesium to iron ratio in stars of Milky Way GCs, the stellar stream 300S, the GSE and GSE GCs. The Milky Way and GSE GCs star abundances are colored points with white and black outlines respectively. The abundances of GSE stars are represented by gray triangles, while our 300S measurements are represented by pink stars with black errorbars. GCs sample the [Mg/Fe] ratio of its host galaxy at its time of formation. The 1P stars for each cluster are the most metal rich at the top of the plot, while 2P stars have depleted Mg and stretch to the bottom of the figure. 300S does not resemble Milky Way GCs, but matches the GSE, indicating it formed *ex situ*. This chemical resemblance further supports the stream's dynamic association with GES given its highly eccentric and retrograde orbit: its energy and angular momenta similarly match that of GES [Fu et al., 2018]. The globular cluster abundances here are data APOGEE data from Mészáros et al. [2020], while the GSE abundances are APOGEE data from Limberg et al. [2021b].

one of eight stars to be enriched, the stream is likely to have an inherent enrichment fraction of $f_{enrich} = 0.13^{+0.19}_{-0.05}$, as is reflected in the figure. If we choose to exclude the cool star entirely from the sample due to its ambiguous enrichment, we calculate the stream's inherent enrichment fraction to be $f_{enrich} = 0.14^{+0.21}_{-0.06}$. We estimated 300S's current stream mass to be $10^{4.5}\,M_\odot$, as described in Section 3.6. The total stream mass should be higher than this, since more stream members beyond the footprint of S^5 were not included in this estimate. Interpolating a linear relationship between the current mass of intact Milky Way GCs and their fraction of enriched stars (as seen in the left panel of Fig. 3.8), we expected half of the stars in our sample to be enriched. Given our small sample size, we cannot completely exclude a 50% enrichment fraction, but we proceed taking the observed enriched fraction at face value.

With just one of the eight stars being enriched, 300S appears underenriched when compared to the present day masses of GCs, but is fairly reasonable when we compare the *progenitor* mass to the *initial* masses of intact Milky Way GCs. Intact Milky Way GCs have lost, on average, 80% of their initial mass over their lifetimes [Baumgardt et al., 2019] due to a combination of evaporation and tidal stripping. In Section 3.6 we estimated limits on the progenitor mass of 300S to be in the range of $10^{4.5-4.9}\,M_\odot$. In the right panel of Fig. 3.8, we compare the initial masses of intact Milky Way GCs with our best constraints on the initial mass of 300S. 300S does not appear anomalous in this framework, as it appears relatively in line with the relationship of enrichment fraction to initial mass as can be seen in other clusters containing MSPs [Belokurov and Kravtsov, 2023]. The stream progenitor could still be considered underenriched

if we assume a linear relationship between fractional enrichment and initial mass of the globular cluster, but it could also indicate a non-linear relationship between the cluster parameters.

The masses of GCs in the Large and Small Magellanic Clouds (represented by black stars in Fig. 3.8, as measured by Mucciarelli et al. 2009, Mateluna et al. 2012, Mucciarelli et al. 2014, Hollyhead et al. 2017, Niederhofer et al. 2017b,a, Martocchia et al. 2017, Hollyhead et al. 2018, Zhang et al. 2018, Martocchia et al. 2018, and Hollyhead et al. 2019 and compiled by Gratton et al. 2019) support this theory. It has been suggested that these clusters may have lost less mass, since the Magellanic Clouds are significantly less massive than the Milky Way [e.g., Milone et al., 2020]. We therefore assume that the Magellanic Cloud GC initial masses are relatively similar to the masses we see now. These clusters' masses fall in line with calculated initial masses of intact Milky Way GCs, and trend towards having a non-linear increase in enrichment above $10^5\,M_\odot$.

It has been suggested a minimum critical mass must be achieved in order to create MSPs [e.g., Gratton et al., 2019], though this threshold mass is currently undetermined. The initial mass of 300S may hover near the critical threshold, allowing the unusually low enrichment we see here. Further improvements to modelling of GCs to better calculate initial masses will allow us to more strongly constrain the mass-enrichment relationship. Additionally, spectroscopic follow-up of more globular cluster stellar streams may further serve as a useful probe to finding a critical mass needed to achieve chemical enrichment found in most GCs. Theoretically, Bland-Hawthorn et al. [2010] suggests that a single-population globular cluster is

achievable up to an initial mass of $10^{6.5}$ $M_{\odot}$. If this corresponds to the minimum mass threshold, it would suggest significant revisions are needed to globular cluster mass loss.

3.8.3 CH Star and Cluster Dynamics

We find a CH star in our stellar stream, enriched in carbon, barium, yttrium, and strontium. In this text, we have referred to our *s*-process enhanced star as a CH star, though it also fits the criteria of a Ba star (but is too metal-rich to be considered a CEMP-s star). We therefore look to previous literature on Ba stars to shed light on our *s*-process enhanced star, specifically to understand their rarity.

Binary systems are scarce in globular clusters compared to the field, perhaps due to their high density disrupting bound binary orbits [Côté et al., 1997]. Since Ba stars are thought to form due to accretion from a companion star [McClure et al., 1980], we would expect Ba stars to be similarly unusual in globular clusters.

For comparison, Luck and Bond [1991] found the fraction of Ba stars in the field to be ∼2%. The more recent study Norfolk et al. [2019] used the LAMOST survey to find that approximately 0.2% of their sample of 454,180 giant stars to be s-process enhanced. 26% of these stars (0.05% of the total sample) have detectable amounts of Ba, though this may be an underestimate due to limitations from LAMOST's low-resolution spectra. Therefore the rate of Ba stars in the field is probably in the range 0.05% to 2% of stars.

D'Orazi et al. [2010] specifically explored the rate of Ba stars in globular clusters and found 5 of the 1,205 red giant stars observed (0.4%) were Ba stars, endorsing

previous theories that Ba stars are rare in globular clusters. However, this rate appeared dependent on whether the star was part of the enriched or unenriched star populations. The authors found four of the five Ba stars were unenriched stars, estimating that about ∼2% of unenriched stars in globular clusters. The Ba star rate in enriched star populations can therefore be calculated to be ∼0.1% using Bayes' theorem.

Finding a Ba star in our small star sample is therefore very surprising and unexpected. Assuming a binomial distribution, we can infer that the intrinsic rate of Ba stars in 300S's unenriched star population is $f_{Ba} = 14^{+21}_{-5}\%$. This is significantly higher than the rate of ∼2% found by D'Orazi et al. [2010] for unenriched star populations in intact star clusters. This could indicate that the disruption of globular clusters allows for binary systems to survive longer than would've been possible in an intact cluster environment, enabling them to reach a stage where accretion from a binary companion can be achieved. Further spectroscopic study of globular cluster stellar streams could help clarify whether streams in general provide a fruitful environment for the survival of binaries.

3.9 Conclusion

The discovery and analysis of 300S has led to interesting implications for the formation of MSPs and of the survival of binaries in GCs. Through our observation of 10 red giant branch candidate stars and subsequent spectroscopic analysis of 8 member stars, we find that:

- The progenitor of 300S is a globular cluster.

  - The stream is relatively metal-rich and magnesium-poor when compared to Milky Way GCs, but its orbit indicates that it formed *ex situ,* perhaps inside the GSE. The stream's metallicity and Mg abundance is a reflection of its host galaxy, not the nature of its progenitor, as can be seen in Fig. 3.7.
  - An analysis by Fu et al. [2018] indicated 300S had a measurable metallicity dispersion, indicating its progenitor was a dwarf galaxy. However, we found the most metal-poor star in the sample to have a discrepant radial velocity (shown in Table 3.1). The remaining stars have no significant spread in metallicity.
  - We identify one star, J1020+1555, as a second-population star, enriched in sodium and nitrogen while depleted in oxygen. MSPs are a hallmark of GCs, confirming the nature of the stream's progenitor. The comparison of these key elements are shown in Fig. 3.4 and Fig. 3.5.

- The progenitor of 300S straddled the threshold of the critical mass for making MSPs. We calculate the initial mass of 300S based on its orbital parameters and compare it to the initial masses of intact GCs as calculated by Baumgardt et al. [2019]. We find it to have an initial mass of $M_{Ini} = 10^{4.5-4.9}$ $M_{\odot}$, which aligns with the initial masses of GCs with small fractions of enriched stars. This comparison is shown in Fig. 3.8. 300S is therefore a good benchmark for the critical mass threshold of MSPs.

- We find a CH star, which is unusual inside of intact GCs. The star is shown to

be enriched in carbon and *s*-process elements such as strontium, yttrium, and barium, as shown in Fig. 3.6. This could be an indication that stellar streams may provide a more suitable environment for the formation and sustained lifetime of binary systems than intact GCs.

Future work is needed to further explore the relationship between initial mass and MSPs in GCs. Exploring globular cluster streams would allow us to further probe this relationship using *ex situ* sources. Another way to confirm this would be to look at a galaxy of similar size, such as M31, and perform a similar calculation as found in Baumgardt et al. [2019]. This would allow us to test for a consistency in the relationship between mass and fraction of enriched stars in galaxies outside of our own. By better constraining the relationship between initial mass and enrichment, we could then reverse engineer the correlation to estimate the mass loss of GCs in a galaxy. The trend of GCs' fractional enrichment compared to their mass could then be compared to the confirmed initial mass threshold for multiple population formation. This be a novel way to estimate the initial mass for GCs in distant galaxies.

Acknowledgements

This paper includes data gathered with the 6.5 meter Magellan Telescopes located at Las Campanas Observatory, Chile. We thank all the LCO staff for enabling astronomical observations during a global pandemic. This paper includes data obtained with the Anglo-Australian Telescope in Australia. We acknowledge the traditional owners of the land on which the AAT stands, the Gamilaraay people, and pay our

respects to elders past and present. For the purpose of open access, the author has applied a Creative Commons Attribution (CC BY) licence to any Author Accepted Manuscript version arising from this submission.

We thank Jeffrey Gerber for his insightful feedback about CH stars. S.A.U. and A.P.J. acknowledge financial support from NSF grant AST-2206264. T.S.L. acknowledges financial support from Natural Sciences and Engineering Research Council of Canada (NSERC) through grant RGPIN-2022-04794. A.B.P. is supported by NSF grant AST-1813881.

This work has made use of data from the European Space Agency (ESA) mission *Gaia* (https://www.cosmos.esa.int/gaia), processed by the *Gaia* Data Processing and Analysis Consortium (DPAC, https://www.cosmos.esa.int/web/gaia/dpac/consortium). Funding for the DPAC has been provided by national institutions, in particular the institutions participating in the *Gaia* Multilateral Agreement.

This research has made use of the SIMBAD database, operated at CDS, Strasbourg, France [Wenger et al., 2000]. This research has made use of NASA's Astrophysics Data System Bibliographic Services.

Data Availability

The individual line measurements are provided as supplementary material. The reduced spectra can be obtained by reasonable request to the corresponding author.

Table 3.7 The following is a sample table of data for the star 0956+1603. Full data tables are available online.

Star	El.	N	ul	$\log\epsilon$	[X/H]	$\sigma_{\rm [X/H]}$	[X/Fe]	$\sigma_{\rm [X/Fe]}$	Δ_T	Δ_g	Δ_v	Δ_M	s_X
0956+1603	C-H	2		+6.51	−1.95	0.23	−0.63	0.22	0.18	-0.01	-0.01	0.21	0.04
0956+1603	C-N	1		+6.43	−1.40	0.37	−0.08	0.34	0.34	0.01	-0.02	0.27	0.00
0956+1603	O I	1		+7.65	−1.04	0.16	+0.28	0.16	0.03	0.10	0.01	0.09	0.00
0956+1603	Na I	2		+4.49	−1.76	0.12	−0.44	0.12	0.10	0.00	-0.01	0.00	0.00
0956+1603	Mg I	4		+6.27	−1.36	0.10	−0.04	0.13	0.06	-0.05	-0.03	0.02	0.09
0956+1603	Si I	4		+6.37	−1.15	0.10	+0.17	0.12	0.07	0.03	-0.01	0.02	0.00
0956+1603	K I	2		+4.42	−0.65	0.28	+0.67	0.25	0.20	-0.05	-0.13	-0.04	0.00
0956+1603	Ca I	7		+5.18	−1.12	0.12	+0.20	0.14	0.09	0.03	0.05	0.01	0.05
0956+1603	Ti I	2		+4.05	−0.85	0.33	+0.47	0.32	0.17	0.00	-0.00	0.00	0.34
0956+1603	Mn I	6		+3.66	−1.69	0.20	−0.37	0.19	0.15	-0.00	-0.01	0.00	0.15
0956+1603	Fe I	20		+6.09	−1.32	0.11	+0.00	0.00	0.07	0.01	0.04	0.02	0.15
0956+1603	Fe II	5		+6.17	−1.34	0.12	+0.00	0.00	-0.03	0.10	-0.02	0.06	0.03
0956+1603	Ni I	4		+4.58	−1.49	0.23	−0.17	0.22	0.14	0.03	0.03	0.02	0.23
0956+1603	Zn I	2		+2.98	−1.57	0.15	−0.25	0.15	0.03	0.07	-0.06	0.05	0.07
0956+1603	Sr II	1		+1.12	−1.75	0.38	−0.41	0.28	0.21	0.06	-0.11	0.20	0.00
0956+1603	Y II	4		+0.39	−1.80	0.19	−0.46	0.12	0.05	0.10	-0.02	0.08	0.04
0956+1603	Ba II	5		+0.68	−1.50	0.27	−0.16	0.20	0.04	0.05	-0.13	0.06	0.26
0956+1603	Eu II	1		−0.68	−1.20	0.17	+0.14	0.16	-0.01	0.10	0.02	0.08	0.00

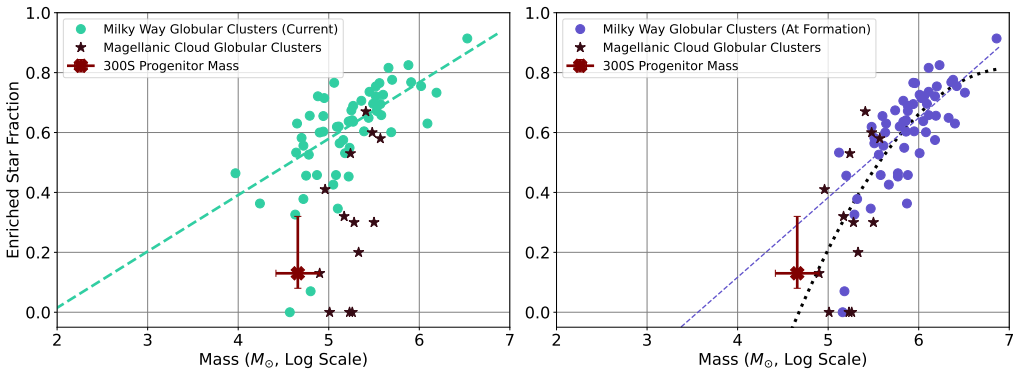

Figure 3.8 The current masses (green circles, left) and initial masses (purple circles, right) of intact Milky Way GCs [Milone et al., 2017, Baumgardt et al., 2019]. The measurements for the Magellanic Clouds come from Mucciarelli et al. [2009], Mateluna et al. [2012], Mucciarelli et al. [2014], Hollyhead et al. [2017], Niederhofer et al. [2017b,a], Martocchia et al. [2017], Hollyhead et al. [2018], Zhang et al. [2018], Martocchia et al. [2018], and Hollyhead et al. [2019] and were compiled by Gratton et al. 2019. The lower limit for 300S's mass is its current stream mass, while the upper limit of its mass is calculated from based on a fully dissolved cluster as described in Section 3.6. In the left panel, we see a correlation between the present-day mass of intact Milky Way GCs and the fraction of enriched stars found therein. If we extrapolate a linear relationship, we would expect a system with a mass of $10^{4.5}\,M_\odot$ like 300S would have about half of its stars enriched. Instead, just one of our eight stars exhibited enrichment. In the right panel, we compare the initial masses and the fraction of enriched stars for these same systems. We find a much tighter correlation. If we again assume a linear relationship, 300S still appears underenriched for its mass, but does not appear as significantly displaced. A quadratic relation, however, may be better at representing a critical threshold limit needed to create stellar enrichment. Extrapolating from this relationship (the black, dotted line), 300S appears more closely in line with predictions. In both panels, 300S is marginally more enriched than two other Milky Way globular clusters: Ruprecht 106 and Terzan 8.

CHAPTER 4

MASS-TRANSFER STARS IN DISRUPTING AND FULLY DISRUPTED GLOBULAR CLUSTERS: A BA STAR FOUND IN THE GD-1 STELLAR STREAM

This paper is currently in development for publication in the Open Journal of Astrophysics.

4.1 Abstract

We spectroscopically observe ten red giant branch stars in the globular cluster stellar stream GD-1 using the Hobby-Eberly Telescope at McDonald Observatory, the Lowell Discovery Telescope at Lowell Observatory, and the Magellan telescopes at Las Campanas Observatory. We identify one star enriched in sodium, indicating that it is a second-population (*2P*) star: a distinct type of star uniquely found in globular clusters with a characteristic correlated abundance pattern. The same star also has high enrichment of barium and yttrium, indicative of enrichment via accretion from a binary companion. Such mass-transfer enrichment is thought to be unusual in globular clusters, due to their high density which disrupts tight binaries before mass transfer can be achieved due to Roche lobe overflow. However, mass-transfer stars have been recently identified in significantly disrupted globular cluster ESO 280-SC06 and stellar stream 300S and now GD-1. Here, we explore the relationship between globular cluster mass loss and binary enrichment fraction. We suggest that globular

clusters that experience significant mass loss or are fully disrupted may support the formation and long-term survival of binaries.

4.2 Introduction

Globular clusters (*GCs*) are dense stellar clusters that provide a unique natal environment for star formation. The uniquely high density of these clusters may contribute to their chemical pattern: they contain *multiple populations,* correlated abundance patterns. These populations are comprised of a base population of stars that remains chemically similar to solar abundances, called the *first population* (*1P*), and an enriched population that contains enhancements in elements such as nitrogen, aluminum and sodium and depletions in carbon, magnesium and oxygen [Osborn, 1971, Bell and Dickens, 1980, Cottrell and Da Costa, 1981, Norris et al., 1981], called the *second populatoin* (*2P*). While these abundance patterns have been identified in almost every globular cluster in the Milky Way, the exact mechanism is not well understood [Carretta, 2006, Carretta et al., 2009b, Mészáros et al., 2015, Bastian and Lardo, 2018]. Almost every globular cluster in the Milky Way contains multiple populations, with the exception of Ruprecht 106 and E3 in the Milky Way [Villanova et al. 2013; Salinas and Strader 2015] and NGC 419 in the Small Magellanic Cloud [Martocchia et al., 2017].

One hint to the origin of this unique chemical pattern is the clear correlation between the mass of a globular cluster and the fraction of 2P stars found therein. Higher-mass clusters have a higher fraction of 2P stars relative to less massive clusters (e.g. Gratton et al. 2019, which combines enrichment fractions from Milone et al.

2017 and masses from Baumgardt and Hilker 2018). The relationship becomes even more tightly correlated when comparing the 2P star fraction to the cluster's *initial mass* [Gratton et al., 2019] and can even be identified in globular cluster stellar streams [Usman et al., 2024, 2025].

Globular cluster stellar streams provide a unique opportunity to probe the lowest-mass end of the relationship between the mass and 2P star population. Stellar streams have been observed and chemically tagged by the Southern Stellar Stream Spectroscopic Survey (S^5Collaboration), which provided low-resolution follow-up of dozens of dwarf galaxy and globular cluster stellar streams [Li et al., 2019, 2022].

The high density of stars within globular clusters causes binary stars to be disrupted via three-body interactions [Côté et al., 1997]. Binary systems in the field can live long enough to experience mass-transfer, as one companion puffs up in later stages of the star's life cycle and expands beyond its Roche lobe. For this reason, we find very few stars that show chemical enrichment indicative of mass-transfer in globular clusters. However, mass-transfer stars have recently been identified in strongly disrupted globular clusters or their fully disrupted remnants; stellar streams.

In Section 4.3, we describe the target selection and observations. Section 4.4 describes the determination of stellar parameters. Section 4.5 describes the abundance analysis, including how the abundance dispersion was calculated. The current stream mass and the initial mass of its progenitor are calculated in Section 4.7. The results are shown in Section 4.6. We summarize our interpretations in Section 4.8. Lastly, we discuss the broader implications for MSPs and future work in Section 4.9.

4.3 Observations

Our observations combine high-resolution spectroscopy from the Magellan Telescopes at Las Campanas Observatory, the Hobby-Elerby Telescope at McDonald Observatory and the Lowell Discovery Telescope at Lowell Observatory. Of the thirteen stars observed, four were found to be non-members due to discrepant radial velocities and/or discrepant metallicities. Fig. 4.1 depicts the position and velocities of observed stars and member-candidate stars in GD-1.

Two stars were observed using the Magellan/MIKE high-resolution spectrograph in December 20/21 2024, using a $0.7''$ slit and 2×2 on-chip binning [Bernstein et al., 2003]. The data were reduced using `CarPy` [Kelson, 2003]. We achieve SNRs measured per pixel ranging from 80 for red wavelengths around 8,000 Å and 30 for blue wavelengths around 4,500 Å. We calculate the radial velocity by cross-correlating the Mg b triplet with the spectrum of HD122563.

Four stars were observed with the McDonald/HRS2 high-resolution spectrograph. We achieve an SNR of about 70 for these stars around 7,000 Å. One of these stars, 165*, was observed again by Lowell/EXPRES high-resolution spectrograph, in addition to three unique stars. We achieve an SNR of 15-20 for these stars around 7,000 Å. Due to the difference in SNR, we present here abundances from McDonald/Lowell for the redundant star 165*, though we did find that the abundances from both spectra to be in agreement.

Table 4.1 Observed stars and their parameters. Stars are labeled with the first four digits of their *Gaia* IDs.

***Gaia* ID**	**RA** (°)	**Dec** (°)	**Telescope**	**G_0** (mag, dereddened)	**Distance** (kpc)	**Radial Velocity** (km s^{-1})
3066883902369513472	126.37507608660462	-3.128855288440547	Magellan	14.62	7.74	267.84
3076433195215851136	127.10021105303333	-0.48909636560161596	Magellan	15.04	7.73	258.62
693718792618722432	141.0514380978146	25.639724734530226	McDonald	12.12	7.49	76.90
696220731328715648	142.6711769895131	29.032957552696324	Lowell	14.23	7.48	47.99
796217426927895168	148.80420204466864	35.888583277355494	Lowell	13.40	7.566	-12.432
796574222749717376	149.06446587749423	35.70878190426444	Lowell	14.04	7.56	-14.93
805475834527735168	153.78744651279303	42.23035361941378	McDonald	13.23	7.73	-61.71
830562635424605312	159.99051733336714	46.23394236173885	McDonald	13.40	7.94	-95.38
1659307361510695808	207.3169938051616	58.52644757023654	Lowell & McDonald	13.42	10.33	-275.61
5713049502967159680	120.99776094857648	-20.791693902986886	Magellan	13.95	7.94	349.74
610774070664976384	134.9872268489017	16.610656728579176	Lowell	13.51	7.63	-11.34
612409564147659264	135.11013105499023	18.909716931577375	McDonald	13.28	7.59	204.50
697029078533610240	141.65382879441523	29.35076785142866	McDonald	12.90	7.48	19.90

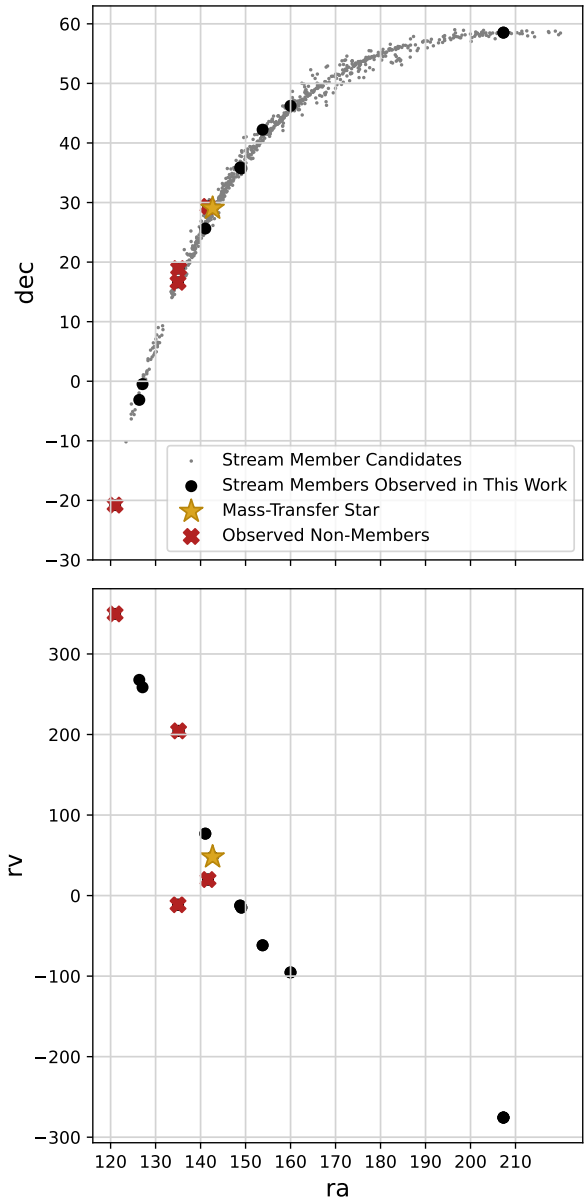

Figure 4.1 The sky location (top panel), radial velocities (bottom panel) of member and member-candidate stars in the GD-1 stellar stream. The gray points represent member candidate stars identified by Ibata et al. [2024]. The black circles and the gold star represent member stars observed in this work, with the latter being the 2P and mass-transfer star. The red crosses represent stars that were observed but were found to be non-members, either due to discrepant radial velocities and/or discrepant metallicities.

Table 4.2 Stellar parameters of observed stars. Effective temperatures and surface gravities are estimated using photometry. The stars observed with Magellan, 306* and 307*, have surface gravities, metallicity, and microturbulence uncertainties of 0.15, 0.2, and 0.2 km s^{-1}. Due to higher SNR, we use uncertainties 0.2, 0.3 and 0.3 km $s^{-1}$for stars observed with McDonald and Lowell.

***Gaia* ID**	Abbv.	T_{eff} (K)	log g	[Fe/H]	$e_{[Fe/H]}$	ν_t (km s^{-1})	e_{ν_t}	Distance (kpc)
3066883902369513472	306*	4947	2.19	-2.49	0.20	1.48	0.2	7.7
3076433195215851136	307*	4988	2.40	-2.56	0.20	1.46	0.2	7.7
693718792618722432	693*	4388	0.94	-2.54	0.30	1.45	0.3	7.5
696220731328715648	696*	5143	2.15	-2.64	0.30	2.35	0.3	7.5
796217426927895168	7962*	4860	1.70	-2.67	0.30	1.01	0.3	7.6
796574222749717376	7965*	4882	1.96	-2.67	0.30	2.04	0.3	7.6
805475834527735168	805*	4693	1.53	-2.56	0.30	1.68	0.3	7.7
830562635424605312	830*	4865	1.65	-2.58	0.30	1.38	0.3	7.9
1659307361510695808	165*	4536	1.28	-2.43	0.30	1.80	0.3	10.3

4.4 Stellar Parameter Determination

For all stars, we use photometric effective temperatures $T_{\rm eff}$ and surface gravities $\log g$. We use photometry from Gaia DR3, which we deredden using Equation 1 from Collaboration et al. [2018] and reddening data from Schlegel et al. [1998] with applied corrections from Schlafly and Finkbeiner [2011]. [1]

For the former, we leverage Equation (1) from Mucciarelli et al. [2021] for red giant branch stars using the color BP-RP. We use an uncertainty of 75 K for $T_{\rm eff}$, which is consistent with the uncertainty estimated in Mucciarelli et al. [2021].

We then use Equation 3 from Venn et al. [2017] to estimate $\log g$. This equation requires a distance modulus, which we estimate as a function of stream coordinates according to Koposov et al. [2010]. We use a surface gravity uncertainty of 0.15 for Magellan observations, and 0.20 for Lowell and McDonald observations. The remaining stellar parameters, metallicity and microturbulence, are estimated spectroscopically. For both of these parameters, we use an uncertainty of 0.2 for Magellan observations and 0.3 for Lowell and McDonald observations.

4.5 Abundance Analysis

We analyzed these spectra using `LESSPayne` [Ji et al., 2025], an automated analysis pipeline built off of the analysis interface `smhr` [Casey, 2014, Ji et al., 2020b, Casey et al., 2025]. Our analysis consists of a standard spectroscopic analysis which assumes stars are in local thermodynamic equilibrium (LTE) and leverages radiative transfer

1. This data was obtained through the IRSA database: https://irsa.ipac.caltech.edu/applications/DUST/.

code `moog` [Sneden, 1973, Sobeck et al., 2011] and one-dimensional stellar atmosphere models [Castelli and Kurucz, 2003]. At each step in the process, the automated results are manually reviewed for correctness and internal consistency.

For MacDonald and Lowell spectra, the observations are co-added and orders stitched manually prior to the automated analysis. For Magellan spectra, `LESSPayne` normalizes and stitches together all spectral orders.

`LESSPayne` then automatically fits the equivalent widths of all available absorption lines. In our analysis, we adopt the line list used in Ji et al. [2020b].

4.5.1 Measurements

Metallicity. Metallicity was determined by fitting equivalent widths for Fe I and Fe II lines in all stars.

C, N Carbon and nitrogen were only measured in the two Magellan stars. Carbon abundances were measured by synthesizing models of the C-H band in the range of 4300-4325 Å. Nitrogen abundances were measured by synthesizing the C-N band in the range 3860-3890 Å. These bands must be synthesized, as the absorption is complex due to the molecular structures.

α-elements: Mg, Si, Ca, Ti. Magnesium and calcium were measured using equivalent widths in all stars. In the Magellan stars, Mg I was measured using eight absorption lines between 4300 and 6800 Åand Ca I had seven lines in the range of 5800 and 6500 Å. In the McDonald and Lowell stars, Mg I was measured using around four absorption lines between 4700 and 5700 Å. In the stars observed by Lowell, Ca I had

up to seven lines in the range of 5200 and 6500 Å. The McDonald stars used about two dozen lines between 4300 and 6700 Å. Silicon and titanium were only measured in the Magellan stars. Si I was measured by two lines at 3906 Åand 4102 Å. Ti I and Ti II were measured using 50 lines between 3700 and 5400 Å.

Odd-Z Elements: Na, K. Sodium was measured in data from all telescopes using the sodium D lines at 5889 and 5895 Å. Unfortunately, in some stars observed with McDonald, one or both of the sodium lines fell outside of the observed orders. For this reason, one star, 693*, has no sodium observed. Potassium was observed in Magellan stars using lines at 7665 and 7699 Å.

Fe-Peak Elements: Mn, Ni, Zn. Manganese, nickel, and zinc were measured in the Magellan stars with a mix of synthesis and equivalent widths. Mn was synthesized in the range of 4700-4900 Å and 6023 Å. Ni was measured using equivalent widths around 20 lines between 3700 and 7800 Å. Zn was measured at 4722 and 4810 Å using equivalent widths.

Neutron-Capture Elements: Sr, Y, Ba, Eu. Of these elements, only barium could be measured in all stars. Ba II was synthesized with up to five lines between 4500 and 6500 Å. In the McDonald and Magellan stars, Sr II and Eu II were measured using synthesis Sr II lines were measured at 4078 and 4215 Å, while Eu II lines were measured at 4129 and 4205 Å. Y II was measured in the Magellan stars using three lines around 4400 to 4900 Åand in one Lowell star, 696*.

The full measured abundances described here are shown at the end of the paper, in Tables 4.4−4.10.

4.6 Abundance Results

From our derived chemical abundances, we find sodium enrichment in just one of the eight stars in which sodium was measured, star 696*. We can observe the increased absorption in Figure 4.2, where we compare one star's spectrum from each telescope. We compare abundances indicative of multiple populations in Figure 4.3.

Lastly, the same 2P star also shows enhance barium and yttrium abundances, as demonstrated in 4.4. This indicates that a binary companion accreted enriched material onto star 696*. The identification of carbon or other *s*-process elements, such as strontium, would further confirm that 696* is a mass-transfer star.

We also not that one star, 693*, exhibits extremely low strontium relative to other stars in the cluster. This may be indicative of a spread in neutron capture elements, as has been observed in other globular clusters.

4.6.1 Abundance Dispersion Analysis

We infer the abundance means and constrain the abundance dispersions for GD-1. We follow the same method used in [Usman et al., 2024], leveraging the nested sampling algorithm `dynesty` [Speagle, 2020, Higson et al., 2019, Koposov et al., 2022] to sample and the log-likelihood function (Equation 4, Usman et al. 2024) of random samples of the cluster's abundances.

We exclude the 2P / mass-transfer star for the elements [Na/Fe] and [Ba/Fe], as its chemical enhancement does not reflect the inherent cluster abundance. We also exclude upper limit estimates. We list the number of stars included in the cluster

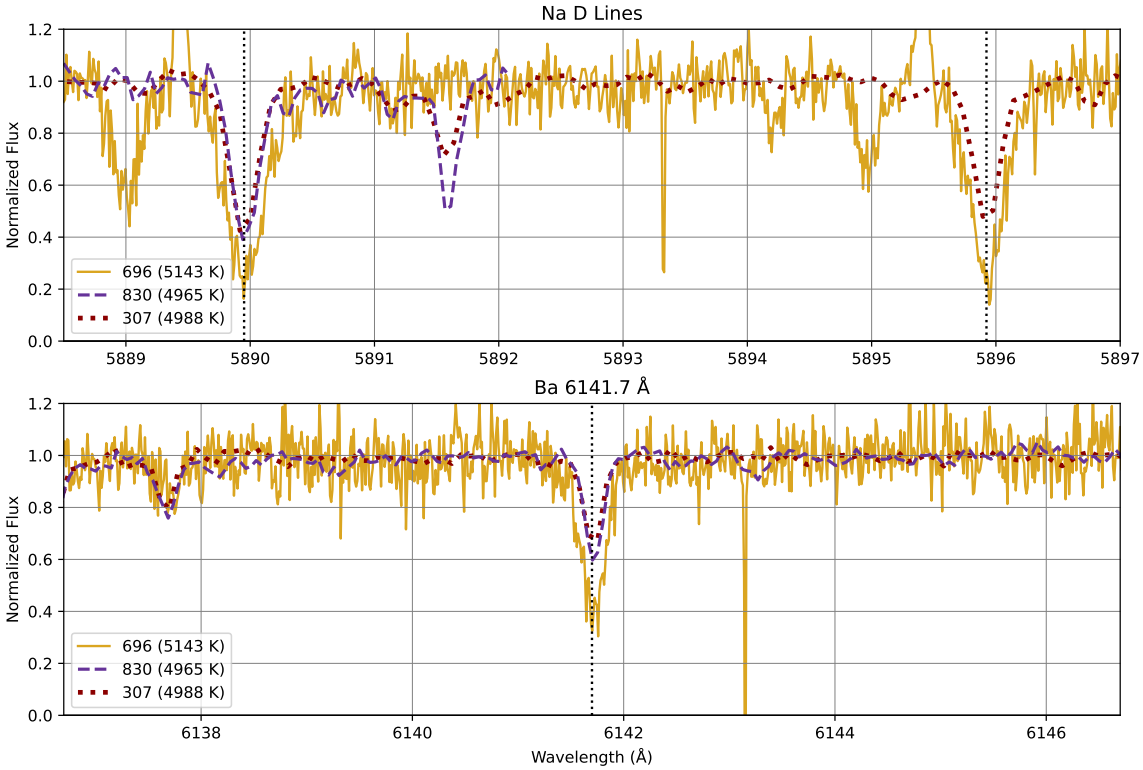

Figure 4.2 The spectra of three stars around key wavelengths. The yellow, solid line represents the sodium- and barium-enriched star 696*, observed at Lowell Observatory. The purple, dashed line represents a star of most similar temperature, 830*, observed using McDonald Observatory. The red, dotted line represent a star of most similar temperature, 307*, observed with the Magellan Telescopes. The top and bottom panels demonstrate the sodium D lines and a barium line, respectively. Despite 696*'s higher temperature, the star exhibits significantly more absorption, demonstrating its enrichment in both of these elements.

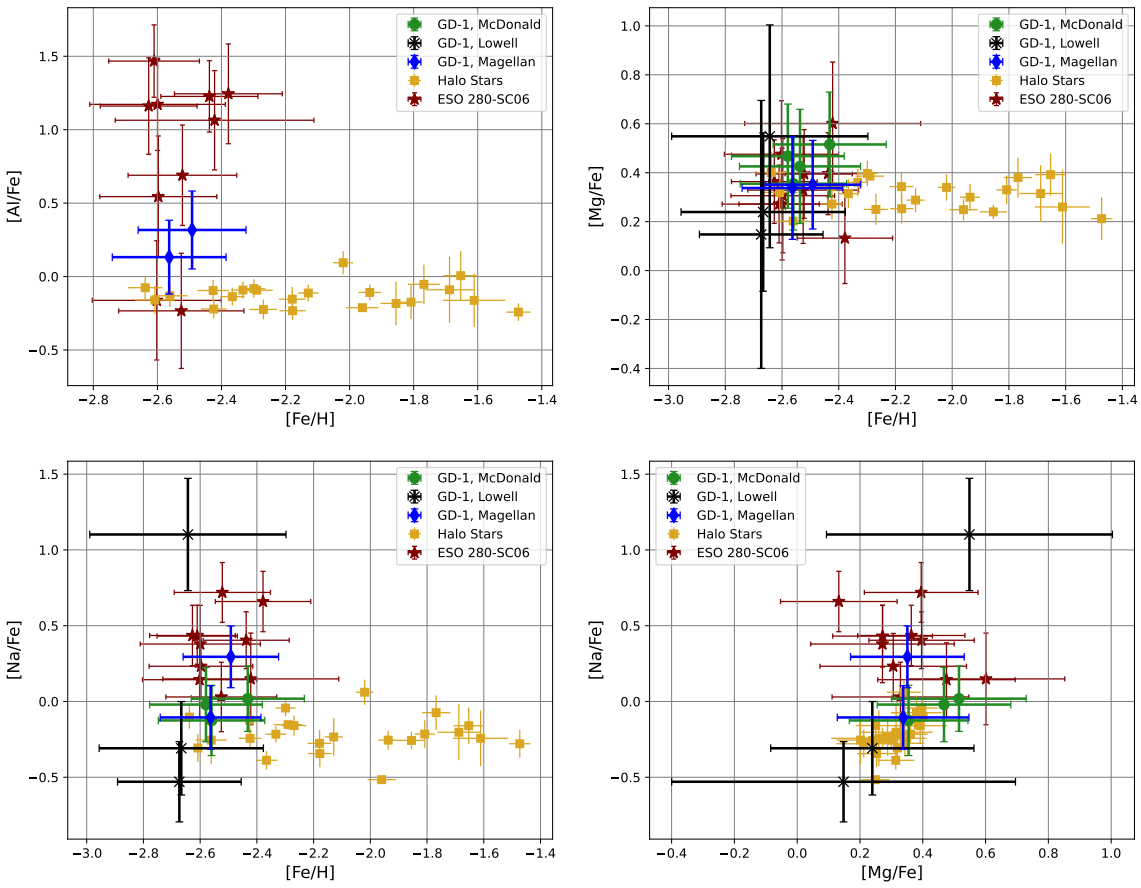

Figure 4.3 Abundances characteristic of multiple populations. The top left, top right and bottom left panels show the [Al/Fe], [Mg/Fe] and [Na/Fe] with respect to [Fe/H], respectively. The bottom right panel shows [Na/Fe] vs [Fe/H]. Our abundances from stars observed with the McDonald Observatory, Lowell Observatory and the Magellan telescopes are represented by green circles, black crosses, and blue diamonds. For comparison, we also display abundances from ESO 280-SC06 [Usman et al., 2024] and halo stars [Reggiani et al., 2019]. Our analysis assumes local thermodynamic equilibrium, and therefore does not inherently include corrections due to non-local thermodynamic equilibrium. To account for this, we add +0.8 and -0.4 approximate corrections to [Al/Fe] and [Na/Fe] in order to compare to similar datasets presented here. Only one star has high sodium indicative of multiple populations.

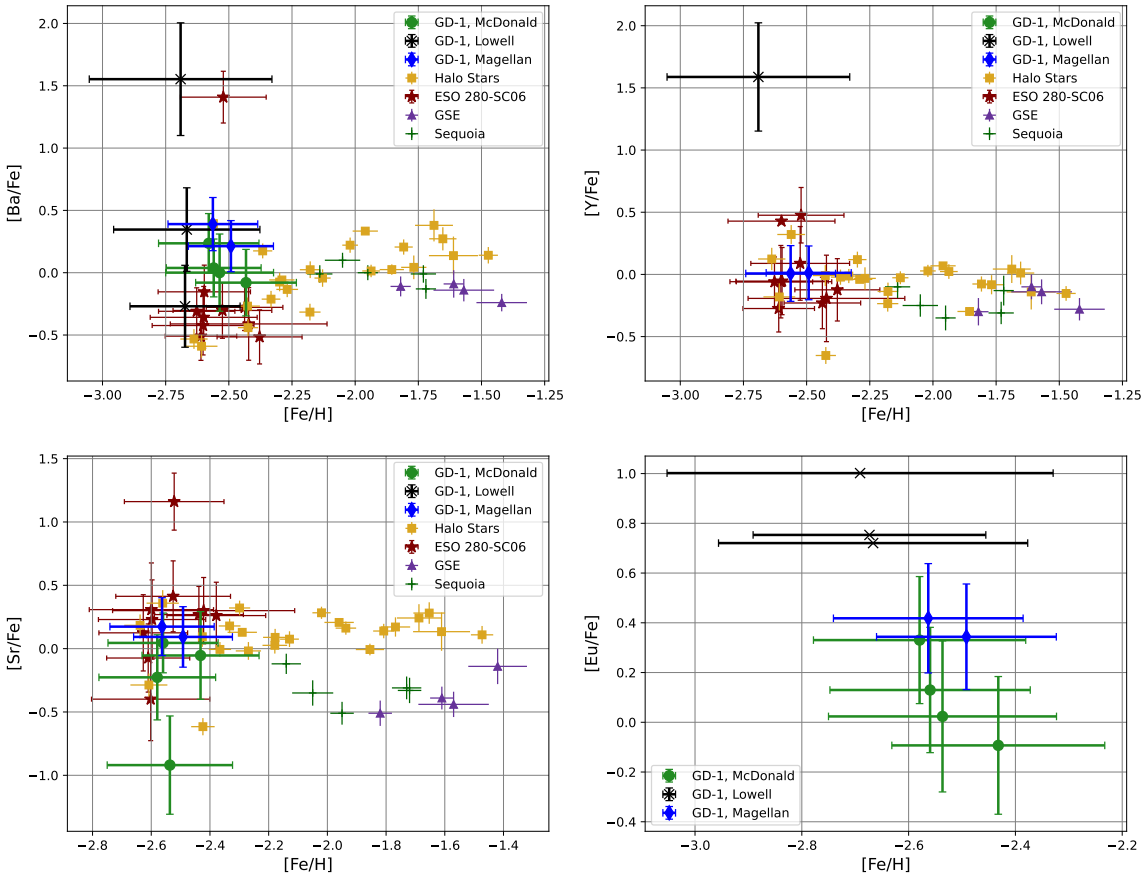

Figure 4.4 Neutron-capture abundances. The top left, top right, bottom left and bottom right panels show the [Ba/Fe], [Y/Fe], [Sr/Fe] and [Eu/Fe] with respect to [Fe/H], respectively. The bottom right panel shows [Na/Fe] vs [Fe/H]. Stars without y-error bars indicate 3σ upper limit measurements. Our abundances from stars observed with McDonald Observatory, Lowell Observatory and the Magellan telescopes are represented by green circles, black crosses, and blue diamonds. For comparison, we also display abundances from Sequoia, Gaia-Sausage-Enceladus (both Aguado et al. 2021a), ESO 280-SC06 [Usman et al., 2024] and halo stars [Reggiani et al., 2019]. One Lowell star demonstrates high enrichment in barium, which is indicative of mass-transfer.

Element	N	Mean Abundance	Dispersion
[Mg/Fe]	9	0.39 ± 0.08	< 0.15
[Mg/Fe II]	9	0.29 ± 0.09	< 0.17
[Ca/Fe]	9	0.41 ± 0.09	< 0.16
[Ca/Fe II]	9	0.3 ± 0.09	< 0.18
[Fe/H]	9	-2.56 ± 0.07	< 0.13
[Fe II/H]	9	-2.44 ± 0.06	< 0.12
[Ba/Fe]	8	0.14 ± 0.10	<0.22
[Ba/Fe II]	8	0.04 ± 0.08	< 0.20
[Eu/Fe]	6	0.63 ± 0.11	< 0.24
[Eu/Fe II]	6	0.52 ± 0.09	< 0.21

Table 4.3 Cluster Mean Abundances and Dispersions. N denotes the number of measurements incorporated into the mean abundance and dispersion.

abundances.

Results are given in Table 4.3.

4.7 Stream Progenitor Mass Estimate

We calculate the initial mass using the stream's orbital parameters and the estimate for dissolution time from Baumgardt and Hilker [2018]:

$$T_{\rm Diss} = 1.35 \times \left(\frac{M_{\rm Ini}}{\ln(0.02 N_{\rm Ini})} \right)^{0.75} \times \frac{r_{\rm apo}}{V_G} \times (1 - \epsilon), \tag{4.1}$$

where $r_{\rm apo}$, V_G, and ϵ are the distance at apocenter in kpc, the circular velocity of the Milky Way (assumed to be 220 km s^{-1}) and the eccentricity respectively. We use orbital parameters measured in Mestre et al. [2024], $r_{\rm apo} = 14.3$ kpc and $r_{\rm peri} = 24.5$ kpc. We assume that the cluster has dissolved within the age of the universe, $\sim$14 Gyr. We find that, based on its parameters, GD-1 has a maximum initial mass of about $10^{4.5}$.

At such a low mass, we would not expect a globular cluster to be able to form stellar streams: there appears to be a critical initial mass threshold a globular cluster must achieve in order to create multiple populations, somewhere in the range of $10^{4.7-5.0}$ $M_\odot$ [Gratton et al., 2019, Usman et al., 2024, 2025]. With an initial mass of just $10^{4.5}$, GD-1 should not have been able to produce 2P stars. However, GD-1 is a unique globular cluster stream: recent studies have found that it contains extra material surrounding it, though it is unclear whether this material is due to a dark matter halo [Carlberg, 2020, Carlberg and Agler, 2023] or a cocoon of gas stripped by GD-1's host galaxy prior to being accreted onto the Milky Way [Ibata et al., 2024, Valluri et al., 2025]. In the former scenario, the presence of a dark matter halo would cause the globular cluster progenitor to remain cohesive for much longer than otherwise predicted. In the latter scenario, the host galaxy's tidal stripping of GD-1's progenitor would significantly both reduce the cluster's mass *and* increase the rate at which the cluster dissolves, as the rate of dissolution is inversely proportional to the current mass [Baumgardt and Makino, 2003].

Either way, our general application of the dissolution time cannot accurately represent the progenitor's true mass: either the cluster is within a dark matter and vio-

lates our initial assumptions, or the tidal interaction with its host galaxy introduces an accelerated mass loss that cannot be accounted for with our model [Baumgardt and Hilker, 2018]. We conclude that the progenitor of GD-1 was likely a much higher mass than can be properly accounted for with our current model. Indeed, the most recent initial mass estimates for the stream are much closer to the threshold for multiple populations ($10^{4.7}$ $M_\odot$ by Gialluca et al. 2021, $10^{4.8}$ $M_\odot$ by Bonaca et al. 2019 and $10^{5.0}$ $M_\odot$ by Price-Whelan and Bonaca 2018). These initial masses are consistent with our estimate of multiple populations, as globular clusters with initial masses $10^{4.7-5.0}$ $M_\odot$ would have contained approximately $10-25\%$ enrichment [Usman et al., 2024], consistent with the $\frac{1}{8}$ enrichment found in this work.

4.8 Discussion

4.8.1 Multiple Populations in GD-1

We detect one 2P star, 696*, indicated by its high sodium abundance. Sodium could not be measured in all stars, as one or both sodium D lines fell outside of the observable range for the McDonald observations. We therefore calculate a 2P star fraction of $f_{2P} = 0.13^{+0.19}_{-0.05}$

We calculate an initial mass of $10^{4.5}$ for the globular cluster progenitor of GD-1, which should make the cluster too small to create 2P stars. However, recent studies note that GD-1 is enveloped in a cocoon of material, and suggest that the cluster was tidally stripped by its host galaxy prior to being accreted onto the Milky Way [Ibata et al., 2024, Valluri et al., 2025], or that it is contained in a dark matter halo

[Carlberg, 2020, Carlberg and Agler, 2023]. Either of these scenarios violate fundamental assumptions of our mass calculations, and therefore indicate our estimate is not valid. Indeed, other papers estimate the initial mass to be in the range $10^{4.7-5.0}$ [Price-Whelan and Bonaca, 2018, Bonaca et al., 2019, Gialluca et al., 2021]. These mass estimates are more consistent with the enrichment fraction we find here.

In Figure 4.5, we demonstrate how GD-1 compares to other globular clusters and globular cluster stellar streams. Using the initial mass estimates from the literature, we find that GD-1's 2P star fraction is extremely consistent with Milky Way globular clusters of comparable initial mass.

4.8.2 Neutron-Capture Range

We note that one star has significantly lower strontium than the other stars in the system. This could be indicative of a spread in neutron-capture elements. Such abundance spreads have previously been identified in metal-poor clusters such as M15[Sobeck et al., 2011] and M92 [Kirby et al., 2023] (both [Fe/H]≈ -2.5). It has previously been suggested that metal-poor globular clusters may exhibit neutron-capture spreads more easily, and could be indicative of the natal environment of these systems [Kirby et al., 2023]. However, this pattern is not universally true, e.g. ESO 280-SC06 ([Fe/H]≈ -2.54) does not yet have an identified dispersion in neutron-capture abundances [Usman et al., 2025]. While there are too few stars in our sample to strongly constrain the dispersion of strontium, large range of measurements within GD-1 indicates that metal-poor globular cluster streams may also be an avenue for exploring neutron-capture spreads.

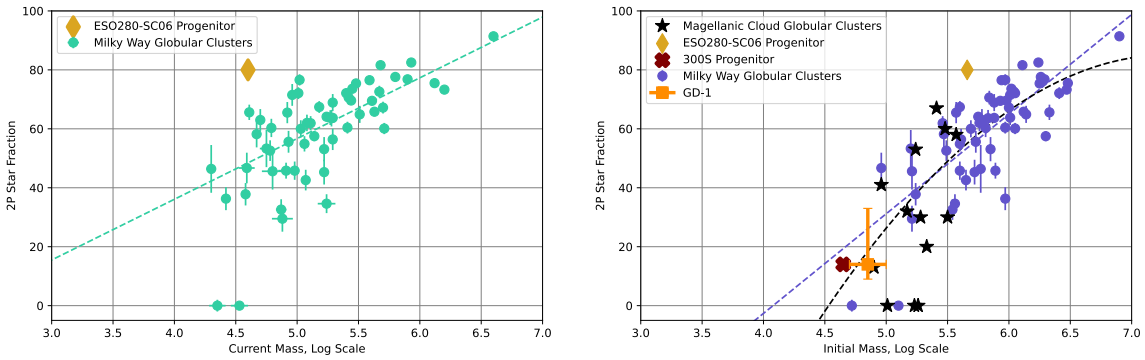

Figure 4.5 The enriched / 2P star fraction as a function of current mass and initial mass. Intact Milky Way globular clusters' (MW GCs) current masses and initial masses are represented by green circles on the left and purple circles, on the right, respectively. The mass estimates for these clusters come from Globular Cluster Database, V4 [Baumgardt et al., 2023], while the 2P star fraction estimates come from Milone et al. [2017] and Milone et al. [2019]. The GD-1 stellar stream is represented by an orange square in the right panel (and is not in the left panel, since stellar streams are completely unbound and have no current mass). For comparison, we include the cluster ESO 280-SC06 [Usman et al., 2025] and the stellar stream 300S [Usman et al., 2024]. We also include globular clusters in the Magellanic Clouds (*MC GCs*), which are not expected to experience signfican mass loss (black stars). (Data for MC GCs are from Mucciarelli et al. 2009, Mateluna et al. 2012, Mucciarelli et al. 2014, Hollyhead et al. 2017, Niederhofer et al. 2017b,a, Martocchia et al. 2017, Hollyhead et al. 2018, Zhang et al. 2018, Martocchia et al. 2018, and Hollyhead et al. 2019 and were compiled by Gratton et al. 2019.)

4.8.3 Mass-Transfer Star and Cluster Dynamics

We identify one star, 696*, which contains very high barium and yttrium enrichment. Significant barium enrichment indicates the star is a binary star who has experienced mass transfer from a binary companion, i.e. whose companion overflowed its Roche lobe while in the asymptotic giant branch phase of its life cycle [Côté et al., 1997]. These stars specifically exhibit enrichment in *s*-process elements, such as barium, yttrium and strontium. They can also be significantly enriched in carbon. Identifying more elements such as strontium and carbon would further confirm that 696* is a mass-transfer star. These stars can be referred to as Ba stars (e.g. D'Orazi et al. 2010), CH stars (e.g. Côté et al. 1997, Da Costa and Nordlander 2025), NEMP-s (e.g. Simpson and Martell 2019, Usman et al. 2025) or CEMP-s stars (e.g. Mashonkina et al. 2023) depending on the context in which they're found and their metallicity. The *s*-process enrichment of all these stars are thought to stem from the process of mass accretion from a massive binary companion.

It is somewhat surprising to find a mass-transfer star in a globular cluster remnant, as globular cluster's high densities tend to disrupt binaries [Hut et al., 1992]. Mass-transfer stars are therefore expected to be quite rare in globular clusters; indeed, D'Orazi et al. [2010] did a spectroscopic survey of 1,205 stars across five globular clusters and found just five mass-transfer stars. The authors therefore estimate mass-transfer stars appear at a rate of approximately 0.04% in globular clusters, significantly less than the rate found in field stars, about 2% [Luck and Bond, 1991]. However, in recent years, globular clusters have been identified in several more globular clusters (e.g. ESO 280-SC06, Simpson and Martell 2019, Usman et al. 2025; M55,

Da Costa and Nordlander 2025) and globular cluster stellar streams (e.g. 300S, Usman et al. 2024; GD-1, this work). There may a more complex relationship at play between globular clusters and mass-transfer stars than previously thought.

When analyzing the red giant branch stars in their sample, D'Orazi et al. [2010] found that just one of the five mass-transfer stars had chemical enrichment characteristic of an enriched, second-population stars. The authors suggest that second-population stars form in high-density environments, which are incondusive to the survival of long-term binaries and therefore mass-transfer stars. Indeed, we can compare the densities, binary fractions and 2P star fractions of globular clusters to confirm this.

Here, we cross-reference several catalogs of data to identify patterns in globular cluster behavior. For mass estimates, we consult the Globular Cluster Database, V4 [Baumgardt et al., 2023]. This catalog details estimates of clusters' current and initial masses and densities, derived by fitting N-body simulations to current estimates of cluster radial velocities and proper motions from Gaia DR3. For binary fraction estimates, we consult Ji and Bregman [2015], which compares photometric imaging of globular clusters compared to archival data. For fractions of multiple population stars, we combine catalogs from Milone et al. [2017] and Milone et al. [2019], which use near-infrared and ultraviolet photometry, respectively, to identify multiple population stars in globular clusters.

By combining these data sets, some interesting patterns come to light. For example, in Figure 4.6, we compare the fraction of binary stars and multiple population stars to each other and to the core density of the globular cluster. We clearly see

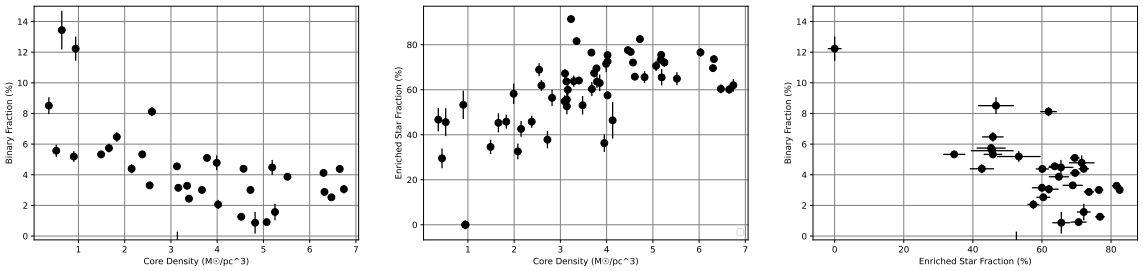

Figure 4.6 The binary fraction (left) and 2P star fraction (center) as a function of core density in Milky Way globular clusters, and as a function of each other (right). We combine catalogs of binary star fraction [Ji and Bregman, 2015], 2P star fraction [Milone et al., 2017, 2019], and mass and densities Baumgardt et al. [2023].

that high densities in globular clusters have higher fractions of 2P stars and lower fractions of binary stars, and low densities produce the opposite effect. This results in a clear anti-correlation between fractions of binary stars and 2P stars.

However, we additionally continue to find mass-transfer stars in disrupting and fully disrupted globular clusters. For example, one mass-transfer star was identified in both the 300S Usman et al. [2024] and the GD-1 streams, presented here. If we assume these clusters each have a binomial distribution of normal and mass-transfer, we can use Bayesian statistics to infer a rate of mass-transfer stars in the stream. In 300S, we can estimate the stream has a rate of $f_{\text{transfer}} = 0.13^{+0.19}_{-0.05}$. Similarly, GD-1 would have an estimated rate of $f_{\text{transfer}} = 0.11^{+0.18}_{-0.04}$. These rates are approximately six and thirty times larger than the estimated rate of mass-transfer stars in the field and in globular clusters, respectively. These exceedingly high rates indicate that the mechanism causing mass loss may *encourage* the long-term survival of binary systems. In Figure 4.7, we compare the rate of binary fraction to the fraction of

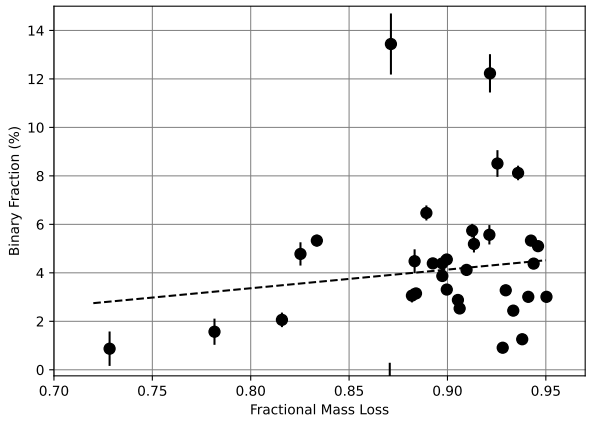

Figure 4.7 The binary star fraction as a function of fraction of stellar mass loss experienced by the cluster. We combine catalogs of binary star fraction [Ji and Bregman, 2015] and mass loss calculations derived from Baumgardt et al. [2023]. The dashed, black line represent a linear correlation fitted to the cluster data.

mass lost by the cluster. There does some to be some loose correlation between the two, with clusters that have experienced higher fractions of mass loss having higher estimated rates of binary stars, though the clusters that have experienced the most mass loss have a significant spread. in the binary star fraction. This could indicate that different types of mass loss may affect the stellar binaries differently. Simulations of binary stars in disrupting globular clusters could shed light into this unique behavior.

4.9 Conclusion

GD-1 represents a unique globular cluster due to its orbital history. The identification of a 2P star confirms the stellar stream is a globular cluster. However, simple models of globular cluster mass loss cannot be applied to the system, as these calculations predict the cluster progenitor had an initial mass of just $10^{4.5}$ $M_{\odot}$, significantly too small to be able to produce multiple populations [Usman et al., 2024]. Indeed, previous studies of the stream estimate its progenitor had an initial mass closer to $10^5\,M_{\odot}$, which more aligns with the chemical composition identified here.

In addition to the 2P star, we identify a mass-transfer star. These stars were once thought to be rare in globular clusters, but have been recently identified in extremely and fully tidally disrupted globular clusters (e.g. ESO 280-SC06, Usman et al. 2025; 300S, Usman et al. 2024. We cross reference multiple catalogs connecting 2P star fraction [Milone et al., 2017, 2019], current and initial mass estimates and core densities [Baumgardt et al., 2023], and binary star fractions [Ji et al., 2025]. We confirm an anti-correlation between binary star fraction and cluster density, and a correlation between 2P star fraction and cluster density. We further identify a loose correlation between the binary star fraction and fraction of mass lost since formation. The clusters which have experienced the most significant mass loss, $>$ 85%, have a significant spread in binary star fraction. This may indicate that while disrupted globular clusters are a better environment for binary star systems, perhaps the mechanism of the mass loss may more directly affect the survival of binaries. Simulations of binary systems in globular clusters are required to shed light on the dynamics of these systems.

Star	Element	Species	N	$\log \epsilon_w$	[X/H]	e[X/H]	[X/Fe]	e[X/Fe]	Upper Limit
165	Fe I	26.0	83	5.07	-2.43	0.2	–	–	
165	Fe II	26.1	20	5.1	-2.4	0.14	–	–	
165	Na I	11.0	2	4.23	-2.01	0.25	0.42	0.22	
165	Mg I	12.0	5	5.68	-1.92	0.19	0.52	0.21	
165	Ca I	20.0	22	4.56	-1.78	0.22	0.65	0.23	
165	Sr II	38.1	1	0.38	-2.49	0.35	-0.08	0.32	
165	Ba II	56.1	4	-0.33	-2.51	0.24	-0.11	0.22	
165	Eu II	63.1	1	-1.6	-2.12	0.19	0.28	0.2	

Table 4.4 Abundances measured in star 165.

Star	Element	Species	N	$\log \epsilon_w$	[X/H]	e[X/H]	[X/Fe]	e[X/Fe]	Upper Limit
693	Fe I	26.0	88	4.96	-2.54	0.21	–	–	
693	Fe II	26.1	22	5.03	-2.47	0.21	–	–	
693	Mg I	12.0	6	5.49	-2.11	0.2	0.43	0.23	
693	Ca I	20.0	15	4.23	-2.11	0.18	0.42	0.22	
693	Sr II	38.1	1	-0.59	-3.46	0.43	-0.99	0.42	
693	Ba I	56.0	1	-0.06	-2.24	0.3	0.3	0.32	
693	Ba II	56.1	4	-0.36	-2.54	0.29	-0.07	0.29	
693	Eu I	63.0	1	-1.68	-2.2	0.2	0.33	0.32	
693	Eu II	63.1	1	-1.59	-2.11	0.19	0.36	0.23	

Table 4.5 Abundances measured in star 693.

Star	Element	Species	N	$\log \epsilon_w$	[X/H]	e[X/H]	[X/Fe]	e[X/Fe]	Upper Limit
696	Fe I	26.0	29	4.81	-2.69	0.36	–	–	
696	Fe II	26.1	3	4.71	-2.79	0.28	–	–	
696	Na I	11.0	2	5.03	-1.21	0.2	1.48	0.38	
696	Mg I	12.0	4	5.45	-2.15	0.33	0.54	0.47	
696	Ca I	20.0	5	4.21	-2.13	0.25	0.56	0.43	
696	Y I	39.0	3	0.94	-1.27	0.35	1.42	0.49	
696	Y II	39.1	1	1.11	-1.1	0.24	1.68	0.37	
696	Ba I	56.0	1	1.19	-0.99	0.27	1.7	0.43	
696	Ba II	56.1	2	1.04	-1.14	0.3	1.65	0.38	
696	Eu II	63.1	1	–	-1.29	–	1.5	–	✓

Table 4.6 Abundances measured in star 696.

Star	Element	Species	N	$\log \epsilon_w$	[X/H]	e[X/H]	[X/Fe]	e[X/Fe]	Upper Limit
805	Fe I	26.0	78	4.94	-2.56	0.19	–	–	
805	Fe II	26.1	19	4.97	-2.53	0.16	–	–	
805	Na I	11.0	1	3.96	-2.28	0.24	0.27	0.23	
805	Mg I	12.0	8	5.4	-2.2	0.14	0.35	0.19	
805	Ca I	20.0	12	4.16	-2.18	0.2	0.38	0.24	
805	Sr II	38.1	2	0.36	-2.51	0.21	0.01	0.23	
805	Ba I	56.0	1	-0.18	-2.36	0.22	0.2	0.26	
805	Ba II	56.1	4	-0.34	-2.52	0.2	0.0	0.21	
805	Eu I	63.0	1	-1.48	-2.0	0.18	0.56	0.25	
805	Eu II	63.1	1	-1.51	-2.03	0.17	0.5	0.21	

Table 4.7 Abundances measured in star 805.

Star	Element	Species	N	$\log \epsilon_w$	[X/H]	e[X/H]	[X/Fe]	e[X/Fe]	Upper Limit
830	Fe I	26.0	47	4.92	-2.58	0.2	–	–	
830	Fe II	26.1	12	5.04	-2.46	0.15	–	–	
830	Na I	11.0	1	4.04	-2.2	0.23	0.38	0.25	
830	Mg I	12.0	3	5.49	-2.11	0.16	0.47	0.21	
830	Ca I	20.0	11	4.15	-2.19	0.24	0.39	0.29	
830	Sr II	38.1	1	0.06	-2.81	0.32	-0.35	0.31	
830	Ba I	56.0	1	0.16	-2.02	0.25	0.56	0.28	
830	Ba II	56.1	4	-0.16	-2.34	0.2	0.11	0.19	
830	Eu I	63.0	1	-1.43	-1.95	0.17	0.63	0.25	
830	Eu II	63.1	1	-1.33	-1.85	0.17	0.61	0.21	

Table 4.8 Abundances measured in star 830.

Star	Element	Species	N	$\log \epsilon_w$	[X/H]	e[X/H]	[X/Fe]	e[X/Fe]	Upper Limit
7962	Fe I	26.0	52	4.83	-2.67	0.29	–	–	
7962	Fe II	26.1	9	4.95	-2.55	0.32	–	–	
7962	Na I	11.0	2	3.66	-2.58	0.22	0.09	0.31	
7962	Mg I	12.0	4	5.17	-2.43	0.21	0.24	0.32	
7962	Ca I	20.0	7	4.05	-2.29	0.27	0.38	0.37	
7962	Ba I	56.0	1	-0.37	-2.55	0.25	0.11	0.35	
7962	Ba II	56.1	3	-0.14	-2.32	0.24	0.23	0.38	
7962	Eu II	63.1	1	–	-1.55	–	1.0	–	✓

Table 4.9 Abundances measured in star 7962.

Star	Element	Species	N	$\log \epsilon_w$	[X/H]	e[X/H]	[X/Fe]	e[X/Fe]	Upper Limit
7965	Fe I	26.0	41	4.83	-2.67	0.22	–	–	
7965	Fe II	26.1	5	5.01	-2.49	0.22	–	–	
7965	Na I	11.0	2	3.44	-2.8	0.23	-0.13	0.26	
7965	Mg I	12.0	3	5.07	-2.53	0.52	0.15	0.55	
7965	Ca I	20.0	6	3.85	-2.49	0.18	0.18	0.26	
7965	Ba I	56.0	1	-0.7	-2.88	0.2	-0.21	0.29	
7965	Ba II	56.1	2	-0.76	-2.94	0.27	-0.46	0.32	
7965	Eu II	63.1	1	–	-1.52	–	0.97	–	✓

Table 4.10 Abundances measured in star 7965.

Acknowledgments

This paper includes data gathered using the McDonald Observatory and Lowell Observatory. This paper includes data gathered with the 6.5 meter Magellan Telescopes located at Las Campanas Observatory, Chile. We thank all the LCO staff for enabling astronomical observations during a global pandemic.

Data Availability

The individual line measurements are provided as supplementary material. The reduced spectra can be obtained by reasonable request to the corresponding author.

CHAPTER 5

CHEMICAL ABUNDANCES IN THE LEIPTR STELLAR STREAM: A DISRUPTED ULTRA-FAINT DWARF GALAXY?

At the time of completion of the PhD, this paper has been published in June 2025 in the Open Journal of Astrophysics, Volume 8, ID 68. Atzberger et al. [2025]

The lead author of the paper, Kaia Atzberger, performed the analysis while an undergraduate at the Ohio State University, under the supervision of PhD student Samantha A. Usman and Prof. Alexander Ji.

5.1 Abstract

Chemical abundances of stellar streams can be used to determine the nature of a stream's progenitor. Here we study the progenitor of the recently discovered Leiptr stellar stream, which was previously suggested to be a tidally disrupted halo globular cluster. We obtain high-resolution spectra of five red giant branch stars selected from the *Gaia* DR2 `STREAMFINDER` catalog with Magellan/MIKE. One star is a clear non-member. The remaining four stars display chemical abundances consistent with those of a low-mass dwarf galaxy: they have a low mean metallicity, $\langle$[Fe/H]$\rangle = -2.2$; they do not all have identical metallicities; and they display low [α/Fe] ~ 0 and [Sr/Fe] and [Ba/Fe] ~ -1. This pattern of low α and neutron-capture element abundances is only found in intact dwarf galaxies with stellar mass $\lesssim 10^5\,\mathrm{M}_\odot$. Although more data are needed to be certain, Leiptr's chemistry is consistent with being the lowest-mass

dwarf galaxy stream without a known intact progenitor, possibly in the mass range of ultra-faint dwarf galaxies. Leiptr thus preserves a record of one of the lowest-mass early accretion events into the Milky Way.

5.2 Introduction

Over the course of their lifetimes, stellar systems can be torn apart by the gravitational potential of massive galaxies. Stellar streams form during the intermediate stage of tidal disruption where they preserve their coherence in phase-space before mixing into a stellar halo [Helmi et al., 1999]. Current models of galaxy formation predict that there should be a large population of globular cluster and dwarf galaxy stellar streams in the Milky Way's stellar halo as a result of past accretion events [Helmi, 2020]. These systems provide observational evidence to evaluate theoretical models of hierarchical structure formation [e.g., Johnston, 1998, Helmi et al., 1999, Freeman and Bland-Hawthorn, 2002, Bullock and Johnston, 2005] and quantify the amount of dark matter substructure [e.g., Ibata et al., 2002, Johnston et al., 2002, Carlberg, 2009, Varghese et al., 2011, Erkal et al., 2016a]. Large photometric surveys such as the Sloan Digital Sky Survey (York et al. 2000) and the Dark Energy Survey (Dark Energy Survey Collaboration et al. 2016) in combination with proper motions from *Gaia* data releases [Gaia Collaboration et al., 2016, Lindegren et al., 2021, Gaia Collaboration et al., 2023a] have revealed over 140 streams [Grillmair and Carlin, 2016, Shipp et al., 2018, Mateu et al., 2018, Mateu, 2023, Ibata et al., 2024, Bonaca and Price-Whelan, 2025].

It is often unclear whether a given stream's progenitor is a dwarf galaxy, a globular

cluster, or possibly a superposition of both [e.g., Carlberg, 2018, Malhan et al., 2021]. In some cases, streams are clearly identified with intact progenitors, such as the Sagittarius dwarf galaxy [Ibata et al., 2001, Majewski et al., 2003], the Antlia II and Crater II dwarf spheroidals [Ji et al., 2021, Coppi et al., 2024], and several globular clusters [e.g., Simpson et al., 2020, Hansen et al., 2020b, Gull et al., 2021]. The majority of streams do not have associated intact progenitors. Instead, a stream's morphology and kinematics can provide a strong prior on the progenitor [e.g., Erkal et al., 2016b, Shipp et al., 2018, Ibata et al., 2024]. The disruption of a dwarf galaxy should be qualitatively different from a globular cluster because they additionally contain gas and dark matter. They leave behind different intrinsic substructure along the stream because of preferential tidal stripping of dark matter followed sequentially by older populations and younger populations [Newberg, 2016]. Globular cluster disruption can also be influenced by density perturbations from epicycles. However, a definitive classification requires studying a stream's chemical abundances [e.g., Li et al., 2019, 2022, Ji et al., 2020b, Martin et al., 2022].

The majority of known streams are thought to have globular cluster progenitors, due to their thin widths and in many cases small or unresolved metallicity dispersions $\lesssim$0.05 dex [Li et al., 2022, Ibata et al., 2024]. These include the Phoenix [Wan et al., 2020, Casey et al., 2021] and C-19 streams [Martin et al., 2022, Yuan et al., 2022b] which are below the globular cluster metallicity "floor"; the dynamically perturbed GD-1 [Grillmair and Dionatos, 2006, Price-Whelan and Bonaca, 2018] and ATLAS-Aliqa Uma streams [Shipp et al., 2018, Li et al., 2021]; disrupted globular clusters embedded within the Indus, Jhelum, and Wukong/LMS-1 dwarf galaxy

streams [Hansen et al., 2021, Awad et al., 2024, Limberg et al., 2024]; and the 300S stream, which was originally thought to be a dwarf galaxy stream [Simon et al., 2011, Frebel et al., 2013b, Fu et al., 2018] but has since been chemically confirmed to be an accreted globular cluster stream [Li et al., 2022, Usman et al., 2024].

Less common by number are the dwarf galaxy streams. Many of the first discovered streams, such as the Helmi stream [Helmi et al., 1999, Roederer et al., 2010, Limberg et al., 2021b, Matsuno et al., 2022] and Sagittarius stream [Ibata et al., 2001, Majewski et al., 2003], were easily identified as dwarf galaxies as these are well-populated streams from relatively massive ($M_\star \gtrsim 10^8\,M_\odot$) dwarf galaxy progenitors. More recently, several lower-mass dwarf galaxy streams have also been identified. Based on their chemical patterns, the Indus and Jhelum streams have progenitor mass $M_\star \sim 10^{6-7}\,M_\odot$ [Hansen et al., 2021]; the Orphan-Chenab stream [Belokurov et al., 2007, Casey et al., 2013, Shipp et al., 2018, Koposov et al., 2019, Erkal et al., 2019] has progenitor mass $M_\star \sim 10^{6.5}\,M_\odot$ [Koposov et al., 2019, Hawkins et al., 2023]; the Wukong/LMS-1 stream has progenitor mass $M_\star \sim 10^7\,M_\odot$ [Naidu et al., 2020, Yuan et al., 2020, Limberg et al., 2024]; the Cetus/Palca stream has progenitor mass $M_\star \sim 10^6\,M_\odot$ [Newberg et al., 2009, Yuan et al., 2022a, Sitnova et al., 2024]; and the Elqui stream has progenitor mass $M_\star \sim 10^6\,M_\odot$ [Shipp et al., 2018, Ji et al., 2020b, Li et al., 2022]. This does not include more disrupted and phase-mixed dwarf galaxies like Gaia-Sausage/Enceladus [GSE, Belokurov et al., 2018, Haywood et al., 2018, Helmi et al., 2018, Carrillo et al., 2022], Sequoia [Myeong et al., 2019, Matsuno et al., 2019], Thamnos [Koppelman et al., 2019], and others [Naidu et al., 2020, Helmi, 2020, Deason and Belokurov, 2024].

Current predictions for globular cluster streams are that the Milky Way has ∼1000 globular cluster stellar streams that have yet to be fully phase-mixed. These are predicted by mock stellar streams from the orbital histories of progenitors generated by hierarchical models of globular cluster formation [Pearson et al., 2024]. There are also expected to be many hundreds of dwarf galaxies that have been tidally disrupted around the Milky Way. A number of strategies have been developed for this over time, such as semi-analytic methods for determining phase-space populations of tidal debris, simulations of satellite galaxy disruption, and clustering stellar dynamics in 4D phase space [e.g., Johnston, 1998, Helmi et al., 1999, Santistevan et al., 2020, Brauer et al., 2022, Gandhi et al., 2024]. However, it is harder to identify the dwarf galaxy streams. Current stream searches, especially those relying on *Gaia* parallaxes [e.g., Ibata et al., 2019, 2024, Dodd et al., 2023], mostly search at nearby galactocentric radii, where globular cluster streams are likely more numerous than dwarf galaxy streams [Johnston et al., 2008, Gómez et al., 2013, Pearson et al., 2024, Bonaca and Price-Whelan, 2025]. Dwarf galaxy stars have larger velocity dispersions and metallicity spreads, so at fixed stellar mass they are harder to find compared to globular clusters that are more spatially compact and at single metallicities. Finally, the vast majority of the tidally disrupted dwarf galaxies are very low-mass, with $M_\star \lesssim 10^5$ $M_\odot$, i.e. ultra-faint dwarf galaxies [e.g., Weisz and Boylan-Kolchin, 2017, Simon, 2019, Brauer et al., 2019, Santistevan et al., 2020, Gandhi et al., 2024], so they should be even harder to identify. Obtaining a full census of the Milky Way's accretion history thus requires extending stream discoveries down to this regime of ultra-faint dwarf galaxies. Since these ultra-faint dwarf galaxies are also the most

dark matter-dominated galaxies that live in the lowest-mass star-forming dark matter halos, understanding the number of these streams in the Milky Way could contribute to understanding reionization and the small scale structure of dark matter [e.g., Bullock and Boylan-Kolchin, 2017, Jethwa et al., 2018, Simon, 2019, Nadler et al., 2021].

In recent years, much progress has been made in finding streams from the lowest-mass dwarf galaxies. The first clear stream around an intact ultra-faint dwarf galaxy was found around the Tucana III system [Drlica-Wagner et al., 2015, Shipp et al., 2018], which has been spectroscopically confirmed [Hansen et al., 2017, Li et al., 2018]. More recently, a tidal stream likely emanating from the Hydrus I dwarf galaxy was found [Ibata et al., 2024]. Several individual stars with chemistry similar to ultra-faint dwarf galaxy stars have also been found throughout the Milky Way halo [e.g., Casey and Schlaufman, 2017, Roederer, 2017]. Motivated by the discovery of the highly r-process (rapid neutron-capture process) enhanced ultra-faint dwarf Reticulum II [Ji et al., 2016a, Roederer et al., 2016], several stellar dynamical groups within the Milky Way that are highly enhanced in r-process elements have also been suggested to originate from ultra-faint dwarf galaxies [e.g., Roederer et al., 2018a, Lee et al., 2019, Limberg et al., 2021a, Gudin et al., 2021], but the probability that the stars in these groups all come from individual ultra-faint dwarf galaxies is statistically unlikely [Brauer et al., 2022]. Thus far, there is no progenitor-free bona-fide stellar stream that can be cleanly associated with an ultra-faint dwarf galaxy. The only claimed candidate, Specter [Chandra et al., 2022], has a high mean metallicity that suggests we are only seeing part of the stream from a much higher-mass progenitor dwarf galaxy.

Table 5.1 SNR 4500 Å and 6500 Å is the signal-to-noise per pixel at 4500 Å and 6500 Å. RV is the heliocentric radial velocity with 1 km s^{-1} uncertainty. (* indicates the non-member star.)

Name	*Gaia* DR3 Source ID	ExpTime	SNR	SNR	RV	RA	Dec	G	BP	RP
		(s)	4500 Å	6500 Å	(km s^{-1})	(°)	(°)	(mag)	(mag)	(mag)
Leiptr-186	2909738294618626048	300	44	80	191.1	89.11202	−28.18913	12.33	12.90	11.61
Leiptr-208	2963688139034857472	1500	35	53	144.2	84.19212	−23.48547	14.84	15.26	14.25
Leiptr-252*	3181161746481442432	5400	35	53	−4.2	71.34197	−11.61942	16.21	16.63	15.61
Leiptr-321	5531991922485962624	2400	29	55	372.0	115.32295	−44.58400	15.21	15.81	14.44
Leiptr-342	5561352147121401216	300	38	77	337.4	108.16171	−40.85943	12.43	13.14	11.61

Here we investigate the progenitor of the Leiptr stellar stream, which was previously thought to be a tidally disrupted globular cluster. Leiptr was discovered among a group of inner galaxy streams in the *Gaia* DR2 catalog by Ibata et al. [2019] using the `STREAMFINDER` algorithm. They identified candidates from streams with distinct and coherent sky positions, proper motions, and parallaxes that were clearly distinguishable from the Galactic disk or bulge. They determined Leiptr was 48° long and located toward the Galactic anticenter with a heliocentric distance of 7.9 ± 0.4 kpc, pericenter distance of 12.8 ± 0.6 kpc, apocenter distance of 85.2 ± 26.0 kpc, and strong retrograde motion of $L_z = 4689 \pm 314$ km s^{-1} kpc where L_z is the vertical component of angular momentum in a Galactocentric Cartesian frame. Malhan et al. [2022] updated these orbital parameters, estimating the pericenter to be 12.3± 0.1 kpc and the apocenter to be 45.1 ± 0.2 kpc, with a resulting eccentricity of 0.57. Leiptr has the highest $|L_z|$ of stellar streams in their sample, next to Gaia-12. Bonaca et al. [2021] identified Leiptr, Gjöll, GD-1, Phlegethon, Ylgr, and Wambelong as potential members of a highly aligned "plane of streams" that may share a common origin. They suggested the retrograde streams are most likely globular clusters from the Sequoia/Arjuna dwarf galaxy [Myeong et al., 2019, Naidu et al., 2020] based on photometry and clustering in orbital poles; Gjöll in particular has been shown to be connected to the NGC 3201 globular cluster [Hansen et al., 2020b, Riley and Strigari, 2020]. Bonaca and Price-Whelan [2025] independently determined that Leiptr has a mean heliocentric distance of 7.4 kpc, mean Galactic radius of 13.8 kpc, angular length of 73°, angular width of 0.5° (74 pc), and a stellar mass of $10^{3.8}$ $M_\odot$. However, there have been no previous chemical studies of Leiptr.

We present the chemical abundances of four member stars in the Leiptr stream and one non-member using high-resolution spectroscopy. We find that Leiptr is likely the first spectroscopically confirmed ultra-faint dwarf galaxy stream without an intact progenitor. Section 5.3 explains the observations. Section 5.4 describes the abundance analysis. Section 5.5 compares the chemical abundances of Leiptr to those of halo, dwarf galaxy and globular cluster stars. We discuss what these results suggest about Leiptr's chemical signature and progenitor in Section 5.6 and conclude in Section 5.7.

5.3 Observations

Of 67 original Leiptr candidate stars from the *Gaia* DR2 `STREAMFINDER` catalog [Ibata et al., 2019], we selected five of the brightest candidate stars to observe, giving them arbitrary ID numbers. We obtained spectra of these stars on November 2, 2022 using the 6.5-meter Magellan Clay Telescope's Magellan Inamori Kyocera Echelle (MIKE; Bernstein et al. 2003) spectrograph at Las Campanas Observatory in Chile. Figure 5.1 shows the declinations and radial velocities against right ascensions of these stars compared to the other Leiptr candidates from the *Gaia* DR3 `STREAMFINDER` catalog in Ibata et al. [2024]. The arrows represent reflex-corrected proper motions. One of these five stars, Leiptr-252, is no longer a kinematic Leiptr member star in the *Gaia* DR3 `STREAMFINDER` catalog [Ibata et al., 2024], which will also be apparent from its chemistry. This non-member star is shown as a red X in Figure 5.1 and all subsequent figures.

We used the $0.7'' \times 5.0''$ entrance slit resulting in $R \sim 35,000$ in the blue arm

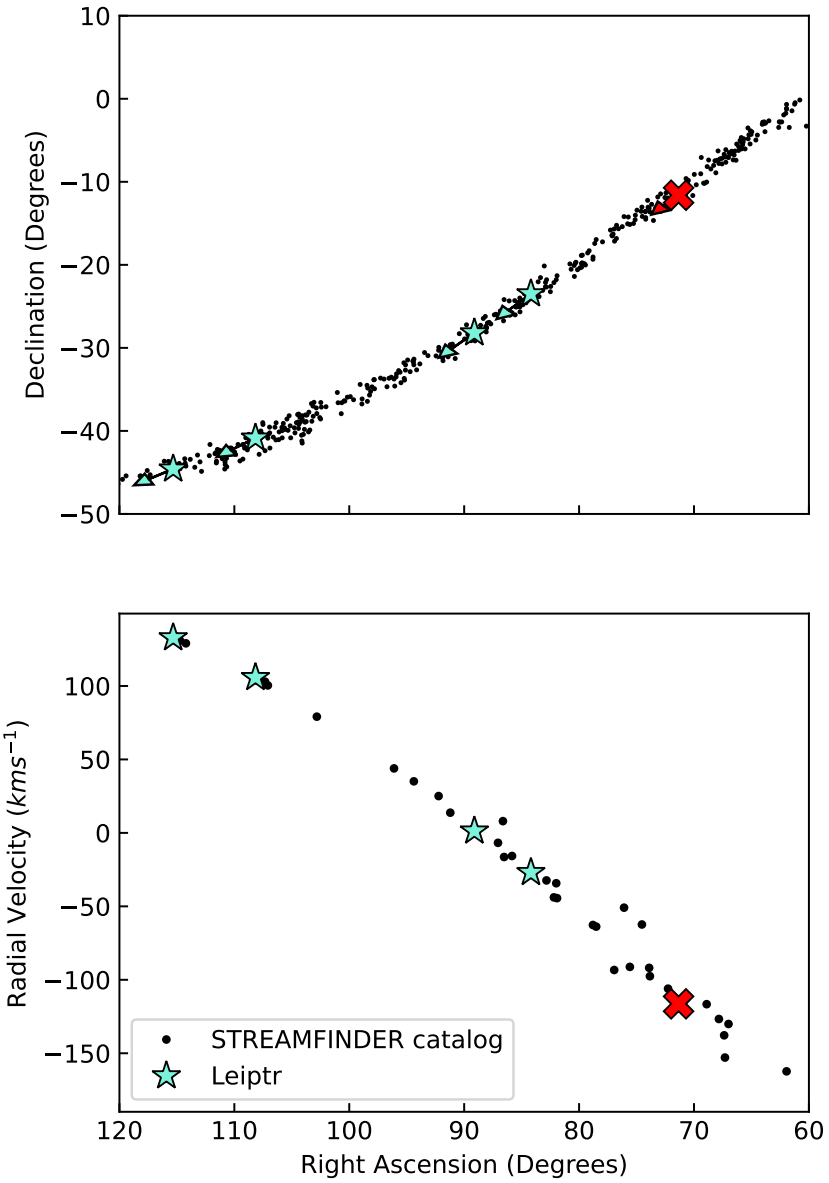

Figure 5.1 Positions and reflex-corrected radial velocities of Leiptr candidate stars. The members from the STREAMFINDER catalog are represented by black circles and four members analyzed in this work are represented by light-blue stars. The non-member, Leiptr-252, is emphasized as a red X. The reflex-corrected proper motions in degrees per Myr are indicated by arrows in the top panel. Any stars in the STREAMFINDER catalog without confirmed radial velocities were omitted.

from $3300 - 5000$ Å and $R \sim 28,000$ in the red arm from $5000 - 9000$ Å. The data were reduced using the CarPy software package's MIKE reduction pipeline [Kelson, 2003]. A metal-poor template spectrum of HD122563 was cross-correlated with the echelle order containing the Mg b triplet to determine radial velocities. The uncertainty is dominated by wavelength calibration accuracy and is about 1 km s^{-1} [Ji et al., 2020a]. Table 5.1 reports each star, exposure time, signal-to-noise per pixel at 4500 Å and 6500 Å, heliocentric radial velocity, right ascension, declination, and *Gaia* magnitudes. *Gaia* DR3 RVS [Gaia Collaboration et al., 2023b] gives velocities of 190.43 ± 0.49 km s^{-1} and 335.96 ± 0.43 km s^{-1} for Leiptr-186 and Leiptr-342, respectively, which closely agree with our results. Figure 5.2 shows spectral regions around Ba II at 4554.0 Å, the Mg b triplet, and Sr II at 4077.7 Å.

5.4 Abundance Analysis

The chemical abundance analysis was performed using a custom analysis code `LESSPayne` (Ji et al. in prep), generally following Ji et al. [2020b]. As described in Limberg et al. [2024], `LESSPayne` is a combination of the PayneEchelle [Ting et al., 2019] and SMHR [Casey, 2014] programs. First, we ran a full spectrum fit between $5000 - 6800$ Å using a neural network emulator of high-resolution spectra. We did not use the stellar parameters from this fit, but instead used the best-fit spectrum to locate and mask regions where absorption lines were expected to occur and initialize an SMHR analysis. We manually inspected and corrected the normalization for every spectral order before stitching them together. We then fit Gaussian profiles to determine equivalent widths using the line list from Ji et al. [2020b], which is based on atomic data from

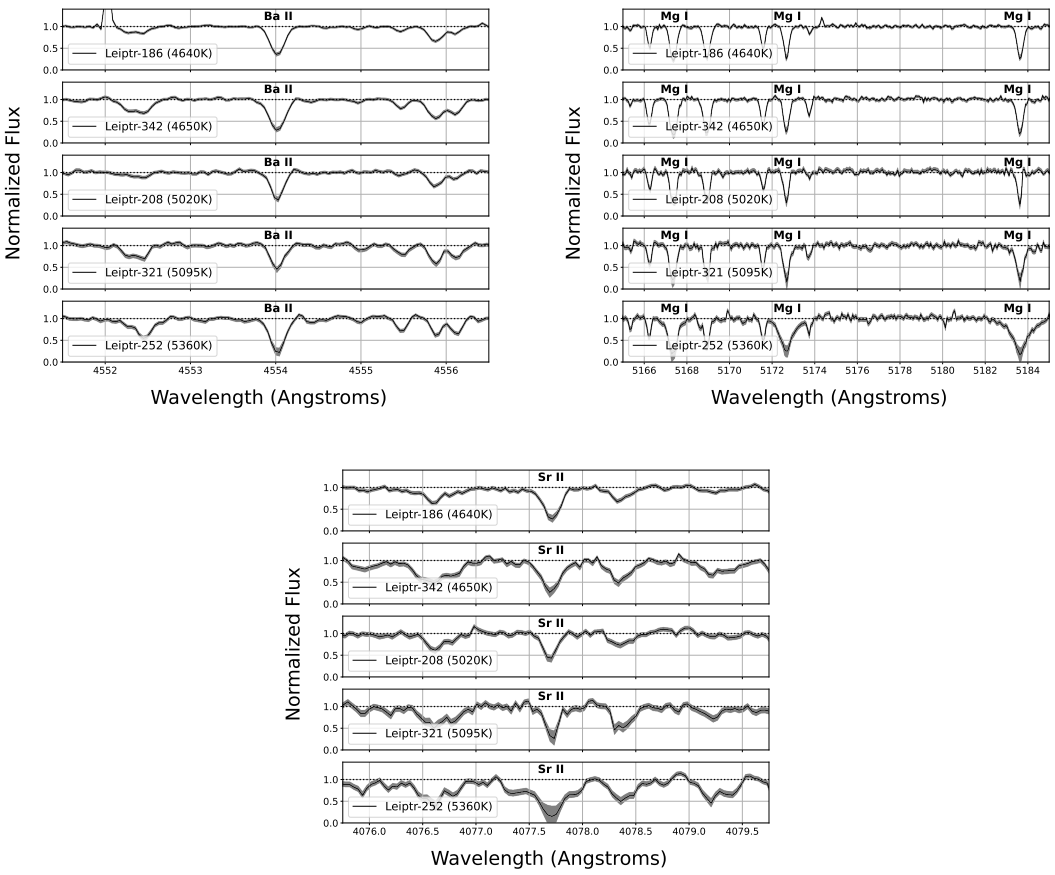

Figure 5.2 Spectra around the Ba II line at 4554.0 Å; Mg I b triplet; and the Sr II line at 4077.7 Å. The stars are ordered top to bottom from coolest to hottest. The shaded region around the spectra shows the uncertainty in normalized flux. Leiptr-252 is a clear outlier with stronger and broader lines.

`linemake` [Placco et al., 2021], mostly keeping to lines with 4000 Å $< \lambda <$ 7000 Å. Some stronger lines required Voigt profile fits. We also fit some lines using spectral synthesis with the same line lists as Ji et al. [2020b].

We determined chemical abundances using the 1D local thermodynamic equilibrium (LTE) radiative transfer code `MOOG` [Sneden, 1973] and the ATLAS model atmospheres [Castelli and Kurucz, 2003]. Stellar parameters were determined spectroscopically following Frebel et al. [2013a], due to uncertain distances to the Leiptr stars. Effective temperature was derived by balancing Fe I abundance against excitation potential, surface gravity by balancing Fe I and II abundances, and microturbulence by balancing Fe II abundance against reduced equivalent width. Next, we applied the correction to a photometric temperature scale from Frebel et al. [2013a] and redetermined the other stellar parameters. We estimate the microturbulence using Fe II lines because of the photometric correction: using Fe I lines computed in LTE with photometric temperatures result in artificially high microturbulence [Ji et al., 2020b]. This is possible as we used ∼20 Fe II lines per star. The corrected effective temperature ($T_{\rm eff}$), surface gravity (log g), microturbulence (v_t), metallicity ([Fe/H]), and their associated uncertainties (e_T, e_g, e_v, and e_{Fe}, respectively) are given in Table 5.2. $T_{\rm eff}$ systematic uncertainty was estimated at 150 K due to intrinsic scatter in the temperature correction from Frebel et al. [2013a]. The corresponding systematic uncertainties for the remaining stellar parameters, log g, v_t, and [Fe/H], were set to 0.3 dex, 0.2 km s^{-1}, and 0.2 dex, respectively. These are added in quadrature to the statistical uncertainties in the slopes and standard errors of the spectroscopic balance to determine the total stellar parameter uncertainties

[see Ji et al., 2020b, for details].

Overall, we detected or put upper limits on 29 species of 24 elements, where CH, CN, Al I, Sc II, V I, V II, Mn I, Co I, Sr II, Y II, Ba II, La II, and Eu II were synthesized and O I, Na I, Mg I, K I, Ca I, Ti I, Ti II, Cr I, Cr II, Fe I, Fe II, Ni I, Zn I, Sr I, Zr II, and Dy II were determined with equivalent widths. Mean abundances for each species are computed with a weighted average of individual absorption lines and compared to their respective solar abundances from Asplund et al. [2009].

For a given absorption line i for element X, we measure an abundance $\log \epsilon_i(X)$. The measured abundance is uncertain, due to uncertainties in the stellar parameters and the measurement itself. We therefore measure abundance uncertainties for each absorption line by independently propagating the stellar parameter uncertainties, denoted $e_{T_{\rm eff},i}$, $e_{g,i}$, $e_{M,i}$, and $e_{v,i}$.Additionally, uncertainty in the measured equivalent width propagates into an abundance uncertainty denoted $e_{stat,i}$.

To measure the overall abundance for the star, we use a weighted average of measured abundances from all absorption lines. Weighting is introduced in order to de-prioritize measurements with high errors to most accurately represent the measured abundance of the star. The weighted abundance $\log \epsilon_w(X)$ is calculated as:

$$\log \epsilon_w(X) = \frac{\Sigma_i(\log \epsilon_i(X) \times w_i)}{\Sigma_i w_i}. \tag{5.1}$$

The weight w_i for a measured line i reflects the total uncertainty of a measurement by combining all of the measured uncertainties described above. The weight is calculated

Table 5.2. Leiptr Candidate Stellar Parameters and Uncertainties

Name	$T_{\rm eff}$	e_T	$T_{\rm eff,\ phot}$	log g	e_g	v_t	e_v	[Fe/H]	$e_{\rm Fe}$
Leiptr-186	4640	152	4607	1.00	0.31	2.51	0.24	−2.54	0.21
Leiptr-208	5020	157	5126	1.90	0.31	1.85	0.24	−2.25	0.21
Leiptr-252	5360	163	5329	3.60	0.31	1.31	0.25	−1.20	0.33
Leiptr-321	5095	160	5059	2.40	0.31	1.95	0.27	−1.80	0.22
Leiptr-342	4650	153	4513	1.00	0.30	2.32	0.25	−1.93	0.21

Note. — Temperatures are given in K and microturbulence in km s^{-1}. $T_{\rm eff}$ is spectroscopic effective temperature with the correction from Frebel et al. [2013a], log g is surface gravity, and v_t is microturbulence. We also include the photometric temperature $T_{\rm eff,\ phot}$, as calculated using Mucciarelli et al. [2017] color-temperature relations for *Gaia* BP-RP colors. The e values represent the stellar parameters' respective uncertainties, which are a quadrature sum of the statistical uncertainty calculated from the iron lines and adopted systematic uncertainties for Teff, log g, v_t, and [Fe/H] of 150 K, 0.3 dex, 0.2 km s^{-1}, and 0.2 dex, respectively.

as the inverse of the quadrature sum of each contributing source of uncertainty:

$$\frac{1}{w_i} = e^2_{T_{\rm eff},i} + e^2_{g,i} + e^2_{M,i} + e^2_{v,i} + e^2_{stat,i}. \tag{5.2}$$

We also calculate the total standard error, $\sigma^2_{\rm stat}$, which represents the contributed systematic and statistical uncertainties from each individual line measurement to the overall error of the element abundance, and is calculated as:

$$\sigma^2_{\rm stat} = \frac{1}{\Sigma_i \left(e^2_{{\rm sys},i} + e^2_{{\rm stat},i}\right)^{-1}}. \tag{5.3}$$

We set the per-line systematic error floor $e_{sys,i} = 0.1$ to account for unforeseen systematics in our stellar models and inferred abundance measurements.

We calculate the variance of our measurements, and continue to weight the contribution of each measurement, to appropriately estimate the systematic uncertainty in line-to-line scatter. The square of the weighted standard deviation σ^2_w is calculated as:

$$\sigma^2_w(X) = \frac{\Sigma_i \left(w_i \times (\log \epsilon_i(X) - \log \epsilon_w(X))^2\right)}{\Sigma_i w_i}. \tag{5.4}$$

We also calculate the contribution of the uncertainty relative to each stellar parameters. The propagated stellar parameter uncertainty, $\sigma^2_{\rm SP}$, is:

$$\begin{aligned}\sigma^2_{\rm SP} = &\left(\frac{\Sigma_i(e_{T_{\rm eff},i} \times w_i)}{\Sigma_i w_i}\right)^2 + \left(\frac{\Sigma_i(e_{g,i} \times w_i)}{\Sigma_i w_i}\right)^2 \\ &+ \left(\frac{\Sigma_i(e_{v,i} \times w_i)}{\Sigma_i w_i}\right)^2 + \left(\frac{\Sigma_i(e_{M,i} \times w_i)}{\Sigma_i w_i}\right)^2.\end{aligned} \tag{5.5}$$

Each of these terms is treated as the total uncertainty of the element X due to the corresponding stellar parameter, e.g.:

$$e_{T_{\rm eff}} = \frac{\Sigma_i (e_{T_{\rm eff},i} \times w_i)}{\Sigma_i w_i}. \tag{5.6}$$

Here, we neglect correlations between stellar parameters. Ji et al. [2020b] gave a formalism for how to propagate correlated stellar parameter uncertainties to abundances, but it required the assumption that abundances depend linearly on stellar parameters. We have unfortunately found that this assumption often breaks down, which can result in systematic biases in the resulting abundances. By ignoring the correlations, we find that we slightly overestimate the stellar parameter uncertainties, which we find preferable to obtaining biased abundances.

The total uncertainty for the abundance of element X in the star, $[X/{\rm H}]$, combines all previous uncertainties. $\sigma_{\rm [X/H]}$ is the quadrature sum of the total standard error, the stellar parameter uncertainties, and the weighted standard deviation:

$$\sigma_{\rm [X/H]} = \sqrt{\sigma^2_{\rm stat} + \sigma^2_{\rm SP} + \max\left(\sigma^2_w, 0.1^2\right)}. \tag{5.7}$$

We include a minimum floor of 0.1^2 on the weighted variance of measurements to account for elements with too few lines to measure a standard deviation. In our tables and figures, we also include the abundance uncertainty excluding this systematic uncertainty buffer and weighted variance:

$$\sigma_{\rm [X/H],\ no\ sys} = \sqrt{\sigma^2_{\rm stat} + \sigma^2_{\rm SP}}. \tag{5.8}$$

We present both sets of uncertainties, one that gives our best estimate of a total uncertainty, and the other to estimate abundance precision.

We use [Fe I/H] to calculate [X/Fe]. The uncertainty of [X/Fe] needs to account for statistical uncertainties for both X and Fe, in addition to correlated abundance uncertainties from stellar parameters and the weighted variance with corresponding uncertainty floors:

$$\begin{aligned}\sigma^2_{\rm [X/Fe]} = &\sigma^2_{\rm stat} + \sigma^2_{\rm stat,Fe} \\ &+ (e_{T_{\rm eff}} - e_{T_{\rm eff},\rm Fe})^2 + (e_g - e_{g,\rm Fe})^2 \\ &+ (e_v - e_{v,\rm Fe})^2 + (e_M - e_{M,\rm Fe})^2 \\ &+ \max\left(\sigma^2_w, 0.1^2\right) + \max\left(\sigma^2_{w,\rm Fe}, 0.1^2\right).\end{aligned} \tag{5.9}$$

Again, we exclude the uncertainty floor to give an approximate error without a conservative error buffer:

$$\begin{aligned}\sigma^2_{\rm [X/Fe],\ no\ sys} = &\sigma^2_{\rm stat} + \sigma^2_{\rm stat,Fe} \\ &+ (e_{T_{\rm eff}} - e_{T_{\rm eff},\rm Fe})^2 + (e_g - e_{g,\rm Fe})^2 \\ &+ (e_v - e_{v,\rm Fe})^2 + (e_M - e_{M,\rm Fe})^2.\end{aligned} \tag{5.10}$$

We present the start of a list of line measurements for the Leiptr candidate stars in Table 5.3 which provides each line's wavelength, excitation potential, oscillator strength, equivalent width, and full width at half maximum. The full table is available in the arXiv source as a CSV file. The SMHR analysis files that include the spectra and line fits are available upon request to the first author. The final abun-

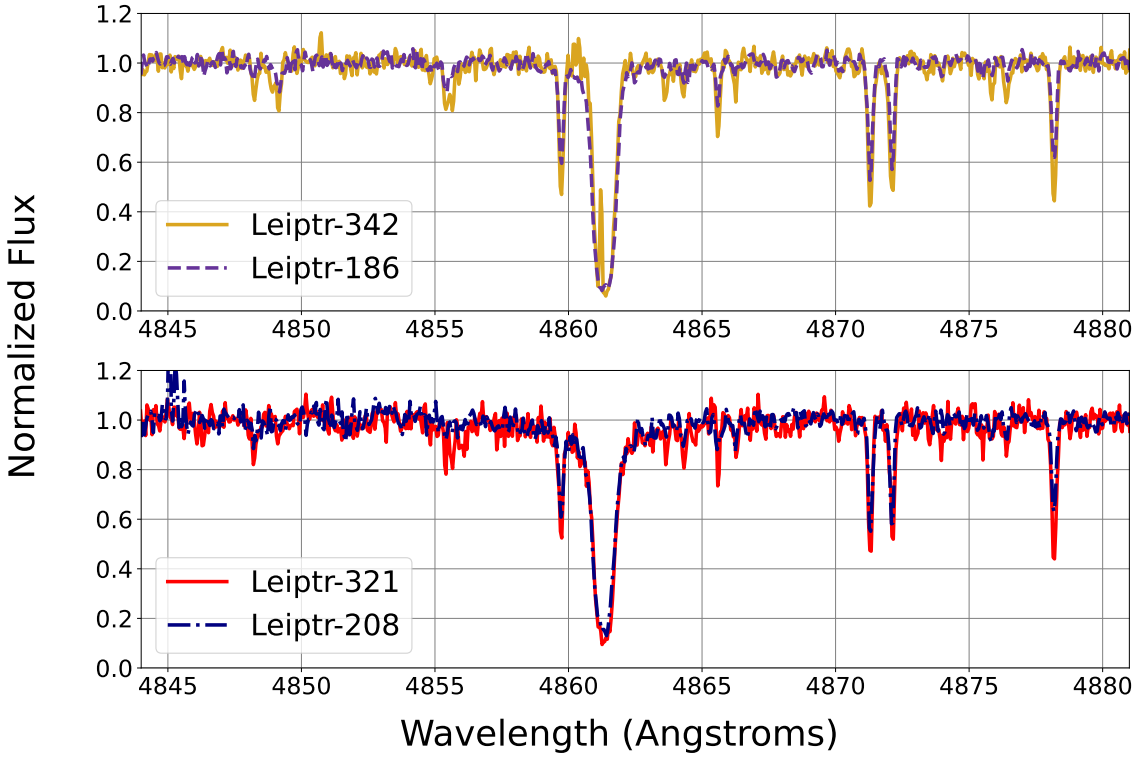

Figure 5.3 A comparison of normalized spectra of stars with similar stellar parameters around the Hβ line at 4861 Å. Additional absorption lines are shown adjacent to the central line. The top plot has the stars Leiptr-186 (purple dashed line) and Leiptr-342 (gold solid line), both with $T_{\rm eff}$ around 4650 K. The bottom plot has stars Leiptr-208 (blue dot-dashed line) and Leiptr-321 (red solid line), both with $T_{\rm eff}$ around 5050 K. The similarity of the hydrogen line profiles suggest each pair of stars has very similar temperatures; but Leiptr-321 and Leiptr-342 have stronger metal lines than Leiptr-208 and Leiptr-186, respectively, indicating their metallicities must differ.

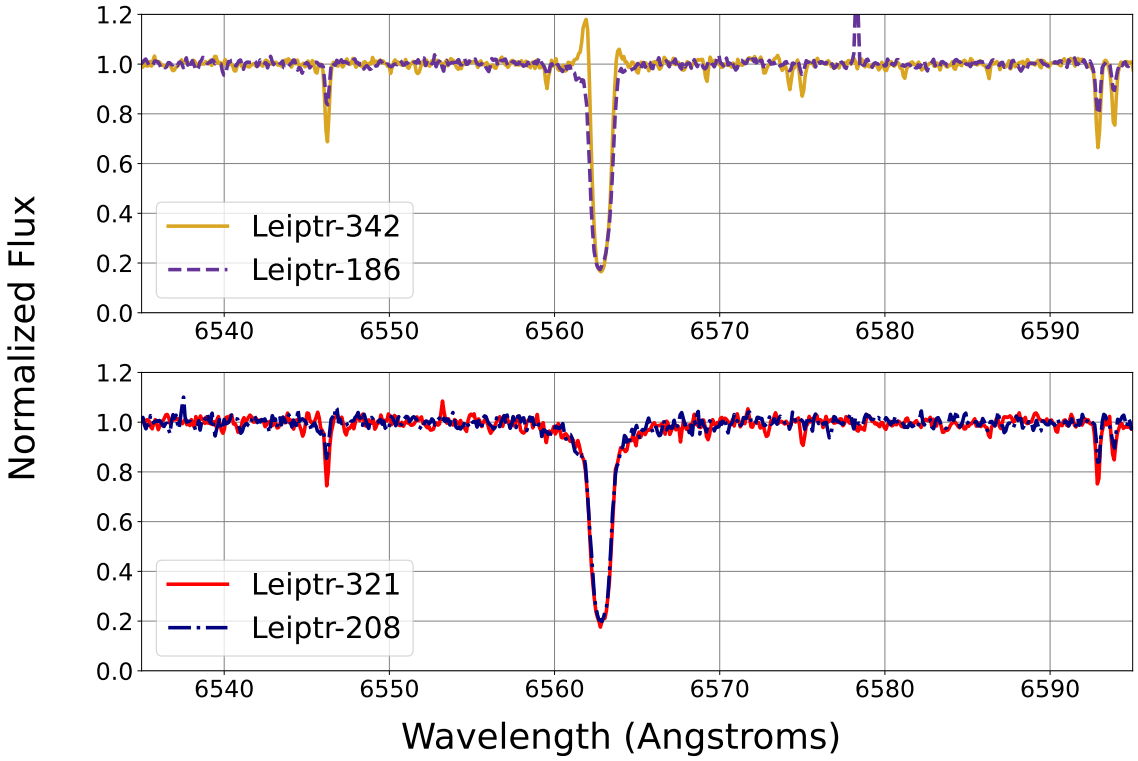

Figure 5.4 A comparison of normalized spectra of stars with similar stellar parameters around the Hα line at 6563 Å. Additional absorption lines are shown adjacent to the central line. The top plot has the stars Leiptr-186 (purple dashed line) and Leiptr-342 (gold solid line), both with $T_{\rm eff}$ around 4650 K. The bottom plot has stars Leiptr-208 (blue dot-dashed line) and Leiptr-321 (red solid line), both with $T_{\rm eff}$ around 5050 K. The similarity of the hydrogen line profiles suggest each pair of stars has very similar temperatures; but Leiptr-321 and Leiptr-342 have stronger metal lines than Leiptr-208 and Leiptr-186, respectively, indicating their metallicities must differ.

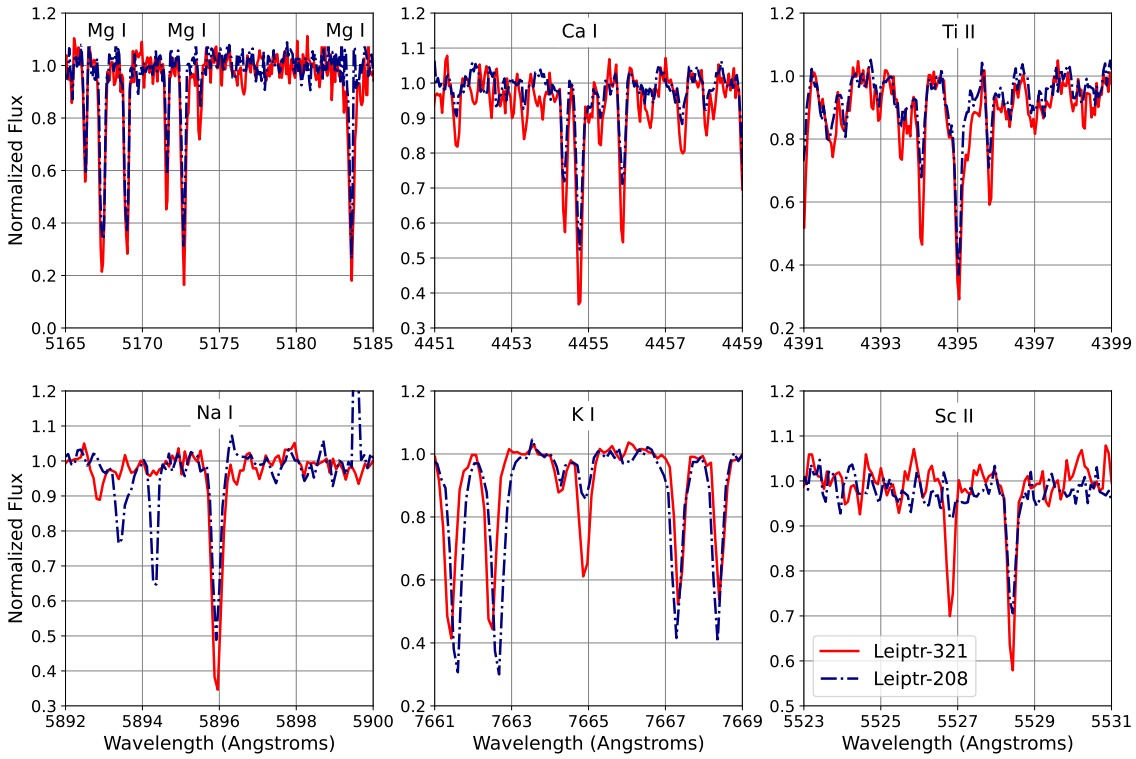

Figure 5.5 A comparison of normalized rest-frame spectra of Leiptr-321 and Leiptr-208 that have similar stellar parameters, centered around the Mg I b triplet; Ca I line at 4454.8 Å; Ti II line at 4395.0 Å; Na I line at 5895.9 Å; K I line at 7664.9 Å; and Sc II line at 5526.8 Å. Additional absorption lines are shown adjacent to the central line, including interstellar medium and telluric features in the sodium and potassium panels, respectively. The telluric features around K I are offset because the stars are shifted to rest frame. The plots have stars Leiptr-208 (blue dot-dashed line) and Leiptr-321 (red solid line), both with $T_{\rm eff}$ around 5050 K. It is clear that Leiptr-321 has overall higher metallicity, as well as much higher abundances of sodium, potassium, and scandium.

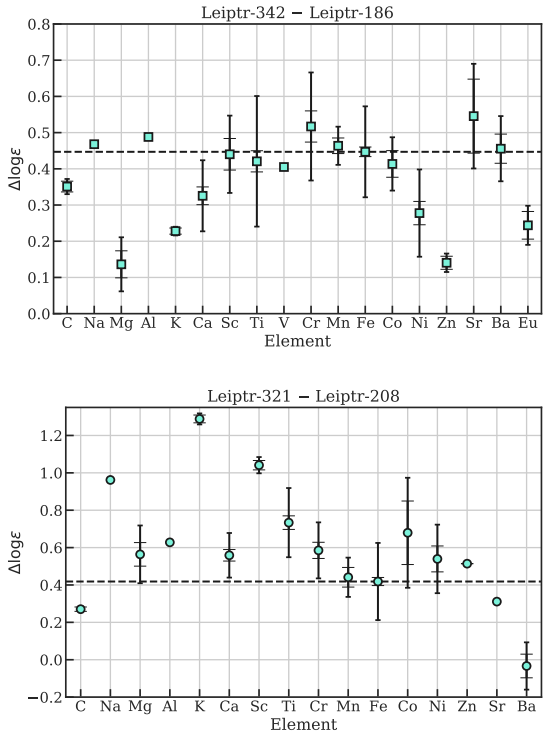

Figure 5.6 Abundance differences between matched pairs of stars with similar temperatures. The top panel shows the difference between the cooler pair, Leiptr-342 and Leiptr-186, indicated by light-blue squares in this and future figures. The bottom panel shows the difference between the warmer pair, Leiptr-321 and Leiptr-208, indicated by light-blue circles in this and future figures. The longer error bars with smaller cap sizes show the standard deviation. The shorter error bars with larger cap sizes show the standard error. No error bar is shown if just one line is used. A horizontal dashed line is shown corresponding to $\Delta \log \epsilon(\mathrm{Fe})$; differences of other elements relative to this line indicate Δ[X/Fe].

dances for our five stars are given in Tables 5.4-5.8. We record element, number of lines used, and log ϵ, as well as [X/H] and [X/Fe] and their respective uncertainties, $\sigma_{[X/H]}$ and $\sigma_{[X/Fe]}$, for each star. $[X/Fe]_N$ gives the non-LTE (NLTE) abundances for sodium, aluminum, potassium, and manganese (see Sections 5.5.4 and 5.5.5). We comment on the NLTE effects for all significantly impacted elements, ignoring smaller contributions that are not informative to this analysis.

Star Name	Element	Species	λ	expot	loggf	logeps	e_{stat}	e_{sys}	eqw	e_{eqw}	FWHM	$e_{T_{\rm eff}}$	e_g	e_v	e_M
Leiptr-186	Mg I	12.0	3986.75	4.35	−1.06	5.27	0.06	0.10	36.5	3.7	0.14	0.09	−0.02	−0.01	−0.00
Leiptr-186	Fe I	26.0	4001.66	2.17	−1.90	4.92	0.04	0.10	57.9	2.8	0.13	0.19	−0.03	−0.03	−0.02
Leiptr-186	Ti I	22.1	4012.38	0.57	−1.78	2.58	0.08	0.10	118.2	3.8	0.20	0.07	0.08	−0.16	0.03
Leiptr-186	Ti I	22.1	4025.13	0.61	−2.11	2.47	0.07	0.10	94.6	3.7	0.18	0.08	0.09	−0.09	0.03
...	...	...	...	...	...	...	...	...	...	...	...	...	...	...	...

Table 5.3 Leiptr Candidate Line List

Table 5.4. Leiptr-186 Abundances

Element	N	log ϵ	[X/H]	$\sigma_{[X/H]}$	[X/Fe]	$[X/Fe]_N$	$\sigma_{[X/Fe]}$
CH	2	5.38	-3.05	0.44	-0.50	–	0.36
CN	1	6.12	< -1.70	–	< 0.84	–	–
Na I	2	3.52	-2.72	0.33	-0.18	-0.41	0.27
Mg I	9	5.22	-2.38	0.16	0.17	–	0.18
Al I	1	3.06	-3.39	0.40	-0.84	-0.24	0.41
K I	2	2.87	-2.16	0.21	0.39	-0.11	0.20
Ca I	23	3.92	-2.42	0.16	0.13	–	0.19
Sc II	8	0.35	-2.80	0.17	-0.26	–	0.27
Ti I	29	2.38	-2.57	0.25	-0.02	–	0.20
Ti II	49	2.54	-2.41	0.17	0.13	–	0.26

Table 5.4 (cont'd)

Element	N	log ϵ	[X/H]	$\sigma_{[X/H]}$	[X/Fe]	$[X/Fe]_N$	$\sigma_{[X/Fe]}$
V I	2	1.13	−2.80	0.28	−0.25	–	0.25
V II	2	1.28	−2.65	0.19	−0.11	–	0.31
Cr I	14	2.85	−2.79	0.23	−0.24	–	0.18
Cr II	4	2.96	−2.68	0.14	−0.14	–	0.29
Mn I	6	2.51	−2.92	0.18	−0.38	0.05	0.18
Fe I	124	4.95	−2.55	0.23	0.00	–	–
Fe II	21	4.96	−2.54	0.14	–	–	–
Co I	4	2.39	−2.60	0.36	−0.05	–	0.31
Ni I	19	3.67	−2.55	0.21	−0.00	–	0.20
Zn I	2	2.15	−2.41	0.14	0.14	–	0.22

Table 5.4 (cont'd)

Element	N	log ϵ	[X/H]	$\sigma_{[X/H]}$	[X/Fe]	$[X/Fe]_N$	$\sigma_{[X/Fe]}$
Sr II	2	−0.73	−3.60	0.32	−1.05	–	0.34
Ba II	5	−1.26	−3.44	0.20	−0.90	–	0.26
Eu II	2	−2.30	−2.82	0.22	−0.28	–	0.30

Note. — CN is an upper limit. $[X/Fe]_N$ gives the NLTE abundances.

Table 5.5. Leiptr-208 Abundances

Element	N	log ϵ	[X/H]	$\sigma_{[X/H]}$	[X/Fe]	$[X/Fe]_N$	$\sigma_{[X/Fe]}$
CH	2	6.4	−2.03	0.26	0.22	–	0.24
CN	1	6.08	< -1.75	–	< 0.51	–	–
Na I	2	3.68	−2.56	0.23	−0.30	−0.70	0.23
Mg I	6	5.29	−2.31	0.15	−0.05	–	0.18
Al I	1	3.22	−3.23	0.37	−0.97	−0.37	0.38
K I	2	2.86	−2.17	0.13	0.09	−0.21	0.17
Ca I	16	4.16	−2.18	0.12	0.08	–	0.16
Sc II	7	0.50	−2.65	0.15	−0.39	–	0.21
Ti I	20	2.74	−2.21	0.18	0.05	–	0.20
Ti II	32	2.72	−2.23	0.18	0.03	–	0.23

Table 5.5 (cont'd)

Element	N	log ϵ	[X/H]	$\sigma_{[X/H]}$	[X/Fe]	$[X/Fe]_N$	$\sigma_{[X/Fe]}$
V II	2	1.64	−2.29	0.14	−0.03	–	0.23
Cr I	12	3.15	−2.49	0.16	−0.23	–	0.18
Cr II	3	3.19	−2.45	0.15	−0.19	–	0.23
Mn I	4	2.68	−2.75	0.13	−0.49	−0.12	0.17
Fe I	111	5.24	−2.26	0.16	0.00	–	–
Fe II	22	5.21	−2.29	0.17	–	–	–
Co I	3	2.68	−2.31	0.21	−0.06	–	0.23
Ni I	11	3.85	−2.37	0.14	−0.11	–	0.18
Zn I	2	2.23	−2.33	0.11	−0.07	–	0.18
Sr II	2	−0.56	−3.43	0.45	−1.17	–	0.46

Table 5.5 (cont'd)

Element	N	log ϵ	[X/H]	$\sigma_{[X/H]}$	[X/Fe]	$[X/Fe]_N$	$\sigma_{[X/Fe]}$
Ba II	5	-0.83	-3.01	0.18	-0.75	–	0.22
Eu II	1	-1.71	< -2.23	–	< 0.03	–	–

Note. — CN and Eu II are upper limits. $[X/Fe]_N$ gives the NLTE abundances.

5.4.1 Differential Abundance Analysis

Our overall abundance uncertainties are dominated by stellar parameter uncertainties, in particular the systematic 150 K temperature uncertainty set from the Frebel et al. [2013a] calibration. However, abundance *differences* between two stars of similar stellar parameters can be much more precise [e.g., McWilliam et al., 2013, Nissen and Gustafsson, 2018, Matsuno et al., 2022, McKenzie et al., 2022]. The four Leiptr member stars come in two pairs of stars with similar effective temperatures and surface gravities: Leiptr-186 and Leiptr-342 have $T_{\rm eff} \approx 4650$ K and Leiptr-208 and Leiptr-321 have $T_{\rm eff} \approx 5050$ K. This similarity is clearly visible in the spectra: Figures 5.3 and 5.4 show the Hβ and α lines. The Balmer lines in Leiptr-186 are very similar to Leiptr-342 except that Leiptr-342 has some hydrogen emission; and Leiptr-321 and Leiptr-208 have identical Balmer line shapes. It is also visually clear that the narrow metal absorption lines in Leiptr-321 and Leiptr-342 are substantially stronger than those in Leiptr-208 and Leiptr-186, respectively, suggesting each pair

of stars in fact has different compositions. Figure 5.5 shows several significant differences between the spectra for Leiptr-321 and Leiptr-208 when we zoom in on metal absorption lines for Mg I, Ca I, Ti II, Na I, K I, and Sc II.

We thus conduct a differential abundance analysis between these two pairs of stars to examine whether a more precise analysis can distinguish between the star compositions. Adopting the same stellar parameters as our main analysis, we calculate abundance differences for matched lines between the two pairs of stars using Table 5.3[1]. Unlike the initial abundance analysis, we do not apply any weighting for the differential analysis. We estimate uncertainties by taking the standard deviation and standard error of the line abundance differences, and not propagating any stellar parameter uncertainties that we expect to largely cancel out in this differential analysis.

The results are shown in Figure 5.6. Matching the visual impression from Figures 5.3, 5.4, and 5.5, each pair of stars differs by over 0.4 dex in iron abundance, clearly demonstrating that the Leiptr stars do not all have the same chemical composition. There are also several other [X/Fe] differences (e.g., lower magnesium, europium, and zinc in Leiptr-342 vs Leiptr-186 and higher sodium, potassium, and scandium in Leiptr-321 vs Leiptr-208) that will be discussed in the next section.

1. Note that differential abundance analyses in the literature usually use one reference star to compare to all other stars, but in this case we are simply looking at two pairs of stars with similar stellar parameters.

5.5 Abundance Results

We first discuss the overall metallicity dispersion in the Leiptr stream in Section 5.5.1. Then, we discuss the abundance trends for halo, dwarf galaxy, and globular cluster stars in each element group (Sections 5.5.2-5.5.6) and compare to our results for Leiptr. Total uncertainty is shown in black for accuracy and abundance uncertainty without additional systematic errors is shown in the same color as the stars for statistical precision as described in Section 5.4. Our literature sample is compiled based on references whose analysis process is very similar to ours (i.e., high-resolution optical spectroscopy of individual stars, mostly with spectroscopic stellar parameters). Abundances for stars in the metal-poor Milky Way halo come from selected references in JINAbase (Abohalima and Frebel 2018, from Barklem et al. 2005, Cohen et al. 2013, Roederer et al. 2014, Jacobson et al. 2015) and abundances of GSE stars come from Carrillo et al. [2022]. We take stellar masses of dwarf galaxies from the compilation by Simon [2019]. Massive dwarf galaxy ($M_\star \gtrsim 10^7 M_\odot$) abundances come from Lemasle et al. 2014 (Fornax), Jönsson et al. 2020 (Sagittarius, APOGEE stars), and Hill et al. 2019 (Sculptor). Intermediate-mass dwarf galaxy ($M_\star \gtrsim 10^6 M_\odot$) abundances come from Norris et al. 2017 (Carina), Cohen and Huang 2009 (Draco), Theler et al. 2020 (Sextans), and Cohen and Huang 2010 (Ursa Minor). Ultra-faint dwarf galaxy ($M_\star \lesssim 10^5 M_\odot$) abundances come from Koch et al. [2008], Feltzing et al. [2009], Norris et al. [2010b,a], Simon et al. [2010], Frebel et al. [2010, 2014], Gilmore et al. [2013], Koch et al. [2013], Roederer and Kirby [2014], Ishigaki et al. [2014], François et al. [2016], Ji et al. [2016c,b, 2019, 2020a], Venn et al. [2017], Kirby et al. [2017], Hansen et al. [2017, 2020a, 2024], Nagasawa et al. [2018], Spite

et al. [2018], Marshall et al. [2019], Chiti et al. [2018, 2023], Waller et al. [2023]; and Webber et al. [2023]. Chemical abundances for Milky Way globular clusters come from Carretta et al. [2009a], Cohen and Kirby [2012], Kirby et al. [2023], Roederer et al. [2011], and Worley et al. [2013]. Stars from dwarf galaxy and globular cluster streams come from Ji et al. [2020b].

Before we begin, it is clear that Leiptr-252 is a non-member star, and we have shown it as an X on all figures. Leiptr-252 was originally selected to be a member using *Gaia* DR2 kinematics in Ibata et al. [2019], but our analysis suggests it is a chemical non-member, with a discrepantly high metallicity and abundance ratios all matching background Milky Way stars. After our chemical analysis was complete, Ibata et al. [2024] released a new Leiptr kinematic selection using *Gaia* DR3, and Leiptr-252 is no longer considered a member with the more precise astrometry. Thus Leiptr-252 is a clear chemodynamic non-member, and we do not discuss it further.

The four Leiptr member stars fall into two categories. The three lowest-metallicity stars (Leiptr-186, Leiptr-208 and Leiptr-342) have similar element abundances: low α, odd-z, and neutron-capture ratios. The most metal-rich star (Leiptr-321) has similar abundances to the low-metallicity stars, but higher α and odd-z ratios. We further investigate our pairs from Section 5.4.1 by marking Leiptr-208 and Leiptr-321 as circles and Leiptr-186 and Leiptr-342 as squares in Figures 5.7-5.11. Halo stars are marked as plus signs in gray if from the Milky Way or dark-blue if from GSE; dwarf galaxy stars are marked as triangles in yellow if massive ($M_\star > 10^7$ $M_\odot$), pink if intermediate-mass (10^5 $M_\odot < M_\star < 10^7$ $M_\odot$), or purple if ultra-faint ($M_\star < 10^5$ $M_\odot$); globular clusters are marked as upside-down triangles in dark-red; and stellar

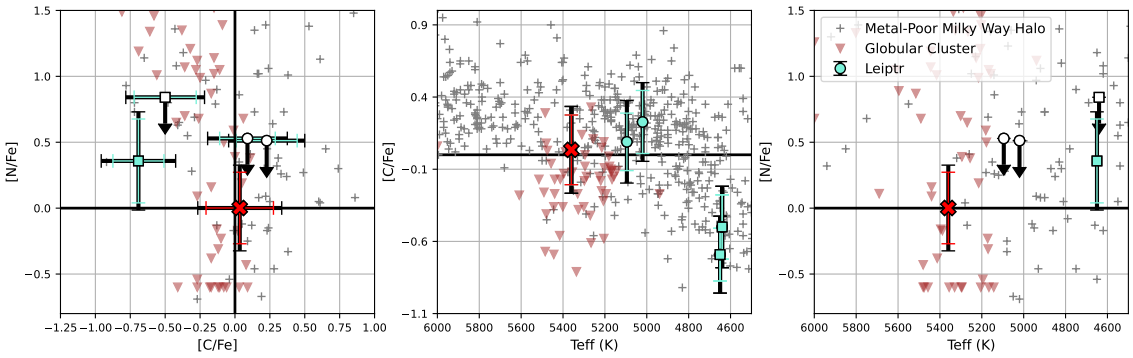

Figure 5.7 Comparison of Leiptr-208 and Leiptr-321 (light-blue circles) and Leiptr-186 and Leiptr-342 (light-blue squares) nitrogen abundances against carbon on the leftmost plot. The other two plots to the right illustrate carbon and nitrogen abundance in relation to effective temperature. The non-member Leiptr-252 is shown as a red X. Total uncertainty is shown in black for accuracy and abundance uncertainty without additional systematic errors is shown in the same color as the stars for statistical precision as described in Section 5.4. [X/Fe] = 0 is plotted as a bold black line. Abundances of metal-poor Milky Way halo stars appear as gray plus signs and abundances from the M15 globular cluster appear as dark-red upside-down triangles.

streams are marked as stars in pink if from a dwarf galaxy or dark-red if from a globular cluster.

5.5.1 Metallicity Mean and Dispersion

Table 5.6. Leiptr-252* Abundances

Element	N	log ϵ	[X/H]	$\sigma_{[X/H]}$	[X/Fe]	$[X/Fe]_N$	$\sigma_{[X/Fe]}$
CH	2	7.26	−1.17	0.33	0.03	–	0.34
CN	1	6.63	−1.20	0.40	−0.00	–	0.40
Na I	4	5.12	−1.12	0.15	0.08	−0.09	0.21
Mg I	4	6.83	−0.77	0.18	0.43	–	0.21
Al I	1	4.67	−1.78	0.37	−0.58	0.02	0.34
K I	2	4.73	−0.30	0.21	0.89	0.30	0.22
Ca I	18	5.49	−0.85	0.15	0.35	–	0.18
Sc II	4	2.07	−1.08	0.15	0.11	–	0.23
Ti I	41	4.05	−0.90	0.22	0.30	–	0.25
Ti II	38	4.15	−0.80	0.18	0.40	–	0.25

Table 5.6 (cont'd)

Element	N	log ϵ	[X/H]	$\sigma_{[X/H]}$	[X/Fe]	$[X/Fe]_N$	$\sigma_{[X/Fe]}$
V I	1	2.69	−1.24	0.24	−0.04	–	0.29
V II	1	2.99	−0.94	0.31	0.26	–	0.39
Cr I	15	4.47	−1.17	0.19	0.03	–	0.20
Cr II	5	4.62	−1.02	0.15	0.18	–	0.25
Mn I	6	4.15	−1.28	0.20	−0.08	0.01	0.24
Fe I	105	6.3	−1.20	0.20	0.00	–	–
Fe II	19	6.3	−1.20	0.18	–	–	–
Co I	4	3.86	−1.13	0.27	0.07	–	0.29
Ni I	19	5.04	−1.18	0.17	0.02	–	0.21
Zn I	2	3.51	−1.05	0.15	0.15	–	0.23

Table 5.6 (cont'd)

Element	N	log ϵ	[X/H]	$\sigma_{[X/H]}$	[X/Fe]	$[X/Fe]_N$	$\sigma_{[X/Fe]}$
Sr I	1	1.83	−1.04	0.21	0.16	–	0.24
Sr II	2	1.94	−0.93	0.21	0.27	–	0.25
Y II	3	1.03	−1.18	0.20	0.02	–	0.27
Zr II	1	1.74	−0.84	0.21	0.35	–	0.31
Ba II	5	1.23	−0.95	0.20	0.25	–	0.23
La II	3	0.24	−0.86	0.20	0.34	–	0.29
Eu II	2	-0.03	−0.55	0.18	0.64	–	0.27
Dy II	1	0.3	−0.80	0.53	0.40	–	0.54

Note. — $[X/Fe]_N$ gives the NLTE abundances. * Non-member

The four Leiptr stars fall between [Fe/H] = −2.54 and −1.80. We follow the method used in Usman et al. [2024] to determine the mean metallicity and intrinsic dispersion, assuming a single Gaussian with heteroskedastic uncertainties, sampled using the nested sampling algorithm `dynesty` [Speagle, 2020, Higson et al., 2019, Koposov et al., 2022] to calculate the Bayesian posteriors of the means and dispersions. The reported uncertainties are determined with 1σ percentiles and 90% upper limits. We acknowledge that [Fe/H] may be underestimated by about 0.2 dex by ignoring NLTE effects on the measured iron lines [e.g., Bergemann et al., 2012c,b, Ezzeddine et al., 2017], but each star will shift a similar amount, so as a whole Leiptr

will maintain the same metallicity dispersion.

Using our full abundance uncertainties, which are dominated by propagating both statistical and systematic uncertainties in stellar parameters, the mean [Fe I/H] metallicity of the four Leiptr stars is -2.20 ± 0.15, with a dispersion 90% upper limit less than 0.38. If instead we use [Fe II/H], the per-star uncertainties are reduced to $\sim$0.15 dex for each star, as the effect of our surface gravity uncertainties on Fe II are much less than the effect of our effective temperature uncertainties on Fe I. We then resolve a [Fe II/H] spread to be $0.29^{+0.23}_{-0.14}$, with >90% confidence that the spread is larger than 0.1 dex. We note the mean metallicity is 0.6 dex lower than the photometric estimate by Ibata et al. [2019].

A resolved metallicity dispersion, indicating internal enrichment by supernovae, is crucial for classifying Leiptr as a dwarf galaxy [Willman and Strader, 2012]. We thus performed a more sensitive test of internal metallicity variations by looking at our pairwise differential abundances (Section 5.4.1, Figure 5.6). These clearly show that our full uncertainties for [Fe I/H] are too conservative for intrinsic dispersion measurements. The four likely Leiptr member stars come in two pairs of stars with similar stellar parameters and clearly distinct chemical abundances. Thus, the metallicity differences and [Fe II/H] metallicity dispersion strongly suggest that Leiptr was a dwarf galaxy, rather than a globular cluster.

5.5.2 C and N

Table 5.7. Leiptr-321 Abundances

Element	N	log ϵ	[X/H]	$\sigma_{[X/H]}$	[X/Fe]	$[X/Fe]_N$	$\sigma_{[X/Fe]}$
CH	2	6.67	-1.76	0.26	0.09	–	0.28
CN	1	6.51	< -1.32	–	< 0.53	–	–
Na I	1	4.59	-1.65	0.29	0.20	-0.29	0.29
Mg I	8	5.87	-1.73	0.17	0.12	–	0.23
Al I	1	3.84	-2.61	0.33	-0.76	-0.15	0.34
K I	2	4.13	-0.90	0.22	0.95	0.25	0.24
Ca I	22	4.75	-1.59	0.13	0.26	–	0.20
Sc II	4	1.6	-1.55	0.16	0.30	–	0.25
Ti I	28	3.34	-1.61	0.19	0.24	–	0.23
Ti II	41	3.49	-1.46	0.17	0.39	–	0.25

Table 5.7 (cont'd)

Element	N	log ϵ	[X/H]	$\sigma_{[X/H]}$	[X/Fe]	$[X/Fe]_N$	$\sigma_{[X/Fe]}$
V I	1	2.15	−1.78	0.19	0.07	–	0.25
V II	2	2.28	−1.65	0.22	0.20	–	0.31
Cr I	13	3.74	−1.90	0.18	−0.05	–	0.22
Cr II	4	3.72	−1.92	0.14	−0.07	–	0.26
Mn I	6	3.14	−2.29	0.12	−0.44	−0.20	0.21
Fe I	109	5.65	−1.85	0.22	0.00	–	–
Fe II	23	5.68	−1.82	0.16	–	–	–
Co I	3	3.31	−1.68	0.27	0.17	–	0.29
Ni I	16	4.39	−1.83	0.15	0.02	–	0.22
Zn I	2	2.75	−1.81	0.12	0.04	–	0.22

Table 5.7 (cont'd)

Element	N	log ϵ	[X/H]	$\sigma_{[X/H]}$	[X/Fe]	$[X/Fe]_N$	$\sigma_{[X/Fe]}$
Sr II	1	0.07	-2.80	0.33	-0.95	–	0.36
Ba II	4	-0.89	-3.07	0.16	-1.22	–	0.24
Eu II	1	-1.32	< -1.84	–	< 0.01	–	–

Note. — CN and Eu II are upper limits. $[X/Fe]_N$ gives the NLTE abundances.

Table 5.8. Leiptr-342 Abundances

Element	N	log ϵ	[X/H]	$\sigma_{[X/H]}$	[X/Fe]	$[X/Fe]_N$	$\sigma_{[X/Fe]}$
CH	2	5.74	-2.69	0.22	-0.70	–	0.27
CN	1	6.19	-1.64	0.41	0.35	–	0.42
O I	1	7.09	-1.60	0.19	0.40	–	0.28
Na I	1	4.16	-2.08	0.33	-0.08	-0.36	0.32
Mg I	4	5.45	-2.15	0.17	-0.15	–	0.21
Al I	1	3.55	-2.90	0.35	-0.91	-0.30	0.38
K I	2	3.21	-1.82	0.17	0.17	-0.42	0.21
Ca I	17	4.32	-2.02	0.13	-0.02	–	0.20
Sc II	6	0.8	-2.35	0.14	-0.35	–	0.25
Ti I	28	2.8	-2.15	0.18	-0.15	–	0.21

Table 5.8 (cont'd)

Element	N	log ϵ	[X/H]	$\sigma_{[X/H]}$	[X/Fe]	$[X/Fe]_N$	$\sigma_{[X/Fe]}$
Ti II	41	2.94	−2.01	0.17	−0.01	–	0.27
V I	1	1.46	−2.47	0.21	−0.48	–	0.25
V II	1	1.94	−1.99	0.19	0.00	–	0.29
Cr I	14	3.53	−2.11	0.19	−0.12	–	0.21
Cr II	6	3.55	−2.09	0.14	−0.10	–	0.26
Mn I	6	2.97	−2.46	0.13	−0.47	−0.16	0.19
Fe I	93	5.51	−1.99	0.21	0.00	–	–
Fe II	20	5.56	−1.94	0.15	–	–	–
Co I	4	2.86	−2.13	0.32	−0.14	–	0.34
Ni I	18	4.06	−2.16	0.20	−0.17	–	0.24

Table 5.8 (cont'd)

Element	N	log ϵ	[X/H]	$\sigma_{[X/H]}$	[X/Fe]	$[X/Fe]_N$	$\sigma_{[X/Fe]}$
Zn I	2	2.35	−2.21	0.10	−0.22	–	0.22
Sr II	2	-0.21	−3.08	0.42	−1.08	–	0.43
Ba II	5	-0.81	−2.99	0.18	−0.99	–	0.26
Eu II	2	-2.06	−2.58	0.16	−0.58	–	0.28

Note. — $[X/Fe]_N$ gives the NLTE abundances.

In principle, carbon and nitrogen abundances can be used to distinguish between globular clusters and dwarf galaxies. This is because the majority of stars in massive globular clusters display unusual carbon depletions and nitrogen enhancements, a phenomenon whose origin is not understood but is empirically well-documented [e.g., Bastian and Lardo, 2018, Gratton et al., 2019]. We use the 4310 and 4323 Å CH absorption bands to determine the carbon abundance and 3877 Å CN band to find upper limits on nitrogen for Leiptr-186, Leiptr-208, and Leiptr-321. The NLTE correction is negligible for carbon [Amarsi et al., 2019a,b] and nitrogen [Amarsi et al., 2020, Mashonkina and Ryabchikova, 2024]. We find that Leiptr-342 has high nitrogen and low carbon. Thus, this star could potentially indicate that Leiptr is a disrupted globular cluster.

However, red giant branch stars also change composition as they ascend the red giant branch due to extra mixing that also depletes carbon and enhances nitrogen

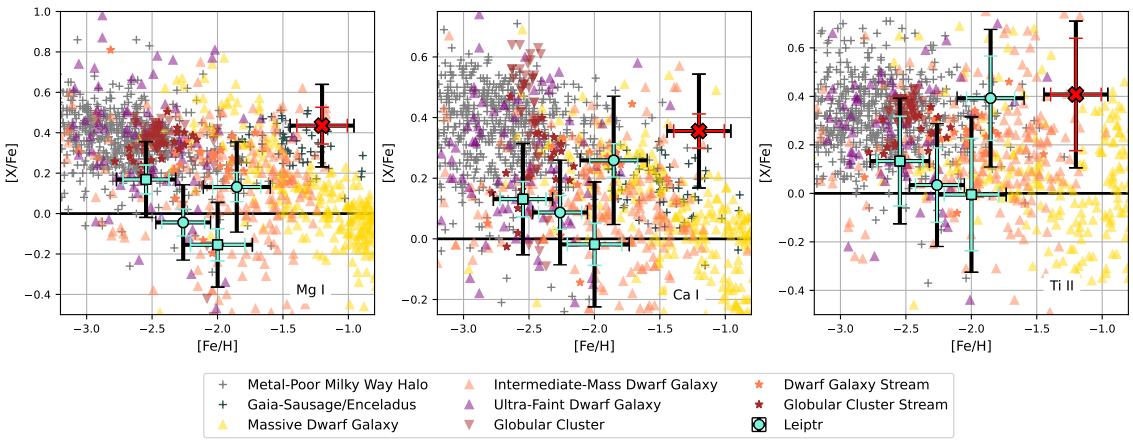

Figure 5.8 Comparison of Leiptr-208 and Leiptr-321 (light-blue circles) and Leiptr-186 and Leiptr-342 (light-blue squares) α abundances with other stellar populations. The non-member Leiptr-252 is shown as a red X. uncertainty is shown in black for accuracy and abundance uncertainty without additional systematic errors is shown in the same color as the stars for statistical precision as described in Section 5.4. [X/Fe] = 0 is plotted as a bold black line. Metal-poor Milky Way halo stars appear as gray plus signs and GSE stars appear as dark-blue plus signs. Abundances of stars from massive dwarf galaxies, intermediate-mass dwarf galaxies, and ultra-faint dwarf galaxies appear as yellow triangles, pink triangles, and purple triangles, respectively. Abundances of stars from the M92 and NGC 2419 Milky Way globular clusters appear as dark-red upside-down triangles. Abundances from dwarf galaxy stream stars appear as pink stars and abundances from globular cluster stream stars appear as dark-red stars.

[e.g., Shetrone et al., 2019], so we must also examine the relationship between chemical abundance and effective temperature. We plot carbon and nitrogen abundance against $T_{\rm eff}$ in the right two panels of Figure 5.7. We expect to see higher nitrogen and lower carbon as $T_{\rm eff}$ decreases due to extra mixing (e.g., Figure 6 of Spite et al. 2005). Enriched globular cluster stars would not follow this temperature dependence and instead show a distinct group of stars with high nitrogen and low carbon, irrespective of measured temperature. Compared to Cohen et al. [2005], which specifically targeted stars in M15 that are on the lower red giant branch to avoid extra mixing, the Leiptr stars are cooler and within the regime of possible extra mixing effects. Since we do observe that the coolest Leiptr stars have higher nitrogen and lower carbon, the trend with $T_{\rm eff}$ suggests that extra mixing is most likely the reason for Leiptr's chemical abundance pattern. Furthermore, the nitrogen increase is not as extreme as it is in globular clusters like M15 [Cohen et al., 2005]. However, with only one nitrogen determination in the Leiptr member stars, more stars would be needed for this to be a strong constraint on whether Leiptr's progenitor is a globular cluster or dwarf galaxy.

5.5.3 α elements (Mg, Ca, Ti)

The [α/Fe] ratio is an excellent indicator of a stream's progenitor due to galactic chemical evolution. α elements are primarily produced by core-collapse supernovae, while iron is produced by both core-collapse and Type Ia supernovae. The [α/Fe] ratio thus starts high early then declines to lower values later as a galaxy forms. Efficiently star-forming galaxies with lower mass-loading factors like the Milky Way

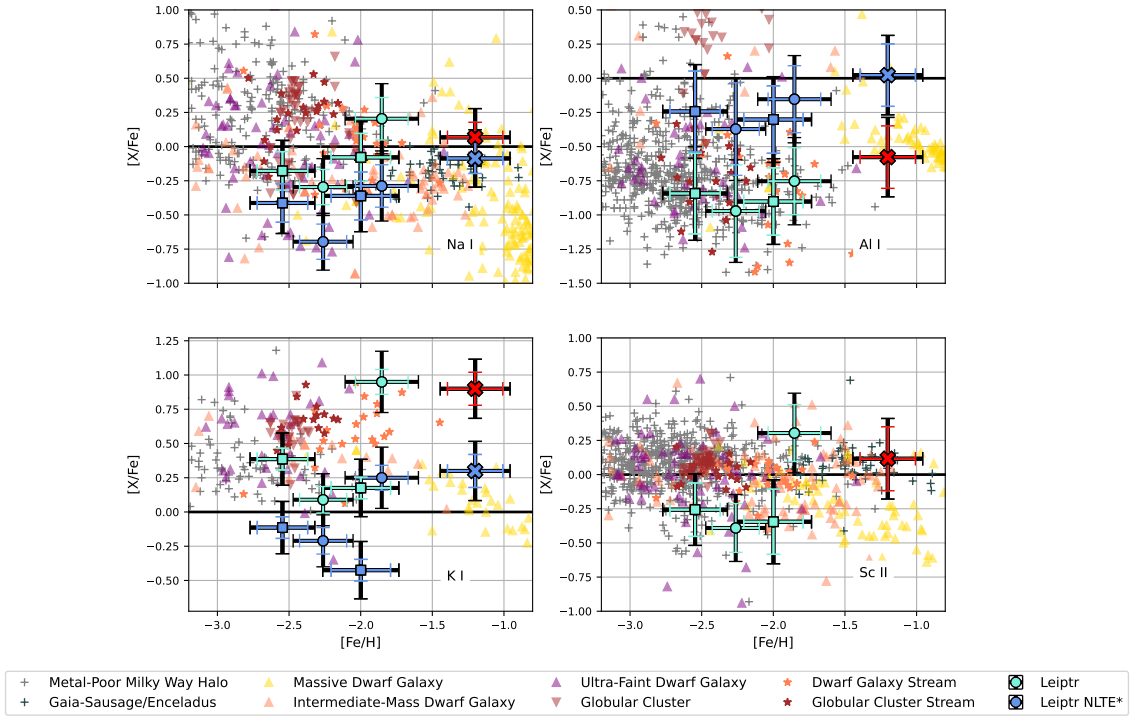

Figure 5.9 Comparison of Leiptr-208 and Leiptr-321 (light-blue circles) and Leiptr-186 and Leiptr-342 (light-blue squares) odd-z abundances with other stellar populations. The non-member Leiptr-252 is shown as a red X. Total uncertainty is shown in black for accuracy and abundance uncertainty without additional systematic errors is shown in the same color as the stars for statistical precision as described in Section 5.4. [X/Fe] = 0 is plotted as a bold black line. Metal-poor Milky Way halo stars appear as gray plus signs and GSE stars appear as dark-blue plus signs. Abundances of stars from massive dwarf galaxies, intermediate-mass dwarf galaxies, and ultra-faint dwarf galaxies appear as yellow triangles, pink triangles, and purple triangles, respectively. Abundances of stars from the M92 and NGC 2419 Milky Way globular clusters appear as dark-red upside-down triangles. Abundances from dwarf galaxy stream stars appear as pink stars and abundances from globular cluster stream stars appear as dark-red stars. Leiptr-208 and Leiptr-321 (blue circles) and Leiptr-186 and Leiptr-342 (blue squares) abundances for sodium, aluminum, and potassium are additionally plotted to correct for especially significant NLTE effects.
*approximate NLTE corrections are calculated as an average for aluminum and independently for sodium and potassium (see text for details)

maintain a high [α/Fe] until relatively high metallicities, while inefficiently star-forming dwarf galaxies with higher mass-loading factors have an α downturn at lower metallicities [e.g., Tinsley, 1979, Matteucci and Brocato, 1990, McWilliam, 1997, Tolstoy et al., 2009, Sheffield et al., 2012]. This downturn, often called an α "knee", tends to occur at lower metallicities in lower-mass galaxies [e.g., Tolstoy et al., 2009, Kirby et al., 2011, 2020, Frebel and Bromm, 2012, Helmi et al., 2018, Hill et al., 2019, Theler et al., 2020]. Globular clusters can be understood in this context as inheriting the chemical patterns of their host galaxies at their birth metallicity, as they are the most massive star clusters to form in a galaxy [e.g., Forbes et al., 2018, Choksi et al., 2018, Reina-Campos et al., 2019]. Thus, globular clusters born in the Milky Way will tend to be high-α, while those born in dwarf galaxies will be low-α [e.g., Mucciarelli et al., 2017, Usman et al., 2024].

Figure 5.8 shows that Leiptr's stars are overall low-α. The NLTE correction is negligible for magnesium [Mashonkina, 2013, Bergemann et al., 2017], calcium [Mashonkina et al., 2007, Spite et al., 2012], and titanium [Bergemann, 2011, Sitnova et al., 2016]. While Milky Way halo stars and stars in Milky Way globular clusters M92 and NGC 2419 have [α/Fe] $\approx 0.3 - 0.4$ (NGC 2419 has some low-magnesium stars, but this is from magnesium depletion due to multiple populations), the three lowest-metallicity Leiptr stars' magnesium, calcium, and titanium abundances are within 1σ of [α/Fe] $= 0$. Thus, the Milky Way halo and its globular clusters' high-α abundances are overall inconsistent with Leiptr. However, several dwarf galaxies have low [α/Fe] ratios similar to Leiptr. At [Fe/H] ≈ -2, lower-mass classical dwarf galaxies ($M_\star \lesssim 10^6 M_\odot$) like Draco, Ursa Minor, and Sextans, as well as the dwarf

galaxy stream Elqui, have low [α/Fe] abundances similar to Leiptr. The lowest-mass ultra-faint dwarf galaxies like Carina II, Reticulum II, and Horologium I ($M_\star \lesssim 10^5 M_\odot$) also mostly have low [$\alpha$/Fe] abundances at [Fe/H] ≈ -2. In contrast, higher-mass dwarf galaxies like Sculptor, Fornax, and GSE ($M_\star \gtrsim 10^7 M_\odot$) still have relatively high [α/Fe] ratios at [Fe/H] $= -2$, not seeing a significant α decline until higher metallicity, [Fe/H] $\gtrsim -1.5$. Thus, Leiptr's α element abundances are most similar to lower-mass dwarf galaxies.

Examining the differential abundances allows us to interpret possible trends with metallicity in the α elements. Comparing Leiptr-186 and Leiptr-342 (light-blue squares in Figure 5.8, top panel of Figure 5.6), there is a significant decline in [Mg/Fe] and potentially small decline in [Ca/Fe] as the metallicity increases by 0.45 dex between these two stars. This decline in [α/Fe] with metallicity would be expected in a dwarf galaxy due to increased Type Ia supernova enrichment. The most metal-rich star, Leiptr-321, is potentially somewhat different than its matched star Leiptr-208 (light-blue circles in Figure 5.8). It has a similar low [Mg/Fe] abundance as the other three Leiptr stars, but it also has slightly higher [Ca/Fe] and [Ti/Fe] abundances. The bottom panel of Figure 5.6 shows the differential abundances give only a 0.1-0.2 dex increase in [Mg,Ca,Ti/Fe] relative to Leiptr-208, which is not very significant compared to the line-to-line scatter, but it will be interesting to interpret this in the context of the odd-Z elements discussed next.

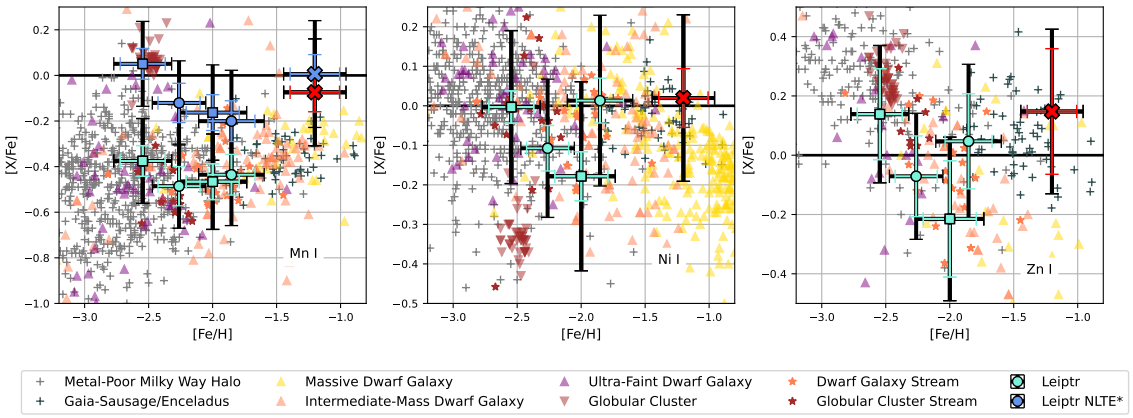

Figure 5.10 Comparison of Leiptr-208 and Leiptr-321 (light-blue circles) and Leiptr-186 and Leiptr-342 (light-blue squares) iron-peak abundances with other stellar populations. The non-member Leiptr-252 is shown as a red X. Total uncertainty is shown in black for accuracy and abundance uncertainty without additional systematic errors is shown in the same color as the stars for statistical precision as described in Section 5.4. [X/Fe] = 0 is plotted as a bold black line. Metal-poor Milky Way halo stars appear as gray plus signs and GSE stars appear as dark-blue plus signs. Abundances of stars from massive dwarf galaxies, intermediate-mass dwarf galaxies, and ultra-faint dwarf galaxies appear as yellow triangles, pink triangles, and purple triangles, respectively. Abundances of stars from the M92 Milky Way globular cluster appear as dark-red upside-down triangles. Abundances from dwarf galaxy stream stars appear as pink stars and abundances from globular cluster stream stars appear as dark-red stars. Leiptr-208 and Leiptr-321 (blue circles) and Leiptr-186 and Leiptr-342 (blue squares) abundances for manganese are additionally plotted to correct for especially significant NLTE effects.
*approximate NLTE corrections are calculated independently for manganese (see text for details)

5.5.4 Odd-Z elements (Na, Al, K, Sc)

Figure 5.9 shows the abundances for the odd-Z elements. In blue points, we show the effect of applying corrections to sodium, aluminum, and potassium for NLTE effects on the lines where the radiation field is partially decoupled from local conditions. Using the calculations for neutral sodium from Lind et al. [2011], we compute the average of the corrections from each of the used lines for each star. All five stars include the 5895 Å sodium line and some of the five also use the 5682, 5688, and 5889 Å lines. The typical size of the correction is -0.35 dex. Aluminum is determined using the 3961 Å resonance line, and we adopt a constant correction for all stars of adding 0.6 to [Al/Fe], following Roederer and Gnedin [2019]. For potassium, we use the two resonance lines at 7664 Å and 7669 Å. The two lines always agree excellently in abundance, and we note the 7664 Å line is not affected by tellurics given Leiptr's range of radial velocities (Figure 5.5). We identify stars in Table A.1 of Reggiani et al. [2019] that have the most comparable stellar parameters as the Leiptr stars and use the corresponding potassium NLTE corrections. We use the corrections from stars HD 186478, CS 29513-014, BD +19 1185A, HD 45282, and HD 126238 with a range from -0.7 to -0.3 dex. The NLTE correction is negligible for scandium [Zhang et al., 2014]. The LTE and NLTE abundances are both reported in Tables 5.4-5.8.

In Figure 5.9, compared to halo stars (whose abundances are mostly computed in LTE and should be compared to the light-blue points), Leiptr lies on the lower end of the abundance scatter for sodium, potassium, and scandium. Abundances of aluminum in the Milky Way globular clusters, M92 and NGC 2419, are also substantially higher than in all four Leiptr stars. The globular clusters should be

compared to the NLTE aluminum abundances (blue points): the M92 stars use the same aluminum 3961 Å line and were corrected using Nordlander and Lind [2017] while the NGC 2419 stars use the subordinate doublet at $6696 - 6698$ Å that are minimally affected by NLTE. These aluminum abundances further disprove that Leiptr may be an accreted globular cluster with multiple populations, which should result in aluminum enhancements as shown by the globular clusters in Figure 5.9 [see Bastian and Lardo, 2018, Gratton et al., 2019, for details].

However, Leiptr is consistent with some odd-z element abundances from ultra-faint and intermediate-mass dwarf galaxies. Overlap between the halo scatter, globular clusters, and dwarf galaxy stars make it difficult to distinguish how Leiptr compares to these systems in most of the elements, but the potassium abundances from stars in ultra-faint dwarf galaxies are the only others as low as Leiptr's three low-metallicity stars. The most metal-rich star, Leiptr-321, appears to be an outlier in the odd-Z elements compared to the other stars, with clearly higher potassium and scandium, and possibly higher sodium, than the three lower-metallicity stars. This is corroborated (in LTE) by comparing to Leiptr-208 in the bottom panel of Figure 5.6 and visually apparent in Figure 5.5. As noted previously, this star also has a mild enhancement in the α elements.

5.5.5 Iron-peak elements (Cr, Mn, Co, Ni, Zn)

Figure 5.10 shows some of the iron-peak abundances in Leiptr. Manganese deserves special discussion due to NLTE effects. We reject the resonance lines at 4030 Å and only use weaker lines around 4800 Å. This was motivated due to expecting relatively

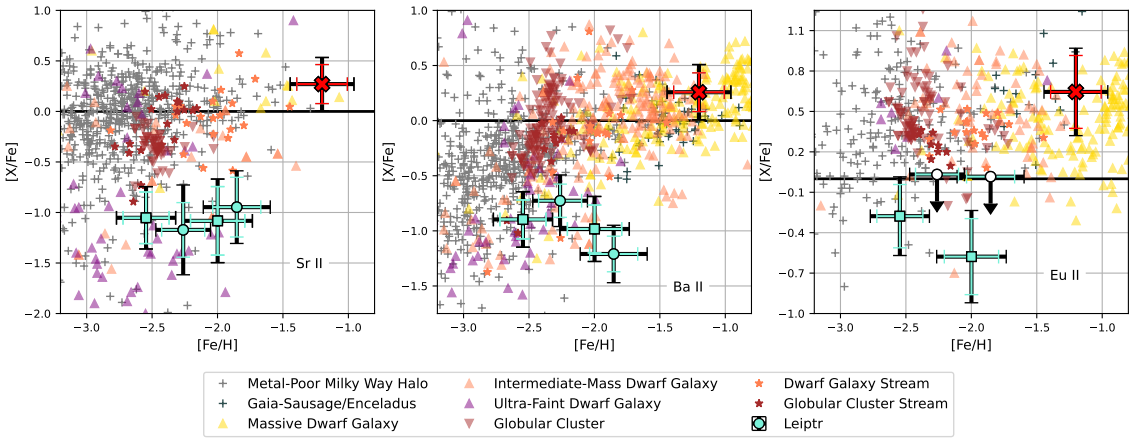

Figure 5.11 Comparison of Leiptr-208 and Leiptr-321 (light-blue circles) and Leiptr-186 and Leiptr-342 (light-blue squares) neutron-capture abundances with other stellar populations. The non-member Leiptr-252 is shown as a red X. Total uncertainty is shown in black for accuracy and abundance uncertainty without additional systematic errors is shown in the same color as the stars for statistical precision as described in Section 5.4. [X/Fe] = 0 is plotted as a bold black line. Metal-poor Milky Way halo stars appear as gray plus signs and GSE stars appear as dark-blue plus signs. Abundances of stars from massive dwarf galaxies, intermediate-mass dwarf galaxies, and ultra-faint dwarf galaxies appear as yellow triangles, pink triangles, and purple triangles, respectively. Abundances of stars from the M15, M22, M92, and NGC 2419 Milky Way globular clusters appear as dark-red upside-down triangles. Abundances from dwarf galaxy stream stars appear as pink stars and abundances from globular cluster stream stars appear as dark-red stars.

small NLTE corrections [Bergemann and Gehren, 2008], but more recent calculations show that the corrections for the weaker lines can also be $0.2 - 0.4$ dex [Bergemann et al., 2019], so we apply an individual NLTE correction from Bergemann et al. [2019] to each star from the average of the corrections for each line, which appear as blue points in Figure 5.10. We note that the comparison stars in Figure 5.10 do not have NLTE corrections applied, so these should be compared to the LTE abundances. The NLTE correction is negligible for nickel [Eitner et al., 2023] and zinc [Takeda et al., 2005, Ezzeddine et al., 2019].

Overall, the iron-peak elements are not that informative for understanding Leiptr's origin, because the [X/Fe] ratios do not vary significantly as a function of environment in the metallicity range of Leiptr stars. In addition to manganese, nickel, and zinc, we record chromium and cobalt abundances for each star in Tables 5.4-5.8. All of Leiptr's stars have approximately equal manganese, cobalt, and chromium abundances, similar to other stars in the Milky Way halo, globular clusters, and dwarf galaxies at [Fe/H] ≈ -2. The nickel and zinc abundances also match the background halo stars, but there are some differences comparing the most metal-poor star, Leiptr-186, to its similar-temperature counterpart, Leiptr-342, which has substantially lower [Ni/Fe] and [Zn/Fe] (light-blue squares in Figure 5.10 and top panel of Figure 5.6).

5.5.6 Neutron-capture elements (Sr, Ba, Eu)

Figure 5.11 shows that Leiptr has very low neutron-capture abundances, [Sr/Fe] $\approx$ [Ba/Fe] ≈ -1. The NLTE correction is negligible for strontium [Mashonkina and

Gehren, 2001, Bergemann et al., 2012a], barium [Mashonkina et al., 1999, Mashonkina and Gehren, 2001], and europium [Mashonkina and Gehren, 2001, Guo et al., 2025]. The four Leiptr member stars have significantly lower [Sr/Fe] and [Ba/Fe] than halo stars, most dwarf galaxy stars, or any of the Milky Way globular clusters. For example, globular clusters M92 and NGC 2419 have higher [Sr/Fe] between -0.5 and 0, and Leiptr's [Sr/Fe] only falls within the extreme tail end of the halo scatter in Figure 5.11. The systems with the most similar neutron-capture element abundances, especially for strontium, are the ultra-faint dwarf galaxies with $M_\star < 10^5\,M_\odot$, which typically have low [Sr/Fe] and [Ba/Fe] between -2 and -1 [Frebel and Norris, 2015, Kirby et al., 2017, Ji et al., 2019].

We detect [Eu/Fe] in the two cooler Leiptr members at quite low values, [Eu/Fe] ~ -0.4. These two stars have [Ba/Eu] ~ -0.5 compared to a pure heavy r-process ratio of -0.8 [e.g., Simmerer et al., 2004], suggesting the neutron-capture element abundances in Leiptr are dominated by production via the r-process but potentially with some contribution from the s-process (slow neutron-capture process) in asymptotic giant branch stars.

The most chemically similar dwarf galaxy stream is Elqui [Ji et al., 2020b], which also has low [α/Fe] at [Fe/H] ≈ -2. Based on its low mean metallicity similar to Leiptr, Li et al. [2022] argued Elqui was an ultra-faint dwarf galaxy using the mass-metallicity relation (as well as the Turranburra stream). But Elqui has sharply rising [Ba/Fe] with increasing metallicity and solar [Sr/Fe], which is more similar to the faintest classical dwarf spheroidal galaxies like Draco, while Leiptr has constant or declining [Sr/Fe] and [Ba/Fe] with metallicity, which is most similar to the ultra-

faint dwarf galaxies. This suggests Leiptr is the stream of an even lower-mass dwarf galaxy than Elqui.

5.6 Discussion

We have observed and analyzed four member stars from the Leiptr stellar stream with the goal of classifying its progenitor, as well as identifying one non-member star Leiptr-252. We now discuss the four main conclusions we draw from these abundances, starting from the most certain and ending with the least certain. Overall, the chemistry of these four stars suggests that Leiptr is likely the first known ultra-faint dwarf galaxy stream without an intact progenitor.

In Figure 5.12, we compare [Mg/Fe] and [Ba/Fe] for known dwarf galaxies to Leiptr-208 and Leiptr-321 marked as light-blue circles and Leiptr-186 and Leiptr-342 marked as light-blue squares. From highest to lowest mass using LOESS smoothing we include GSE as a thick blue line [Ou et al., 2024], Fornax as a purple line [Lemasle et al., 2014], Sculptor as a dotted purple line [Hill et al., 2019], Sextans as a thin gray line [Theler et al., 2020], Draco as a dashed gray line [Cohen and Huang, 2009], Boötes I as a thin green line [Mashonkina et al., 2017], and Carina II as a dot-dashed green line [Ji et al., 2020a]. Additionally, we mark Chenab as a yellow square, Elqui as an orange diamond, Indus as a pink triangle, and Jhelum as a dark-orange star [Ji et al., 2020b].

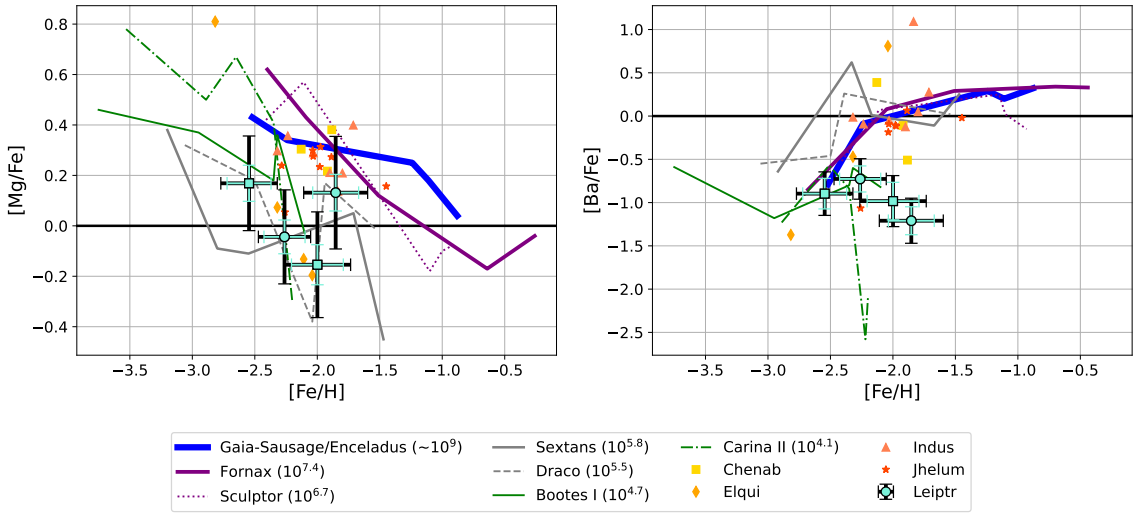

Figure 5.12 [Mg/Fe] and [Ba/Fe] for known dwarf galaxies compared to Leiptr-208 and Leiptr-321 (light-blue circles) and Leiptr-186 and Leiptr-342 (light-blue squares). Total uncertainty is shown in black for accuracy and abundance uncertainty without additional systematic errors is shown in the same color as the stars for statistical precision as described in Section 5.4. [X/Fe] = 0 is plotted as a bold black line. In order from highest to lowest mass using LOESS smoothing, abundances are plotted for GSE (thick blue line), Fornax (purple line), Sculptor (dotted purple line), Sextans (thin gray line), Draco (dashed gray line), Boötes I (thin green line), and Carina II (dot-dashed green line). Solar masses are given in the legend. Abundances are also plotted for the dwarf galaxy streams Chenab (yellow square), Elqui (orange diamond), Indus (pink triangle), and Jhelum (dark-orange star). Leiptr's low-α abundances are most similar to dwarf galaxies of mass $M_\star \lesssim 10^6 M_\odot$. It's neutron-capture abundances are even lower, only consistent with dwarf galaxies of mass $M_\star \lesssim 10^5 M_\odot$. Unlike Elqui, the previous lowest-mass dwarf galaxy stream, Leiptr's neutron-capture abundances are constant or declining with increasing metallicity which suggests that it is even lower-mass.

5.6.1 Extragalactic Origin

Leiptr's eccentric and retrograde orbit is indicative of the progenitor's *ex-situ* formation [Ibata et al., 2019, 2024]. The orbit has most recently been determined by Malhan et al. [2022] to have a pericenter of 12.3 ± 0.1 kpc and the apocenter to be 45.1 ± 0.2 kpc, with a resulting eccentricity of 0.57. The stream is also the second-most retrograde system in that sample. Accreted systems can sometimes be linked together by looking at their energy and angular momentum, indicating that the systems have fallen into the Milky Way together, perhaps having formed with each other. Bonaca et al. [2021] suggested Leiptr could be associated with other retrograde streams, including GD-1, Phlegethon, Ylgr, and especially Gjöll and Wambelong. They suggest this group of streams originated from the retrograde Sequoia/I'itoi group using the average isochrone [Fe/H] = −1.6 from Ibata et al. [2019]. While they did not explicitly address Leiptr, Malhan et al. [2022] also associated these retrograde streams with the Sequoia/I'itoi group[2]. Given the updated metallicity from this work, we further note that Leiptr has clearly distinct chemical abundances from Sequoia [Matsuno et al., 2022], with similarly low [α/Fe] $\sim$ 0 but at lower-metallicity, [Fe/H] = −2.2, compared to Sequoia at [Fe/H] = −1.5 and with lower strontium and barium abundances. Therefore, it is unlikely that Leiptr originated from a globular cluster in this dwarf galaxy. Instead it is expected to be the last stream of a fully disrupted object.

An extragalactic formation would also be consistent with the α elements derived

2. The more metal-rich Arjuna system is also kinematically associated with this group [Naidu et al., 2020], but it is likely debris from an early orbit of GSE [Naidu et al., 2021].

in Leiptr. At a given metallicity, dwarf galaxies have lower values of [α/Fe] than Milky Way *in-situ* stars and globular clusters. Thus, globular clusters that formed *ex-situ* in dwarf galaxies and their remnants show similarly low levels of α elements. For example, the globular cluster stellar stream 300S was originally mistaken for a dwarf galaxy stream due to its low α element abundances [Usman et al., 2024]. With only this information, Leiptr's progenitor could either be a dwarf galaxy, or a globular cluster that formed in an α poor dwarf galaxy and later accreted onto the Milky Way.

5.6.2 A Dwarf Galaxy, Not a Globular Cluster

Stellar metallicity dispersion is the primary chemical distinguisher between disrupted globular clusters and dwarf galaxies. Dwarf galaxy stars have a large spread in their metallicities due to extended chemical evolution, while stars in globular clusters usually have the same metallicity [Willman and Strader, 2012]. Our stars' metallicities span a wide range, [Fe/H] = -2.54 to -1.80. Our conservative metallicity uncertainties for [Fe I/H] only allow a 90% confidence upper limit of 0.38 dex on the metallicity dispersion, but our more precise [Fe II/H] abundances show a resolved metallicity dispersion of $0.29^{+0.23}_{-0.14}$ dex. Additionally, we can clearly see a metallicity difference within Leiptr using differential abundances, as described in Section 5.5.1. The spectra shown in Figures 5.3 and 5.4 demonstrate that the pairs of stars have similar temperatures (based on their matching hydrogen lines), while also showing qualitatively different strengths of the nearby metal lines, indicating that the chemical compositions between the matching stars differ significantly. In

Figure 5.6, the changes in element abundance between these pairs of stars are quantified. The iron abundance clearly shows a large discrepancy between both pairs of stars, with a change of $\Delta\,[\mathrm{Fe/H}] = 0.42 \pm 0.21$ between Leiptr-321 and Leiptr-208 and $\Delta\,[\mathrm{Fe/H}] = 0.45 \pm 0.13$ between Leiptr-342 and Leiptr-186. These disparities are inconsistent with the uniform metallicities found in globular cluster stars, indicating Leiptr's progenitor was a dwarf galaxy.

For completeness, we note that detailed chemical abundances are less useful at classifying a stream as a dwarf galaxy or globular cluster. This is because globular clusters track the overall composition of their birth galaxies [e.g., Mucciarelli et al., 2017, Usman et al., 2024], the [X/Fe] ratios just help confirm whether a stream is accreted or not (as discussed in Section 5.6.1). However, the detection of multiple stellar populations, e.g. high nitrogen, sodium, and aluminum abundances, would be strong evidence that a stellar stream is a globular cluster (Bastian and Lardo 2018, Gratton et al. 2019; or at least contained a disrupted globular cluster, Hansen et al. 2021, Limberg et al. 2024). This is more difficult in low-mass stellar streams, because the fraction of 2P enriched stars with high nitrogen, sodium, and aluminum decreases at lower globular cluster masses [Milone et al., 2017, 2020, Gratton et al., 2019, Usman et al., 2024]. Thus the lack of stars with enhanced nitrogen, sodium, or aluminum in Leiptr prefers a dwarf galaxy, but it is not a strong constraint.

5.6.3 Low-Mass, Possibly Ultra-Faint

Based on the chemistry of our stars, we conclude Leiptr's progenitor was probably a low-mass dwarf galaxy with $M_\star \lesssim 10^5 M_\odot$, possibly small enough to be considered

an ultra-faint dwarf galaxy. First, according to the empirical galaxy mass-metallicity relation [Kirby et al., 2013], Leiptr would have a stellar mass of $10^{4.4\pm0.5}$ $M_\odot$ given its mean [Fe/H] $= -2.2 \pm 0.15$. Second, Leiptr's α abundances are also consistent with low-mass galaxies. This is shown in Figure 5.8, where the low magnesium, calcium, and titanium in Leiptr are consistent with ultra-faint or intermediate-mass galaxies with $M_\star \lesssim 10^6 M_\odot$, but not with higher-mass galaxies like Sculptor, Sagittarius, or Fornax with $M_\star \gtrsim 10^7 M_\odot$. This is also shown with [Mg/Fe] in comparison to intact dwarf galaxies and dwarf galaxy streams in Figure 5.12, showing Leiptr's [Mg/Fe] is most comparable to Sextans, Draco, Boötes I, Carina II, and Elqui. These dwarf galaxies have masses between $10^{4.1}$ and 10^6 $M_\odot$. Leiptr's α chemical evolution therefore most closely resembles a low-mass galaxy with mass $\lesssim 10^6$ $M_\odot$.

The strongest progenitor mass constraint is from the neutron-capture abundances derived in the Leiptr stars. Ultra-faint dwarf galaxies have $M_\star < 10^5 M_\odot$, meaning that a typical ultra-faint dwarf galaxy is enriched by fewer than one rare and prolific r-process event such as a binary neutron star merger, which typically occurs once per $10^5 M_\odot$ of stars formed [Ji et al., 2016a]. This explains the empirical result that the vast majority ($\sim$90%) of ultra-faint dwarf galaxies have such low strontium, barium, and europium abundances ([Sr,Ba/Fe] $\lesssim -1$; Ji et al. 2019, Frebel and Ji 2023) that can be used as a chemical tag to identify stars from these low-mass galaxies [e.g., Casey and Schlaufman, 2017, Roederer, 2017]. Figures 5.11 and 5.12 highlight that the differences are largest at [Fe/H] $= -2$, where all dwarf galaxies with $M_\star \gtrsim 10^6 M_\odot$ have high abundances of strontium and barium, while those with $M_\star \lesssim 10^5 M_\odot$, like Boötes I and Carina II, keep low strontium and barium abundances below -1.

Leiptr's neutron-capture abundances are also lower than the previous lowest-mass dwarf galaxy stream documented, Elqui, whose chemical evolution is similar to the dwarf galaxy Draco [Ji et al., 2020b], suggesting Elqui had a more massive progenitor than Leiptr despite their similar mean metallicity. This suggests that Leiptr was sufficiently low-mass to still be in the stochastic neutron-capture element regime, or stellar mass $\lesssim 10^5\,M_\odot$. We note that the origin of the low but non-zero neutron-capture element abundances in most ultra-faint dwarf galaxies remains unknown, though it could be attributed to neutrino-driven winds, magnetorotationally driven jets, spinstars, or other unknown low-yield r-process sources [Ji et al., 2019].

Leiptr's low mean metallicity of [Fe/H] $= -2.2$, low [α/Fe]$\sim$ 0, and low [Sr, Ba/Fe] ~ -1 all point toward the progenitor of Leiptr being a very low-mass dwarf galaxy. Given that the intact galaxies with the most similar chemical compositions are ultra-faint dwarf galaxies with $M_\star \lesssim 10^5\,M_\odot$, we conclude that Leiptr's progenitor was likely an ultra-faint dwarf galaxy. Leiptr is thus the first confirmed spatially and kinematically coherent stellar stream without a known intact progenitor from the myriad ultra-faint dwarf galaxies that should have contributed to the stellar halo [Brauer et al., 2019, 2022].

5.6.4 Inhomogeneous Core-Collapse Supernova Enrichment?

The four Leiptr stars are very close in composition, but they display some interesting chemical differences. Focusing on the α and odd-Z elements, there is a somewhat decreasing [α/Fe] ratio with increasing [Fe/H] for the three most metal-poor stars, followed by a sharp increase of both the α and odd-Z elements in the most metal-rich

star, Leiptr-321. These differences are visible in Figures 5.8 and 5.9. The differential analysis in Figure 5.6 emphasizes the significant decrease in magnesium, potassium, and calcium [X/Fe] ratios from the metal-poor Leiptr-342 to the more metal-rich Leiptr-186; and a small increase in magnesium, calcium, and titanium [X/Fe] ratios along with a large increase in sodium, aluminum, potassium, and scandium ratios going from the metal-poor Leiptr-208 to the metal-rich Leiptr-321. This is unusual because [α/Fe] is usually expected to monotonically decrease with increasing [Fe/H], and if the odd-Z elements are also produced hydrostatically they should follow this broad trend [e.g., McWilliam et al., 2013].

We suggest Leiptr-321 may show a signature of inhomogeneous enrichment from a core-collapse supernova. Inhomogeneous Type Ia supernova enrichment has previously been suggested as a way to explain unusual magnesium and calcium scatter in Carina [Venn et al., 2012] and an "iron-rich" star in Ursa Minor [McWilliam et al., 2018]. In contrast, in Leiptr we see an enhancement of both α and odd-Z elements, which are synthesized by core-collapse supernovae. If this is inhomogeneous core-collapse supernova enrichment, it would allow probing the nucleosynthesis output of material dominated by a single core-collapse supernova in the same manner that McWilliam et al. [2018] did for a Type Ia supernova. However, with just four member stars, we believe more observations are needed in Leiptr before such an exploration is warranted.

An alternative explanation is that the increase in α and odd-Z elements is due to a late-time starburst. Spikes in star formation can cause rising [X/Fe] [Colavitti et al., 2009] and such a late-time starburst has been suggested to explain a slight [α/Fe]

increase in the highest metallicity stars in the Magellanic Clouds [Nidever et al., 2020, Hasselquist et al., 2021]. While certainly a valid explanation, we consider this a less likely scenario than inhomogeneous enrichment, as it seems like most stars should then be in this higher-α starburst component. However, more stars in Leiptr are needed to make any clear conclusions.

5.7 Conclusion

Prior to this work, it was not known whether Leiptr's progenitor was a dwarf galaxy or globular cluster, though its thin morphology and orbit suggested it might be an *ex situ* globular cluster. We have collected new high-resolution spectroscopic follow-up of four member stars, as well as one non-member star. The chemical abundances of this stream suggest Leiptr's progenitor was likely a very low-mass galaxy, possibly an ultra-faint dwarf galaxy. We have four main conclusions:

- *Extragalactic Origin:* Leiptr's extremely retrograde and eccentric orbit makes it clear the progenitor formed *ex-situ* and was later accreted onto the Milky Way. The stars' low [Mg/Fe] reinforce this, as they are significantly lower than the Milky Way halo stars and globular clusters (see Figure 5.8).

- *Dwarf Galaxy Progenitor:* The metallicity range between the four probable member stars spans [Fe/H] = –2.54 to –1.80. We identify a clear metallicity difference between stars with similar stellar parameters (Figure 5.6) and measure a ∼0.29 metallicity dispersion using [Fe II/H]. This large spread in metallicity shows that Leiptr is more likely a dwarf galaxy than a globular

cluster.

- *Ultra-Faint Dwarf Galaxy Progenitor:* Leiptr's chemical pattern is most similar to ultra-faint dwarf galaxies with $M_\star \lesssim 10^5\,M_\odot$ (Figure 5.12). The mean metallicity of [Fe/H] $= -2.2$, low [Mg/Fe] and other α abundances (Figure 5.8), and low strontium and barium abundances (Figure 5.11) all suggest a low-mass galaxy.

- *Inhomogeneous Mixing?:* We find an intriguing and unusual enrichment in the highest-metallicity star, Leiptr-321, which shows a significant increase in α and odd-Z elements (Figures 5.5, 5.8, and 5.9). This abundance difference could occur due to inhomogeneously mixed material from an individual core-collapse supernova. However, another possible explanation is that Leiptr experienced a late-time starburst.

Leiptr is thus the lowest-mass dwarf galaxy stream known, and likely the first identified ultra-faint dwarf galaxy stream without a known intact progenitor. However, due to our small sample of member stars, further high-resolution spectroscopic follow-up is needed for a more confident mass estimate, as well as being able to verify evidence for inhomogeneous supernova enrichment.

Acknowledgments

This paper includes data gathered with the 6.5 m Magellan Telescopes, located at Las Campanas Observatory, Chile. We thank Joss Bland-Hawthorn and other members of the S5 collaboration for helpful discussions. KRA also thanks Donald Terndrup

for thoughtful feedback on an earlier version of this paper submitted to the Ohio State University Libraries' Knowledge Bank Repository. KRA acknowledges this material is based upon work supported by the National Science Foundation Graduate Research Fellowship under Grant No. 2234693. SAU acknowledges support from the American Association of University Women through the American Dissertation Fellowship. SAU and APJ acknowledge support from the National Science Foundation under grants AST-2206264 and AST-2307599. TTH acknowledges support from the Swedish Research Council (VR 2021-05556). GFL, SLM, and DBZ acknowledge support from the Australian Research Council through Discovery Project grant DP220102254.

This work has made use of data from the European Space Agency (ESA) mission *Gaia* (https://www.cosmos.esa.int/gaia), processed by the *Gaia* Data Processing and Analysis Consortium (DPAC, https://www.cosmos.esa.int/web/gaia/dpac/consortium). Funding for the DPAC has been provided by national institutions, in particular the institutions participating in the *Gaia* Multilateral Agreement.

This work was supported by the Australian Research Council Centre of Excellence for All Sky Astrophysics in 3 Dimensions (ASTRO 3D), through project number CE170100013.

CHAPTER 6

CONCLUSION

To understand the history of our galaxy, we must understand the chemical evolution of both stars formed in the Milky Way *and* stars formed in clusters and dwarf galaxies. While superficially stars formed *ex-situ* may seem irrelevant to the Milky Way's chemistry, we now understand that these systems contribute a significant portion of stars to our galaxy. For example, much of our galactic halo is comprised of the remnants of globular clusters [Martell et al., 2016] and from galaxies that fell into the Milky Way [Naidu et al., 2020], the latter of which is demonstrated in Figure 6.2. By exploring the chemical evolution of these different stellar systems, we can better understand their contributions to larger galaxies and the universe.

Globular clusters in particular have the unsolved phenomenon of multiple stellar populations. While there are many proposed mechanisms for the correlated abundance patterns we find inside these clusters (described in Section 4 of Bastian and Lardo 2018), none fully explain the attributes that we observe. By observing and chemically tagging globular clusters and their disrupted remnants, we can better constrain the initial mass threshold and the environment necessary to form these unusual chemical patterns, and by extension the environment and chemical evolution of the Milky Way.

Globular clusters, unfortunately, are far from being static, unchanging observables: throughout their lifetimes, they interact with other stellar systems, making their chemical evolution more obfuscated and challenging to fully analyze. The process of tidal disruption is complicated, and improving simulations will allow us to

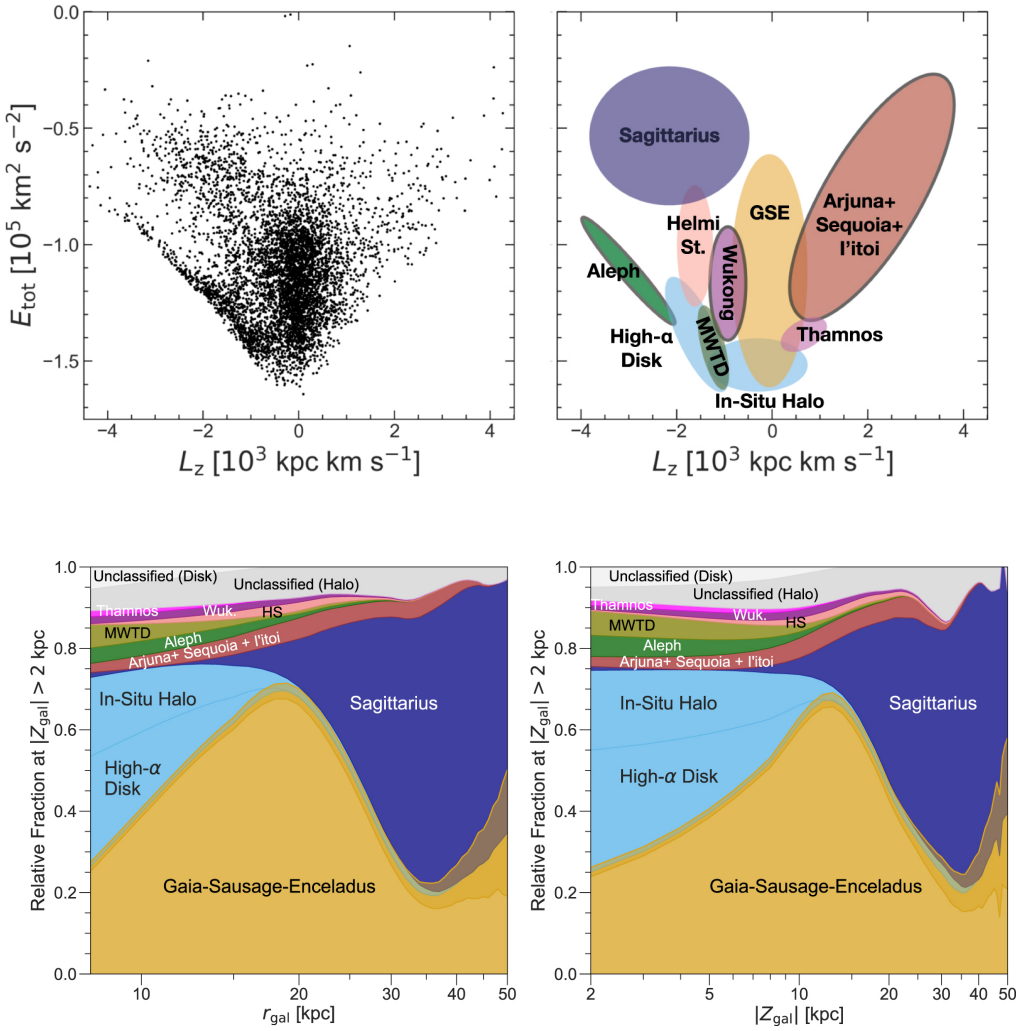

Figure 6.1 Contributions to the Milky Way from *in-situ* and *ex-situ* sources. Both figures from Naidu et al. [2020]. The top row shows the energy-momentum plot for stars in our Milky Way, with the right panel specifically highlighting the stars' origins. The bottom row shows the proportional contribution of stars from different sources as a function of radial distance (left panel) and distance out of the plane of the disk Z (right panel).

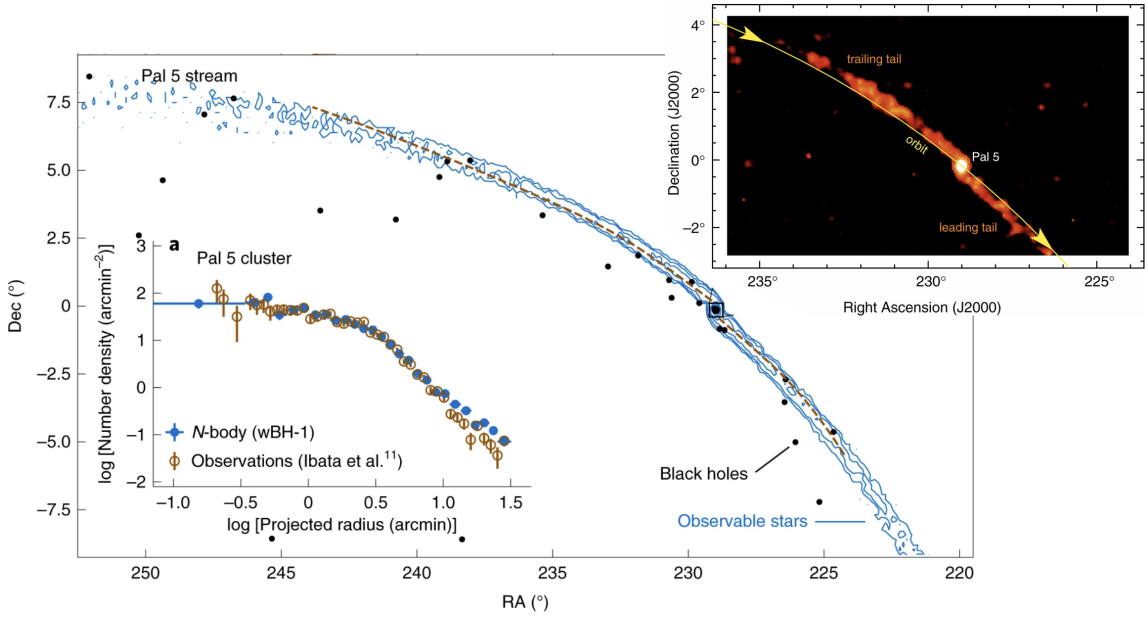

Figure 6.2 Palomar 5 is famous for its impressive tidal tails, spanning 20° across the sky. The tails were first discovered in SDSS data by Odenkirchen et al. [2003]. Gieles et al. [2021] argues an inherent population of stellar-mass black holes would account for the clusters' unusual dynamical properties. However, a black hole population could cause a different distribution of enriched stars than a disruption model caused by tidal forces. Figures adapted from SDSS [2003] (inset) and Gieles et al. [2021].

further understand the contribution of these systems to the halo. Currently, our estimates of initial mass are based on empirical behaviors inferred from N-body simulations, including Baumgardt and Makino [2003], Lamers et al. [2005] and Baumgardt and Hilker [2018]. As our simulations advance, we can further understand this process.

However, we can maximize our understanding of disruption by combining observations with these simulations. By observing and chemically tagging stars in the tidal tails of globular clusters, we could improve our understanding of the disrupting mechanisms. Gieles et al. [2021] suggested that the globular cluster Palomar 5, which

Globular Cluster	Tidal Tails?	Distance (kpc)	RA (°)	Dec (°)	Source
Palomar 5	✓	21.9	229.02	-0.12	Odenkirchen et al. [2003]
M3 (NGC 5272)	✓	10.2	205.55	28.38	Yang et al. [2023]
NGC 288	✓	9.0	13.19	-26.58	Grillmair [2025]
ω Cen (NGC 5139)	✓	5.4	201.67	-47.48	Ibata et al. [2019]
M68 (NGC 4590)	✓	10.4	189.87	-26.74	Palau and Miralda-Escudé [2019]
NGC 5466	✓	16.1	211.36	28.53	Belokurov et al. [2006]
					Grillmair and Dionatos [2006]

Table 6.1 Globular Cluster Tidal Tails. Table is supplemented by the Globular Cluster Database [Baumgardt et al., 2023].

is famous for extended its tidal tails, was disrupted due to an endemic population of stellar mass black holes, as shown in Figure 6.2. However this mechanism would change the resulting chemical properties of the stars in the cluster's tails. As discussed previously in Chapter 2, Section 2.6, clusters are often spatially segregated, with a higher proportion of second-population stars towards the center of a cluster. If black holes were ejecting stars from the cluster core, we would expect the tidal tails to contain enriched stars, while tidal stripping would preferentially strip away unenriched stars, as is the case in ESO 280-SC06. The two resulting enrichment patterns are demonstated in Figure 6.3. We could better understand the disruption mechanism by observing and chemically tagging these systems, not only in Palomar 5's tidal tails but in those of many globular clusters.

Unfortunately, very few tidal tails have been identified. Table 6.1 lists globular clusters with identified tails, which we could potentially observe using photometry or spectroscopy. Fortunately, Rubin Observatory will soon revolutionize the field of

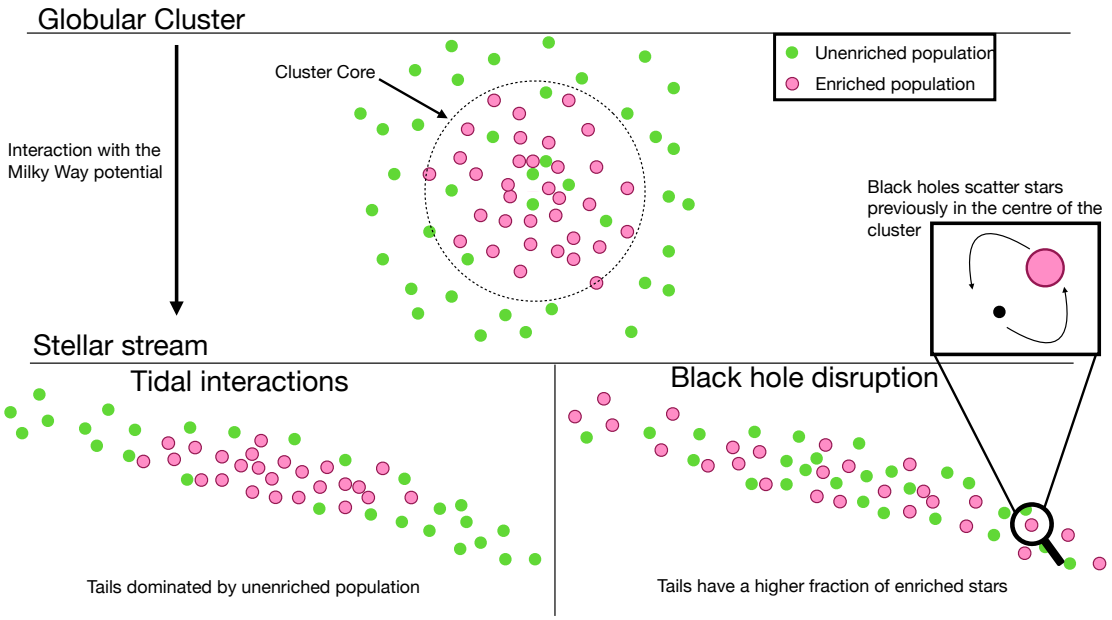

Figure 6.3 A visual representation of the location of enriched stars in a globular cluster stream disrupted via tidal dissipation (left) or black hole ejection (right).

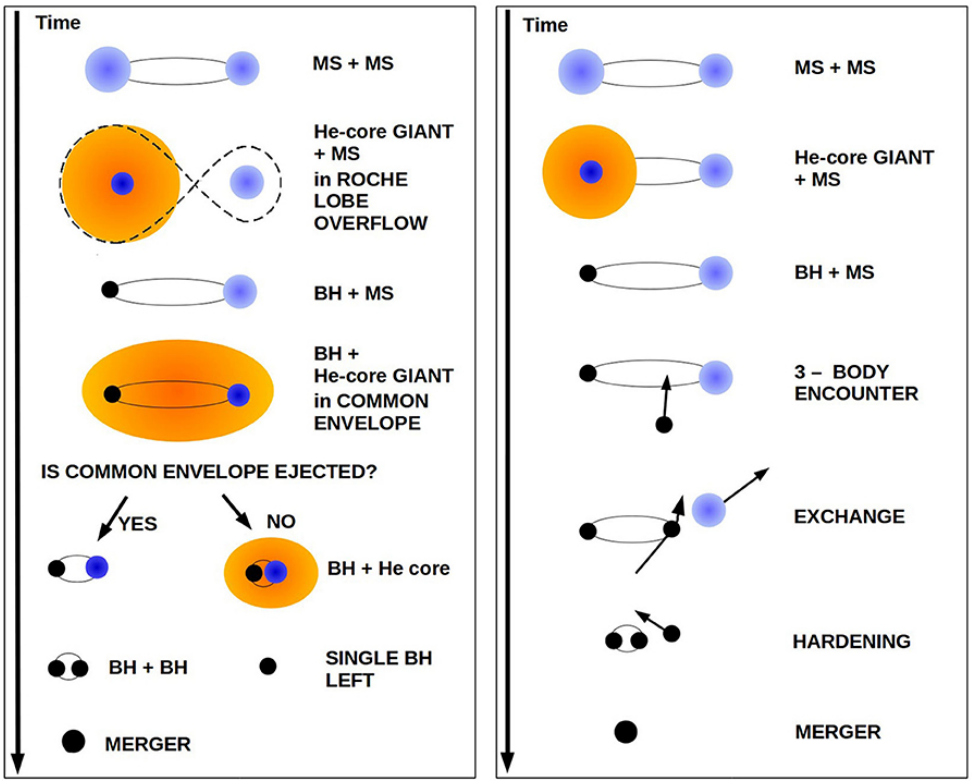

Figure 6.4 Potential formation mechanisms of binary black hole systems. Figure from Mapelli [2020].

astronomy. Rubin is predicted to observe 20 billion stars, which will lead to the discovery of many more tidal tails and fully disrupted stellar streams [Ivezić et al., 2019]. Indeed, machine learning algorithms are already being developed with the intent of identifying stellar streams in wide-field surveys [Gordon et al., 2024]. Rubin will allow us to further identify stellar streams and globular cluster tidal tails, and allow us to distinguish disruption via tidal stripping versus ejection by an endemic population of stellar-mas black holes.

Understanding black hole populations in globular clusters are of particular in-

terest, as they could provide a unique source of gravitational waves. The first gravitational wave directly identified, GW150914, was a landmark detection that revolutionized our understanding of gravity [Abbott et al., 2016]. Similarly, the first gravitational wave from a binary neutron star merger, GW170817, allowed us to further our understanding of the origin of heavy elements in the universe [Abbott et al., 2017]. Through advanced data analysis techniques, we can both identify [Usman et al., 2016] and constrain properties of [Usman et al., 2019] gravitational waves using LIGO. We may even be able to identify features of black hole binaries in these globular clusters, and to search for key characteristics of populations in these systems. Perhaps, for example, a black hole binary which has previously ejected stars from a globular cluster core would have a predictable eccentric orbit or precession, resulting in key characteristics that could indicate its environemental origin.

In addition to the observation of binary black hole gravitational waves, we could also probe the formation of binary black holes by identifying the environment containing mass-transfer stars. In Chapters 2, 3 and 4, we identify in each system a star enriched in *s*-process elements, indicating that it had experienced mass-transfer from a binary companion. Figure 6.4 demonstrates a few proposed formation channels for binary black hole systems.

It was once thought that a shared common envelope was the primary mechanism for binary black hole formation, though more recent studies suggest that binaries could evolve through mass-transfer stars, bypassing the common envelope phase entirely [Shariat et al., 2025]. In Chapter 4, we discuss the extremely high rate of mass-transfer stars we have identified in globular cluster stellar streams. By further

identifying these mass-transfer stars in new environments, we may be able to shed light on the formation mechanism of binary black holes. In my coming work, I aim to merge my two fields of expertise, combining chemical classifications of stars and gravitational-wave observations to further our understanding of these exotic systems in our universe.

I would be remiss if I failed to mention the challenges facing astrophysics research. While uncovering the origins of the universe will never be an easy endeavor, it is an unexpected turn of events to have the entire field of astrophysics be in jeopardy: at the time of writing this, proposed budgeting will decimate research in the United States. A recently proposed budget for the National Science Foundation intends to cut research funding by 56%, and the Astrophysics Division of the National Aeronautics and Space Administration will be cut by 44%. We are already seeing ripple effects from these proposals; universities are canceling searches for faculty positions in physics and astronomy, summer undergraduate research programs were downsized or canceled, and graduate programs across the country rescinded acceptances. Many telescopes or observatories may be downsized or canceled altogether, as shown in Figure 6.5. Combined, NSF and NASA comprise less than 1.4% of the United States federal budget, meaning any change to our scientific funding will have little to no effect on the country's expenses, but will have devastating consequences for the livelihoods of American scientists *and* for the age of scientific progress in America.

While some argue that privatized companies will fill in for any budgeting shortfall, astronomy and astrophysics is not and *never will be* a field which can be monetized: our research has rippling effects in terms of scientific advancement, but our

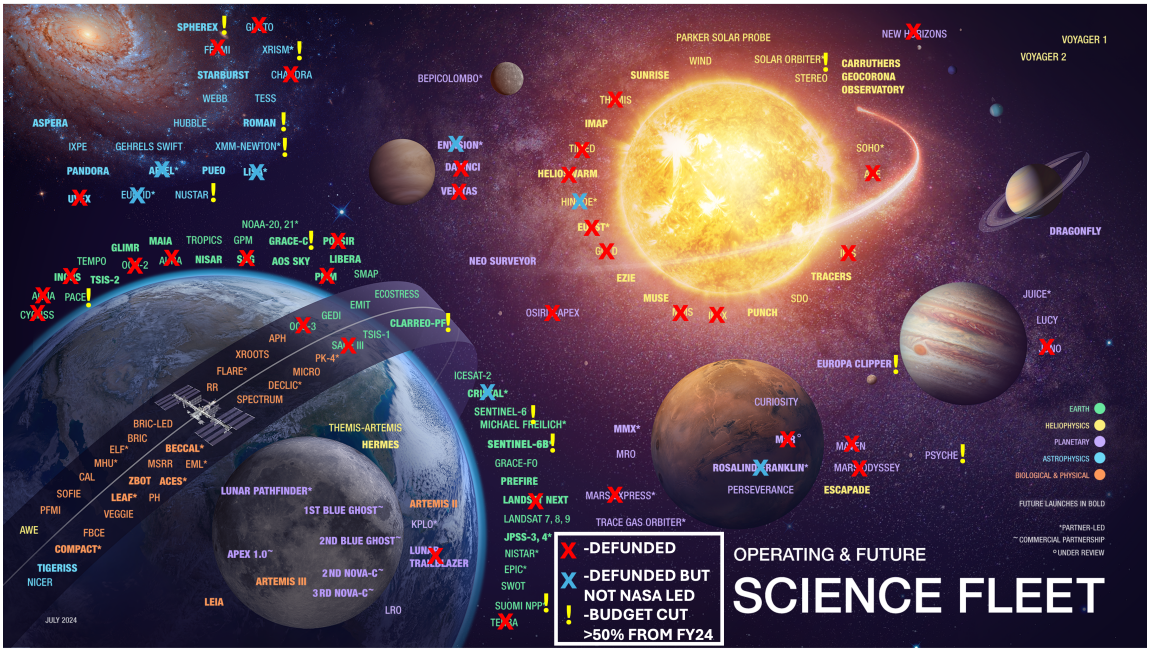

Figure 6.5 Representation of projects that will be reduced and or canceled due to proposed budget cuts. Red crosses represent programs that will be canceled. Blue crosses represent programs in which the NASA contribution will be canceled, but which are lead by another organization, e.g. the European Space Agency. The yellow exclamation point represent programs which will lose more than half of their funding relative to the previous year. Figure from Grayson [2025], adapted from NASA Goddard Space Flight Center.

understanding of the history of our galaxy and our universe is simply not profitable. Companies such as SpaceX or Blue Origin, for example, have made great strides in *space travel,* but will never explain how binary black holes form or why globular cluster have correlated abundance patterns. While our research is not profitable, it is *extraordinarily valuable.* Through funding science, we can understand the origins of nature and how the universe functions. More directly, we train the next generation of students and scientists to think logically, allowing them to carry these problem-solving skills to other aspects of their lives. We also develop technologies for astronomical research that can be then transferred in other aspects of day-to-day life. For example, a former colleague once researched the identification of gravitational-wave signals in noisy LIGO data, and later transferred those skills to developing touchscreens, as the processing techniques for identifying finger taps on a screen is computationally very similar to flagging gravitational-wave signals. Astronomy research may impact aspects of everyday life in unexpected ways.

Funding astronomy and astrophysics research will *never* be a waste. I imagine that most people who take the time to actually read an astrophysics PhD thesis agree with this sentiment. I urge any American who reads this section to call their representatives in Congress and urge them to increase funding for the sciences. Senators and congresspeople can be identified at this website:
https://www.congress.gov/members/find-your-member.

Through consistent funding of the sciences,
we can continue to further our understanding of the universe.

REFERENCES

B. P. Abbott, R. Abbott, T. D. Abbott, M. R. Abernathy, F. Acernese, K. Ackley, C. Adams, T. Adams, P. Addesso, R. X. Adhikari, V. B. Adya, C. Affeldt, M. Agathos, K. Agatsuma, N. Aggarwal, O. D. Aguiar, L. Aiello, A. Ain, P. Ajith, B. Allen, A. Allocca, P. A. Altin, S. B. Anderson, W. G. Anderson, K. Arai, M. A. Arain, M. C. Araya, C. C. Arceneaux, J. S. Areeda, N. Arnaud, K. G. Arun, S. Ascenzi, G. Ashton, M. Ast, S. M. Aston, P. Astone, P. Aufmuth, C. Aulbert, S. Babak, P. Bacon, M. K. M. Bader, P. T. Baker, F. Baldaccini, G. Ballardin, S. W. Ballmer, J. C. Barayoga, S. E. Barclay, B. C. Barish, D. Barker, F. Barone, B. Barr, L. Barsotti, M. Barsuglia, D. Barta, J. Bartlett, M. A. Barton, I. Bartos, R. Bassiri, A. Basti, J. C. Batch, C. Baune, V. Bavigadda, M. Bazzan, B. Behnke, M. Bejger, C. Belczynski, A. S. Bell, C. J. Bell, B. K. Berger, J. Bergman, G. Bergmann, C. P. L. Berry, D. Bersanetti, A. Bertolini, J. Betzwieser, S. Bhagwat, R. Bhandare, I. A. Bilenko, G. Billingsley, J. Birch, I. A. Birney, O. Birnholtz, S. Biscans, A. Bisht, M. Bitossi, C. Biwer, M. A. Bizouard, J. K. Blackburn, C. D. Blair, D. G. Blair, R. M. Blair, S. Bloemen, O. Bock, T. P. Bodiya, M. Boer, G. Bogaert, C. Bogan, A. Bohe, P. Bojtos, C. Bond, F. Bondu, R. Bonnand, B. A. Boom, R. Bork, V. Boschi, S. Bose, Y. Bouffanais, A. Bozzi, C. Bradaschia, P. R. Brady, V. B. Braginsky, M. Branchesi, J. E. Brau, T. Briant, A. Brillet, M. Brinkmann, V. Brisson, P. Brockill, A. F. Brooks, D. A. Brown, D. D. Brown, N. M. Brown, C. C. Buchanan, A. Buikema, T. Bulik, H. J. Bulten, A. Buonanno, D. Buskulic, C. Buy, R. L. Byer, M. Cabero, L. Cadonati, G. Cagnoli, C. Cahillane, J. Calderón Bustillo, T. Callister, E. Calloni, J. B. Camp, K. C. Cannon, J. Cao, C. D. Capano, E. Capocasa, F. Carbognani, S. Caride, J. Casanueva Diaz, C. Casentini, S. Caudill, M. Cavaglià, F. Cavalier, R. Cavalieri, G. Cella, C. B. Cepeda, L. Cerboni Baiardi, G. Cerretani, E. Cesarini, R. Chakraborty, T. Chalermsongsak, S. J. Chamberlin, M. Chan, S. Chao, P. Charlton, E. Chassande-Mottin, H. Y. Chen, Y. Chen, C. Cheng, A. Chincarini, A. Chiummo, H. S. Cho, M. Cho, J. H. Chow, N. Christensen, Q. Chu, S. Chua, S. Chung, G. Ciani, F. Clara, J. A. Clark, F. Cleva, E. Coccia, P. F. Cohadon, A. Colla, C. G. Collette, L. Cominsky, M. Constancio, A. Conte, L. Conti, D. Cook, T. R. Corbitt, N. Cornish, A. Corsi, S. Cortese, C. A. Costa, M. W. Coughlin, S. B. Coughlin, J. P. Coulon, S. T. Countryman, P. Couvares, E. E. Cowan, D. M. Coward, M. J. Cowart, D. C. Coyne, R. Coyne, K. Craig, J. D. E. Creighton, T. D. Creighton, J. Cripe, S. G. Crowder, A. M. Cruise, A. Cumming, L. Cunningham, E. Cuoco, T. Dal Canton, S. L. Danilishin, S. D'Antonio, K. Danzmann, N. S. Darman, C. F. Da Silva Costa, V. Dattilo, I. Dave, H. P. Daveloza, M. Davier, G. S. Davies, E. J. Daw, R. Day, S. De, D. DeBra, G. Debreczeni, J. Degallaix, M. De Laurentis,

S. Deléglise, W. Del Pozzo, T. Denker, T. Dent, H. Dereli, V. Dergachev, R. T. DeRosa, R. De Rosa, R. DeSalvo, S. Dhurandhar, M. C. Díaz, L. Di Fiore, M. Di Giovanni, A. Di Lieto, S. Di Pace, I. Di Palma, A. Di Virgilio, G. Dojcinoski, V. Dolique, F. Donovan, K. L. Dooley, S. Doravari, R. Douglas, T. P. Downes, M. Drago, R. W. P. Drever, J. C. Driggers, Z. Du, M. Ducrot, S. E. Dwyer, T. B. Edo, M. C. Edwards, A. Effler, H. B. Eggenstein, P. Ehrens, J. Eichholz, S. S. Eikenberry, W. Engels, R. C. Essick, T. Etzel, M. Evans, T. M. Evans, R. Everett, M. Factourovich, V. Fafone, H. Fair, S. Fairhurst, X. Fan, Q. Fang, S. Farinon, B. Farr, W. M. Farr, M. Favata, M. Fays, H. Fehrmann, M. M. Fejer, D. Feldbaum, I. Ferrante, E. C. Ferreira, F. Ferrini, F. Fidecaro, L. S. Finn, I. Fiori, D. Fiorucci, R. P. Fisher, R. Flaminio, M. Fletcher, H. Fong, J. D. Fournier, S. Franco, S. Frasca, F. Frasconi, M. Frede, Z. Frei, A. Freise, R. Frey, V. Frey, T. T. Fricke, P. Fritschel, V. V. Frolov, P. Fulda, M. Fyffe, H. A. G. Gabbard, J. R. Gair, L. Gammaitoni, S. G. Gaonkar, F. Garufi, A. Gatto, G. Gaur, N. Gehrels, G. Gemme, B. Gendre, E. Genin, A. Gennai, J. George, L. Gergely, V. Germain, Abhirup Ghosh, Archisman Ghosh, S. Ghosh, J. A. Giaime, K. D. Giardina, A. Giazotto, K. Gill, A. Glaefke, J. R. Gleason, E. Goetz, R. Goetz, L. Gondan, G. González, J. M. Gonzalez Castro, A. Gopakumar, N. A. Gordon, M. L. Gorodetsky, S. E. Gossan, M. Gosselin, R. Gouaty, C. Graef, P. B. Graff, M. Granata, A. Grant, S. Gras, C. Gray, G. Greco, A. C. Green, R. J. S. Greenhalgh, P. Groot, H. Grote, S. Grunewald, G. M. Guidi, X. Guo, A. Gupta, M. K. Gupta, K. E. Gushwa, E. K. Gustafson, R. Gustafson, J. J. Hacker, B. R. Hall, E. D. Hall, G. Hammond, M. Haney, M. M. Hanke, J. Hanks, C. Hanna, M. D. Hannam, J. Hanson, T. Hardwick, J. Harms, G. M. Harry, I. W. Harry, M. J. Hart, M. T. Hartman, C. J. Haster, K. Haughian, J. Healy, J. Heefner, A. Heidmann, M. C. Heintze, G. Heinzel, H. Heitmann, P. Hello, G. Hemming, M. Hendry, I. S. Heng, J. Hennig, A. W. Heptonstall, M. Heurs, S. Hild, D. Hoak, K. A. Hodge, D. Hofman, S. E. Hollitt, K. Holt, D. E. Holz, P. Hopkins, D. J. Hosken, J. Hough, E. A. Houston, E. J. Howell, Y. M. Hu, S. Huang, E. A. Huerta, D. Huet, B. Hughey, S. Husa, S. H. Huttner, T. Huynh-Dinh, A. Idrisy, N. Indik, D. R. Ingram, R. Inta, H. N. Isa, J. M. Isac, M. Isi, G. Islas, T. Isogai, B. R. Iyer, K. Izumi, M. B. Jacobson, T. Jacqmin, H. Jang, K. Jani, P. Jaranowski, S. Jawahar, F. Jiménez-Forteza, W. W. Johnson, N. K. Johnson-McDaniel, D. I. Jones, R. Jones, R. J. G. Jonker, L. Ju, K. Haris, C. V. Kalaghatgi, V. Kalogera, S. Kandhasamy, G. Kang, J. B. Kanner, S. Karki, M. Kasprzack, E. Katsavounidis, W. Katzman, S. Kaufer, T. Kaur, K. Kawabe, F. Kawazoe, F. Kéfélian, M. S. Kehl, D. Keitel, D. B. Kelley, W. Kells, R. Kennedy, D. G. Keppel, J. S. Key, A. Khalaidovski, F. Y. Khalili, I. Khan, S. Khan, Z. Khan, E. A. Khazanov, N. Kijbunchoo, C. Kim,

J. Kim, K. Kim, Nam-Gyu Kim, Namjun Kim, Y. M. Kim, E. J. King, P. J. King, D. L. Kinzel, J. S. Kissel, L. Kleybolte, S. Klimenko, S. M. Koehlenbeck, K. Kokeyama, S. Koley, V. Kondrashov, A. Kontos, S. Koranda, M. Korobko, W. Z. Korth, I. Kowalska, D. B. Kozak, V. Kringel, B. Krishnan, A. Królak, C. Krueger, G. Kuehn, P. Kumar, R. Kumar, L. Kuo, A. Kutynia, P. Kwee, B. D. Lackey, M. Landry, J. Lange, B. Lantz, P. D. Lasky, A. Lazzarini, C. Lazzaro, P. Leaci, S. Leavey, E. O. Lebigot, C. H. Lee, H. K. Lee, H. M. Lee, K. Lee, A. Lenon, M. Leonardi, J. R. Leong, N. Leroy, N. Letendre, Y. Levin, B. M. Levine, T. G. F. Li, A. Libson, T. B. Littenberg, N. A. Lockerbie, J. Logue, A. L. Lombardi, L. T. London, J. E. Lord, M. Lorenzini, V. Loriette, M. Lormand, G. Losurdo, J. D. Lough, C. O. Lousto, G. Lovelace, H. Lück, A. P. Lundgren, J. Luo, R. Lynch, Y. Ma, T. MacDonald, B. Machenschalk, M. MacInnis, D. M. Macleod, F. Magaña-Sandoval, R. M. Magee, M. Mageswaran, E. Majorana, I. Maksimovic, V. Malvezzi, N. Man, I. Mandel, V. Mandic, V. Mangano, G. L. Mansell, M. Manske, M. Mantovani, F. Marchesoni, F. Marion, S. Márka, Z. Márka, A. S. Markosyan, E. Maros, F. Martelli, L. Martellini, I. W. Martin, R. M. Martin, D. V. Martynov, J. N. Marx, K. Mason, A. Masserot, T. J. Massinger, M. Masso-Reid, F. Matichard, L. Matone, N. Mavalvala, N. Mazumder, G. Mazzolo, R. McCarthy, D. E. McClelland, S. McCormick, S. C. McGuire, G. McIntyre, J. McIver, D. J. McManus, S. T. McWilliams, D. Meacher, G. D. Meadors, J. Meidam, A. Melatos, G. Mendell, D. Mendoza-Gandara, R. A. Mercer, E. Merilh, M. Merzougui, S. Meshkov, C. Messenger, C. Messick, P. M. Meyers, F. Mezzani, H. Miao, C. Michel, H. Middleton, E. E. Mikhailov, L. Milano, J. Miller, M. Millhouse, Y. Minenkov, J. Ming, S. Mirshekari, C. Mishra, S. Mitra, V. P. Mitrofanov, G. Mitselmakher, R. Mittleman, A. Moggi, M. Mohan, S. R. P. Mohapatra, M. Montani, B. C. Moore, C. J. Moore, D. Moraru, G. Moreno, S. R. Morriss, K. Mossavi, B. Mours, C. M. Mow-Lowry, C. L. Mueller, G. Mueller, A. W. Muir, Arunava Mukherjee, D. Mukherjee, S. Mukherjee, N. Mukund, A. Mullavey, J. Munch, D. J. Murphy, P. G. Murray, A. Mytidis, I. Nardecchia, L. Naticchioni, R. K. Nayak, V. Necula, K. Nedkova, G. Nelemans, M. Neri, A. Neunzert, G. Newton, T. T. Nguyen, A. B. Nielsen, S. Nissanke, A. Nitz, F. Nocera, D. Nolting, M. E. N. Normandin, L. K. Nuttall, J. Oberling, E. Ochsner, J. O'Dell, E. Oelker, G. H. Ogin, J. J. Oh, S. H. Oh, F. Ohme, M. Oliver, P. Oppermann, Richard J. Oram, B. O'Reilly, R. O'Shaughnessy, C. D. Ott, D. J. Ottaway, R. S. Ottens, H. Overmier, B. J. Owen, A. Pai, S. A. Pai, J. R. Palamos, O. Palashov, C. Palomba, A. Pal-Singh, H. Pan, Y. Pan, C. Pankow, F. Pannarale, B. C. Pant, F. Paoletti, A. Paoli, M. A. Papa, H. R. Paris, W. Parker, D. Pascucci, A. Pasqualetti, R. Passaquieti, D. Passuello, B. Patricelli, Z. Patrick, B. L. Pearlstone, M. Pedraza, R. Pedurand,

L. Pekowsky, A. Pele, S. Penn, A. Perreca, H. P. Pfeiffer, M. Phelps, O. Piccinni, M. Pichot, M. Pickenpack, F. Piergiovanni, V. Pierro, G. Pillant, L. Pinard, I. M. Pinto, M. Pitkin, J. H. Poeld, R. Poggiani, P. Popolizio, A. Post, J. Powell, J. Prasad, V. Predoi, S. S. Premachandra, T. Prestegard, L. R. Price, M. Prijatelj, M. Principe, S. Privitera, R. Prix, G. A. Prodi, L. Prokhorov, O. Puncken, M. Punturo, P. Puppo, M. Pürrer, H. Qi, J. Qin, V. Quetschke, E. A. Quintero, R. Quitzow-James, F. J. Raab, D. S. Rabeling, H. Radkins, P. Raffai, S. Raja, M. Rakhmanov, C. R. Ramet, P. Rapagnani, V. Raymond, M. Razzano, V. Re, J. Read, C. M. Reed, T. Regimbau, L. Rei, S. Reid, D. H. Reitze, H. Rew, S. D. Reyes, F. Ricci, K. Riles, N. A. Robertson, R. Robie, F. Robinet, A. Rocchi, L. Rolland, J. G. Rollins, V. J. Roma, J. D. Romano, R. Romano, G. Romanov, J. H. Romie, D. Rosińska, S. Rowan, A. Rüdiger, P. Ruggi, K. Ryan, S. Sachdev, T. Sadecki, L. Sadeghian, L. Salconi, M. Saleem, F. Salemi, A. Samajdar, L. Sammut, L. M. Sampson, E. J. Sanchez, V. Sandberg, B. Sandeen, G. H. Sanders, J. R. Sanders, B. Sassolas, B. S. Sathyaprakash, P. R. Saulson, O. Sauter, R. L. Savage, A. Sawadsky, P. Schale, R. Schilling, J. Schmidt, P. Schmidt, R. Schnabel, R. M. S. Schofield, A. Schönbeck, E. Schreiber, D. Schuette, B. F. Schutz, J. Scott, S. M. Scott, D. Sellers, A. S. Sengupta, D. Sentenac, V. Sequino, A. Sergeev, G. Serna, Y. Setyawati, A. Sevigny, D. A. Shaddock, T. Shaffer, S. Shah, M. S. Shahriar, M. Shaltev, Z. Shao, B. Shapiro, P. Shawhan, A. Sheperd, D. H. Shoemaker, D. M. Shoemaker, K. Siellez, X. Siemens, D. Sigg, A. D. Silva, D. Simakov, A. Singer, L. P. Singer, A. Singh, R. Singh, A. Singhal, A. M. Sintes, B. J. J. Slagmolen, J. R. Smith, M. R. Smith, N. D. Smith, R. J. E. Smith, E. J. Son, B. Sorazu, F. Sorrentino, T. Souradeep, A. K. Srivastava, A. Staley, M. Steinke, J. Steinlechner, S. Steinlechner, D. Steinmeyer, B. C. Stephens, S. P. Stevenson, R. Stone, K. A. Strain, N. Straniero, G. Stratta, N. A. Strauss, S. Strigin, R. Sturani, A. L. Stuver, T. Z. Summerscales, L. Sun, P. J. Sutton, B. L. Swinkels, M. J. Szczepańczyk, M. Tacca, D. Talukder, D. B. Tanner, M. Tápai, S. P. Tarabrin, A. Taracchini, R. Taylor, T. Theeg, M. P. Thirugnanasambandam, E. G. Thomas, M. Thomas, P. Thomas, K. A. Thorne, K. S. Thorne, E. Thrane, S. Tiwari, V. Tiwari, K. V. Tokmakov, C. Tomlinson, M. Tonelli, C. V. Torres, C. I. Torrie, D. Töyrä, F. Travasso, G. Traylor, D. Trifirò, M. C. Tringali, L. Trozzo, M. Tse, M. Turconi, D. Tuyenbayev, D. Ugolini, C. S. Unnikrishnan, A. L. Urban, S. A. Usman, H. Vahlbruch, G. Vajente, G. Valdes, M. Vallisneri, N. van Bakel, M. van Beuzekom, J. F. J. van den Brand, C. Van Den Broeck, D. C. Vander-Hyde, L. van der Schaaf, J. V. van Heijningen, A. A. van Veggel, M. Vardaro, S. Vass, M. Vasúth, R. Vaulin, A. Vecchio, G. Vedovato, J. Veitch, P. J. Veitch, K. Venkateswara, D. Verkindt, F. Vetrano, A. Viceré, S. Vinciguerra, D. J. Vine,

J. Y. Vinet, S. Vitale, T. Vo, H. Vocca, C. Vorvick, D. Voss, W. D. Vousden, S. P. Vyatchanin, A. R. Wade, L. E. Wade, M. Wade, S. J. Waldman, M. Walker, L. Wallace, S. Walsh, G. Wang, H. Wang, M. Wang, X. Wang, Y. Wang, H. Ward, R. L. Ward, J. Warner, M. Was, B. Weaver, L. W. Wei, M. Weinert, A. J. Weinstein, R. Weiss, T. Welborn, L. Wen, P. Weßels, T. Westphal, K. Wette, J. T. Whelan, S. E. Whitcomb, D. J. White, B. F. Whiting, K. Wiesner, C. Wilkinson, P. A. Willems, L. Williams, R. D. Williams, A. R. Williamson, J. L. Willis, B. Willke, M. H. Wimmer, L. Winkelmann, W. Winkler, C. C. Wipf, A. G. Wiseman, H. Wittel, G. Woan, J. Worden, J. L. Wright, G. Wu, J. Yablon, I. Yakushin, W. Yam, H. Yamamoto, C. C. Yancey, M. J. Yap, H. Yu, M. Yvert, A. ZadroŻny, L. Zangrando, M. Zanolin, J. P. Zendri, M. Zevin, F. Zhang, L. Zhang, M. Zhang, Y. Zhang, C. Zhao, M. Zhou, Z. Zhou, X. J. Zhu, M. E. Zucker, S. E. Zuraw, J. Zweizig, LIGO Scientific Collaboration, and Virgo Collaboration. Observation of Gravitational Waves from a Binary Black Hole Merger. *Physical Review Letters*, 116(6):061102, February 2016. doi:10.1103/PhysRevLett.116.061102.

B. P. Abbott, R. Abbott, T. D. Abbott, F. Acernese, K. Ackley, C. Adams, T. Adams, P. Addesso, R. X. Adhikari, V. B. Adya, C. Affeldt, M. Afrough, B. Agarwal, M. Agathos, K. Agatsuma, N. Aggarwal, O. D. Aguiar, L. Aiello, A. Ain, P. Ajith, B. Allen, G. Allen, A. Allocca, P. A. Altin, A. Amato, A. Ananyeva, S. B. Anderson, W. G. Anderson, S. V. Angelova, S. Antier, S. Appert, K. Arai, M. C. Araya, J. S. Areeda, N. Arnaud, K. G. Arun, S. Ascenzi, G. Ashton, M. Ast, S. M. Aston, P. Astone, D. V. Atallah, P. Aufmuth, C. Aulbert, K. AultONeal, C. Austin, A. Avila-Alvarez, S. Babak, P. Bacon, M. K. M. Bader, S. Bae, M. Bailes, P. T. Baker, F. Baldaccini, G. Ballardin, S. W. Ballmer, S. Banagiri, J. C. Barayoga, S. E. Barclay, B. C. Barish, D. Barker, K. Barkett, F. Barone, B. Barr, L. Barsotti, M. Barsuglia, D. Barta, S. D. Barthelmy, J. Bartlett, I. Bartos, R. Bassiri, A. Basti, J. C. Batch, M. Bawaj, J. C. Bayley, M. Bazzan, B. Bécsy, C. Beer, M. Bejger, I. Belahcene, A. S. Bell, B. K. Berger, G. Bergmann, S. Bernuzzi, J. J. Bero, C. P. L. Berry, D. Bersanetti, A. Bertolini, J. Betzwieser, S. Bhagwat, R. Bhandare, I. A. Bilenko, G. Billingsley, C. R. Billman, J. Birch, R. Birney, O. Birnholtz, S. Biscans, S. Biscoveanu, A. Bisht, M. Bitossi, C. Biwer, M. A. Bizouard, J. K. Blackburn, J. Blackman, C. D. Blair, D. G. Blair, R. M. Blair, S. Bloemen, O. Bock, N. Bode, M. Boer, G. Bogaert, A. Bohe, F. Bondu, E. Bonilla, R. Bonnand, B. A. Boom, R. Bork, V. Boschi, S. Bose, K. Bossie, Y. Bouffanais, A. Bozzi, C. Bradaschia, P. R. Brady, M. Branchesi, J. E. Brau, T. Briant, A. Brillet, M. Brinkmann, V. Brisson, P. Brockill, J. E. Broida, A. F. Brooks, D. A. Brown, D. D. Brown, S. Brunett, C. C. Buchanan, A. Buikema, T. Bulik, H. J.

Bulten, A. Buonanno, D. Buskulic, C. Buy, R. L. Byer, M. Cabero, L. Cadonati, G. Cagnoli, C. Cahillane, J. Calderón Bustillo, T. A. Callister, E. Calloni, J. B. Camp, M. Canepa, P. Canizares, K. C. Cannon, H. Cao, J. Cao, C. D. Capano, E. Capocasa, F. Carbognani, S. Caride, M. F. Carney, G. Carullo, J. Casanueva Diaz, C. Casentini, S. Caudill, M. Cavaglià, F. Cavalier, R. Cavalieri, G. Cella, C. B. Cepeda, P. Cerdá-Durán, G. Cerretani, E. Cesarini, S. J. Chamberlin, M. Chan, S. Chao, P. Charlton, E. Chase, E. Chassande-Mottin, D. Chatterjee, K. Chatziioannou, B. D. Cheeseboro, H. Y. Chen, X. Chen, Y. Chen, H. P. Cheng, H. Chia, A. Chincarini, A. Chiummo, T. Chmiel, H. S. Cho, M. Cho, J. H. Chow, N. Christensen, Q. Chu, A. J. K. Chua, and S. Chua. GW170817: Observation of Gravitational Waves from a Binary Neutron Star Inspiral. *Physical Review Letters*, 119(16):161101, October 2017. doi:10.1103/PhysRevLett.119.161101.

Abdu Abohalima and Anna Frebel. JINAbase—A Database for Chemical Abundances of Metal-poor Stars. *Astrophysical Journal, Supplement*, 238(2):36, October 2018. doi:10.3847/1538-4365/aadfe9.

David S. Aguado, Vasily Belokurov, G. C. Myeong, N. Wyn Evans, Chiaki Kobayashi, Luca Sbordone, Julio Chanamé, Camila Navarrete, and Sergey E. Koposov. Elevated r-process Enrichment in Gaia Sausage and Sequoia. *Astrophysical Journal, Letters*, 908(1):L8, February 2021a. doi:10.3847/2041-8213/abdbb8.

David S. Aguado, G. C. Myeong, Vasily Belokurov, N. Wyn Evans, Sergey E. Koposov, Carlos Allende Prieto, Gustavo A. Lanfranchi, Francesca Matteucci, Matthew Shetrone, Luca Sbordone, Camila Navarrete, Jonay I. González Hernández, Julio Chanamé, Luis Peralta de Arriba, and Zhen Yuan. The S2 stream: the shreds of a primitive dwarf galaxy. *Monthly Notices of the Royal Astronomical Society*, 500(1):889–910, January 2021b. doi:10.1093/mnras/staa3250.

A. M. Amarsi, P. E. Nissen, M. Asplund, K. Lind, and P. S. Barklem. Carbon and oxygen in metal-poor halo stars. *Astronomy and Astrophysics*, 622:L4, February 2019a. doi:10.1051/0004-6361/201834480.

A. M. Amarsi, P. E. Nissen, and Á. Skúladóttir. Carbon, oxygen, and iron abundances in disk and halo stars. Implications of 3D non-LTE spectral line formation. *Astronomy and Astrophysics*, 630:A104, October 2019b. doi:10.1051/0004-6361/201936265.

A. M. Amarsi, N. Grevesse, J. Grumer, M. Asplund, P. S. Barklem, and R. Collet. The 3D non-LTE solar nitrogen abundance from atomic lines. *Astronomy and Astrophysics*, 636:A120, April 2020. doi:10.1051/0004-6361/202037890.

Wako Aoki, Timothy C. Beers, Norbert Christlieb, John E. Norris, Sean G. Ryan, and Stelios Tsangarides. Carbon-enhanced Metal-poor Stars. I. Chemical Compositions of 26 Stars. *Astrophysical Journal*, 655(1):492–521, January 2007. doi:10.1086/509817.

Martin Asplund, Nicolas Grevesse, A. Jacques Sauval, and Pat Scott. The Chemical Composition of the Sun. *Annual Review of Astronomy and Astrophysics*, 47(1): 481–522, September 2009. doi:10.1146/annurev.astro.46.060407.145222.

Kaia R. Atzberger, Sam A. Usman, Alexander P. Ji, Lara R. Cullinane, Denis Erkal, Terese T. Hansen, Geraint F. Lewis, Ting S. Li, Guilherme Limberg, Alice Luna, Sarah L. Martell, Madeleine McKenzie, Andrew B. Pace, and Daniel B. Zucker. Chemical Abundances in the Leiptr Stellar Stream: A Disrupted Ultra-faint Dwarf Galaxy? *The Open Journal of Astrophysics*, 8:68, June 2025. doi:10.33232/001c.139013.

P. Awad, M. Canducci, E. Balbinot, A. Viswanathan, H. C. Woudenberg, O. Koop, R. Peletier, P. Tiňo, E. Starkenburg, R. Smith, and K. Bunte. Swarming in stellar streams: Unveiling the structure of the Jhelum stream with ant colony-inspired computation. *Astronomy and Astrophysics*, 683:A14, March 2024. doi:10.1051/0004-6361/202347848.

Eduardo Balbinot, Ivan Cabrera-Ziri, and Carmela Lardo. Evidence for C and Mg variations in the GD-1 stellar stream. *Monthly Notices of the Royal Astronomical Society*, 515(4):5802–5812, October 2022. doi:10.1093/mnras/stac1953.

P. S. Barklem, N. Christlieb, T. C. Beers, V. Hill, M. S. Bessell, J. Holmberg, B. Marsteller, S. Rossi, F. J. Zickgraf, and D. Reimers. The Hamburg/ESO R-process enhanced star survey (HERES). II. Spectroscopic analysis of the survey sample. *Astronomy and Astrophysics*, 439(1):129–151, August 2005. doi:10.1051/0004-6361:20052967.

Nate Bastian and Carmela Lardo. Multiple Stellar Populations in Globular Clusters. *Annual Review of Astronomy and Astrophysics*, 56:83–136, September 2018. doi:10.1146/annurev-astro-081817-051839.

H. Baumgardt and M. Hilker. A catalogue of masses, structural parameters, and velocity dispersion profiles of 112 Milky Way globular clusters. *Monthly Notices of the Royal Astronomical Society*, 478(2):1520–1557, August 2018. doi:10.1093/mnras/sty1057.

H. Baumgardt and E. Vasiliev. Accurate distances to Galactic globular clusters through a combination of Gaia EDR3, HST, and literature data. *Monthly Notices of the Royal Astronomical Society*, 505(4):5957–5977, August 2021. doi:10.1093/mnras/stab1474.

H. Baumgardt, M. Hilker, A. Sollima, and A. Bellini. Mean proper motions, space orbits, and velocity dispersion profiles of Galactic globular clusters derived from Gaia DR2 data. *Monthly Notices of the Royal Astronomical Society*, 482(4):5138–5155, February 2019. doi:10.1093/mnras/sty2997.

H. Baumgardt, A. Sollima, and M. Hilker. Absolute V-band magnitudes and mass-to-light ratios of Galactic globular clusters. *Publications of the Astron. Soc. of Australia*, 37:e046, November 2020. doi:10.1017/pasa.2020.38.

Holger Baumgardt and Junichiro Makino. Dynamical evolution of star clusters in tidal fields. *Monthly Notices of the Royal Astronomical Society*, 340(1):227–246, March 2003. doi:10.1046/j.1365-8711.2003.06286.x.

Holger Baumgardt, Antonio Sollima, Michael Hilker, Andrea Bellini, Eugene Vasiliev, Vincent Henault-Brunet, and Nolan Dickson. Globular cluster database, v4, 3 2023.

Timothy C. Beers and Norbert Christlieb. The Discovery and Analysis of Very Metal-Poor Stars in the Galaxy. *Annual Review of Astronomy and Astrophysics*, 43(1): 531–580, September 2005. doi:10.1146/annurev.astro.42.053102.134057.

R. A. Bell and R. J. Dickens. Chemical abundances in the globular clusters M 3, M 13, and NGC 6752. *Astrophysical Journal*, 242:657–672, December 1980. doi:10.1086/158502.

V. Belokurov, D. B. Zucker, N. W. Evans, G. Gilmore, S. Vidrih, D. M. Bramich, H. J. Newberg, R. F. G. Wyse, M. J. Irwin, M. Fellhauer, P. C. Hewett, N. A. Walton, M. I. Wilkinson, N. Cole, B. Yanny, C. M. Rockosi, T. C. Beers, E. F. Bell, J. Brinkmann, Ž. Ivezić, and R. Lupton. The Field of Streams: Sagittarius and Its Siblings. *Astrophysical Journal, Letters*, 642(2):L137–L140, May 2006. doi:10.1086/504797.

V. Belokurov, N. W. Evans, M. J. Irwin, D. Lynden-Bell, B. Yanny, S. Vidrih, G. Gilmore, G. Seabroke, D. B. Zucker, M. I. Wilkinson, P. C. Hewett, D. M. Bramich, M. Fellhauer, H. J. Newberg, R. F. G. Wyse, T. C. Beers, E. F. Bell, J. C. Barentine, J. Brinkmann, N. Cole, K. Pan, and D. G. York. An Orphan

in the "Field of Streams". *Astrophysical Journal*, 658(1):337–344, March 2007. doi:10.1086/511302.

V. Belokurov, D. Erkal, N. W. Evans, S. E. Koposov, and A. J. Deason. Co-formation of the disc and the stellar halo. *Monthly Notices of the Royal Astronomical Society*, 478(1):611–619, July 2018. doi:10.1093/mnras/sty982.

Vasily Belokurov and Andrey Kravtsov. Nitrogen enrichment and clustered star formation at the dawn of the Galaxy. *Monthly Notices of the Royal Astronomical Society*, 525(3):4456–4473, November 2023. doi:10.1093/mnras/stad2241.

M. Bergemann and T. Gehren. NLTE abundances of Mn in a sample of metal-poor stars. *Astronomy and Astrophysics*, 492(3):823–831, December 2008. doi:10.1051/0004-6361:200810098.

M. Bergemann, C. J. Hansen, M. Bautista, and G. Ruchti. NLTE analysis of Sr lines in spectra of late-type stars with new R-matrix atomic data. *Astronomy and Astrophysics*, 546:A90, October 2012a. doi:10.1051/0004-6361/201219406.

Maria Bergemann. Ionization balance of Ti in the photospheres of the Sun and four late-type stars. *Monthly Notices of the Royal Astronomical Society*, 413(3):2184–2198, May 2011. doi:10.1111/j.1365-2966.2011.18295.x.

Maria Bergemann, Rolf-Peter Kudritzki, Bertrand Plez, Ben Davies, Karin Lind, and Zach Gazak. Red Supergiant Stars as Cosmic Abundance Probes: NLTE Effects in J-band Iron and Titanium Lines. *Astrophysical Journal*, 751(2):156, June 2012b. doi:10.1088/0004-637X/751/2/156.

Maria Bergemann, K. Lind, R. Collet, Z. Magic, and M. Asplund. Non-LTE line formation of Fe in late-type stars - I. Standard stars with 1D and <3D> model atmospheres. *Monthly Notices of the Royal Astronomical Society*, 427(1):27–49, November 2012c. doi:10.1111/j.1365-2966.2012.21687.x.

Maria Bergemann, Remo Collet, Anish M. Amarsi, Mikhail Kovalev, Greg Ruchti, and Zazralt Magic. Non-local Thermodynamic Equilibrium Stellar Spectroscopy with 1D and <3D> Models. I. Methods and Application to Magnesium Abundances in Standard Stars. *Astrophysical Journal*, 847(1):15, September 2017. doi:10.3847/1538-4357/aa88cb.

Maria Bergemann, Andrew J. Gallagher, Philipp Eitner, Manuel Bautista, Remo Collet, Svetlana A. Yakovleva, Anja Mayriedl, Bertrand Plez, Mats Carlsson, Jorrit

Leenaarts, Andrey K. Belyaev, and Camilla Hansen. Observational constraints on the origin of the elements. I. 3D NLTE formation of Mn lines in late-type stars. *Astronomy and Astrophysics*, 631:A80, November 2019. doi:10.1051/0004-6361/201935811.

Rebecca Bernstein, Stephen A. Shectman, Steven M. Gunnels, Stefan Mochnacki, and Alex E. Athey. MIKE: A Double Echelle Spectrograph for the Magellan Telescopes at Las Campanas Observatory. In Masanori Iye and Alan F. M. Moorwood, editors, *Instrument Design and Performance for Optical/Infrared Ground-based Telescopes*, volume 4841 of *Society of Photo-Optical Instrumentation Engineers (SPIE) Conference Series*, pages 1694–1704, March 2003. doi:10.1117/12.461502.

E. Bica, C. Bonatto, B. Barbuy, and S. Ortolani. Globular cluster system and Milky Way properties revisited. *Astronomy and Astrophysics*, 450(1):105–115, April 2006. doi:10.1051/0004-6361:20054351.

Joss Bland-Hawthorn, Mark R. Krumholz, and Ken Freeman. The Long-term Evolution of the Galactic Disk Traced by Dissolving Star Clusters. *Astrophysical Journal*, 713(1):166–179, April 2010. doi:10.1088/0004-637X/713/1/166.

Ana Bonaca and Adrian M. Price-Whelan. Stellar streams in the Gaia era. *New Astronomy Review*, 100:101713, June 2025. doi:10.1016/j.newar.2024.101713.

Ana Bonaca, David W. Hogg, Adrian M. Price-Whelan, and Charlie Conroy. The Spur and the Gap in GD-1: Dynamical Evidence for a Dark Substructure in the Milky Way Halo. *Astrophysical Journal*, 880(1):38, July 2019. doi:10.3847/1538-4357/ab2873.

Ana Bonaca, Rohan P. Naidu, Charlie Conroy, Nelson Caldwell, Phillip A. Cargile, Jiwon Jesse Han, Benjamin D. Johnson, J. M. Diederik Kruijssen, G. C. Myeong, Joshua S. Speagle, Yuan-Sen Ting, and Dennis Zaritsky. Orbital Clustering Identifies the Origins of Galactic Stellar Streams. *Astrophysical Journal, Letters*, 909 (2):L26, March 2021. doi:10.3847/2041-8213/abeaa9.

C. Bonatto and E. Bica. Structural parameters of 11 faint Galactic globular clusters derived with 2MASS. *Astronomy and Astrophysics*, 479(3):741–750, March 2008. doi:10.1051/0004-6361:20078687.

Kaley Brauer, Alexander P. Ji, Anna Frebel, Gregory A. Dooley, Facundo A. Gómez, and Brian W. O'Shea. The Origin of r-process Enhanced Metal-poor Halo Stars

In Now-destroyed Ultra-faint Dwarf Galaxies. *Astrophysical Journal*, 871(2):247, February 2019. doi:10.3847/1538-4357/aafafb.

Kaley Brauer, Hillary Diane Andales, Alexander P. Ji, Anna Frebel, Mohammad K. Mardini, Facundo A. Gómez, and Brian W. O'Shea. Possibilities and Limitations of Kinematically Identifying Stars from Accreted Ultra-faint Dwarf Galaxies. *Astrophysical Journal*, 937(1):14, September 2022. doi:10.3847/1538-4357/ac85b9.

James S. Bullock and Michael Boylan-Kolchin. Small-Scale Challenges to the ΛCDM Paradigm. *Annual Review of Astronomy and Astrophysics*, 55(1):343–387, August 2017. doi:10.1146/annurev-astro-091916-055313.

James S. Bullock and Kathryn V. Johnston. Tracing Galaxy Formation with Stellar Halos. I. Methods. *Astrophysical Journal*, 635(2):931–949, December 2005. doi:10.1086/497422.

Jonathan Cabrera Garcia, Charli M. Sakari, Ian U. Roederer, Donavon W. Evans, Pedro Silva, Mario Mateo, Ying-Yi Song, Anthony Kremin, John I. Bailey, and Matthew G. Walker. Abundances of Neutron-capture Elements in 62 Stars in the Globular Cluster Messier 15. *Astrophysical Journal*, 967(2):101, June 2024. doi:10.3847/1538-4357/ad380b.

Thomas M. Callingham, Marius Cautun, Alis J. Deason, Carlos S. Frenk, Robert J. J. Grand, and Federico Marinacci. The chemo-dynamical groups of Galactic globular clusters. *Monthly Notices of the Royal Astronomical Society*, 513(3):4107–4129, July 2022. doi:10.1093/mnras/stac1145.

R. G. Carlberg. Star Stream Folding by Dark Galactic Subhalos. *Astrophysical Journal, Letters*, 705(2):L223–L226, November 2009. doi:10.1088/0004-637X/705/2/L223.

Raymond G. Carlberg. Globular Clusters in a Cosmological N-body Simulation. *Astrophysical Journal*, 861(1):69, July 2018. doi:10.3847/1538-4357/aac88a.

Raymond G. Carlberg. The Density Structure of Simulated Stellar Streams. *Astrophysical Journal*, 889(2):107, February 2020. doi:10.3847/1538-4357/ab61f0.

Raymond G. Carlberg and Hayley Agler. Subhalo Spreading of Thin Tidal Star Streams. *Astrophysical Journal*, 953(1):99, August 2023. doi:10.3847/1538-4357/ace4be.

E. Carretta, A. Bragaglia, R. Gratton, and S. Lucatello. Na-O anticorrelation and HB. VIII. Proton-capture elements and metallicities in 17 globular clusters from UVES spectra. *Astronomy and Astrophysics*, 505(1):139–155, October 2009a. doi:10.1051/0004-6361/200912097.

E. Carretta, A. Bragaglia, R. G. Gratton, S. Lucatello, G. Catanzaro, F. Leone, M. Bellazzini, R. Claudi, V. D'Orazi, Y. Momany, S. Ortolani, E. Pancino, G. Piotto, A. Recio-Blanco, and E. Sabbi. Na-O anticorrelation and HB. VII. The chemical composition of first and second-generation stars in 15 globular clusters from GIRAFFE spectra. *Astronomy and Astrophysics*, 505(1):117–138, October 2009b. doi:10.1051/0004-6361/200912096.

Eugenio Carretta. Abundances in Red Giant Stars of NGC 2808 and Correlations between Chemical Anomalies and Global Parameters in Globular Clusters. *Astronomical Journal*, 131(3):1766–1783, March 2006. doi:10.1086/499565.

Andreia Carrillo, Keith Hawkins, Paula Jofré, Danielle de Brito Silva, Payel Das, and Madeline Lucey. The detailed chemical abundance patterns of accreted halo stars from the optical to infrared. *Monthly Notices of the Royal Astronomical Society*, 513(2):1557–1580, June 2022. doi:10.1093/mnras/stac518.

L. Casagrande and Don A. VandenBerg. On the use of Gaia magnitudes and new tables of bolometric corrections. *Monthly Notices of the Royal Astronomical Society*, 479(1):L102–L107, September 2018. doi:10.1093/mnrasl/sly104.

Andrew R. Casey. *A Tale of Tidal Tales in the Milky Way*. PhD thesis, Australian National University, Canberra, May 2014.

Andrew R. Casey and Kevin C. Schlaufman. The Universality of the Rapid Neutron-capture Process Revealed by a Possible Disrupted Dwarf Galaxy Star. *Astrophysical Journal*, 850(2):179, December 2017. doi:10.3847/1538-4357/aa9079.

Andrew R. Casey, Gary Da Costa, Stefan C. Keller, and Elizabeth Maunder. Hunting the Parent of the Orphan Stream: Identifying Stream Members from Low-resolution Spectroscopy. *Astrophysical Journal*, 764(1):39, February 2013. doi:10.1088/0004-637X/764/1/39.

Andrew R. Casey, Alexander P. Ji, Terese T. Hansen, Ting S. Li, Sergey E. Koposov, Gary S. Da Costa, Joss Bland-Hawthorn, Lara Cullinane, Denis Erkal, Geraint F. Lewis, Kyler Kuehn, Dougal Mackey, Sarah L. Martell, Andrew B. Pace, Jeffrey D. Simpson, and Daniel B. Zucker. Signature of a Massive Rotating Metal-poor

Star Imprinted in the Phoenix Stellar Stream. *Astrophysical Journal*, 921(1):67, November 2021. doi:10.3847/1538-4357/ac1346.

Andrew R Casey, Alex Ji, and Erika Holmbeck. smhr: Automatic curve-of-growth analyses of high-resolution stellar spectra, 2 2025.

F. Castelli and R. L. Kurucz. New Grids of ATLAS9 Model Atmospheres. In N. Piskunov, W. W. Weiss, and D. F. Gray, editors, *Modelling of Stellar Atmospheres*, volume 210, page A20, January 2003. doi:10.48550/arXiv.astro-ph/0405087.

Vedant Chandra, Charlie Conroy, Nelson Caldwell, Ana Bonaca, Rohan P. Naidu, Dennis Zaritsky, Phillip A. Cargile, Jiwon Jesse Han, Benjamin D. Johnson, Joshua S. Speagle, Yuan-Sen Ting, and Turner Woody. A Ghost in Boötes: The Least-Luminous Disrupted Dwarf Galaxy. *Astrophysical Journal*, 940(2):127, December 2022. doi:10.3847/1538-4357/ac9b4b.

Anirudh Chiti, Anna Frebel, Alexander P. Ji, Helmut Jerjen, Dongwon Kim, and John E. Norris. Chemical Abundances of New Member Stars in the Tucana II Dwarf Galaxy. *Astrophysical Journal*, 857(1):74, April 2018. doi:10.3847/1538-4357/aab4fc.

Anirudh Chiti, Anna Frebel, Alexander P. Ji, Mohammad K. Mardini, Xiaowei Ou, Joshua D. Simon, Helmut Jerjen, Dongwon Kim, and John E. Norris. Detailed Chemical Abundances of Stars in the Outskirts of the Tucana II Ultrafaint Dwarf Galaxy. *Astronomical Journal*, 165(2):55, February 2023. doi:10.3847/1538-3881/aca416.

Jieun Choi, Aaron Dotter, Charlie Conroy, Matteo Cantiello, Bill Paxton, and Benjamin D. Johnson. Mesa Isochrones and Stellar Tracks (MIST). I. Solar-scaled Models. *Astrophysical Journal*, 823(2):102, June 2016. doi:10.3847/0004-637X/823/2/102.

Nick Choksi, Oleg Y. Gnedin, and Hui Li. Formation of globular cluster systems: from dwarf galaxies to giants. *Monthly Notices of the Royal Astronomical Society*, 480(2):2343–2356, October 2018. doi:10.1093/mnras/sty1952.

Judith G. Cohen. No Heavy-element Dispersion in the Globular Cluster M92. *Astrophysical Journal, Letters*, 740(2):L38, October 2011. doi:10.1088/2041-8205/740/2/L38.

Judith G. Cohen and Wenjin Huang. The Chemical Evolution of the Draco Dwarf Spheroidal Galaxy. *Astrophysical Journal*, 701(2):1053–1075, August 2009. doi:10.1088/0004-637X/701/2/1053.

Judith G. Cohen and Wenjin Huang. The Chemical Evolution of the Ursa Minor Dwarf Spheroidal Galaxy. *Astrophysical Journal*, 719(1):931–949, August 2010. doi:10.1088/0004-637X/719/1/931.

Judith G. Cohen and Evan N. Kirby. The Bizarre Chemical Inventory of NGC 2419, An Extreme Outer Halo Globular Cluster. *Astrophysical Journal*, 760(1):86, November 2012. doi:10.1088/0004-637X/760/1/86.

Judith G. Cohen, Michael M. Briley, and Peter B. Stetson. C and N Abundances in Stars at the Base of the Red Giant Branch in M15. *Astronomical Journal*, 130(3): 1177–1193, September 2005. doi:10.1086/431974.

Judith G. Cohen, Norbert Christlieb, Ian Thompson, Andrew McWilliam, Stephen Shectman, Dieter Reimers, Lutz Wisotzki, and Evan Kirby. Normal and Outlying Populations of the Milky Way Stellar Halo at [Fe/H] <-2. *Astrophysical Journal*, 778(1):56, November 2013. doi:10.1088/0004-637X/778/1/56.

E. Colavitti, A. Pipino, and F. Matteucci. Cosmological formation and chemical evolution of an elliptical galaxy. *Astronomy and Astrophysics*, 499(2):409–415, May 2009. doi:10.1051/0004-6361/200811379.

Gaia Collaboration, Babusiaux C., van Leeuwen F., Barstow M. A., Jordi C., Vallenari A., Bossini D., Bressan A., Cantat-Gaudin T., van Leeuwen M., Brown A. G. A., Prusti T., de Bruijne J. H. J., Bailer-Jones C. A. L., Biermann M., Evans D. W., Eyer L., Jansen F., Klioner S. A., Lammers U., Lindegren L., Luri X., Mignard F., Panem C., Pourbaix D., Randich S., Sartoretti P., Siddiqui H. I., Soubiran C., Walton N. A., Arenou F., Bastian U., Cropper M., Drimmel R., Katz D., Lattanzi M. G., Bakker J., Cacciari C., Castañeda J., Chaoul L., Cheek N., De Angeli F., Fabricius C., Guerra R., Holl B., Masana E., Messineo R., Mowlavi N., Nienartowicz K., Panuzzo P., Portell J., Riello M., Seabroke G. M., Tanga P., Thévenin F., Gracia-Abril G., Comoretto G., Garcia-Reinaldos M., Teyssier D., Altmann M., Andrae R., Audard M., Bellas-Velidis I., Benson K., Berthier J., Blomme R., Burgess P., Busso G., Carry B., Cellino A., Clementini G., Clotet M., Creevey O., Davidson M., De Ridder J., Delchambre L., Dell{́}Oro A., Ducourant C., Fernández-Hernández J., Fouesneau M., Frémat Y., Galluccio L., Garc{́ı}a-Torres M., González-Núñez J., González-Vidal J. J., Gosset E., Guy L. P., Halbwachs

J.-L., Hambly N. C., Harrison D. L., Hernández J., Hestroffer D., Hodgkin S. T., Hutton A., Jasniewicz G., Jean-Antoine-Piccolo A., Jordan S., Korn A. J., Krone-Martins A., Lanzafame A. C., Lebzelter T., Löffler W., Manteiga M., Marrese P. M., Mart{ı}n-Fleitas J. M., Moitinho A., Mora A., Muinonen K., Osinde J., Pancino E., Pauwels T., Petit J.-M., Recio-Blanco A., Richards P. J., Rimoldini L., Robin A. C., Sarro L. M., Siopis C., Smith M., Sozzetti A., Süveges M., Torra J., van Reeven W., Abbas U., Abreu Aramburu A., Accart S., Aerts C., Altavilla G., Álvarez M. A., Alvarez R., Alves J., Anderson R. I., Andrei A. H., Anglada Varela E., Antiche E., Antoja T., Arcay B., Astraatmadja T. L., Bach N., Baker S. G., Balaguer-Núñez L., Balm P., Barache C., Barata C., Barbato D., Barblan F., Barklem P. S., Barrado D., Barros M., Bartholomé Muñoz L., Bassilana J.-L., Becciani U., Bellazzini M., Berihuete A., Bertone S., Bianchi L., Bienaymé O., Blanco-Cuaresma S., Boch T., Boeche C., Bombrun A., Borrachero R., Bouquillon S., Bourda G., Bragaglia A., Bramante L., Breddels M. A., Brouillet N., Brüsemeister T., Brugaletta E., Bucciarelli B., Burlacu A., Busonero D., Butkevich A. G., Buzzi R., Caffau E., Cancelliere R., Cannizzaro G., Carballo R., Carlucci T., Carrasco J. M., Casamiquela L., Castellani M., Castro-Ginard A., Charlot P., Chemin L., Chiavassa A., Cocozza G., Costigan G., Cowell S., Crifo F., Crosta M., Crowley C., Cuypers J., Dafonte C., Damerdji Y., Dapergolas A., David P., David M., de Laverny P., De Luise F., De March R., de Martino D., de Souza R., de Torres A., Debosscher J., del Pozo E., Delbo M., Delgado A., Delgado H. E., Diakite S., Diener C., Distefano E., Dolding C., Drazinos P., Durán J., Edvardsson B., Enke H., Eriksson K., Esquej P., Eynard Bontemps G., Fabre C., Fabrizio M., Faigler S., Falcão A. J., Farràs Casas M., Federici L., Fedorets G., Fernique P., Figueras F., Filippi F., Findeisen K., Fonti A., Fraile E., Fraser M., Frézouls B., Gai M., Galleti S., Garabato D., Garc{ı}a-Sedano F., Garofalo A., Garralda N., Gavel A., Gavras P., Gerssen J., Geyer R., Giacobbe P., Gilmore G., Girona S., Giuffrida G., Glass F., Gomes M., Granvik M., Gueguen A., Guerrier A., Guiraud J., Gutié R., Haigron R., Hatzidimitriou D., Hauser M., Haywood M., Heiter U., Helmi A., Heu J., Hilger T., Hobbs D., Hofmann W., Holland G., Huckle H. E., Hypki A., Icardi V., Janß{}en K., Jevardat de Fombelle G., Jonker P. G., Juhász Á. L., Julbe F., Karampelas A., Kewley A., Klar J., Kochoska A., Kohley R., Kolenberg K., Kontizas M., Kontizas E., Koposov S. E., Kordopatis G., Kostrzewa-Rutkowska Z., Koubsky P., Lambert S., Lanza A. F., Lasne Y., Lavigne J.-B., Le Fustec Y., Le Poncin-Lafitte C., Lebreton Y., Leccia S., Leclerc N., Lecoeur-Taibi I., Lenhardt H., Leroux F., Liao S., Licata E., Lindstrø{}m H. E. P., Lister T. A., Livanou E., Lobel A., López M., Managau S., Mann R. G., Mantelet G., Marchal O., Marchant J. M., Marconi M., Marinoni S., Marschalkó G.,

Marshall D. J., Martino M., Marton G., Mary N., Massari D., Matijevic G., Mazeh T., McMillan P. J., Messina S., Michalik D., Millar N. R., Molina D., Molinaro R., Molnár L., Montegriffo P., Mor R., Morbidelli R., Morel T., Morris D., Mulone A. F., Muraveva T., Musella I., Nelemans G., Nicastro L., Noval L., O{}Mullane W., Ordénovic C., Ordóñez-Blanco D., Osborne P., Pagani C., Pagano I., Pailler F., Palacin H., Palaversa L., Panahi A., Pawlak M., Piersimoni A. M., Pineau F.-X., Plachy E., Plum G., Poggio E., Poujoulet E., Prsa A., Pulone L., Racero E., Ragaini S., Rambaux N., Ramos-Lerate M., Regibo S., Reylé C., Riclet F., Ripepi V., Riva A., Rivard A., Rixon G., Roegiers T., Roelens M., Romero-Gómez M., Rowell N., Royer F., Ruiz-Dern L., Sadowski G., Sagristà Sellés T., Sahlmann J., Salgado J., Salguero E., Sanna N., Santana-Ros T., Sarasso M., Savietto H., Schultheis M., Sciacca E., Segol M., Segovia J. C., Ségransan D., Shih I-C., Siltala L., Silva A. F., Smart R. L., Smith K. W., Solano E., Solitro F., Sordo R., Soria Nieto S., Souchay J., Spagna A., Spoto F., Stampa U., Steele I. A., Steidelmüller H., Stephenson C. A., Stoev H., Suess F. F., Surdej J., Szabados L., Szegedi-Elek E., Tapiador D., Taris F., Tauran G., Taylor M. B., Teixeira R., Terrett D., Teyssandier P., Thuillot W., Titarenko A., Torra Clotet F., Turon C., Ulla A., Utrilla E., Uzzi S., Vaillant M., Valentini G., Valette V., van Elteren A., Van Hemelryck E., Vaschetto M., Vecchiato A., Veljanoski J., Viala Y., Vicente D., Vogt S., von Essen C., Voss H., Votruba V., Voutsinas S., Walmsley G., Weiler M., Wertz O., Wevers T., Wyrzykowski L., Yoldas A., Zerjal M., Ziaeepour H., Zorec J., Zschocke S., Zucker S., Zurbach C., Zwitter, and T. Gaia data release 2 - observational hertzsprung-russell diagrams. *A&A*, 616:A10, 2018. doi:10.1051/0004-6361/201832843. URL https://doi.org/10.1051/0004-6361/201832843.

P. S. Coppi, R. Zinn, C. Baltay, D. Rabinowitz, T. Girard, R. Howard, K. Ment, and R. Rahman. La silla-QUEST RR lyrae star survey II: The crater II tidal streams. *Monthly Notices of the Royal Astronomical Society*, February 2024. doi:10.1093/mnras/stae488.

Patrick Côté, David A. Hanes, Dean E. McLaughlin, T. J. Bridges, James E. Hesser, and Gretchen L. H. Harris. Discovery of a Probable CH Star in the Globular Cluster M14 and Implications for the Evolution of Binaries in Clusters. *Astrophysical Journal, Letters*, 476(1):L15–L18, February 1997. doi:10.1086/310488.

P. L. Cottrell and G. S. Da Costa. Correlated cyanogen and sodium anomalies in the globular clusters 47 TUC and NGC 6752. *Astrophysical Journal, Letters*, 245: L79–L82, April 1981. doi:10.1086/183527.

Gary S. Da Costa and Thomas Nordlander. A main sequence CH-star in the globular

cluster M55 (NGC 6809). *Publications of the Astron. Soc. of Australia*, 42:e044, April 2025. doi:10.1017/pasa.2025.31.

Emanuele Dalessandro, Davide Massari, Michele Bellazzini, Paolo Miocchi, Alessio Mucciarelli, Maurizio Salaris, Santi Cassisi, Francesco R. Ferraro, and Barbara Lanzoni. First Evidence of Fully Spatially Mixed First and Second Generations in Globular Clusters: The Case of NGC 6362. *Astrophysical Journal, Letters*, 791 (1):L4, August 2014. doi:10.1088/2041-8205/791/1/L4.

Dark Energy Survey Collaboration, T. Abbott, F. B. Abdalla, J. Aleksić, S. Allam, A. Amara, D. Bacon, E. Balbinot, M. Banerji, K. Bechtol, A. Benoit-Lévy, G. M. Bernstein, E. Bertin, J. Blazek, C. Bonnett, S. Bridle, D. Brooks, R. J. Brunner, E. Buckley-Geer, D. L. Burke, G. B. Caminha, D. Capozzi, J. Carlsen, A. Carnero-Rosell, M. Carollo, M. Carrasco-Kind, J. Carretero, F. J. Castander, L. Clerkin, T. Collett, C. Conselice, M. Crocce, C. E. Cunha, C. B. D'Andrea, L. N. da Costa, T. M. Davis, S. Desai, H. T. Diehl, J. P. Dietrich, S. Dodelson, P. Doel, A. Drlica-Wagner, J. Estrada, J. Etherington, A. E. Evrard, J. Fabbri, D. A. Finley, B. Flaugher, R. J. Foley, P. Fosalba, J. Frieman, J. García-Bellido, E. Gaztanaga, D. W. Gerdes, T. Giannantonio, D. A. Goldstein, D. Gruen, R. A. Gruendl, P. Guarnieri, G. Gutierrez, W. Hartley, K. Honscheid, B. Jain, D. J. James, T. Jeltema, S. Jouvel, R. Kessler, A. King, D. Kirk, R. Kron, K. Kuehn, N. Kuropatkin, O. Lahav, T. S. Li, M. Lima, H. Lin, M. A. G. Maia, M. Makler, M. Manera, C. Maraston, J. L. Marshall, P. Martini, R. G. McMahon, P. Melchior, A. Merson, C. J. Miller, R. Miquel, J. J. Mohr, X. Morice-Atkinson, K. Naidoo, E. Neilsen, R. C. Nichol, B. Nord, R. Ogando, F. Ostrovski, A. Palmese, A. Papadopoulos, H. V. Peiris, J. Peoples, W. J. Percival, A. A. Plazas, S. L. Reed, A. Refregier, A. K. Romer, A. Roodman, A. Ross, E. Rozo, E. S. Rykoff, I. Sadeh, M. Sako, C. Sánchez, E. Sanchez, B. Santiago, V. Scarpine, M. Schubnell, I. Sevilla-Noarbe, E. Sheldon, M. Smith, R. C. Smith, M. Soares-Santos, F. Sobreira, M. Soumagnac, E. Suchyta, M. Sullivan, M. Swanson, G. Tarle, J. Thaler, D. Thomas, R. C. Thomas, D. Tucker, J. D. Vieira, V. Vikram, A. R. Walker, R. H. Wechsler, J. Weller, W. Wester, L. Whiteway, H. Wilcox, B. Yanny, Y. Zhang, and J. Zuntz. The Dark Energy Survey: more than dark energy - an overview. *Monthly Notices of the Royal Astronomical Society*, 460(2):1270–1299, August 2016. doi:10.1093/mnras/stw641.

Alis J. Deason and Vasily Belokurov. Galactic Archaeology with Gaia. *New Astronomy Review*, 99:101706, December 2024. doi:10.1016/j.newar.2024.101706.

Arjun Dey, David J. Schlegel, Dustin Lang, Robert Blum, Kaylan Burleigh, Xiaohui Fan, Joseph R. Findlay, Doug Finkbeiner, David Herrera, Stéphanie Juneau, Martin Landriau, Michael Levi, Ian McGreer, Aaron Meisner, Adam D. Myers, John Moustakas, Peter Nugent, Anna Patej, Edward F. Schlafly, Alistair R. Walker, Francisco Valdes, Benjamin A. Weaver, Christophe Yèche, Hu Zou, Xu Zhou, Behzad Abareshi, T. M. C. Abbott, Bela Abolfathi, C. Aguilera, Shadab Alam, Lori Allen, A. Alvarez, James Annis, Behzad Ansarinejad, Marie Aubert, Jacqueline Beechert, Eric F. Bell, Segev Y. BenZvi, Florian Beutler, Richard M. Bielby, Adam S. Bolton, César Briceño, Elizabeth J. Buckley-Geer, Karen Butler, Annalisa Calamida, Raymond G. Carlberg, Paul Carter, Ricard Casas, Francisco J. Castander, Yumi Choi, Johan Comparat, Elena Cukanovaite, Timothée Delubac, Kaitlin DeVries, Sharmila Dey, Govinda Dhungana, Mark Dickinson, Zhejie Ding, John B. Donaldson, Yutong Duan, Christopher J. Duckworth, Sarah Eftekharzadeh, Daniel J. Eisenstein, Thomas Etourneau, Parker A. Fagrelius, Jay Farihi, Mike Fitzpatrick, Andreu Font-Ribera, Leah Fulmer, Boris T. Gänsicke, Enrique Gaztanaga, Koshy George, David W. Gerdes, Satya Gontcho A. Gontcho, Claudio Gorgoni, Gregory Green, Julien Guy, Diane Harmer, M. Hernandez, Klaus Honscheid, Lijuan Wendy Huang, David J. James, Buell T. Jannuzi, Linhua Jiang, Richard Joyce, Armin Karcher, Sonia Karkar, Robert Kehoe, Jean-Paul Kneib, Andrea Kueter-Young, Ting-Wen Lan, Tod R. Lauer, Laurent Le Guillou, Auguste Le Van Suu, Jae Hyeon Lee, Michael Lesser, Laurence Perreault Levasseur, Ting S. Li, Justin L. Mann, Robert Marshall, C. E. Martínez-Vázquez, Paul Martini, Hélion du Mas des Bourboux, Sean McManus, Tobias Gabriel Meier, Brice Ménard, Nigel Metcalfe, Andrea Muñoz-Gutiérrez, Joan Najita, Kevin Napier, Gautham Narayan, Jeffrey A. Newman, Jundan Nie, Brian Nord, Dara J. Norman, Knut A. G. Olsen, Anthony Paat, Nathalie Palanque-Delabrouille, Xiyan Peng, Claire L. Poppett, Megan R. Poremba, Abhishek Prakash, David Rabinowitz, Anand Raichoor, Mehdi Rezaie, A. N. Robertson, Natalie A. Roe, Ashley J. Ross, Nicholas P. Ross, Gregory Rudnick, Sasha Safonova, Abhijit Saha, F. Javier Sánchez, Elodie Savary, Heidi Schweiker, Adam Scott, Hee-Jong Seo, Huanyuan Shan, David R. Silva, Zachary Slepian, Christian Soto, David Sprayberry, Ryan Staten, Coley M. Stillman, Robert J. Stupak, David L. Summers, Suk Sien Tie, H. Tirado, Mariana Vargas-Magaña, A. Katherina Vivas, Risa H. Wechsler, Doug Williams, Jinyi Yang, Qian Yang, Tolga Yapici, Dennis Zaritsky, A. Zenteno, Kai Zhang, Tianmeng Zhang, Rongpu Zhou, and Zhimin Zhou. Overview of the DESI Legacy Imaging Surveys. *Astronomical Journal*, 157(5):168, May 2019. doi:10.3847/1538-3881/ab089d.

Emma Dodd, Thomas M. Callingham, Amina Helmi, Tadafumi Matsuno, Tomás Ruiz-Lara, Eduardo Balbinot, and Sofie Lövdal. Gaia DR3 view of dynamical substructure in the stellar halo near the Sun. *Astronomy and Astrophysics*, 670: L2, February 2023. doi:10.1051/0004-6361/202244546.

Valentina D'Orazi, Raffaele Gratton, Sara Lucatello, Eugenio Carretta, Angela Bragaglia, and Anna F. Marino. Ba Stars and Other Binaries in First and Second Generation Stars in Globular Clusters. *Astrophysical Journal, Letters*, 719(2): L213–L217, August 2010. doi:10.1088/2041-8205/719/2/L213.

Aaron Dotter. MESA Isochrones and Stellar Tracks (MIST) 0: Methods for the Construction of Stellar Isochrones. *Astrophysical Journal, Supplement*, 222(1):8, January 2016. doi:10.3847/0067-0049/222/1/8.

Aaron Dotter, Brian Chaboyer, Darko Jevremović, Veselin Kostov, E. Baron, and Jason W. Ferguson. The Dartmouth Stellar Evolution Database. *Astrophysical Journal, Supplement*, 178(1):89–101, September 2008. doi:10.1086/589654.

A. Drlica-Wagner, K. Bechtol, E. S. Rykoff, E. Luque, A. Queiroz, Y. Y. Mao, R. H. Wechsler, J. D. Simon, B. Santiago, B. Yanny, E. Balbinot, S. Dodelson, A. Fausti Neto, D. J. James, T. S. Li, M. A. G. Maia, J. L. Marshall, A. Pieres, K. Stringer, A. R. Walker, T. M. C. Abbott, F. B. Abdalla, S. Allam, A. Benoit-Lévy, G. M. Bernstein, E. Bertin, D. Brooks, E. Buckley-Geer, D. L. Burke, A. Carnero Rosell, M. Carrasco Kind, J. Carretero, M. Crocce, L. N. da Costa, S. Desai, H. T. Diehl, J. P. Dietrich, P. Doel, T. F. Eifler, A. E. Evrard, D. A. Finley, B. Flaugher, P. Fosalba, J. Frieman, E. Gaztanaga, D. W. Gerdes, D. Gruen, R. A. Gruendl, G. Gutierrez, K. Honscheid, K. Kuehn, N. Kuropatkin, O. Lahav, P. Martini, R. Miquel, B. Nord, R. Ogando, A. A. Plazas, K. Reil, A. Roodman, M. Sako, E. Sanchez, V. Scarpine, M. Schubnell, I. Sevilla-Noarbe, R. C. Smith, M. Soares-Santos, F. Sobreira, E. Suchyta, M. E. C. Swanson, G. Tarle, D. Tucker, V. Vikram, W. Wester, Y. Zhang, J. Zuntz, and DES Collaboration. Eight Ultra-faint Galaxy Candidates Discovered in Year Two of the Dark Energy Survey. *Astrophysical Journal*, 813(2):109, November 2015. doi:10.1088/0004-637X/813/2/109.

P. Eitner, M. Bergemann, A. J. Ruiter, O. Avril, I. R. Seitenzahl, M. R. Gent, and B. Côté. Observational constraints on the origin of the elements. V. NLTE abundance ratios of [Ni/Fe] in Galactic stars and enrichment by sub-Chandrasekhar mass supernovae. *Astronomy and Astrophysics*, 677:A151, September 2023. doi:10.1051/0004-6361/202244286.

D. Erkal, V. Belokurov, C. F. P. Laporte, S. E. Koposov, T. S. Li, C. J. Grillmair, N. Kallivayalil, A. M. Price-Whelan, N. W. Evans, K. Hawkins, D. Hendel, C. Mateu, J. F. Navarro, A. del Pino, C. T. Slater, S. T. Sohn, and Orphan Aspen Treasury Collaboration. The total mass of the Large Magellanic Cloud from its perturbation on the Orphan stream. *Monthly Notices of the Royal Astronomical Society*, 487(2):2685–2700, August 2019. doi:10.1093/mnras/stz1371.

Denis Erkal, Vasily Belokurov, Jo Bovy, and Jason L. Sanders. The number and size of subhalo-induced gaps in stellar streams. *Monthly Notices of the Royal Astronomical Society*, 463(1):102–119, November 2016a. doi:10.1093/mnras/stw1957.

Denis Erkal, Jason L. Sanders, and Vasily Belokurov. Stray, swing and scatter: angular momentum evolution of orbits and streams in aspherical potentials. *Monthly Notices of the Royal Astronomical Society*, 461(2):1590–1604, September 2016b. doi:10.1093/mnras/stw1400.

Rana Ezzeddine, Anna Frebel, and Bertrand Plez. Ultra-metal-poor Stars: Spectroscopic Determination of Stellar Atmospheric Parameters Using Iron Non-LTE Line Abundances. *Astrophysical Journal*, 847(2):142, October 2017. doi:10.3847/1538-4357/aa8875.

Rana Ezzeddine, Anna Frebel, Ian U. Roederer, Nozomu Tominaga, Jason Tumlinson, Miho Ishigaki, Ken'ichi Nomoto, Vinicius M. Placco, and Wako Aoki. Evidence for an Aspherical Population III Supernova Explosion Inferred from the Hyper-metal-poor Star HE 1327-2326. *Astrophysical Journal*, 876(2):97, May 2019. doi:10.3847/1538-4357/ab14e7.

S. Feltzing, K. Eriksson, J. Kleyna, and M. I. Wilkinson. Evidence of enrichment by individual SN from elemental abundance ratios in the very metal-poor dSph galaxy Boötes I. *Astronomy and Astrophysics*, 508(1):L1–L4, December 2009. doi:10.1051/0004-6361/200912833.

José G. Fernández-Trincado, Timothy C. Beers, Dante Minniti, Leticia Carigi, Beatriz Barbuy, Vinicius M. Placco, Christian Moni Bidin, Sandro Villanova, Alexandre Roman-Lopes, and Christian Nitschelm. Discovery of a Large Population of Nitrogen-enhanced Stars in the Magellanic Clouds. *Astrophysical Journal, Letters*, 903(1):L17, November 2020. doi:10.3847/2041-8213/abc01d.

Francesco R. Ferraro, Alessio Mucciarelli, Barbara Lanzoni, Cristina Pallanca, Mario Cadelano, Alex Billi, Alison Sills, Enrico Vesperini, Emanuele Dalessandro, Giacomo Beccari, Lorenzo Monaco, and Mario Mateo. Fast rotating blue

stragglers prefer loose clusters. *Nature Communications*, 14:2584, May 2023. doi:10.1038/s41467-023-38153-w.

Duncan A. Forbes, Nate Bastian, Mark Gieles, Robert A. Crain, J. M. Diederik Kruijssen, Søren S. Larsen, Sylvia Ploeckinger, Oscar Agertz, Michele Trenti, Annette M. N. Ferguson, Joel Pfeffer, and Oleg Y. Gnedin. Globular cluster formation and evolution in the context of cosmological galaxy assembly: open questions. *Proceedings of the Royal Society of London Series A*, 474(2210):20170616, February 2018. doi:10.1098/rspa.2017.0616.

Duncan A. Forbes, Anna Ferré-Mateu, Mark Durré, Jean P. Brodie, and Aaron J. Romanowsky. Keck Cosmic Web Imager (KCWI) spectra of globular clusters and ultracompact dwarfs in the halo of M87. *Monthly Notices of the Royal Astronomical Society*, 497(1):765–775, September 2020. doi:10.1093/mnras/staa1924.

R. Forsberg, H. Jönsson, N. Ryde, and F. Matteucci. Abundances of disk and bulge giants from high-resolution optical spectra. IV. Zr, La, Ce, Eu. *Astronomy and Astrophysics*, 631:A113, November 2019. doi:10.1051/0004-6361/201936343.

P. François, L. Monaco, P. Bonifacio, C. Moni Bidin, D. Geisler, and L. Sbordone. Abundance ratios of red giants in low-mass ultra-faint dwarf spheroidal galaxies. *Astronomy and Astrophysics*, 588:A7, April 2016. doi:10.1051/0004-6361/201527181.

Anna Frebel and Volker Bromm. Chemical Signatures of the First Galaxies: Criteria for One-shot Enrichment. *Astrophysical Journal*, 759(2):115, November 2012. doi:10.1088/0004-637X/759/2/115.

Anna Frebel and Alexander P. Ji. Observations of R-Process Stars in the Milky Way and Dwarf Galaxies. In *Handbook of Nuclear Physics*. arXiv, February 2023. URL https://ui.adsabs.harvard.edu/abs/2023arXiv230209188F. ADS Bibcode: 2023arXiv230209188F.

Anna Frebel and John E. Norris. Near-Field Cosmology with Extremely Metal-Poor Stars. *Annual Review of Astronomy and Astrophysics*, 53:631–688, August 2015. doi:10.1146/annurev-astro-082214-122423.

Anna Frebel, Evan N. Kirby, and Joshua D. Simon. Linking dwarf galaxies to halo building blocks with the most metal-poor star in Sculptor. *Nature*, 464(7285): 72–75, March 2010. doi:10.1038/nature08772.

Anna Frebel, Andrew R. Casey, Heather R. Jacobson, and Qinsi Yu. Deriving Stellar Effective Temperatures of Metal-poor Stars with the Excitation Potential Method. *Astrophysical Journal*, 769(1):57, May 2013a. doi:10.1088/0004-637X/769/1/57.

Anna Frebel, Ragnhild Lunnan, Andrew R. Casey, John E. Norris, Rosemary F. G. Wyse, and Gerard Gilmore. The 300 km s^{-1} Stellar Stream near Segue 1: Insights from High-resolution Spectroscopy of Its Brightest Star. *Astrophysical Journal*, 771(1):39, July 2013b. doi:10.1088/0004-637X/771/1/39.

Anna Frebel, Joshua D. Simon, and Evan N. Kirby. Segue 1: An Unevolved Fossil Galaxy from the Early Universe. *Astrophysical Journal*, 786(1):74, May 2014. doi:10.1088/0004-637X/786/1/74.

Ken Freeman and Joss Bland-Hawthorn. The New Galaxy: Signatures of Its Formation. *Annual Review of Astronomy and Astrophysics*, 40:487–537, January 2002. doi:10.1146/annurev.astro.40.060401.093840.

Sal Wanying Fu, Joshua D. Simon, Matthew Shetrone, Jo Bovy, Timothy C. Beers, J. G. Fernández-Trincado, Vinicius M. Placco, Olga Zamora, Carlos Allende Prieto, D. A. García-Hernández, Paul Harding, Inese Ivans, Richard Lane, Christian Nitschelm, Alexandre Roman-Lopes, and Jennifer Sobeck. The Origin of the 300 km s^{-1} Stream near Segue 1. *Astrophysical Journal*, 866(1):42, October 2018. doi:10.3847/1538-4357/aad9f9.

Gaia Collaboration, T. Prusti, J. H. J. de Bruijne, A. G. A. Brown, A. Vallenari, C. Babusiaux, C. A. L. Bailer-Jones, U. Bastian, M. Biermann, D. W. Evans, and et al. The Gaia mission. *Astronomy and Astrophysics*, 595:A1, November 2016. doi:10.1051/0004-6361/201629272.

Gaia Collaboration, A. Recio-Blanco, G. Kordopatis, P. de Laverny, P. A. Palicio, A. Spagna, L. Spina, D. Katz, P. Re Fiorentin, E. Poggio, P. J. McMillan, A. Vallenari, M. G. Lattanzi, G. M. Seabroke, L. Casamiquela, A. Bragaglia, T. Antoja, C. A. L. Bailer-Jones, M. Schultheis, R. Andrae, M. Fouesneau, M. Cropper, T. Cantat-Gaudin, A. Bijaoui, U. Heiter, A. G. A. Brown, T. Prusti, J. H. J. de Bruijne, F. Arenou, C. Babusiaux, M. Biermann, O. L. Creevey, C. Ducourant, D. W. Evans, L. Eyer, R. Guerra, A. Hutton, C. Jordi, S. A. Klioner, U. L. Lammers, L. Lindegren, X. Luri, F. Mignard, C. Panem, D. Pourbaix, S. Randich, P. Sartoretti, C. Soubiran, P. Tanga, N. A. Walton, U. Bastian, R. Drimmel, F. Jansen, F. van Leeuwen, J. Bakker, C. Cacciari, J. Castañeda, F. De Angeli, C. Fabricius, Y. Frémat, L. Galluccio, A. Guerrier, E. Masana, R. Messineo, N. Mowlavi, C. Nicolas, K. Nienartowicz, F. Pailler, P. Panuzzo, F. Riclet,

W. Roux, R. Sordo, F. Thévenin, G. Gracia-Abril, J. Portell, D. Teyssier, M. Altmann, M. Audard, I. Bellas-Velidis, K. Benson, J. Berthier, R. Blomme, P. W. Burgess, D. Busonero, G. Busso, H. Cánovas, B. Carry, A. Cellino, N. Cheek, G. Clementini, Y. Damerdji, M. Davidson, P. de Teodoro, M. Nuñez Campos, L. Delchambre, A. Dell'Oro, P. Esquej, J. Fernández-Hernández, E. Fraile, D. Garabato, P. García-Lario, E. Gosset, R. Haigron, J. L. Halbwachs, N. C. Hambly, D. L. Harrison, J. Hernández, D. Hestroffer, S. T. Hodgkin, B. Holl, K. Janßen, G. Jevardat de Fombelle, S. Jordan, A. Krone-Martins, A. C. Lanzafame, W. Löffler, O. Marchal, P. M. Marrese, A. Moitinho, K. Muinonen, P. Osborne, E. Pancino, T. Pauwels, C. Reylé, M. Riello, L. Rimoldini, T. Roegiers, J. Rybizki, L. M. Sarro, C. Siopis, M. Smith, A. Sozzetti, E. Utrilla, M. van Leeuwen, U. Abbas, P. Ábrahám, A. Abreu Aramburu, C. Aerts, J. J. Aguado, M. Ajaj, F. Aldea-Montero, G. Altavilla, M. A. Álvarez, J. Alves, F. Anders, R. I. Anderson, E. Anglada Varela, D. Baines, S. G. Baker, L. Balaguer-Núñez, E. Balbinot, Z. Balog, C. Barache, D. Barbato, M. Barros, M. A. Barstow, S. Bartolomé, J. L. Bassilana, N. Bauchet, U. Becciani, M. Bellazzini, A. Berihuete, M. Bernet, S. Bertone, L. Bianchi, A. Binnenfeld, S. Blanco-Cuaresma, T. Boch, A. Bombrun, D. Bossini, S. Bouquillon, L. Bramante, E. Breedt, A. Bressan, N. Brouillet, E. Brugaletta, B. Bucciarelli, A. Burlacu, A. G. Butkevich, R. Buzzi, E. Caffau, R. Cancelliere, R. Carballo, T. Carlucci, M. I. Carnerero, J. M. Carrasco, M. Castellani, A. Castro-Ginard, L. Chaoul, P. Charlot, L. Chemin, V. Chiaramida, A. Chiavassa, N. Chornay, G. Comoretto, G. Contursi, W. J. Cooper, T. Cornez, S. Cowell, F. Crifo, M. Crosta, C. Crowley, C. Dafonte, A. Dapergolas, P. David, F. De Luise, R. De March, J. De Ridder, R. de Souza, A. de Torres, E. F. del Peloso, E. del Pozo, M. Delbo, A. Delgado, J. B. Delisle, C. Demouchy, T. E. Dharmawardena, P. Di Matteo, S. Diakite, C. Diener, E. Distefano, C. Dolding, B. Edvardsson, H. Enke, C. Fabre, M. Fabrizio, S. Faigler, G. Fedorets, P. Fernique, F. Figueras, Y. Fournier, C. Fouron, F. Fragkoudi, M. Gai, A. Garcia-Gutierrez, M. Garcia-Reinaldos, M. García-Torres, A. Garofalo, A. Gavel, P. Gavras, E. Gerlach, R. Geyer, P. Giacobbe, G. Gilmore, S. Girona, G. Giuffrida, R. Gomel, A. Gomez, J. González-Núñez, I. González-Santamaría, J. J. González-Vidal, M. Granvik, P. Guillout, J. Guiraud, R. Gutiérrez-Sánchez, L. P. Guy, D. Hatzidimitriou, M. Hauser, M. Haywood, A. Helmer, A. Helmi, M. H. Sarmiento, S. L. Hidalgo, N. Hładczuk, D. Hobbs, G. Holland, H. E. Huckle, K. Jardine, G. Jasniewicz, A. Jean-Antoine Piccolo, Ó. Jiménez-Arranz, J. Juaristi Campillo, F. Julbe, L. Karbevska, P. Kervella, S. Khanna, A. J. Korn, Á. Kóspál, Z. Kostrzewa-Rutkowska, K. Kruszyńska, M. Kun, P. Laizeau, S. Lambert, A. F. Lanza, Y. Lasne, J. F. Le Campion, Y. Lebreton, T. Lebzelter, S. Lec-

cia, N. Leclerc, I. Lecoeur-Taibi, S. Liao, E. L. Licata, H. E. P. Lindstrøm, T. A. Lister, E. Livanou, A. Lobel, A. Lorca, C. Loup, P. Madrero Pardo, A. Magdaleno Romeo, S. Managau, R. G. Mann, M. Manteiga, J. M. Marchant, M. Marconi, J. Marcos, M. M. S. Marcos Santos, D. Marín Pina, S. Marinoni, F. Marocco, D. J. Marshall, L. Martin Polo, J. M. Martín-Fleitas, G. Marton, N. Mary, A. Masip, D. Massari, A. Mastrobuono-Battisti, T. Mazeh, S. Messina, D. Michalik, N. R. Millar, A. Mints, D. Molina, R. Molinaro, L. Molnár, G. Monari, M. Monguió, P. Montegriffo, A. Montero, R. Mor, A. Mora, R. Morbidelli, T. Morel, D. Morris, T. Muraveva, C. P. Murphy, I. Musella, Z. Nagy, L. Noval, F. Ocaña, A. Ogden, C. Ordenovic, J. O. Osinde, C. Pagani, I. Pagano, L. Palaversa, L. Pallas-Quintela, A. Panahi, S. Payne-Wardenaar, X. Peñalosa Esteller, A. Penttilä, B. Pichon, A. M. Piersimoni, F. X. Pineau, E. Plachy, G. Plum, A. Prša, L. Pulone, E. Racero, S. Ragaini, M. Rainer, C. M. Raiteri, P. Ramos, M. Ramos-Lerate, S. Regibo, P. J. Richards, C. Rios Diaz, V. Ripepi, A. Riva, H. W. Rix, G. Rixon, N. Robichon, A. C. Robin, C. Robin, M. Roelens, H. R. O. Rogues, L. Rohrbasser, M. Romero-Gómez, N. Rowell, F. Royer, D. Ruz Mieres, K. A. Rybicki, G. Sadowski, A. Sáez Núñez, A. Sagristà Sellés, J. Sahlmann, E. Salguero, N. Samaras, V. Sanchez Gimenez, N. Sanna, R. Santoveña, M. Sarasso, E. Sciacca, M. Segol, J. C. Segovia, D. Ségransan, D. Semeux, S. Shahaf, H. I. Siddiqui, A. Siebert, L. Siltala, A. Silvelo, E. Slezak, I. Slezak, R. L. Smart, O. N. Snaith, E. Solano, F. Solitro, D. Souami, J. Souchay, F. Spoto, I. A. Steele, H. Steidelmüller, C. A. Stephenson, M. Süveges, J. Surdej, L. Szabados, E. Szegedi-Elek, F. Taris, M. B. Taylor, R. Teixeira, L. Tolomei, N. Tonello, F. Torra, J. Torra, G. Torralba Elipe, M. Trabucchi, A. T. Tsounis, C. Turon, A. Ulla, N. Unger, M. V. Vaillant, E. van Dillen, W. van Reeven, O. Vanel, A. Vecchiato, Y. Viala, D. Vicente, S. Voutsinas, M. Weiler, T. Wevers, Ł. Wyrzykowski, A. Yoldas, P. Yvard, H. Zhao, J. Zorec, S. Zucker, and T. Zwitter. Gaia Data Release 3. Chemical cartography of the Milky Way. *Astronomy and Astrophysics*, 674:A38, June 2023a. doi:10.1051/0004-6361/202243511.

Gaia Collaboration, A. Vallenari, A. G. A. Brown, T. Prusti, J. H. J. de Bruijne, F. Arenou, C. Babusiaux, M. Biermann, O. L. Creevey, C. Ducourant, D. W. Evans, L. Eyer, R. Guerra, A. Hutton, C. Jordi, S. A. Klioner, U. L. Lammers, L. Lindegren, X. Luri, F. Mignard, C. Panem, D. Pourbaix, S. Randich, P. Sartoretti, C. Soubiran, P. Tanga, N. A. Walton, C. A. L. Bailer-Jones, U. Bastian, R. Drimmel, F. Jansen, D. Katz, M. G. Lattanzi, F. van Leeuwen, J. Bakker, C. Cacciari, J. Castañeda, F. De Angeli, C. Fabricius, M. Fouesneau, Y. Frémat, L. Galluccio, A. Guerrier, U. Heiter, E. Masana, R. Messineo, N. Mowlavi,

C. Nicolas, K. Nienartowicz, F. Pailler, P. Panuzzo, F. Riclet, W. Roux, G. M. Seabroke, R. Sordo, F. Thévenin, G. Gracia-Abril, J. Portell, D. Teyssier, M. Altmann, R. Andrae, M. Audard, I. Bellas-Velidis, K. Benson, J. Berthier, R. Blomme, P. W. Burgess, D. Busonero, G. Busso, H. Cánovas, B. Carry, A. Cellino, N. Cheek, G. Clementini, Y. Damerdji, M. Davidson, P. de Teodoro, M. Nuñez Campos, L. Delchambre, A. Dell'Oro, P. Esquej, J. Fernández-Hernández, E. Fraile, D. Garabato, P. García-Lario, E. Gosset, R. Haigron, J. L. Halbwachs, N. C. Hambly, D. L. Harrison, J. Hernández, D. Hestroffer, S. T. Hodgkin, B. Holl, K. Janßen, G. Jevardat de Fombelle, S. Jordan, A. Krone-Martins, A. C. Lanzafame, W. Löffler, O. Marchal, P. M. Marrese, A. Moitinho, K. Muinonen, P. Osborne, E. Pancino, T. Pauwels, A. Recio-Blanco, C. Reylé, M. Riello, L. Rimoldini, T. Roegiers, J. Rybizki, L. M. Sarro, C. Siopis, M. Smith, A. Sozzetti, E. Utrilla, M. van Leeuwen, U. Abbas, P. Ábrahám, A. Abreu Aramburu, C. Aerts, J. J. Aguado, M. Ajaj, F. Aldea-Montero, G. Altavilla, M. A. Álvarez, J. Alves, F. Anders, R. I. Anderson, E. Anglada Varela, T. Antoja, D. Baines, S. G. Baker, L. Balaguer-Núñez, E. Balbinot, Z. Balog, C. Barache, D. Barbato, M. Barros, M. A. Barstow, S. Bartolomé, J. L. Bassilana, N. Bauchet, U. Becciani, M. Bellazzini, A. Berihuete, M. Bernet, S. Bertone, L. Bianchi, A. Binnenfeld, S. Blanco-Cuaresma, A. Blazere, T. Boch, A. Bombrun, D. Bossini, S. Bouquillon, A. Bragaglia, L. Bramante, E. Breedt, A. Bressan, N. Brouillet, E. Brugaletta, B. Bucciarelli, A. Burlacu, A. G. Butkevich, R. Buzzi, E. Caffau, R. Cancelliere, T. Cantat-Gaudin, R. Carballo, T. Carlucci, M. I. Carnerero, J. M. Carrasco, L. Casamiquela, M. Castellani, A. Castro-Ginard, L. Chaoul, P. Charlot, L. Chemin, V. Chiaramida, A. Chiavassa, N. Chornay, G. Comoretto, G. Contursi, W. J. Cooper, T. Cornez, S. Cowell, F. Crifo, M. Cropper, M. Crosta, C. Crowley, C. Dafonte, A. Dapergolas, M. David, P. David, P. de Laverny, F. De Luise, R. De March, J. De Ridder, R. de Souza, A. de Torres, E. F. del Peloso, E. del Pozo, M. Delbo, A. Delgado, J. B. Delisle, C. Demouchy, T. E. Dharmawardena, P. Di Matteo, S. Diakite, C. Diener, E. Distefano, C. Dolding, B. Edvardsson, H. Enke, C. Fabre, M. Fabrizio, S. Faigler, G. Fedorets, P. Fernique, A. Fienga, F. Figueras, Y. Fournier, C. Fouron, F. Fragkoudi, M. Gai, A. Garcia-Gutierrez, M. Garcia-Reinaldos, M. García-Torres, A. Garofalo, A. Gavel, P. Gavras, E. Gerlach, R. Geyer, P. Giacobbe, G. Gilmore, S. Girona, G. Giuffrida, R. Gomel, A. Gomez, J. González-Núñez, I. González-Santamaría, J. J. González-Vidal, M. Granvik, P. Guillout, J. Guiraud, R. Gutiérrez-Sánchez, L. P. Guy, D. Hatzidimitriou, M. Hauser, M. Haywood, A. Helmer, A. Helmi, M. H. Sarmiento, S. L. Hidalgo, T. Hilger, N. Hładczuk, D. Hobbs, G. Holland, H. E. Huckle, K. Jardine, G. Jasniewicz, A. Jean-Antoine Piccolo, Ó. Jiménez-Arranz, A. Jorissen, J. Juaristi Campillo, F. Julbe, L. Karbevska, P. Kervella, S. Khanna,

M. Kontizas, G. Kordopatis, A. J. Korn, Á. Kóspál, Z. Kostrzewa-Rutkowska, K. Kruszyńska, M. Kun, P. Laizeau, S. Lambert, A. F. Lanza, Y. Lasne, J. F. Le Campion, Y. Lebreton, T. Lebzelter, S. Leccia, N. Leclerc, I. Lecoeur-Taibi, S. Liao, E. L. Licata, H. E. P. Lindstrøm, T. A. Lister, E. Livanou, A. Lobel, A. Lorca, C. Loup, P. Madrero Pardo, A. Magdaleno Romeo, S. Managau, R. G. Mann, M. Manteiga, J. M. Marchant, M. Marconi, J. Marcos, M. M. S. Marcos Santos, D. Marín Pina, S. Marinoni, F. Marocco, D. J. Marshall, L. Martin Polo, J. M. Martín-Fleitas, G. Marton, N. Mary, A. Masip, D. Massari, A. Mastrobuono-Battisti, T. Mazeh, P. J. McMillan, S. Messina, D. Michalik, N. R. Millar, A. Mints, D. Molina, R. Molinaro, L. Molnár, G. Monari, M. Monguió, P. Montegriffo, A. Montero, R. Mor, A. Mora, R. Morbidelli, T. Morel, D. Morris, T. Muraveva, C. P. Murphy, I. Musella, Z. Nagy, L. Noval, F. Ocaña, A. Ogden, C. Ordenovic, J. O. Osinde, C. Pagani, I. Pagano, L. Palaversa, P. A. Palicio, L. Pallas-Quintela, A. Panahi, S. Payne-Wardenaar, X. Peñalosa Esteller, A. Penttilä, B. Pichon, A. M. Piersimoni, F. X. Pineau, E. Plachy, G. Plum, E. Poggio, A. Prša, L. Pulone, E. Racero, S. Ragaini, M. Rainer, C. M. Raiteri, N. Rambaux, P. Ramos, M. Ramos-Lerate, P. Re Fiorentin, S. Regibo, P. J. Richards, C. Rios Diaz, V. Ripepi, A. Riva, H. W. Rix, G. Rixon, N. Robichon, A. C. Robin, C. Robin, M. Roelens, H. R. O. Rogues, L. Rohrbasser, M. Romero-Gómez, N. Rowell, F. Royer, D. Ruz Mieres, K. A. Rybicki, G. Sadowski, A. Sáez Núñez, A. Sagristà Sellés, J. Sahlmann, E. Salguero, N. Samaras, V. Sanchez Gimenez, N. Sanna, R. Santoveña, M. Sarasso, M. Schultheis, E. Sciacca, M. Segol, J. C. Segovia, D. Ségransan, D. Semeux, S. Shahaf, H. I. Siddiqui, A. Siebert, L. Siltala, A. Silvelo, E. Slezak, I. Slezak, R. L. Smart, O. N. Snaith, E. Solano, F. Solitro, D. Souami, J. Souchay, A. Spagna, L. Spina, F. Spoto, I. A. Steele, H. Steidelmüller, C. A. Stephenson, M. Süveges, J. Surdej, L. Szabados, E. Szegedi-Elek, F. Taris, M. B. Taylor, R. Teixeira, L. Tolomei, N. Tonello, F. Torra, J. Torra, G. Torralba Elipe, M. Trabucchi, A. T. Tsounis, C. Turon, A. Ulla, N. Unger, M. V. Vaillant, E. van Dillen, W. van Reeven, O. Vanel, A. Vecchiato, Y. Viala, D. Vicente, S. Voutsinas, M. Weiler, T. Wevers, Ł. Wyrzykowski, A. Yoldas, P. Yvard, H. Zhao, J. Zorec, S. Zucker, and T. Zwitter. Gaia Data Release 3. Summary of the content and survey properties. *Astronomy and Astrophysics*, 674:A1, June 2023b. doi:10.1051/0004-6361/202243940.

A. J. Gallagher, S. G. Ryan, A. Hosford, A. E. García Pérez, W. Aoki, and S. Honda. The barium isotopic fractions in five metal-poor stars. *Astronomy and Astrophysics*, 538:A118, February 2012. doi:10.1051/0004-6361/201118382.

Pratik J. Gandhi, Andrew Wetzel, Michael Boylan-Kolchin, Robyn E. Sanderson,

Alessandro Savino, Daniel R. Weisz, Erik J. Tollerud, Guochao Sun, and Claude-André Faucher-Giguère. Testing the near-far connection with FIRE simulations: inferring the stellar mass function of the proto-Local Group at z $>$ 6 using the fossil record of present-day galaxies. *Monthly Notices of the Royal Astronomical Society*, 533(1):1059–1074, September 2024. doi:10.1093/mnras/stae1584.

Marla Geha, Beth Willman, Joshua D. Simon, Louis E. Strigari, Evan N. Kirby, David R. Law, and Jay Strader. The Least-Luminous Galaxy: Spectroscopy of the Milky Way Satellite Segue 1. *Astrophysical Journal*, 692(2):1464–1475, February 2009. doi:10.1088/0004-637X/692/2/1464.

Megan T. Gialluca, Rohan P. Naidu, and Ana Bonaca. Velocity Dispersion of the GD-1 Stellar Stream. *Astrophysical Journal, Letters*, 911(2):L32, April 2021. doi:10.3847/2041-8213/abf491.

Mark Gieles, Denis Erkal, Fabio Antonini, Eduardo Balbinot, and Jorge Peñarrubia. A supra-massive population of stellar-mass black holes in the globular cluster Palomar 5. *Nature Astronomy*, 5:957–966, July 2021. doi:10.1038/s41550-021-01392-2.

Gerard Gilmore, John E. Norris, Lorenzo Monaco, David Yong, Rosemary F. G. Wyse, and D. Geisler. Elemental Abundances and their Implications for the Chemical Enrichment of the Boötes I Ultrafaint Galaxy. *Astrophysical Journal*, 763(1): 61, January 2013. doi:10.1088/0004-637X/763/1/61.

Oleg Y. Gnedin and Jeremiah P. Ostriker. Destruction of the Galactic Globular Cluster System. *Astrophysical Journal*, 474(1):223–255, January 1997. doi:10.1086/303441.

Facundo A. Gómez, Amina Helmi, Andrew P. Cooper, Carlos S. Frenk, Julio F. Navarro, and Simon D. M. White. Streams in the Aquarius stellar haloes. *Monthly Notices of the Royal Astronomical Society*, 436(4):3602–3613, December 2013. doi:10.1093/mnras/stt1838.

Alexander J. Gordon, Annette M. N. Ferguson, and Robert G. Mann. Uncovering tidal treasures: automated classification of faint tidal features in DECaLS data. *Monthly Notices of the RAS*, 534(2):1459–1480, October 2024. doi:10.1093/mnras/stae2169.

Raffaele Gratton, Angela Bragaglia, Eugenio Carretta, Valentina D'Orazi, Sara Lucatello, and Antonio Sollima. What is a globular cluster? An observational

perspective. *Astronomy and Astrophysics Reviews*, 27(1):8, November 2019. doi:10.1007/s00159-019-0119-3.

Skylar Grayson. NSF and NASA Budget Requests Pose an Unprecedented Threat to Astronomy, July 2025. URL https://astrobites.org/2025/06/02/budget-cuts-threaten-astronomy/.

C. J. Grillmair and O. Dionatos. Detection of a 63° Cold Stellar Stream in the Sloan Digital Sky Survey. *Astrophysical Journal, Letters*, 643(1):L17–L20, May 2006. doi:10.1086/505111.

Carl J. Grillmair. The Multiple Extended Tidal Tails of NGC 288. *Astrophysical Journal*, 979(1):75, January 2025. doi:10.3847/1538-4357/ada2ea.

Carl J. Grillmair and Jeffrey L. Carlin. Stellar Streams and Clouds in the Galactic Halo. In Heidi Jo Newberg and Jeffrey L. Carlin, editors, *Tidal Streams in the Local Group and Beyond*, volume 420 of *Astrophysics and Space Science Library*, page 87, January 2016. doi:10.1007/978-3-319-19336-6_4.

Dmitrii Gudin, Derek Shank, Timothy C. Beers, Zhen Yuan, Guilherme Limberg, Ian U. Roederer, Vinicius Placco, Erika M. Holmbeck, Sarah Dietz, Kaitlin C. Rasmussen, Terese T. Hansen, Charli M. Sakari, Rana Ezzeddine, and Anna Frebel. The R-Process Alliance: Chemodynamically Tagged Groups of Halo r-process-enhanced Stars Reveal a Shared Chemical-evolution History. *Astrophysical Journal*, 908(1):79, February 2021. doi:10.3847/1538-4357/abd7ed.

Maude Gull, Anna Frebel, Karina Hinojosa, Ian U. Roederer, Alexander P. Ji, and Kaley Brauer. R-process-rich Stellar Streams in the Milky Way. *Astrophysical Journal*, 912(1):52, May 2021. doi:10.3847/1538-4357/abea1a.

Yanjun Guo, Nicholas Storm, Maria Bergemann, Jianhui Lian, Sofya Alexeeva, Yangyang Li, Rana Ezzeddine, Gerber Jeffrey, and XueFei Chen. Non-local thermodynamic equilibrium (NLTE) abundances of europium (Eu) for a sample of metal-poor stars in the galactic halo and metal-poor disk with 1D and <3D> models. *Astronomy and Astrophysics*, 693:A211, January 2025. doi:10.1051/0004-6361/202451536.

T. T. Hansen, J. Andersen, B. Nordström, T. C. Beers, V. M. Placco, J. Yoon, and L. A. Buchhave. The role of binaries in the enrichment of the early Galactic halo. III. Carbon-enhanced metal-poor stars - CEMP-s stars. *Astronomy and Astrophysics*, 588:A3, April 2016. doi:10.1051/0004-6361/201527409.

T. T. Hansen, J. D. Simon, J. L. Marshall, T. S. Li, D. Carollo, D. L. DePoy, D. Q. Nagasawa, R. A. Bernstein, A. Drlica-Wagner, F. B. Abdalla, S. Allam, J. Annis, K. Bechtol, A. Benoit-Lévy, D. Brooks, E. Buckley-Geer, A. Carnero Rosell, M. Carrasco Kind, J. Carretero, C. E. Cunha, L. N. da Costa, S. Desai, T. F. Eifler, A. Fausti Neto, B. Flaugher, J. Frieman, J. García-Bellido, E. Gaztanaga, D. W. Gerdes, D. Gruen, R. A. Gruendl, J. Gschwend, G. Gutierrez, D. J. James, E. Krause, K. Kuehn, N. Kuropatkin, O. Lahav, R. Miquel, A. A. Plazas, A. K. Romer, E. Sanchez, B. Santiago, V. Scarpine, R. C. Smith, M. Soares-Santos, F. Sobreira, E. Suchyta, M. E. C. Swanson, G. Tarle, A. R. Walker, and DES Collaboration. An r-process Enhanced Star in the Dwarf Galaxy Tucana III. *Astrophysical Journal*, 838(1):44, March 2017. doi:10.3847/1538-4357/aa634a.

T. T. Hansen, J. L. Marshall, J. D. Simon, T. S. Li, R. A. Bernstein, A. B. Pace, P. Ferguson, D. Q. Nagasawa, K. Kuehn, D. Carollo, M. Geha, D. James, A. Walker, H. T. Diehl, M. Aguena, S. Allam, S. Avila, E. Bertin, D. Brooks, E. Buckley-Geer, D. L. Burke, A. Carnero Rosell, M. Carrasco Kind, J. Carretero, M. Costanzi, L. N. Da Costa, S. Desai, J. De Vicente, P. Doel, K. Eckert, T. F. Eifler, S. Everett, I. Ferrero, J. Frieman, J. García-Bellido, E. Gaztanaga, D. W. Gerdes, D. Gruen, R. A. Gruendl, J. Gschwend, G. Gutierrez, S. R. Hinton, D. L. Hollowood, K. Honscheid, N. Kuropatkin, M. A. G. Maia, M. March, R. Miquel, A. Palmese, F. Paz-Chinchón, A. A. Plazas, E. Sanchez, B. Santiago, V. Scarpine, S. Serrano, M. Smith, M. Soares-Santos, E. Suchyta, M. E. C. Swanson, G. Tarle, T. N. Varga, R. Wilkinson, and DES Collaboration. Chemical Analysis of the Ultrafaint Dwarf Galaxy Grus II. Signature of High-mass Stellar Nucleosynthesis. *Astrophysical Journal*, 897(2):183, July 2020a. doi:10.3847/1538-4357/ab9643.

T. T. Hansen, A. H. Riley, L. E. Strigari, J. L. Marshall, P. S. Ferguson, J. Zepeda, and C. Sneden. A Chemo-dynamical Link between the Gjöll Stream and NGC 3201. *Astrophysical Journal*, 901(1):23, September 2020b. doi:10.3847/1538-4357/ababa5.

Terese T. Hansen, Alexander P. Ji, Gary S. Da Costa, Ting S. Li, Andrew R. Casey, Andrew B. Pace, Lara R. Cullinane, Denis Erkal, Sergey E. Koposov, Kyler Kuehn, Geraint F. Lewis, Dougal Mackey, Jeffrey D. Simpson, Nora Shipp, Daniel B. Zucker, Joss Bland-Hawthorn, and S5 Collaboration. S^5: The Destruction of a Bright Dwarf Galaxy as Revealed by the Chemistry of the Indus Stellar Stream. *Astrophysical Journal*, 915(2):103, July 2021. doi:10.3847/1538-4357/abfc54.

Terese T. Hansen, Joshua D. Simon, Ting S. Li, Domani Sharkey, Alexander P. Ji, Ian B. Thompson, Henrique M. Reggiani, and Jhon Yana Galarza. Chemi-

cal Diversity on Small Scales: Abundance Analysis of the Tucana V Ultrafaint Dwarf Galaxy. *Astrophysical Journal*, 968(1):21, June 2024. doi:10.3847/1538-4357/ad3a52.

William E. Harris. A Catalog of Parameters for Globular Clusters in the Milky Way. *Astronomical Journal*, 112:1487, October 1996. doi:10.1086/118116.

Sten Hasselquist, Christian R. Hayes, Jianhui Lian, David H. Weinberg, Gail Zasowski, Danny Horta, Rachael Beaton, Diane K. Feuillet, Elisa R. Garro, Carme Gallart, Verne V. Smith, Jon A. Holtzman, Dante Minniti, Ivan Lacerna, Matthew Shetrone, Henrik Jönsson, Maria-Rosa L. Cioni, Sean P. Fillingham, Katia Cunha, Robert O'Connell, José G. Fernández-Trincado, Ricardo R. Muñoz, Ricardo Schiavon, Andres Almeida, Borja Anguiano, Timothy C. Beers, Dmitry Bizyaev, Joel R. Brownstein, Roger E. Cohen, Peter Frinchaboy, D. A. García-Hernández, Doug Geisler, Richard R. Lane, Steven R. Majewski, David L. Nidever, Christian Nitschelm, Joshua Povick, Adrian Price-Whelan, Alexandre Roman-Lopes, Margarita Rosado, Jennifer Sobeck, Guy Stringfellow, Octavio Valenzuela, Sandro Villanova, and Fiorenzo Vincenzo. APOGEE Chemical Abundance Patterns of the Massive Milky Way Satellites. *Astrophysical Journal*, 923(2):172, December 2021. doi:10.3847/1538-4357/ac25f9.

Keith Hawkins, Adrian M. Price-Whelan, Allyson A. Sheffield, Aidan Z. Subrahimovic, Rachael L. Beaton, Vasily Belokurov, Denis Erkal, Sergey E. Koposov, Richard R. Lane, Chervin F. P. Laporte, and Christian Nitschelm. On the Hunt for the Origins of the Orphan-Chenab Stream: Detailed Element Abundances with APOGEE and Gaia. *Astrophysical Journal*, 948(2):123, May 2023. doi:10.3847/1538-4357/acb698.

M. Haywood, P. Di Matteo, M. D. Lehnert, O. Snaith, S. Khoperskov, and A. Gómez. In Disguise or Out of Reach: First Clues about In Situ and Accreted Stars in the Stellar Halo of the Milky Way from Gaia DR2. *Astrophysical Journal*, 863(2):113, August 2018. doi:10.3847/1538-4357/aad235.

Amina Helmi. Streams, Substructures, and the Early History of the Milky Way. *Annual Review of Astronomy and Astrophysics*, 58:205–256, August 2020. doi:10.1146/annurev-astro-032620-021917.

Amina Helmi, Simon D. M. White, P. Tim de Zeeuw, and Hongsheng Zhao. Debris streams in the solar neighbourhood as relicts from the formation of the Milky Way. *Nature*, 402(6757):53–55, November 1999. doi:10.1038/46980.

Amina Helmi, Carine Babusiaux, Helmer H. Koppelman, Davide Massari, Jovan Veljanoski, and Anthony G. A. Brown. The merger that led to the formation of the Milky Way's inner stellar halo and thick disk. *Nature*, 563(7729):85–88, October 2018. doi:10.1038/s41586-018-0625-x.

Edward Higson, Will Handley, Mike Hobson, and Anthony Lasenby. Dynamic nested sampling: an improved algorithm for parameter estimation and evidence calculation. *Statistics and Computing*, 29(5):891–913, September 2019. doi:10.1007/s11222-018-9844-0.

V. Hill, Á. Skúladóttir, E. Tolstoy, K. A. Venn, M. D. Shetrone, P. Jablonka, F. Primas, G. Battaglia, T. J. L. de Boer, P. François, A. Helmi, A. Kaufer, B. Letarte, E. Starkenburg, and M. Spite. VLT/FLAMES high-resolution chemical abundances in Sculptor: a textbook dwarf spheroidal galaxy. *Astronomy and Astrophysics*, 626:A15, June 2019. doi:10.1051/0004-6361/201833950.

K. Hollyhead, N. Kacharov, C. Lardo, N. Bastian, M. Hilker, M. Rejkuba, A. Koch, E. K. Grebel, and I. Georgiev. Evidence for multiple populations in the intermediate-age cluster Lindsay 1 in the SMC. *Monthly Notices of the Royal Astronomical Society*, 465(1):L39–L43, February 2017. doi:10.1093/mnrasl/slw179.

K. Hollyhead, C. Lardo, N. Kacharov, N. Bastian, M. Hilker, M. Rejkuba, A. Koch, E. K. Grebel, and I. Georgiev. Kron 3: a fourth intermediate age cluster in the SMC with evidence of multiple populations. *Monthly Notices of the Royal Astronomical Society*, 476(1):114–121, May 2018. doi:10.1093/mnras/sty230.

K. Hollyhead, S. Martocchia, C. Lardo, N. Bastian, N. Kacharov, F. Niederhofer, I. Cabrera-Ziri, E. Dalessandro, A. Mucciarelli, M. Salaris, and C. Usher. Spectroscopic detection of multiple populations in the ∼2 Gyr old cluster Hodge 6 in the LMC. *Monthly Notices of the Royal Astronomical Society*, 484(4):4718–4725, April 2019. doi:10.1093/mnras/stz317.

E. B. Holmberg, A. Lauberts, H. E. Schuster, and R. M. West. The ESO/Uppsala survey of the ESO (B) Atlas of the Southern Sky. IV. *Astronomy and Astrophysics, Supplement*, 27:295–342, March 1977.

John D. Hunter. Matplotlib: A 2d graphics environment. *Computing in Science & Engineering*, 9(3):90–95, 2007. doi:http://dx.doi.org/10.1109/MCSE.2007.55. URL `http://scitation.aip.org/content/aip/journal/cise/9/3/10.1109/MCSE.2007.55`.

Piet Hut, Steve McMillan, Jeremy Goodman, Mario Mateo, E. S. Phinney, Carlton Pryor, Harvey B. Richer, Frank Verbunt, and Martin Weinberg. Binaries in Globular Clusters. *Publications of the ASP*, 104:981, November 1992. doi:10.1086/133085.

R. A. Ibata, G. F. Lewis, M. J. Irwin, and T. Quinn. Uncovering cold dark matter halo substructure with tidal streams. *Monthly Notices of the Royal Astronomical Society*, 332(4):915–920, June 2002. doi:10.1046/j.1365-8711.2002.05358.x.

Rodrigo Ibata, Michael Irwin, Geraint F. Lewis, and Andrea Stolte. Galactic Halo Substructure in the Sloan Digital Sky Survey: The Ancient Tidal Stream from the Sagittarius Dwarf Galaxy. *Astrophysical Journal, Letters*, 547(2):L133–L136, February 2001. doi:10.1086/318894.

Rodrigo Ibata, Khyati Malhan, Wassim Tenachi, Anke Ardern-Arentsen, Michele Bellazzini, Paolo Bianchini, Piercarlo Bonifacio, Elisabetta Caffau, Foivos Diakogiannis, Raphael Errani, Benoit Famaey, Salvatore Ferrone, Nicolas F. Martin, Paola di Matteo, Giacomo Monari, Florent Renaud, Else Starkenburg, Guillaume Thomas, Akshara Viswanathan, and Zhen Yuan. Charting the Galactic Acceleration Field. II. A Global Mass Model of the Milky Way from the STREAMFINDER Atlas of Stellar Streams Detected in Gaia DR3. *Astrophysical Journal*, 967(2):89, June 2024. doi:10.3847/1538-4357/ad382d.

Rodrigo A. Ibata, Khyati Malhan, and Nicolas F. Martin. The Streams of the Gaping Abyss: A Population of Entangled Stellar Streams Surrounding the Inner Galaxy. *Astrophysical Journal*, 872(2):152, February 2019. doi:10.3847/1538-4357/ab0080.

Giuliano Iorio and Vasily Belokurov. The shape of the Galactic halo with Gaia DR2 RR Lyrae. Anatomy of an ancient major merger. *Monthly Notices of the Royal Astronomical Society*, 482(3):3868–3879, January 2019. doi:10.1093/mnras/sty2806.

M. N. Ishigaki, W. Aoki, N. Arimoto, and S. Okamoto. Chemical compositions of six metal-poor stars in the ultra-faint dwarf spheroidal galaxy Boötes I. *Astronomy and Astrophysics*, 562:A146, February 2014. doi:10.1051/0004-6361/201322796.

Željko Ivezić, Steven M. Kahn, J. Anthony Tyson, Bob Abel, Emily Acosta, Robyn Allsman, David Alonso, Yusra AlSayyad, Scott F. Anderson, John Andrew, James Roger P. Angel, George Z. Angeli, Reza Ansari, Pierre Antilogus, Constanza Araujo, Robert Armstrong, Kirk T. Arndt, Pierre Astier, Éric Aubourg, Nicole Auza, Tim S. Axelrod, Deborah J. Bard, Jeff D. Barr, Aurelian Barrau, James G. Bartlett, Amanda E. Bauer, Brian J. Bauman, Sylvain Baumont, Ellen Bechtol,

Keith Bechtol, Andrew C. Becker, Jacek Becla, Cristina Beldica, Steve Bellavia, Federica B. Bianco, Rahul Biswas, Guillaume Blanc, Jonathan Blazek, Roger D. Blandford, Josh S. Bloom, Joanne Bogart, Tim W. Bond, Michael T. Booth, Anders W. Borgland, Kirk Borne, James F. Bosch, Dominique Boutigny, Craig A. Brackett, Andrew Bradshaw, William Nielsen Brandt, Michael E. Brown, James S. Bullock, Patricia Burchat, David L. Burke, Gianpietro Cagnoli, Daniel Calabrese, Shawn Callahan, Alice L. Callen, Jeffrey L. Carlin, Erin L. Carlson, Srinivasan Chandrasekharan, Glenaver Charles-Emerson, Steve Chesley, Elliott C. Cheu, Hsin-Fang Chiang, James Chiang, Carol Chirino, Derek Chow, David R. Ciardi, Charles F. Claver, Johann Cohen-Tanugi, Joseph J. Cockrum, Rebecca Coles, Andrew J. Connolly, Kem H. Cook, Asantha Cooray, Kevin R. Covey, Chris Cribbs, Wei Cui, Roc Cutri, Philip N. Daly, Scott F. Daniel, Felipe Daruich, Guillaume Daubard, Greg Daues, William Dawson, Francisco Delgado, Alfred Dellapenna, Robert de Peyster, Miguel de Val-Borro, Seth W. Digel, Peter Doherty, Richard Dubois, Gregory P. Dubois-Felsmann, Josef Durech, Frossie Economou, Tim Eifler, Michael Eracleous, Benjamin L. Emmons, Angelo Fausti Neto, Henry Ferguson, Enrique Figueroa, Merlin Fisher-Levine, Warren Focke, Michael D. Foss, James Frank, Michael D. Freemon, Emmanuel Gangler, Eric Gawiser, John C. Geary, Perry Gee, Marla Geha, Charles J. B. Gessner, Robert R. Gibson, D. Kirk Gilmore, Thomas Glanzman, William Glick, Tatiana Goldina, Daniel A. Goldstein, Iain Goodenow, Melissa L. Graham, William J. Gressler, Philippe Gris, Leanne P. Guy, Augustin Guyonnet, Gunther Haller, Ron Harris, Patrick A. Hascall, Justine Haupt, Fabio Hernandez, Sven Herrmann, Edward Hileman, Joshua Hoblitt, John A. Hodgson, Craig Hogan, James D. Howard, Dajun Huang, Michael E. Huffer, Patrick Ingraham, Walter R. Innes, Suzanne H. Jacoby, Bhuvnesh Jain, Fabrice Jammes, M. James Jee, Tim Jenness, Garrett Jernigan, Darko Jevremović, Kenneth Johns, Anthony S. Johnson, Margaret W. G. Johnson, R. Lynne Jones, Claire Juramy-Gilles, Mario Jurić, Jason S. Kalirai, Nitya J. Kallivayalil, Bryce Kalmbach, Jeffrey P. Kantor, Pierre Karst, Mansi M. Kasliwal, Heather Kelly, Richard Kessler, Veronica Kinnison, David Kirkby, Lloyd Knox, Ivan V. Kotov, Victor L. Krabbendam, K. Simon Krughoff, Petr Kubánek, John Kuczewski, Shri Kulkarni, John Ku, Nadine R. Kurita, Craig S. Lage, Ron Lambert, Travis Lange, J. Brian Langton, Laurent Le Guillou, Deborah Levine, Ming Liang, Kian-Tat Lim, Chris J. Lintott, Kevin E. Long, Margaux Lopez, Paul J. Lotz, Robert H. Lupton, Nate B. Lust, Lauren A. MacArthur, Ashish Mahabal, Rachel Mandelbaum, Thomas W. Markiewicz, Darren S. Marsh, Philip J. Marshall, Stuart Marshall, Morgan May, Robert McKercher, Michelle McQueen, Joshua Meyers, Myriam Migliore, Michelle Miller, David J. Mills, Connor Miraval, Joachim Moeyens,

Fred E. Moolekamp, David G. Monet, Marc Moniez, Serge Monkewitz, Christopher Montgomery, Christopher B. Morrison, Fritz Mueller, Gary P. Muller, Freddy Muñoz Arancibia, Douglas R. Neill, Scott P. Newbry, Jean-Yves Nief, Andrei Nomerotski, Martin Nordby, Paul O'Connor, John Oliver, Scot S. Olivier, Knut Olsen, William O'Mullane, Sandra Ortiz, Shawn Osier, Russell E. Owen, Reynald Pain, Paul E. Palecek, John K. Parejko, James B. Parsons, Nathan M. Pease, J. Matt Peterson, John R. Peterson, Donald L. Petravick, M. E. Libby Petrick, Cathy E. Petry, Francesco Pierfederici, Stephen Pietrowicz, Rob Pike, Philip A. Pinto, Raymond Plante, Stephen Plate, Joel P. Plutchak, Paul A. Price, Michael Prouza, Veljko Radeka, Jayadev Rajagopal, Andrew P. Rasmussen, Nicolas Regnault, Kevin A. Reil, David J. Reiss, Michael A. Reuter, Stephen T. Ridgway, Vincent J. Riot, Steve Ritz, Sean Robinson, William Roby, Aaron Roodman, Wayne Rosing, Cecille Roucelle, Matthew R. Rumore, Stefano Russo, Abhijit Saha, Benoit Sassolas, Terry L. Schalk, Pim Schellart, Rafe H. Schindler, Samuel Schmidt, Donald P. Schneider, Michael D. Schneider, William Schoening, German Schumacher, Megan E. Schwamb, Jacques Sebag, Brian Selvy, Glenn H. Sembroski, Lynn G. Seppala, Andrew Serio, Eduardo Serrano, Richard A. Shaw, Ian Shipsey, Jonathan Sick, Nicole Silvestri, Colin T. Slater, J. Allyn Smith, R. Chris Smith, Shahram Sobhani, Christine Soldahl, Lisa Storrie-Lombardi, Edward Stover, Michael A. Strauss, Rachel A. Street, Christopher W. Stubbs, Ian S. Sullivan, Donald Sweeney, John D. Swinbank, Alexander Szalay, Peter Takacs, Stephen A. Tether, Jon J. Thaler, John Gregg Thayer, Sandrine Thomas, Adam J. Thornton, Vaikunth Thukral, Jeffrey Tice, David E. Trilling, Max Turri, Richard Van Berg, Daniel Vanden Berk, Kurt Vetter, Francoise Virieux, Tomislav Vucina, William Wahl, Lucianne Walkowicz, Brian Walsh, Christopher W. Walter, Daniel L. Wang, Shin-Yawn Wang, Michael Warner, Oliver Wiecha, Beth Willman, Scott E. Winters, David Wittman, Sidney C. Wolff, W. Michael Wood-Vasey, Xiuqin Wu, Bo Xin, Peter Yoachim, and Hu Zhan. LSST: From Science Drivers to Reference Design and Anticipated Data Products. *Astrophysical Journal*, 873(2): 111, March 2019. doi:10.3847/1538-4357/ab042c.

R. G. Izzard, E. Glebbeek, R. J. Stancliffe, and O. R. Pols. Population synthesis of binary carbon-enhanced metal-poor stars. *Astronomy and Astrophysics*, 508(3): 1359–1374, December 2009. doi:10.1051/0004-6361/200912827.

Heather R. Jacobson, Stefan Keller, Anna Frebel, Andrew R. Casey, Martin Asplund, Michael S. Bessell, Gary S. Da Costa, Karin Lind, Anna F. Marino, John E. Norris, José M. Peña, Brian P. Schmidt, Patrick Tisserand, Jennifer M. Walsh, David Yong, and Qinsi Yu. High-Resolution Spectroscopic Study of Extremely Metal-

Poor Star Candidates from the SkyMapper Survey. *Astrophysical Journal*, 807(2): 171, July 2015. doi:10.1088/0004-637X/807/2/171.

P. Jethwa, D. Erkal, and V. Belokurov. The upper bound on the lowest mass halo. *Monthly Notices of the Royal Astronomical Society*, 473(2):2060–2083, January 2018. doi:10.1093/mnras/stx2330.

A. P. Ji, T. S. Li, J. D. Simon, J. Marshall, A. K. Vivas, A. B. Pace, K. Bechtol, A. Drlica-Wagner, S. E. Koposov, T. T. Hansen, S. Allam, R. A. Gruendl, M. D. Johnson, M. McNanna, N. E. D. Noël, D. L. Tucker, and A. R. Walker. Detailed Abundances in the Ultra-faint Magellanic Satellites Carina II and III. *Astrophysical Journal*, 889(1):27, January 2020a. doi:10.3847/1538-4357/ab6213.

Alexander P. Ji, Anna Frebel, Anirudh Chiti, and Joshua D. Simon. R-process enrichment from a single event in an ancient dwarf galaxy. *Nature*, 531(7596): 610–613, March 2016a. doi:10.1038/nature17425.

Alexander P. Ji, Anna Frebel, Joshua D. Simon, and Anirudh Chiti. Complete Element Abundances of Nine Stars in the r-process Galaxy Reticulum II. *Astrophysical Journal*, 830(2):93, October 2016b. doi:10.3847/0004-637X/830/2/93.

Alexander P. Ji, Anna Frebel, Joshua D. Simon, and Marla Geha. High-resolution Spectroscopy of Extremely Metal-poor Stars in the Least-evolved Galaxies: Bootes II. *Astrophysical Journal*, 817(1):41, January 2016c. doi:10.3847/0004-637X/817/1/41.

Alexander P. Ji, Joshua D. Simon, Anna Frebel, Kim A. Venn, and Terese T. Hansen. Chemical Abundances in the Ultra-faint Dwarf Galaxies Grus I and Triangulum II: Neutron-capture Elements as a Defining Feature of the Faintest Dwarfs. *Astrophysical Journal*, 870(2):83, January 2019. doi:10.3847/1538-4357/aaf3bb.

Alexander P. Ji, Ting S. Li, Terese T. Hansen, Andrew R. Casey, Sergey E. Koposov, Andrew B. Pace, Dougal Mackey, Geraint F. Lewis, Jeffrey D. Simpson, Joss Bland-Hawthorn, Lara R. Cullinane, Gary. S. Da Costa, Kohei Hattori, Sarah L. Martell, Kyler Kuehn, Denis Erkal, Nora Shipp, Zhen Wan, and Daniel B. Zucker. The Southern Stellar Stream Spectroscopic Survey (S^5): Chemical Abundances of Seven Stellar Streams. *Astronomical Journal*, 160(4):181, October 2020b. doi:10.3847/1538-3881/abacb6.

Alexander P. Ji, Sergey E. Koposov, Ting S. Li, Denis Erkal, Andrew B. Pace, Joshua D. Simon, Vasily Belokurov, Lara R. Cullinane, Gary S. Da Costa, Kyler

Kuehn, Geraint F. Lewis, Dougal Mackey, Nora Shipp, Jeffrey D. Simpson, Daniel B. Zucker, Terese T. Hansen, Joss Bland-Hawthorn, and S5 Collaboration. Kinematics of Antlia 2 and Crater 2 from the Southern Stellar Stream Spectroscopic Survey (S^5). *Astrophysical Journal*, 921(1):32, November 2021. doi:10.3847/1538-4357/ac1869.

Alexander P. Ji, Andrew R. Casey, Yuan-Sen Ting, Erika M. Holmbeck, Anna Frebel, Sam A. Usman, Guilherme Limberg, Shivani P. Shah, Anirudh Chiti, Rana Ezzeddine, Terese T. Hansen, Vinicius M. Placco, Ian U. Roederer, and Charli M. Sakari. LESSPayne: Labeling Echelle Spectra with SMHR and Payne. Astrophysics Source Code Library, record ascl:2503.025, March 2025.

Jun Ji and Joel N. Bregman. Binary Frequencies in a Sample of Globular Clusters. II. Sample Analysis and Comparison to Models. *The Astrophysical Journal*, 807 (1):32, July 2015. doi:10.1088/0004-637X/807/1/32.

Jennifer A. Johnson, Falk Herwig, Timothy C. Beers, and Norbert Christlieb. A Search for Nitrogen-enhanced Metal-poor Stars. *Astrophysical Journal*, 658(2): 1203–1216, April 2007. doi:10.1086/510114.

Kathryn V. Johnston. A Prescription for Building the Milky Way's Halo from Disrupted Satellites. *Astrophysical Journal*, 495(1):297–308, March 1998. doi:10.1086/305273.

Kathryn V. Johnston, David N. Spergel, and Christian Haydn. How Lumpy Is the Milky Way's Dark Matter Halo? *Astrophysical Journal*, 570(2):656–664, May 2002. doi:10.1086/339791.

Kathryn V. Johnston, James S. Bullock, Sanjib Sharma, Andreea Font, Brant E. Robertson, and Samuel N. Leitner. Tracing Galaxy Formation with Stellar Halos. II. Relating Substructure in Phase and Abundance Space to Accretion Histories. *Astrophysical Journal*, 689(2):936–957, December 2008. doi:10.1086/592228.

H. Jönsson, N. Ryde, T. Nordlander, A. Pehlivan Rhodin, H. Hartman, P. Jönsson, and K. Eriksson. Abundances of disk and bulge giants from high-resolution optical spectra. I. O, Mg, Ca, and Ti in the solar neighborhood and Kepler field samples. *Astronomy and Astrophysics*, 598:A100, February 2017. doi:10.1051/0004-6361/201629128.

Henrik Jönsson, Jon A. Holtzman, Carlos Allende Prieto, Katia Cunha, D. A. García-Hernández, Sten Hasselquist, Thomas Masseron, Yeisson Osorio, Matthew

Shetrone, Verne Smith, Guy S. Stringfellow, Dmitry Bizyaev, Bengt Edvardsson, Steven R. Majewski, Szabolcs Mészáros, Diogo Souto, Olga Zamora, Rachael L. Beaton, Jo Bovy, John Donor, Marc H. Pinsonneault, Vijith Jacob Poovelil, and Jennifer Sobeck. APOGEE Data and Spectral Analysis from SDSS Data Release 16: Seven Years of Observations Including First Results from APOGEE-South. *Astronomical Journal*, 160(3):120, September 2020. doi:10.3847/1538-3881/aba592.

D. Katz, P. Sartoretti, A. Guerrier, P. Panuzzo, G. M. Seabroke, F. Thévenin, M. Cropper, K. Benson, R. Blomme, R. Haigron, O. Marchal, M. Smith, S. Baker, L. Chemin, Y. Damerdji, M. David, C. Dolding, Y. Frémat, E. Gosset, K. Janßen, G. Jasniewicz, A. Lobel, G. Plum, N. Samaras, O. Snaith, C. Soubiran, O. Vanel, T. Zwitter, T. Antoja, F. Arenou, C. Babusiaux, N. Brouillet, E. Caffau, P. Di Matteo, C. Fabre, C. Fabricius, F. Fragkoudi, M. Haywood, H. E. Huckle, C. Hottier, Y. Lasne, N. Leclerc, A. Mastrobuono-Battisti, F. Royer, D. Teyssier, J. Zorec, F. Crifo, A. Jean-Antoine Piccolo, C. Turon, and Y. Viala. Gaia Data Release 3. Properties and validation of the radial velocities. *Astronomy and Astrophysics*, 674:A5, June 2023. doi:10.1051/0004-6361/202244220.

Daniel D. Kelson. Optimal Techniques in Two-dimensional Spectroscopy: Background Subtraction for the 21st Century. *Publications of the ASP*, 115(808):688–699, June 2003. doi:10.1086/375502.

Evan N. Kirby, Judith. G. Cohen, Graeme H. Smith, Steven R. Majewski, Sangmo Tony Sohn, and Puragra Guhathakurta. Multi-element Abundance Measurements from Medium-resolution Spectra. IV. Alpha Element Distributions in Milky Way Satellite Galaxies. *Astrophysical Journal*, 727(2):79, February 2011. doi:10.1088/0004-637X/727/2/79.

Evan N. Kirby, Judith G. Cohen, Puragra Guhathakurta, Lucy Cheng, James S. Bullock, and Anna Gallazzi. The Universal Stellar Mass-Stellar Metallicity Relation for Dwarf Galaxies. *Astrophysical Journal*, 779(2):102, December 2013. doi:10.1088/0004-637X/779/2/102.

Evan N. Kirby, Judith G. Cohen, Joshua D. Simon, Puragra Guhathakurta, Anders O. Thygesen, and Gina E. Duggan. Triangulum II. Not Especially Dense After All. *Astrophysical Journal*, 838(2):83, April 2017. doi:10.3847/1538-4357/aa6570.

Evan N. Kirby, Karoline M. Gilbert, Ivanna Escala, Jennifer Wojno, Puragra Guhathakurta, Steven R. Majewski, and Rachael L. Beaton. Elemental Abundances in M31: The Kinematics and Chemical Evolution of Dwarf

Spheroidal Satellite Galaxies. *Astronomical Journal*, 159(2):46, February 2020. doi:10.3847/1538-3881/ab5f0f.

Evan N. Kirby, Alexander P. Ji, and Mikhail Kovalev. r-process Abundance Patterns in the Globular Cluster M92. *Astrophysical Journal*, 958(1):45, November 2023. doi:10.3847/1538-4357/acf309.

A. Koch, S. Feltzing, D. Adén, and F. Matteucci. Neutron-capture element deficiency of the Hercules dwarf spheroidal galaxy. *Astronomy and Astrophysics*, 554:A5, June 2013. doi:10.1051/0004-6361/201220742.

Andreas Koch, Andrew McWilliam, Eva K. Grebel, Daniel B. Zucker, and Vasily Belokurov. The Highly Unusual Chemical Composition of the Hercules Dwarf Spheroidal Galaxy. *Astrophysical Journal, Letters*, 688(1):L13, November 2008. doi:10.1086/595001.

S. E. Koposov, V. Belokurov, T. S. Li, C. Mateu, D. Erkal, C. J. Grillmair, D. Hendel, A. M. Price-Whelan, C. F. P. Laporte, K. Hawkins, S. T. Sohn, A. del Pino, N. W. Evans, C. T. Slater, N. Kallivayalil, J. F. Navarro, and Orphan Aspen Treasury Collaboration. Piercing the Milky Way: an all-sky view of the Orphan Stream. *Monthly Notices of the Royal Astronomical Society*, 485(4):4726–4742, June 2019. doi:10.1093/mnras/stz457.

Sergey Koposov, Josh Speagle, Kyle Barbary, Gregory Ashton, Ed Bennett, Johannes Buchner, Carl Scheffler, Ben Cook, Colm Talbot, James Guillochon, Patricio Cubillos, Andrés Asensio Ramos, Ben Johnson, Dustin Lang, Ilya, Matthieu Dartiailh, Alex Nitz, Andrew McCluskey, Anne Archibald, Christoph Deil, Dan Foreman-Mackey, Danny Goldstein, Erik Tollerud, Joel Leja, Matthew Kirk, Matt Pitkin, Patrick Sheehan, Phillip Cargile, Ruskin23, and Ruth Angus. joshspeagle/dynesty: v2.0.3. Zenodo, December 2022.

Sergey E. Koposov, Hans-Walter Rix, and David W. Hogg. Constraining the Milky Way Potential with a Six-Dimensional Phase-Space Map of the GD-1 Stellar Stream. *Astrophysical Journal*, 712(1):260–273, March 2010. doi:10.1088/0004-637X/712/1/260.

Helmer H. Koppelman, Amina Helmi, Davide Massari, Adrian M. Price-Whelan, and Tjitske K. Starkenburg. Multiple retrograde substructures in the Galactic halo: A shattered view of Galactic history. *Astronomy and Astrophysics*, 631:L9, November 2019. doi:10.1051/0004-6361/201936738.

Pavel Kroupa. On the variation of the initial mass function. *Monthly Notices of the Royal Astronomical Society*, 322(2):231–246, April 2001. doi:10.1046/j.1365-8711.2001.04022.x.

J. M. D. Kruijssen and H. J. G. L. M. Lamers. The photometric evolution of star clusters and the preferential loss of low-mass bodies - with an application to globular clusters. *Astronomy and Astrophysics*, 490(1):151–171, October 2008. doi:10.1051/0004-6361:200810167.

J. M. D. Kruijssen and S. Mieske. Dissolution is the solution: on the reduced mass-to-light ratios of Galactic globular clusters. *Astronomy and Astrophysics*, 500(2): 785–799, June 2009. doi:10.1051/0004-6361/200811453.

H. J. G. L. M. Lamers, M. Gieles, N. Bastian, H. Baumgardt, N. V. Kharchenko, and S. Portegies Zwart. An analytical description of the disruption of star clusters in tidal fields with an application to Galactic open clusters. *Astronomy and Astrophysics*, 441(1):117–129, October 2005. doi:10.1051/0004-6361:20042241.

Henny J. G. L. M. Lamers, Holger Baumgardt, and Mark Gieles. Mass-loss rates and the mass evolution of star clusters. *Monthly Notices of the Royal Astronomical Society*, 409(1):305–328, November 2010. doi:10.1111/j.1365-2966.2010.17309.x.

C. Lardo, M. Bellazzini, E. Pancino, E. Carretta, A. Bragaglia, and E. Dalessandro. Mining SDSS in search of multiple populations in globular clusters. *Astronomy and Astrophysics*, 525:A114, January 2011. doi:10.1051/0004-6361/201015662.

A. Lauberts. *ESO/Uppsala survey of the ESO(B) atlas*. European Southern Observatory, 1982.

Jae-Woo Lee. Multiple Stellar Populations of Globular Clusters from Homogeneous Ca-CN Photometry. II. M5 (NGC 5904) and a New Filter System. *Astrophysical Journal*, 844(1):77, July 2017. doi:10.3847/1538-4357/aa7b8c.

Young Sun Lee, Timothy C. Beers, and Young Kwang Kim. Chemical Cartography. II. The Assembly History of the Galactic Stellar Halo Traced by Carbon-enhanced Metal-poor Stars. *Astrophysical Journal*, 885(2):102, November 2019. doi:10.3847/1538-4357/ab4791.

B. Lemasle, T. J. L. de Boer, V. Hill, E. Tolstoy, M. J. Irwin, P. Jablonka, K. Venn, G. Battaglia, E. Starkenburg, M. Shetrone, B. Letarte, P. François, A. Helmi, F. Primas, A. Kaufer, and T. Szeifert. VLT/FLAMES spectroscopy of red giant

branch stars in the Fornax dwarf spheroidal galaxy. *Astronomy and Astrophysics*, 572:A88, December 2014. doi:10.1051/0004-6361/201423919.

Hefan Li, Francois Hammer, Carine Babusiaux, Marcel S. Pawlowski, Yanbin Yang, Frederic Arenou, Cuihua Du, and Jianling Wang. Gaia EDR3 Proper Motions of Milky Way Dwarfs. I. 3D Motions and Orbits. *Astrophysical Journal*, 916(1):8, July 2021. doi:10.3847/1538-4357/ac0436.

T. S. Li, J. D. Simon, K. Kuehn, A. B. Pace, D. Erkal, K. Bechtol, B. Yanny, A. Drlica-Wagner, J. L. Marshall, C. Lidman, E. Balbinot, D. Carollo, S. Jenkins, C. E. Martínez-Vázquez, N. Shipp, K. M. Stringer, A. K. Vivas, A. R. Walker, R. H. Wechsler, F. B. Abdalla, S. Allam, J. Annis, S. Avila, E. Bertin, D. Brooks, E. Buckley-Geer, D. L. Burke, A. Carnero Rosell, M. Carrasco Kind, J. Carretero, C. E. Cunha, C. B. D'Andrea, L. N. da Costa, C. Davis, J. De Vicente, P. Doel, T. F. Eifler, A. E. Evrard, B. Flaugher, J. Frieman, J. García-Bellido, E. Gaztanaga, D. W. Gerdes, D. Gruen, R. A. Gruendl, J. Gschwend, G. Gutierrez, W. G. Hartley, D. L. Hollowood, K. Honscheid, D. J. James, E. Krause, M. A. G. Maia, M. March, F. Menanteau, R. Miquel, A. A. Plazas, E. Sanchez, B. Santiago, V. Scarpine, R. Schindler, M. Schubnell, I. Sevilla-Noarbe, M. Smith, R. C. Smith, M. Soares-Santos, F. Sobreira, E. Suchyta, M. E. C. Swanson, G. Tarle, D. L. Tucker, and DES Collaboration. The First Tidally Disrupted Ultra-faint Dwarf Galaxy?: A Spectroscopic Analysis of the Tucana III Stream. *Astrophysical Journal*, 866(1):22, October 2018. doi:10.3847/1538-4357/aadf91.

T. S. Li, S. E. Koposov, D. B. Zucker, G. F. Lewis, K. Kuehn, J. D. Simpson, A. P. Ji, N. Shipp, Y. Y. Mao, M. Geha, A. B. Pace, A. D. Mackey, S. Allam, D. L. Tucker, G. S. Da Costa, D. Erkal, J. D. Simon, J. R. Mould, S. L. Martell, Z. Wan, G. M. De Silva, K. Bechtol, E. Balbinot, V. Belokurov, J. Bland-Hawthorn, A. R. Casey, L. Cullinane, A. Drlica-Wagner, S. Sharma, A. K. Vivas, R. H. Wechsler, B. Yanny, and S5 Collaboration. The southern stellar stream spectroscopic survey (S^5): Overview, target selection, data reduction, validation, and early science. *Monthly Notices of the Royal Astronomical Society*, 490(3):3508–3531, December 2019. doi:10.1093/mnras/stz2731.

Ting S. Li, Alexander P. Ji, Andrew B. Pace, Denis Erkal, Sergey E. Koposov, Nora Shipp, Gary S. Da Costa, Lara R. Cullinane, Kyler Kuehn, Geraint F. Lewis, Dougal Mackey, Jeffrey D. Simpson, Daniel B. Zucker, Peter S. Ferguson, Sarah L. Martell, Joss Bland-Hawthorn, Eduardo Balbinot, Kiyan Tavangar, Alex Drlica-Wagner, Gayandhi M. De Silva, and Joshua D. Simon. S ^{5}: The Orbital and

Chemical Properties of One Dozen Stellar Streams. *Astrophysical Journal*, 928(1): 30, March 2022. doi:10.3847/1538-4357/ac46d3.

Guilherme Limberg, Silvia Rossi, Timothy C. Beers, Hélio D. Perottoni, Angeles Pérez-Villegas, Rafael M. Santucci, Yuri Abuchaim, Vinicius M. Placco, Young Sun Lee, Norbert Christlieb, John E. Norris, Michael S. Bessell, Sean G. Ryan, Ronald Wilhelm, Jaehyon Rhee, and Anna Frebel. Dynamically Tagged Groups of Very Metal-poor Halo Stars from the HK and Hamburg/ESO Surveys. *Astrophysical Journal*, 907(1):10, January 2021a. doi:10.3847/1538-4357/abcb87.

Guilherme Limberg, Rafael M. Santucci, Silvia Rossi, Anna B. A. Queiroz, Cristina Chiappini, Stefano O. Souza, Hélio D. Perottoni, Angeles Pérez-Villegas, and Fabrícia O. Barbosa. Abundance Patterns of α and Neutron-capture Elements in the Helmi Stream. *Astrophysical Journal, Letters*, 913(2):L28, June 2021b. doi:10.3847/2041-8213/ac0056.

Guilherme Limberg, Stefano O. Souza, Angeles Pérez-Villegas, Silvia Rossi, Hélio D. Perottoni, and Rafael M. Santucci. Reconstructing the Disrupted Dwarf Galaxy Gaia-Sausage/Enceladus Using Its Stars and Globular Clusters. *Astrophysical Journal*, 935(2):109, August 2022. doi:10.3847/1538-4357/ac8159.

Guilherme Limberg, Alexander P. Ji, Rohan P. Naidu, Anirudh Chiti, Silvia Rossi, Sam A. Usman, Yuan-Sen Ting, Dennis Zaritsky, Ana Bonaca, Lais Borbolato, Joshua S. Speagle, Vedant Chandra, and Charlie Conroy. Extending the chemical reach of the H3 survey: detailed abundances of the dwarf-galaxy stellar stream Wukong/LMS-1. *Monthly Notices of the Royal Astronomical Society*, 530(3):2512–2525, May 2024. doi:10.1093/mnras/stae969.

K. Lind, M. Asplund, P. S. Barklem, and A. K. Belyaev. Non-LTE calculations for neutral Na in late-type stars using improved atomic data. *Astronomy and Astrophysics*, 528:A103, April 2011. doi:10.1051/0004-6361/201016095.

K. Lind, M. Bergemann, and M. Asplund. Non-LTE line formation of Fe in late-type stars - II. 1D spectroscopic stellar parameters. *Monthly Notices of the Royal Astronomical Society*, 427(1):50–60, November 2012. doi:10.1111/j.1365-2966.2012.21686.x.

L. Lindegren, S. A. Klioner, J. Hernández, A. Bombrun, M. Ramos-Lerate, H. Steidelmüller, U. Bastian, M. Biermann, A. de Torres, E. Gerlach, R. Geyer, T. Hilger, D. Hobbs, U. Lammers, P. J. McMillan, C. A. Stephenson, J. Castañeda, M. Davidson, C. Fabricius, G. Gracia-Abril, J. Portell, N. Rowell, D. Teyssier, F. Torra,

S. Bartolomé, M. Clotet, N. Garralda, J. J. González-Vidal, J. Torra, U. Abbas, M. Altmann, E. Anglada Varela, L. Balaguer-Núñez, Z. Balog, C. Barache, U. Becciani, M. Bernet, S. Bertone, L. Bianchi, S. Bouquillon, A. G. A. Brown, B. Bucciarelli, D. Busonero, A. G. Butkevich, R. Buzzi, R. Cancelliere, T. Carlucci, P. Charlot, M. R. L. Cioni, M. Crosta, C. Crowley, E. F. del Peloso, E. del Pozo, R. Drimmel, P. Esquej, A. Fienga, E. Fraile, M. Gai, M. Garcia-Reinaldos, R. Guerra, N. C. Hambly, M. Hauser, K. Janßen, S. Jordan, Z. Kostrzewa-Rutkowska, M. G. Lattanzi, S. Liao, E. Licata, T. A. Lister, W. Löffler, J. M. Marchant, A. Masip, F. Mignard, A. Mints, D. Molina, A. Mora, R. Morbidelli, C. P. Murphy, C. Pagani, P. Panuzzo, X. Peñalosa Esteller, E. Poggio, P. Re Fiorentin, A. Riva, A. Sagristà Sellés, V. Sanchez Gimenez, M. Sarasso, E. Sciacca, H. I. Siddiqui, R. L. Smart, D. Souami, A. Spagna, I. A. Steele, F. Taris, E. Utrilla, W. van Reeven, and A. Vecchiato. Gaia Early Data Release 3. The astrometric solution. *Astronomy and Astrophysics*, 649:A2, May 2021. doi:10.1051/0004-6361/202039709.

M. Lomaeva, H. Jönsson, N. Ryde, M. Schultheis, and B. Thorsbro. Abundances of disk and bulge giants from high-resolution optical spectra. III. Sc, V, Cr, Mn, Co, Ni. *Astronomy and Astrophysics*, 625:A141, May 2019. doi:10.1051/0004-6361/201834247.

Sara Lucatello, Raffaele Gratton, Judith G. Cohen, Timothy C. Beers, Norbert Christlieb, Eugenio Carretta, and Solange Ramírez. Stellar Archaeology: A Keck Pilot Program on Extremely Metal-Poor Stars From the Hamburg/ESO Survey. III. The Lead (Pb) Star HE 0024-2523. *Astronomical Journal*, 125(2):875–893, February 2003. doi:10.1086/345886.

R. E. Luck and Howard E. Bond. Subgiant CH Stars. II. Chemical Compositions and the Evolutionary Connection with Barium Stars. *Astrophysical Journal, Supplement*, 77:515, December 1991. doi:10.1086/191615.

Steven R. Majewski, M. F. Skrutskie, Martin D. Weinberg, and James C. Ostheimer. A Two Micron All Sky Survey View of the Sagittarius Dwarf Galaxy. I. Morphology of the Sagittarius Core and Tidal Arms. *Astrophysical Journal*, 599(2):1082–1115, December 2003. doi:10.1086/379504.

Khyati Malhan, Monica Valluri, and Katherine Freese. Probing the nature of dark matter with accreted globular cluster streams. *Monthly Notices of the Royal Astronomical Society*, 501(1):179–200, February 2021. doi:10.1093/mnras/staa3597.

Khyati Malhan, Rodrigo A. Ibata, Sanjib Sharma, Benoit Famaey, Michele Bellazzini, Raymond G. Carlberg, Richard D'Souza, Zhen Yuan, Nicolas F. Martin, and Guillaume F. Thomas. The Global Dynamical Atlas of the Milky Way Mergers: Constraints from Gaia EDR3-based Orbits of Globular Clusters, Stellar Streams, and Satellite Galaxies. *Astrophysical Journal*, 926(2):107, February 2022. doi:10.3847/1538-4357/ac4d2a.

Michela Mapelli. Binary black hole mergers: formation and populations. *Frontiers in Astronomy and Space Sciences*, 7:38, July 2020. doi:10.3389/fspas.2020.00038.

J. L. Marshall, T. Hansen, J. D. Simon, T. S. Li, R. A. Bernstein, K. Kuehn, A. B. Pace, D. L. DePoy, A. Palmese, A. Pieres, L. Strigari, A. Drlica-Wagner, K. Bechtol, C. Lidman, D. Q. Nagasawa, E. Bertin, D. Brooks, E. Buckley-Geer, D. L. Burke, A. Carnero Rosell, M. Carrasco Kind, J. Carretero, C. E. Cunha, C. B. D'Andrea, L. N. da Costa, J. De Vicente, S. Desai, P. Doel, T. F. Eifler, B. Flaugher, P. Fosalba, J. Frieman, J. García-Bellido, E. Gaztanaga, D. W. Gerdes, R. A. Gruendl, J. Gschwend, G. Gutierrez, W. G. Hartley, D. L. Hollowood, K. Honscheid, B. Hoyle, D. J. James, N. Kuropatkin, M. A. G. Maia, F. Menanteau, C. J. Miller, R. Miquel, A. A. Plazas, E. Sanchez, B. Santiago, V. Scarpine, M. Schubnell, S. Serrano, I. Sevilla-Noarbe, M. Smith, M. Soares-Santos, E. Suchyta, M. E. C. Swanson, G. Tarle, W. Wester, and DES Collaboration. Chemical Abundance Analysis of Tucana III, the Second r-process Enhanced Ultra-faint Dwarf Galaxy. *Astrophysical Journal*, 882(2):177, September 2019. doi:10.3847/1538-4357/ab3653.

S. L. Martell, J. P. Smolinski, T. C. Beers, and E. K. Grebel. Building the Galactic halo from globular clusters: evidence from chemically unusual red giants. *Astronomy and Astrophysics*, 534:A136, October 2011. doi:10.1051/0004-6361/201117644.

Sarah L. Martell, Matthew D. Shetrone, Sara Lucatello, Ricardo P. Schiavon, Szabolcs Mészáros, Carlos Allende Prieto, D. A. García-Hernández, Timothy C. Beers, and David L. Nidever. Chemical Tagging in the SDSS-III/APOGEE Survey: New Identifications of Halo Stars with Globular Cluster Origins. *Astrophysical Journal*, 825(2):146, July 2016. doi:10.3847/0004-637X/825/2/146.

Nicolas F. Martin, Jelte T. A. de Jong, and Hans-Walter Rix. A Comprehensive Maximum Likelihood Analysis of the Structural Properties of Faint Milky Way Satellites. *Astrophysical Journal*, 684(2):1075–1092, September 2008. doi:10.1086/590336.

Nicolas F. Martin, Rodrigo A. Ibata, Geraint F. Lewis, Alan McConnachie, Arif Babul, Nicholas F. Bate, Edouard Bernard, Scott C. Chapman, Michelle M. L. Collins, Anthony R. Conn, Denija Crnojević, Mark A. Fardal, Annette M. N. Ferguson, Michael Irwin, A. Dougal Mackey, Brendan McMonigal, Julio F. Navarro, and R. Michael Rich. The PAndAS View of the Andromeda Satellite System. II. Detailed Properties of 23 M31 Dwarf Spheroidal Galaxies. *Astrophysical Journal*, 833(2):167, December 2016. doi:10.3847/1538-4357/833/2/167.

Nicolas F. Martin, Rodrigo A. Ibata, Else Starkenburg, Zhen Yuan, Khyati Malhan, Michele Bellazzini, Akshara Viswanathan, David Aguado, Anke Arentsen, Piercarlo Bonifacio, Ray Carlberg, Jonay I. González Hernández, Vanessa Hill, Pascale Jablonka, Georges Kordopatis, Carmela Lardo, Alan W. McConnachie, Julio Navarro, Rubén Sánchez-Janssen, Federico Sestito, Guillaume F. Thomas, Kim A. Venn, Sara Vitali, and Karina T. Voggel. The Pristine survey - XVI. The metallicity of 26 stellar streams around the Milky Way detected with the STREAMFINDER in Gaia EDR3. *Monthly Notices of the RAS*, 516(4):5331–5354, November 2022. doi:10.1093/mnras/stac2426.

S. Martocchia, N. Bastian, C. Usher, V. Kozhurina-Platais, F. Niederhofer, I. Cabrera-Ziri, E. Dalessandro, K. Hollyhead, N. Kacharov, C. Lardo, S. Larsen, A. Mucciarelli, I. Platais, M. Salaris, M. Cordero, D. Geisler, M. Hilker, C. Li, and D. Mackey. The search for multiple populations in Magellanic Cloud Clusters - III. No evidence for multiple populations in the SMC cluster NGC 419. *Monthly Notices of the Royal Astronomical Society*, 468(3):3150–3158, July 2017. doi:10.1093/mnras/stx660.

S. Martocchia, F. Niederhofer, E. Dalessandro, N. Bastian, N. Kacharov, C. Usher, I. Cabrera-Ziri, C. Lardo, S. Cassisi, D. Geisler, M. Hilker, K. Hollyhead, V. Kozhurina-Platais, S. Larsen, D. Mackey, A. Mucciarelli, I. Platais, and M. Salaris. The search for multiple populations in Magellanic Cloud clusters - IV. Coeval multiple stellar populations in the young star cluster NGC 1978. *Monthly Notices of the Royal Astronomical Society*, 477(4):4696–4705, July 2018. doi:10.1093/mnras/sty916.

L. Mashonkina. Astrophysical tests of atomic data important for the stellar Mg abundance determinations. *Astronomy and Astrophysics*, 550:A28, February 2013. doi:10.1051/0004-6361/201220761.

L. Mashonkina and T. Gehren. Heavy element abundances in cool dwarf stars: An

implication for the evolution of the Galaxy. *Astronomy and Astrophysics*, 376: 232–247, September 2001. doi:10.1051/0004-6361:20010965.

L. Mashonkina, T. Gehren, and I. Bikmaev. Barium abundances in cool dwarf stars as a constraint to s- and r-process nucleosynthesis. *Astronomy and Astrophysics*, 343:519–530, March 1999.

L. Mashonkina, A. J. Korn, and N. Przybilla. A non-LTE study of neutral and singly-ionized calcium in late-type stars. *Astronomy and Astrophysics*, 461(1):261–275, January 2007. doi:10.1051/0004-6361:20065999.

L. Mashonkina, P. Jablonka, T. Sitnova, Yu. Pakhomov, and P. North. The formation of the Milky Way halo and its dwarf satellites; a NLTE-1D abundance analysis. II. Early chemical enrichment, December 2017.

L. Mashonkina, A. Arentsen, D. S. Aguado, A. Smogorzhevskii, M. Hampel, A. I. Karakas, F. Sestito, N. F. Martin, K. A. Venn, and J. I. González Hernández. The Pristine Inner Galaxy Survey (PIGS) VII: a discovery of the first inner Galaxy CEMP-r/s star. *Monthly Notices of the Royal AStronomical Society*, 523(2):2111–2125, August 2023. doi:10.1093/mnras/stad1536.

L. I. Mashonkina and T. A. Ryabchikova. Non-LTE abundances of nitrogen in the Sun and reference A-F type stars. *arXiv e-prints*, art. arXiv:2406.11367, June 2024. doi:10.48550/arXiv.2406.11367.

D. Massari, H. H. Koppelman, and A. Helmi. Origin of the system of globular clusters in the Milky Way. *Astronomy and Astrophysics*, 630:L4, October 2019. doi:10.1051/0004-6361/201936135.

R. Mateluna, D. Geisler, S. Villanova, G. Carraro, A. Grocholski, A. Sarajedini, A. Cole, and V. Smith. Chemical abundances in the old LMC globular cluster Hodge 11. *Astronomy and Astrophysics*, 548:A82, December 2012. doi:10.1051/0004-6361/201219750.

Cecilia Mateu. galstreams: A library of Milky Way stellar stream footprints and tracks. *Monthly Notices of the Royal Astronomical Society*, 520(4):5225–5258, April 2023. doi:10.1093/mnras/stad321.

Cecilia Mateu, Justin I. Read, and Daisuke Kawata. Fourteen candidate RR Lyrae star streams in the inner Galaxy. *Monthly Notices of the Royal Astronomical Society*, 474(3):4112–4129, March 2018. doi:10.1093/mnras/stx2937.

Tadafumi Matsuno, Wako Aoki, and Takuma Suda. Origin of the Excess of High-energy Retrograde Stars in the Galactic Halo. *Astrophysical Journal, Letters*, 874 (2):L35, April 2019. doi:10.3847/2041-8213/ab0ec0.

Tadafumi Matsuno, Emma Dodd, Helmer H. Koppelman, Amina Helmi, Miho N. Ishigaki, Wako Aoki, Jingkun Zhao, Zhen Yuan, and Kohei Hattori. High-precision chemical abundances of Galactic building blocks. II. Revisiting the chemical distinctness of the Helmi streams. *Astronomy and Astrophysics*, 665:A46, September 2022. doi:10.1051/0004-6361/202243609.

Francesca Matteucci and Enzo Brocato. Metallicity Distribution and Abundance Ratios in the Stars of the Galactic Bulge. *Astrophysical Journal*, 365:539, December 1990. doi:10.1086/169508.

R. D. McClure, J. M. Fletcher, and J. M. Nemec. The binary nature of the barium stars. *Astrophysical Journal, Letters*, 238:L35–L38, May 1980. doi:10.1086/183252.

Robert D. McClure and A. W. Woodsworth. The Binary Nature of the Barium and CH Stars. III. Orbital Parameters. *Astrophysical Journal*, 352:709, April 1990. doi:10.1086/168573.

M. McKenzie, D. Yong, A. F. Marino, S. Monty, E. Wang, A. I. Karakas, A. P. Milone, M. V. Legnardi, I. U. Roederer, S. Martell, and D. Horta. The complex stellar system M 22: confirming abundance variations with high precision differential measurements. *Monthly Notices of the Royal Astronomical Society*, 516(3): 3515–3531, November 2022. doi:10.1093/mnras/stac2254.

Andrew McWilliam. Abundance Ratios and Galactic Chemical Evolution. *Annual Review of Astronomy and Astrophysics*, 35:503–556, January 1997. doi:10.1146/annurev.astro.35.1.503.

Andrew McWilliam, George Wallerstein, and Marta Mottini. Chemistry of the Sagittarius Dwarf Galaxy: A Top-light Initial Mass Function, Outflows, and the R-process. *Astrophysical Journal*, 778(2):149, December 2013. doi:10.1088/0004-637X/778/2/149.

Andrew McWilliam, Anthony L. Piro, Carles Badenes, and Eduardo Bravo. Evidence for a Sub-Chandrasekhar-mass Type Ia Supernova in the Ursa Minor Dwarf Galaxy. *Astrophysical Journal*, 857(2):97, April 2018. doi:10.3847/1538-4357/aab772.

Martín Federico Mestre, Carlos Raul Argüelles, Daniel Diego Carpintero, Valentina Crespi, and Andreas Krut. Modeling the track of the GD-1 stellar stream inside a host with a fermionic dark matter core-halo distribution. *Astronomy and Astrophysics*, 689:A194, September 2024. doi:10.1051/0004-6361/202348626.

Sz. Mészáros, C. Allende Prieto, B. Edvardsson, F. Castelli, A. E. García Pérez, B. Gustafsson, S. R. Majewski, B. Plez, R. Schiavon, M. Shetrone, and A. de Vicente. New ATLAS9 and MARCS Model Atmosphere Grids for the Apache Point Observatory Galactic Evolution Experiment (APOGEE). *Astronomical Journal*, 144(4):120, October 2012. doi:10.1088/0004-6256/144/4/120.

Szabolcs Mészáros, Sarah L. Martell, Matthew Shetrone, Sara Lucatello, Nicholas W. Troup, Jo Bovy, Katia Cunha, Domingo A. García-Hernández, Jamie C. Overbeek, Carlos Allende Prieto, Timothy C. Beers, Peter M. Frinchaboy, Ana E. García Pérez, Fred R. Hearty, Jon Holtzman, Steven R. Majewski, David L. Nidever, Ricardo P. Schiavon, Donald P. Schneider, Jennifer S. Sobeck, Verne V. Smith, Olga Zamora, and Gail Zasowski. Exploring Anticorrelations and Light Element Variations in Northern Globular Clusters Observed by the APOGEE Survey. *Astronomical Journal*, 149(5):153, May 2015. doi:10.1088/0004-6256/149/5/153.

Szabolcs Mészáros, Thomas Masseron, D. A. García-Hernández, Carlos Allende Prieto, Timothy C. Beers, Dmitry Bizyaev, Drew Chojnowski, Roger E. Cohen, Katia Cunha, Flavia Dell'Agli, Garrett Ebelke, José G. Fernández-Trincado, Peter Frinchaboy, Doug Geisler, Sten Hasselquist, Fred Hearty, Jon Holtzman, Jennifer Johnson, Richard R. Lane, Ivan Lacerna, Penelopé Longa-Peña, Steven R. Majewski, Sarah L. Martell, Dante Minniti, David Nataf, David L. Nidever, Kaike Pan, Ricardo P. Schiavon, Matthew Shetrone, Verne V. Smith, Jennifer S. Sobeck, Guy S. Stringfellow, László Szigeti, Baitian Tang, John C. Wilson, and Olga Zamora. Homogeneous analysis of globular clusters from the APOGEE survey with the BACCHUS code - II. The Southern clusters and overview. *Monthly Notices of the Royal Astronomical Society*, 492(2):1641–1670, February 2020. doi:10.1093/mnras/stz3496.

A. P. Milone, A. F. Marino, G. Piotto, L. R. Bedin, J. Anderson, A. Aparicio, A. Bellini, S. Cassisi, F. D'Antona, F. Grundahl, M. Monelli, and D. Yong. A WFC3/HST View of the Three Stellar Populations in the Globular Cluster NGC 6752. *The Astrophysical Journal*, 767(2):120, April 2013. doi:10.1088/0004-637X/767/2/120.

A. P. Milone, G. Piotto, A. Renzini, A. F. Marino, L. R. Bedin, E. Vesperini,

F. D'Antona, D. Nardiello, J. Anderson, I. R. King, D. Yong, A. Bellini, A. Aparicio, B. Barbuy, T. M. Brown, S. Cassisi, S. Ortolani, M. Salaris, A. Sarajedini, and R. P. van der Marel. The Hubble Space Telescope UV Legacy Survey of Galactic globular clusters - IX. The Atlas of multiple stellar populations. *Monthly Notices of the Royal Astronomical Society*, 464(3):3636–3656, January 2017. doi:10.1093/mnras/stw2531.

A. P. Milone, A. F. Marino, L. R. Bedin, J. Anderson, D. Apai, A. Bellini, A. Dieball, M. Salaris, M. Libralato, D. Nardiello, P. Bergeron, A. J. Burgasser, J. M. Rees, R. M. Rich, and H. B. Richer. The HST Large Programme on NGC 6752 - II. Multiple populations at the bottom of the main sequence probed in NIR. *Monthly Notices of the Royal Astronomical Society*, 484(3):4046–4053, April 2019. doi:10.1093/mnras/stz277.

A. P. Milone, A. F. Marino, G. S. Da Costa, E. P. Lagioia, F. D'Antona, P. Goudfrooij, H. Jerjen, D. Massari, A. Renzini, D. Yong, H. Baumgardt, G. Cordoni, E. Dondoglio, C. Li, M. Tailo, R. Asa'd, and E. M. Ventura. Multiple populations in globular clusters and their parent galaxies. *Monthly Notices of the Royal Astronomical Society*, 491(1):515–531, January 2020. doi:10.1093/mnras/stz2999.

Antonino P Milone and Anna F Marino. Multiple populations in star clusters. *Universe*, 8:359, 6 2022. doi:10.3390/universe8070359.

A. Mucciarelli, E. Dalessandro, F. R. Ferraro, L. Origlia, and B. Lanzoni. No Evidence of Chemical Anomalies in the Bimodal Turnoff Cluster NGC 1806 in the Large Magellanic Cloud. *Astrophysical Journal, Letters*, 793(1):L6, September 2014. doi:10.1088/2041-8205/793/1/L6.

A. Mucciarelli, M. Bellazzini, R. Ibata, D. Romano, S. C. Chapman, and L. Monaco. Chemical abundances in the nucleus of the Sagittarius dwarf spheroidal galaxy. *Astronomy and Astrophysics*, 605:A46, September 2017. doi:10.1051/0004-6361/201730707.

A. Mucciarelli, M. Bellazzini, and D. Massari. Exploiting the Gaia EDR3 photometry to derive stellar temperatures. *Astronomy and Astrophysics*, 653:A90, September 2021. doi:10.1051/0004-6361/202140979.

Alessio Mucciarelli, Livia Origlia, Francesco R. Ferraro, and Elena Pancino. Looking Outside the Galaxy: The Discovery of Chemical Anomalies in Three Old Large Magellanic Cloud Clusters. *Astrophysical Journal, Letters*, 695(2):L134–L139, April 2009. doi:10.1088/0004-637X/695/2/L134.

G. C. Myeong, N. W. Evans, V. Belokurov, J. L. Sanders, and S. E. Koposov. The Sausage Globular Clusters. *Astrophysical Journal, Letters*, 863(2):L28, August 2018. doi:10.3847/2041-8213/aad7f7.

G. C. Myeong, E. Vasiliev, G. Iorio, N. W. Evans, and V. Belokurov. Evidence for two early accretion events that built the Milky Way stellar halo. *Monthly Notices of the Royal Astronomical Society*, 488(1):1235–1247, September 2019. doi:10.1093/mnras/stz1770.

E. O. Nadler, A. Drlica-Wagner, K. Bechtol, S. Mau, R. H. Wechsler, V. Gluscevic, K. Boddy, A. B. Pace, T. S. Li, M. McNanna, A. H. Riley, J. García-Bellido, Y. Y. Mao, G. Green, D. L. Burke, A. Peter, B. Jain, T. M. C. Abbott, M. Aguena, S. Allam, J. Annis, S. Avila, D. Brooks, M. Carrasco Kind, J. Carretero, M. Costanzi, L. N. da Costa, J. De Vicente, S. Desai, H. T. Diehl, P. Doel, S. Everett, A. E. Evrard, B. Flaugher, J. Frieman, D. W. Gerdes, D. Gruen, R. A. Gruendl, J. Gschwend, G. Gutierrez, S. R. Hinton, K. Honscheid, D. Huterer, D. J. James, E. Krause, K. Kuehn, N. Kuropatkin, O. Lahav, M. A. G. Maia, J. L. Marshall, F. Menanteau, R. Miquel, A. Palmese, F. Paz-Chinchón, A. A. Plazas, A. K. Romer, E. Sanchez, V. Scarpine, S. Serrano, I. Sevilla-Noarbe, M. Smith, M. Soares-Santos, E. Suchyta, M. E. C. Swanson, G. Tarle, D. L. Tucker, A. R. Walker, W. Wester, and DES Collaboration. Constraints on Dark Matter Properties from Observations of Milky Way Satellite Galaxies. *Physical Review Letters*, 126(9):091101, March 2021. doi:10.1103/PhysRevLett.126.091101.

D. Q. Nagasawa, J. L. Marshall, T. S. Li, T. T. Hansen, J. D. Simon, R. A. Bernstein, E. Balbinot, A. Drlica-Wagner, A. B. Pace, L. E. Strigari, C. M. Pellegrino, D. L. DePoy, N. B. Suntzeff, K. Bechtol, A. R. Walker, T. M. C. Abbott, F. B. Abdalla, S. Allam, J. Annis, A. Benoit-Lévy, E. Bertin, D. Brooks, A. Carnero Rosell, M. Carrasco Kind, J. Carretero, C. E. Cunha, C. B. D'Andrea, L. N. da Costa, C. Davis, S. Desai, P. Doel, T. F. Eifler, B. Flaugher, P. Fosalba, J. Frieman, J. García-Bellido, E. Gaztanaga, D. W. Gerdes, D. Gruen, R. A. Gruendl, J. Gschwend, G. Gutierrez, W. G. Hartley, K. Honscheid, D. J. James, T. Jeltema, E. Krause, K. Kuehn, S. Kuhlmann, N. Kuropatkin, M. March, R. Miquel, B. Nord, A. Roodman, E. Sanchez, B. Santiago, V. Scarpine, R. Schindler, M. Schubnell, I. Sevilla-Noarbe, M. Smith, R. C. Smith, M. Soares-Santos, F. Sobreira, E. Suchyta, G. Tarle, D. Thomas, D. L. Tucker, R. H. Wechsler, R. C. Wolf, and B. Yanny. Chemical Abundance Analysis of Three α-poor, Metal-poor Stars in the Ultrafaint Dwarf Galaxy Horologium I. *Astrophysical Journal*, 852(2):99, January 2018. doi:10.3847/1538-4357/aaa01d.

Rohan P. Naidu, Charlie Conroy, Ana Bonaca, Benjamin D. Johnson, Yuan-Sen Ting, Nelson Caldwell, Dennis Zaritsky, and Phillip A. Cargile. Evidence from the H3 Survey That the Stellar Halo Is Entirely Comprised of Substructure. *Astrophysical Journal*, 901(1):48, September 2020. doi:10.3847/1538-4357/abaef4.

Rohan P. Naidu, Charlie Conroy, Ana Bonaca, Dennis Zaritsky, Rainer Weinberger, Yuan-Sen Ting, Nelson Caldwell, Sandro Tacchella, Jiwon Jesse Han, Joshua S. Speagle, and Phillip A. Cargile. Reconstructing the Last Major Merger of the Milky Way with the H3 Survey. *Astrophysical Journal*, 923(1):92, December 2021. doi:10.3847/1538-4357/ac2d2d.

Rohan P. Naidu, Alexander P. Ji, Charlie Conroy, Ana Bonaca, Yuan-Sen Ting, Dennis Zaritsky, Lieke A. C. van Son, Floor S. Broekgaarden, Sandro Tacchella, Vedant Chandra, Nelson Caldwell, Phillip Cargile, and Joshua S. Speagle. Evidence from Disrupted Halo Dwarfs that r-process Enrichment via Neutron Star Mergers is Delayed by $\gtrsim$500 Myr. *Astrophysical Journal, Letters*, 926(2):L36, February 2022. doi:10.3847/2041-8213/ac5589.

D. Nardiello, A. P. Milone, G. Piotto, J. Anderson, L. R. Bedin, A. Bellini, S. Cassisi, M. Libralato, and A. F. Marino. The Hubble Space Telescope UV Legacy Survey of Galactic globular clusters - XIV. Multiple stellar populations within M 15 and their radial distribution. *Monthly Notices of the Royal Astronomical Society*, 477 (2):2004–2019, June 2018. doi:10.1093/mnras/sty719.

Heidi Jo Newberg. Introduction to Tidal Streams. In Heidi Jo Newberg and Jeffrey L. Carlin, editors, *Tidal Streams in the Local Group and Beyond*, volume 420 of *Astrophysics and Space Science Library*, page 1, January 2016. doi:10.1007/978-3-319-19336-6_1.

Heidi Jo Newberg, Brian Yanny, and Benjamin A. Willett. Discovery of a New, Polar-Orbiting Debris Stream in the Milky Way Stellar Halo. *Astrophysical Journal, Letters*, 700(2):L61–L64, August 2009. doi:10.1088/0004-637X/700/2/L61.

David L. Nidever, Sten Hasselquist, Christian R. Hayes, Keith Hawkins, Joshua Povick, Steven R. Majewski, Verne V. Smith, Borja Anguiano, Guy S. Stringfellow, Jennifer S. Sobeck, Katia Cunha, Timothy C. Beers, Joachim M. Bestenlehner, Roger E. Cohen, D. A. Garcia-Hernandez, Henrik Jönsson, Christian Nitschelm, Matthew Shetrone, Ivan Lacerna, Carlos Allende Prieto, Rachael L. Beaton, Flavia Dell'Agli, José G. Fernández-Trincado, Diane Feuillet, Carme Gallart, Fred R. Hearty, Jon Holtzman, Arturo Manchado, Ricardo R. Muñoz, Robert O'Connell,

and Margarita Rosado. The Lazy Giants: APOGEE Abundances Reveal Low Star Formation Efficiencies in the Magellanic Clouds. *Astrophysical Journal*, 895(2):88, June 2020. doi:10.3847/1538-4357/ab7305.

F. Niederhofer, N. Bastian, V. Kozhurina-Platais, S. Larsen, K. Hollyhead, C. Lardo, I. Cabrera-Ziri, N. Kacharov, I. Platais, M. Salaris, M. Cordero, E. Dalessandro, D. Geisler, M. Hilker, C. Li, D. Mackey, and A. Mucciarelli. The search for multiple populations in Magellanic Cloud clusters - II. The detection of multiple populations in three intermediate-age SMC clusters. *Monthly Notices of the Royal Astronomical Society*, 465(4):4159–4165, March 2017a. doi:10.1093/mnras/stw3084.

F. Niederhofer, N. Bastian, V. Kozhurina-Platais, S. Larsen, M. Salaris, E. Dalessandro, A. Mucciarelli, I. Cabrera-Ziri, M. Cordero, D. Geisler, M. Hilker, K. Hollyhead, N. Kacharov, C. Lardo, C. Li, D. Mackey, and I. Platais. The search for multiple populations in Magellanic Cloud clusters - I. Two stellar populations in the Small Magellanic Cloud globular cluster NGC 121. *Monthly Notices of the Royal Astronomical Society*, 464(1):94–103, January 2017b. doi:10.1093/mnras/stw2269.

Poul Erik Nissen and Bengt Gustafsson. High-precision stellar abundances of the elements: methods and applications. *Astronomy and Astrophysics Reviews*, 26(1): 6, October 2018. doi:10.1007/s00159-018-0111-3.

T. Nordlander and K. Lind. Non-LTE aluminium abundances in late-type stars. *Astronomy and Astrophysics*, 607:A75, November 2017. doi:10.1051/0004-6361/201730427.

Thomas Nordlander. Private communication. *Private communication.*, July 2019.

Brodie J. Norfolk, Andrew R. Casey, Amanda I. Karakas, Matthew T. Miles, Alex J. Kemp, Kevin C. Schlaufman, Melissa Ness, Anna Y. Q. Ho, John C. Lattanzio, and Alexander P. Ji. Discovery of s-process enhanced stars in the LAMOST survey. *Monthly Notices of the Royal Astronomical Society*, 490(2):2219–2227, December 2019. doi:10.1093/mnras/stz2630.

J. Norris, P. L. Cottrell, K. C. Freeman, and G. S. Da Costa. The abundance spread in the giants of NGC 6752. *Astrophysical Journal*, 244:205–220, February 1981. doi:10.1086/158698.

John E. Norris, Gerard Gilmore, Rosemary F. G. Wyse, David Yong, and Anna Frebel. An Extremely Carbon-rich, Extremely Metal-poor Star in the Segue

1 System. *Astrophysical Journal, Letters*, 722(1):L104–L109, October 2010a. doi:10.1088/2041-8205/722/1/L104.

John E. Norris, David Yong, Gerard Gilmore, and Rosemary F. G. Wyse. Boo-1137—an Extremely Metal-Poor Star in the Ultra-Faint Dwarf Spheroidal Galaxy Boötes I. *Astrophysical Journal*, 711(1):350–360, March 2010b. doi:10.1088/0004-637X/711/1/350.

John E. Norris, David Yong, Kim A. Venn, Gerard Gilmore, Luca Casagrande, and Aaron Dotter. The Populations of Carina. II. Chemical Enrichment. *Astrophysical Journal, Supplement*, 230(2):28, June 2017. doi:10.3847/1538-4365/aa755e.

Michael Odenkirchen, Eva K. Grebel, Walter Dehnen, Hans-Walter Rix, Brian Yanny, Heidi Jo Newberg, Constance M. Rockosi, David Martínez-Delgado, Jon Brinkmann, and Jeffrey R. Pier. The Extended Tails of Palomar 5: A 10° Arc of Globular Cluster Tidal Debris. *Astronomical Journal*, 126(5):2385–2407, November 2003. doi:10.1086/378601.

S. Ortolani, E. Bica, and B. Barbuy. ESO 280-SC06: a new globular cluster in the Galaxy. *Astronomy and Astrophysics*, 361:L57–L59, September 2000.

W. Osborn. Two new CN-strong globular cluster stars. *The Observatory*, 91:223–224, December 1971.

Kaori Otsuki, Satoshi Honda, Wako Aoki, Toshitaka Kajino, and Grant J. Mathews. Neutron-Capture Elements in the Metal-poor Globular Cluster M15. *Astrophysical Journal, Letters*, 641(2):L117–L120, April 2006. doi:10.1086/504106.

Xiaowei Ou, Alexander P. Ji, Anna Frebel, Rohan P. Naidu, and Guilherme Limberg. The Rise of the r-process in the Gaia-Sausage/Enceladus Dwarf Galaxy. *Astrophysical Journal*, 974(2):232, October 2024. doi:10.3847/1538-4357/ad6f9b.

Carles G. Palau and Jordi Miralda-Escudé. Statistical detection of a tidal stream associated with the globular cluster M68 using Gaia data. *Monthly Notices of the RAS*, 488(2):1535–1557, September 2019. doi:10.1093/mnras/stz1790.

Sarah Pearson, Ana Bonaca, Yingtian Chen, and Oleg Y. Gnedin. Forecasting the Population of Globular Cluster Streams in Milky Way–type Galaxies. *Astrophysical Journal*, 976(1):54, November 2024. doi:10.3847/1538-4357/ad8348.

Hélio D. Perottoni, Guilherme Limberg, João A. S. Amarante, Silvia Rossi, Anna B. A. Queiroz, Rafael M. Santucci, Angeles Pérez-Villegas, and Cristina Chiappini. The Unmixed Debris of Gaia-Sausage/Enceladus in the Form of a Pair of Halo Stellar Overdensities. *Astrophysical Journal, Letters*, 936(1):L2, September 2022. doi:10.3847/2041-8213/ac88d6.

G. Piotto, A. P. Milone, L. R. Bedin, J. Anderson, I. R. King, A. F. Marino, D. Nardiello, A. Aparicio, B. Barbuy, A. Bellini, T. M. Brown, S. Cassisi, A. M. Cool, A. Cunial, E. Dalessandro, F. D'Antona, F. R. Ferraro, S. Hidalgo, B. Lanzoni, M. Monelli, S. Ortolani, A. Renzini, M. Salaris, A. Sarajedini, R. P. van der Marel, E. Vesperini, and M. Zoccali. The Hubble Space Telescope UV Legacy Survey of Galactic Globular Clusters. I. Overview of the Project and Detection of Multiple Stellar Populations. *Astronomical Journal*, 149(3):91, March 2015. doi:10.1088/0004-6256/149/3/91.

Vinicius M. Placco, Anna Frebel, Timothy C. Beers, and Richard J. Stancliffe. Carbon-enhanced Metal-poor Star Frequencies in the Galaxy: Corrections for the Effect of Evolutionary Status on Carbon Abundances. *Astrophysical Journal*, 797 (1):21, December 2014. doi:10.1088/0004-637X/797/1/21.

Vinicius M. Placco, Christopher Sneden, Ian U. Roederer, James E. Lawler, Elizabeth A. Den Hartog, Neda Hejazi, Zachary Maas, and Peter Bernath. Linemake: An Atomic and Molecular Line List Generator. *Research Notes of the American Astronomical Society*, 5(4):92, April 2021. doi:10.3847/2515-5172/abf651.

O. R. Pols, R. G. Izzard, R. J. Stancliffe, and E. Glebbeek. The occurrence of nitrogen-enhanced metal-poor stars: implications for the initial mass function in the early Galactic halo. *Astronomy and Astrophysics*, 547:A76, November 2012. doi:10.1051/0004-6361/201219597.

A. M. Price-Whelan, B. M. Sipőcz, H. M. Günther, P. L. Lim, S. M. Crawford, S. Conseil, D. L. Shupe, M. W. Craig, N. Dencheva, A. Ginsburg, J. T. VanderPlas, L. D. Bradley, D. Pérez-Suárez, M. de Val-Borro, (Primary Paper Contributors, T. L. Aldcroft, K. L. Cruz, T. P. Robitaille, E. J. Tollerud, (Astropy Coordination Committee, C. Ardelean, T. Babej, Y. P. Bach, M. Bachetti, A. V. Bakanov, S. P. Bamford, G. Barentsen, P. Barmby, A. Baumbach, K. L. Berry, F. Biscani, M. Boquien, K. A. Bostroem, L. G. Bouma, G. B. Brammer, E. M. Bray, H. Breytenbach, H. Buddelmeijer, D. J. Burke, G. Calderone, J. L. Cano Rodríguez, M. Cara, J. V. M. Cardoso, S. Cheedella, Y. Copin, L. Corrales, D. Crichton, D. D'Avella,

C. Deil, É. Depagne, J. P. Dietrich, A. Donath, M. Droettboom, N. Earl, T. Erben, S. Fabbro, L. A. Ferreira, T. Finethy, R. T. Fox, L. H. Garrison, S. L. J. Gibbons, D. A. Goldstein, R. Gommers, J. P. Greco, P. Greenfield, A. M. Groener, F. Grollier, A. Hagen, P. Hirst, D. Homeier, A. J. Horton, G. Hosseinzadeh, L. Hu, J. S. Hunkeler, Ž. Ivezić, A. Jain, T. Jenness, G. Kanarek, S. Kendrew, N. S. Kern, W. E. Kerzendorf, A. Khvalko, J. King, D. Kirkby, A. M. Kulkarni, A. Kumar, A. Lee, D. Lenz, S. P. Littlefair, Z. Ma, D. M. Macleod, M. Mastropietro, C. McCully, S. Montagnac, B. M. Morris, M. Mueller, S. J. Mumford, D. Muna, N. A. Murphy, S. Nelson, G. H. Nguyen, J. P. Ninan, M. Nöthe, S. Ogaz, S. Oh, J. K. Parejko, N. Parley, S. Pascual, R. Patil, A. A. Patil, A. L. Plunkett, J. X. Prochaska, T. Rastogi, V. Reddy Janga, J. Sabater, P. Sakurikar, M. Seifert, L. E. Sherbert, H. Sherwood-Taylor, A. Y. Shih, J. Sick, M. T. Silbiger, S. Singanamalla, L. P. Singer, P. H. Sladen, K. A. Sooley, S. Sornarajah, O. Streicher, P. Teuben, S. W. Thomas, G. R. Tremblay, J. E. H. Turner, V. Terrón, M. H. van Kerkwijk, A. de la Vega, L. L. Watkins, B. A. Weaver, J. B. Whitmore, J. Woillez, V. Zabalza, and (Astropy Contributors. The Astropy Project: Building an Open-science Project and Status of the v2.0 Core Package. *Astronomical Journal*, 156: 123, September 2018. doi:10.3847/1538-3881/aabc4f.

Adrian Price-Whelan, Brigitta Sipőcz, Daniel Lenz, Johnny Greco, Syrtis Major, Sergey Koposov, Semyeong Oh, and P. L. Lim. adrn/gala: v1.3, October 2020. URL `https://doi.org/10.5281/zenodo.593786`.

Adrian M. Price-Whelan. Gala: A python package for galactic dynamics. *The Journal of Open Source Software*, 2(18), oct 2017. doi:10.21105/joss.00388. URL `https://doi.org/10.21105%2Fjoss.00388`.

Adrian M. Price-Whelan and Ana Bonaca. Off the Beaten Path: Gaia Reveals GD-1 Stars outside of the Main Stream. *Astrophysical Journal, Letters*, 863(2):L20, August 2018. doi:10.3847/2041-8213/aad7b5.

Henrique Reggiani, Anish M. Amarsi, Karin Lind, Paul S. Barklem, Oleg Zatsarinny, Klaus Bartschat, Dmitry V. Fursa, Igor Bray, Lorenzo Spina, and Jorge Meléndez. Non-LTE analysis of K I in late-type stars. *Astronomy and Astrophysics*, 627:A177, July 2019. doi:10.1051/0004-6361/201935156.

Marta Reina-Campos, J. M. Diederik Kruijssen, Joel L. Pfeffer, Nate Bastian, and Robert A. Crain. Formation histories of stars, clusters, and globular clusters in the E-MOSAICS simulations. *Monthly Notices of the Royal Astronomical Society*, 486(4):5838–5852, July 2019. doi:10.1093/mnras/stz1236.

Alexander H. Riley and Louis E. Strigari. The Milky Way's stellar streams and globular clusters do not align in a Vast Polar Structure. *Monthly Notices of the Royal Astronomical Society*, 494(1):983–1001, May 2020. doi:10.1093/mnras/staa710.

I. U. Roederer, A. F. Marino, and C. Sneden. Characterizing the Heavy Elements in Globular Cluster M22 and an Empirical s-process Abundance Distribution Derived from the Two Stellar Groups. *Astrophysical Journal*, 742(1):37, November 2011. doi:10.1088/0004-637X/742/1/37.

Ian U. Roederer. The Origin of the Heaviest Metals in Most Ultra-faint Dwarf Galaxies. *Astrophysical Journal*, 835(1):23, January 2017. doi:10.3847/1538-4357/835/1/23.

Ian U. Roederer and Oleg Y. Gnedin. High-resolution Optical Spectroscopy of Stars in the Sylgr Stellar Stream. *Astrophysical Journal*, 883(1):84, September 2019. doi:10.3847/1538-4357/ab365c.

Ian U. Roederer and Evan N. Kirby. Detailed abundance analysis of the brightest star in Segue 2, the least massive galaxy. *Monthly Notices of the Royal Astronomical Society*, 440(3):2665–2675, May 2014. doi:10.1093/mnras/stu491.

Ian U. Roederer and Christopher Sneden. Heavy-element Dispersion in the Metal-poor Globular Cluster M92. *Astronomical Journal*, 142(1):22, July 2011. doi:10.1088/0004-6256/142/1/22.

Ian U. Roederer and Ian B. Thompson. Detailed abundances of 15 stars in the metal-poor globular cluster NGC 4833. *Monthly Notices of the Royal Astronomical Society*, 449(4):3889–3910, June 2015. doi:10.1093/mnras/stv546.

Ian U. Roederer, Christopher Sneden, Ian B. Thompson, George W. Preston, and Stephen A. Shectman. Characterizing the Chemistry of the Milky Way Stellar Halo: Detailed Chemical Analysis of a Metal-poor Stellar Stream. *Astrophysical Journal*, 711(2):573–596, March 2010. doi:10.1088/0004-637X/711/2/573.

Ian U. Roederer, George W. Preston, Ian B. Thompson, Stephen A. Shectman, Christopher Sneden, Gregory S. Burley, and Daniel D. Kelson. A Search for Stars of Very Low Metal Abundance. VI. Detailed Abundances of 313 Metal-poor Stars. *Astronomical Journal*, 147(6):136, June 2014. doi:10.1088/0004-6256/147/6/136.

Ian U. Roederer, Mario Mateo, III Bailey, John I., Yingyi Song, Eric F. Bell, Jeffrey D. Crane, Sarah Loebman, David L. Nidever, Edward W. Olszewski,

Stephen A. Shectman, Ian B. Thompson, Monica Valluri, and Matthew G. Walker. Detailed Chemical Abundances in the r-process-rich Ultra-faint Dwarf Galaxy Reticulum 2. *Astronomical Journal*, 151(3):82, March 2016. doi:10.3847/0004-6256/151/3/82.

Ian U. Roederer, Kohei Hattori, and Monica Valluri. Kinematics of Highly r-process-enhanced Field Stars: Evidence for an Accretion Origin and Detection of Several Groups from Disrupted Satellites. *Astronomical Journal*, 156(4):179, October 2018a. doi:10.3847/1538-3881/aadd9c.

Ian U. Roederer, Charli M. Sakari, Vinicius M. Placco, Timothy C. Beers, Rana Ezzeddine, Anna Frebel, and Terese T. Hansen. The R-Process Alliance: A Comprehensive Abundance Analysis of HD 222925, a Metal-poor Star with an Extreme R-process Enhancement of [Eu/H] = -0.14. *Astrophysical Journal*, 865(2):129, October 2018b. doi:10.3847/1538-4357/aadd92.

Ricardo Salinas and Jay Strader. No Evidence for Multiple Stellar Populations in the Low-mass Galactic Globular Cluster E 3. *Astrophysical Journal*, 809(2):169, August 2015. doi:10.1088/0004-637X/809/2/169.

Edwin E. Salpeter. The Luminosity Function and Stellar Evolution. *Astrophysical Journal*, 121:161, January 1955. doi:10.1086/145971.

Isaiah B. Santistevan, Andrew Wetzel, Kareem El-Badry, Joss Bland-Hawthorn, Michael Boylan-Kolchin, Jeremy Bailin, Claude-André Faucher-Giguère, and Samantha Benincasa. The formation times and building blocks of Milky Way-mass galaxies in the FIRE simulations. *Monthly Notices of the Royal Astronomical Society*, 497(1):747–764, September 2020. doi:10.1093/mnras/staa1923.

Ricardo P. Schiavon, Olga Zamora, Ricardo Carrera, Sara Lucatello, A. C. Robin, Melissa Ness, Sarah L. Martell, Verne V. Smith, D. A. García-Hernández, Arturo Manchado, Ralph Schönrich, Nate Bastian, Cristina Chiappini, Matthew Shetrone, J. Ted Mackereth, Rob A. Williams, Szabolcs Mészáros, Carlos Allende Prieto, Friedrich Anders, Dmitry Bizyaev, Timothy C. Beers, S. Drew Chojnowski, Katia Cunha, Courtney Epstein, Peter M. Frinchaboy, Ana E. García Pérez, Fred R. Hearty, Jon A. Holtzman, Jennifer A. Johnson, Karen Kinemuchi, Steven R. Majewski, Demitri Muna, David L. Nidever, Duy Cuong Nguyen, Robert W. O'Connell, Daniel Oravetz, Kaike Pan, Marc Pinsonneault, Donald P. Schneider, Matthias Schultheis, Audrey Simmons, Michael F. Skrutskie, Jennifer Sobeck, John C. Wilson, and Gail Zasowski. Chemical tagging with

APOGEE: discovery of a large population of N-rich stars in the inner Galaxy. *Monthly Notices of the Royal Astronomical Society*, 465(1):501–524, February 2017. doi:10.1093/mnras/stw2162.

Edward F. Schlafly and Douglas P. Finkbeiner. Measuring Reddening with Sloan Digital Sky Survey Stellar Spectra and Recalibrating SFD. *Astrophysical Journal*, 737(2):103, August 2011. doi:10.1088/0004-637X/737/2/103.

David J. Schlegel, Douglas P. Finkbeiner, and Marc Davis. Maps of Dust Infrared Emission for Use in Estimation of Reddening and Cosmic Microwave Background Radiation Foregrounds. *Astrophysical Journal*, 500(2):525–553, June 1998. doi:10.1086/305772.

SDSS. Sky survey unveils star cluster shredded by the milky way, Jun 2003. URL https://www2.mpia-hd.mpg.de/Public/Aktuelles/PR_2/2002/PR020603/PR_020603_en.html.

Cheyanne Shariat, Kareem El-Badry, Smadar Naoz, Antonio Rodriguez, Kyle Akira Rocha, Alexander Stephan, Vasiliki Kalogera, Isabel Angelo, Kevin Burdge, and Jan Van Roestel. The Role of Triples on Accreting Binary Populations: A Combined Observational and Dynamical Approach. In *AAS/Division of Dynamical Astronomy Meeting*, volume 57 of *AAS/Division of Dynamical Astronomy Meeting*, page 501.01, June 2025.

Allyson A. Sheffield, Steven R. Majewski, Kathryn V. Johnston, Katia Cunha, Verne V. Smith, Andrew M. Cheung, Christina M. Hampton, Trevor J. David, Rachel Wagner-Kaiser, Marshall C. Johnson, Evan Kaplan, Jacob Miller, and Richard J. Patterson. Identifying Contributions to the Stellar Halo from Accreted, Kicked-out, and In Situ Populations. *Astrophysical Journal*, 761(2):161, December 2012. doi:10.1088/0004-637X/761/2/161.

Matthew Shetrone, Jamie Tayar, Jennifer A. Johnson, Garrett Somers, Marc H. Pinsonneault, Jon A. Holtzman, Sten Hasselquist, Thomas Masseron, Szabolcs Mészáros, Henrik Jönsson, Keith Hawkins, Jennifer Sobeck, Olga Zamora, and D. A. García-Hernández. Constraining Metallicity-dependent Mixing and Extra Mixing Using [C/N] in Alpha-rich Field Giants. *Astrophysical Journal*, 872(2):137, February 2019. doi:10.3847/1538-4357/aaff66.

N. Shipp, A. Drlica-Wagner, E. Balbinot, P. Ferguson, D. Erkal, T. S. Li, K. Bechtol, V. Belokurov, B. Buncher, D. Carollo, M. Carrasco Kind, K. Kuehn, J. L. Marshall, A. B. Pace, E. S. Rykoff, I. Sevilla-Noarbe, E. Sheldon, L. Strigari, A. K.

Vivas, B. Yanny, A. Zenteno, T. M. C. Abbott, F. B. Abdalla, S. Allam, S. Avila, E. Bertin, D. Brooks, D. L. Burke, J. Carretero, F. J. Castander, R. Cawthon, M. Crocce, C. E. Cunha, C. B. D'Andrea, L. N. da Costa, C. Davis, J. De Vicente, S. Desai, H. T. Diehl, P. Doel, A. E. Evrard, B. Flaugher, P. Fosalba, J. Frieman, J. García-Bellido, E. Gaztanaga, D. W. Gerdes, D. Gruen, R. A. Gruendl, J. Gschwend, G. Gutierrez, W. Hartley, K. Honscheid, B. Hoyle, D. J. James, M. D. Johnson, E. Krause, N. Kuropatkin, O. Lahav, H. Lin, M. A. G. Maia, M. March, P. Martini, F. Menanteau, C. J. Miller, R. Miquel, R. C. Nichol, A. A. Plazas, A. K. Romer, M. Sako, E. Sanchez, B. Santiago, V. Scarpine, R. Schindler, M. Schubnell, M. Smith, R. C. Smith, F. Sobreira, E. Suchyta, M. E. C. Swanson, G. Tarle, D. Thomas, D. L. Tucker, A. R. Walker, R. H. Wechsler, and DES Collaboration. Stellar Streams Discovered in the Dark Energy Survey. *Astrophysical Journal*, 862(2):114, August 2018. doi:10.3847/1538-4357/aacdab.

Jennifer Simmerer, Christopher Sneden, John J. Cowan, Jason Collier, Vincent M. Woolf, and James E. Lawler. The Rise of the s-Process in the Galaxy. *Astrophysical Journal*, 617(2):1091–1114, December 2004. doi:10.1086/424504.

Joshua D. Simon. The Faintest Dwarf Galaxies. *Annual Review of Astronomy and Astrophysics*, 57:375–415, August 2019. doi:10.1146/annurev-astro-091918-104453.

Joshua D. Simon, Anna Frebel, Andrew McWilliam, Evan N. Kirby, and Ian B. Thompson. High-resolution Spectroscopy of Extremely Metal-poor Stars in the Least Evolved Galaxies: Leo IV. *Astrophysical Journal*, 716(1):446–452, June 2010. doi:10.1088/0004-637X/716/1/446.

Joshua D. Simon, Marla Geha, Quinn E. Minor, Gregory D. Martinez, Evan N. Kirby, James S. Bullock, Manoj Kaplinghat, Louis E. Strigari, Beth Willman, Philip I. Choi, Erik J. Tollerud, and Joe Wolf. A Complete Spectroscopic Survey of the Milky Way Satellite Segue 1: The Darkest Galaxy. *Astrophysical Journal*, 733(1):46, May 2011. doi:10.1088/0004-637X/733/1/46.

Jeffrey D Simpson. The most metal-poor galactic globular cluster: the first spectroscopic observations of eso280-sc06. *Monthly Notices of the Royal Astronomical Society*, 477:4565–4576, 7 2018. doi:10.1093/mnras/sty847.

Jeffrey D. Simpson and Sarah L. Martell. A nitrogen-enhanced metal-poor star discovered in the globular cluster ESO280-SC06. *Monthly Notices of the Royal Astronomical Society*, 490(1):741–751, November 2019. doi:10.1093/mnras/stz2611.

Jeffrey D. Simpson, Gayandhi De Silva, Sarah L. Martell, Colin A. Navin, and Daniel B. Zucker. ESO 452-SC11: the lowest mass globular cluster with a potential chemical inhomogeneity. *Monthly Notices of the Royal Astronomical Society*, 472 (3):2856–2868, December 2017. doi:10.1093/mnras/stx2174.

Jeffrey D. Simpson, Sarah L. Martell, Gary Da Costa, Jonathan Horner, Rosemary F. G. Wyse, Yuan-Sen Ting, Martin Asplund, Joss Bland-Hawthorn, Sven Buder, Gayandhi M. De Silva, Ken C. Freeman, Janez Kos, Geraint F. Lewis, Karin Lind, Sanjib Sharma, Daniel B. Zucker, Tomaž Zwitter, Klemen Čotar, Peter L. Cottrell, and Thomas Nordlander. The GALAH Survey: Chemically tagging the Fimbulthul stream to the globular cluster ω Centauri. *Monthly Notices of the Royal Astronomical Society*, 491(3):3374–3384, January 2020. doi:10.1093/mnras/stz3105.

T. M. Sitnova, L. I. Mashonkina, and T. A. Ryabchikova. A non-local thermodynamical equilibrium line formation for neutral and singly ionized titanium in model atmospheres of reference A-K stars. *Monthly Notices of the Royal Astronomical Society*, 461(1):1000–1011, September 2016. doi:10.1093/mnras/stw1202.

T. M. Sitnova, Z. Yuan, T. Matsuno, L. I. Mashonkina, S. A. Alexeeva, E. Holmbeck, F. Sestito, L. Lombardo, P. Banerjee, N. F. Martin, and F. Jiang. HR-GO: I. Comprehensive NLTE abundance analysis of the Cetus stream. *Astronomy and Astrophysics*, 690:A331, October 2024. doi:10.1051/0004-6361/202450981.

Christopher Sneden, Robert P. Kraft, Matthew D. Shetrone, Graeme H. Smith, G. E. Langer, and Charles F. Prosser. Star-To-Star Abundance Variations Among Bright Giants in the Metal-Poor Globular Cluster M15. *Astronomical Journal*, 114:1964, November 1997. doi:10.1086/118618.

Christopher Sneden, Catherine A. Pilachowski, and Robert P. Kraft. Barium and Sodium Abundances in the Globular Clusters M15 and M92. *Astronomical Journal*, 120(3):1351–1363, September 2000. doi:10.1086/301509.

Christopher Alan Sneden. *Carbon and Nitrogen Abundances in Metal-Poor Stars.* PhD thesis, University of Texas, Austin, January 1973.

Jennifer S. Sobeck, Robert P. Kraft, Christopher Sneden, George W. Preston, John J. Cowan, Graeme H. Smith, Ian B. Thompson, Stephen A. Shectman, and Gregory S. Burley. The Abundances of Neutron-capture Species in the Very Metal-poor Globular Cluster M15: A Uniform Analysis of Red Giant Branch and Red Horizontal Branch Stars. *Astronomical Journal*, 141(6):175, June 2011. doi:10.1088/0004-6256/141/6/175.

Joshua S. Speagle. DYNESTY: a dynamic nested sampling package for estimating Bayesian posteriors and evidences. *Monthly Notices of the Royal Astronomical Society*, 493(3):3132–3158, April 2020. doi:10.1093/mnras/staa278.

M. Spite, R. Cayrel, B. Plez, V. Hill, F. Spite, E. Depagne, P. François, P. Bonifacio, B. Barbuy, T. Beers, J. Andersen, P. Molaro, B. Nordström, and F. Primas. First stars VI - Abundances of C, N, O, Li, and mixing in extremely metal-poor giants. Galactic evolution of the light elements. *Astronomy and Astrophysics*, 430:655–668, February 2005. doi:10.1051/0004-6361:20041274.

M. Spite, S. M. Andrievsky, F. Spite, E. Caffau, S. A. Korotin, P. Bonifacio, H. G. Ludwig, P. François, and R. Cayrel. NLTE determination of the calcium abundance and 3D corrections in extremely metal-poor stars. *Astronomy and Astrophysics*, 541:A143, May 2012. doi:10.1051/0004-6361/201218773.

M. Spite, F. Spite, P. François, P. Bonifacio, E. Caffau, and S. Salvadori. A CEMP-no star in the ultra-faint dwarf galaxy Pisces II. *Astronomy and Astrophysics*, 617: A56, September 2018. doi:10.1051/0004-6361/201833548.

Yoichi Takeda, Osamu Hashimoto, Hikaru Taguchi, Kazuo Yoshioka, Masahide Takada-Hidai, Yuji Saito, and Satoshi Honda. Non-LTE Line-Formation and Abundances of Sulfur and Zinc in F, G, and K Stars. *Publications of the ASJ*, 57: 751–768, October 2005. doi:10.1093/pasj/57.5.751.

R. Theler, P. Jablonka, R. Lucchesi, C. Lardo, P. North, M. Irwin, G. Battaglia, V. Hill, E. Tolstoy, K. Venn, A. Helmi, A. Kaufer, F. Primas, and M. Shetrone. The chemical evolution of the dwarf spheroidal galaxy Sextans. *Astronomy and Astrophysics*, 642:A176, October 2020. doi:10.1051/0004-6361/201937146.

Yuan-Sen Ting, Charlie Conroy, Hans-Walter Rix, and Phillip Cargile. The Payne: Self-consistent ab initio Fitting of Stellar Spectra. *Astrophysical Journal*, 879(2): 69, July 2019. doi:10.3847/1538-4357/ab2331.

B. M. Tinsley. Stellar lifetimes and abundance ratios in chemical evolution. *Astrophysical Journal*, 229:1046–1056, May 1979. doi:10.1086/157039.

Eline Tolstoy, Vanessa Hill, and Monica Tosi. Star-Formation Histories, Abundances, and Kinematics of Dwarf Galaxies in the Local Group. *Annual Review of Astronomy and Astrophysics*, 47(1):371–425, September 2009. doi:10.1146/annurev-astro-082708-101650.

S. A. Usman, J. C. Mills, and S. Fairhurst. Constraining the Inclinations of Binary Mergers from Gravitational-wave Observations. *Astrophysical Journal*, 877(2):82, June 2019. doi:10.3847/1538-4357/ab0b3e.

Sam A. Usman, Alexander P. Ji, Ting S. Li, Andrew B. Pace, Lara R. Cullinane, Gary S. Da Costa, Sergey E. Koposov, Geraint F. Lewis, Daniel B. Zucker, Vasily Belokurov, Joss Bland-Hawthorn, Peter S. Ferguson, Terese T. Hansen, Guilherme Limberg, Sarah L. Martell, Madeleine McKenzie, Joshua D. Simon, and S5 Collaboration. Multiple populations and a CH star found in the 300S globular cluster stellar stream. *Monthly Notices of the Royal Astronomical Society*, 529(3):2413–2427, April 2024. doi:10.1093/mnras/stae185.

Sam A. Usman, Alexander P. Ji, Jandrie Rodriguez, Jeffrey D. Simpson, Sarah L. Martell, Ting S. Li, Ana Bonaca, Shivani Shah, and Madeleine McKenzie. Chemical Abundances in the Metal-Poor Globular Cluster ESO 280-SC06: A Formerly Massive, Tidally Disrupted Globular Cluster. *arXiv e-prints*, art. arXiv:2506.15664, June 2025.

Samantha A. Usman, Alexander H. Nitz, Ian W. Harry, Christopher M. Biwer, Duncan A. Brown, Miriam Cabero, Collin D. Capano, Tito Dal Canton, Thomas Dent, Stephen Fairhurst, Marcel S. Kehl, Drew Keppel, Badri Krishnan, Amber Lenon, Andrew Lundgren, Alex B. Nielsen, Larne P. Pekowsky, Harald P. Pfeiffer, Peter R. Saulson, Matthew West, and Joshua L. Willis. The PyCBC search for gravitational waves from compact binary coalescence. *Classical and Quantum Gravity*, 33(21):215004, November 2016. doi:10.1088/0264-9381/33/21/215004.

M. Valluri, P. Fagrelius, S. E. Koposov, T. S. Li, Oleg Y. Gnedin, E. F. Bell, R. G. Carlberg, A. P. Cooper, J. Aguilar, S. Ahlen, C. Allende Prieto, V. Belokurov, L. Beraldo e Silva, D. Brooks, A. Byström, T. Claybaugh, K. Dawson, A. Dey, P. Doel, J. E. Forero-Romero, E. Gaztañaga, S. Gontcho A Gontcho, J. Han, K. Honscheid, T. Kisner, A. Kremin, A. Lambert, M. Landriau, L. Le Guillou, M. E. Levi, A. de la Macorra, M. Manera, P. Martini, G. E. Medina, A. Meisner, R. Miquel, J. Moustakas, A. D. Myers, J. Najita, C. Poppett, F. Prada, M. Rezaie, G. Rossi, A. H. Riley, E. Sanchez, D. Schlegel, M. Schubnell, D. Sprayberry, G. Tarlé, G. Thomas, B. A. Weaver, R. H. Wechsler, R. Zhou, and H. Zou. GD-1 Stellar Stream and Cocoon in the DESI Early Data Release. *Astrophysical Journal*, 980(1):71, February 2025. doi:10.3847/1538-4357/ada690.

Stefan van der Walt, S. Chris Colbert, and Gael Varoquaux. The numpy array: A structure for efficient numerical computation. *Computing in Science & Engi-*

neering, 13(2):22–30, 2011. doi:http://dx.doi.org/10.1109/MCSE.2011.37. URL http://scitation.aip.org/content/aip/journal/cise/13/2/10.1109/MCSE.2011.37.

A. Varghese, R. Ibata, and G. F. Lewis. Stellar streams as probes of dark halo mass and morphology: a Bayesian reconstruction. *Monthly Notices of the Royal Astronomical Society*, 417(1):198–215, October 2011. doi:10.1111/j.1365-2966.2011.19097.x.

K. A. Venn, E. Starkenburg, L. Malo, N. Martin, and B. P. M. Laevens. Gemini/-GRACES spectroscopy of stars in Tri II. *Monthly Notices of the Royal Astronomical Society*, 466(3):3741–3752, April 2017. doi:10.1093/mnras/stw3198.

Kim A. Venn, Matthew D. Shetrone, Mike J. Irwin, Vanessa Hill, Pascale Jablonka, Eline Tolstoy, Bertrand Lemasle, Mike Divell, Else Starkenburg, Bruno Letarte, Charles Baldner, Giuseppina Battaglia, Amina Helmi, Andreas Kaufer, and Francesca Primas. Nucleosynthesis and the Inhomogeneous Chemical Evolution of the Carina Dwarf Galaxy. *Astrophysical Journal*, 751(2):102, June 2012. doi:10.1088/0004-637X/751/2/102.

Enrico Vesperini, Jongsuk Hong, Mirek Giersz, and Arkadiusz Hypki. Dynamical evolution of multiple-population globular clusters. *Monthly Notices of the Royal Astronomical Society*, 502(3):4290–4304, April 2021. doi:10.1093/mnras/stab223.

S. Villanova, D. Geisler, G. Carraro, C. Moni Bidin, and C. Muñoz. Ruprecht 106: The First Single Population Globular Cluster? *Astrophysical Journal*, 778(2):186, December 2013. doi:10.1088/0004-637X/778/2/186.

Fletcher Waller, Kim A. Venn, Federico Sestito, Jaclyn Jensen, Collin L. Kielty, Asya Borukhovetskaya, Christian Hayes, Alan W. McConnachie, and Julio F. Navarro. The Cosmic Hunt for members in the outskirts of ultra-faint dwarf galaxies: Ursa Major I, Coma Berenices, and Boötes I. *Monthly Notices of the Royal Astronomical Society*, 519(1):1349–1365, February 2023. doi:10.1093/mnras/stac3563.

Zhen Wan, Geraint F. Lewis, Ting S. Li, Jeffrey D. Simpson, Sarah L. Martell, Daniel B. Zucker, Jeremy R. Mould, Denis Erkal, Andrew B. Pace, Dougal Mackey, Alexander P. Ji, Sergey E. Koposov, Kyler Kuehn, Nora Shipp, Eduardo Balbinot, Joss Bland-Hawthorn, Andrew R. Casey, Gary S. Da Costa, Prajwal Kafle, Sanjib Sharma, and Gayandhi M. De Silva. The tidal remnant of an unusually metal-poor globular cluster. *Nature*, 583(7818):768–770, July 2020. doi:10.1038/s41586-020-2483-6.

K. B. Webber, T. T. Hansen, J. L. Marshall, J. D. Simon, A. B. Pace, B. Mutlu-Pakdil, A. Drlica-Wagner, C. E. Martínez-Vázquez, M. Aguena, S. S. Allam, O. Alves, E. Bertin, D. Brooks, A. Carnero Rosell, J. Carretero, L. N. da Costa, J. De Vicente, P. Doel, I. Ferrero, D. Friedel, J. Frieman, J. García-Bellido, G. Giannini, D. Gruen, R. A. Gruendl, S. R. Hinton, D. L. Hollowood, K. Honscheid, K. Kuehn, J. Mena-Fernández, F. Menanteau, R. Miquel, R. L. C. Ogando, M. E. S. Pereira, A. Pieres, A. A. Plazas Malagón, E. Sanchez, B. Santiago, J. Allyn Smith, M. Smith, E. Suchyta, G. Tarle, C. To, N. Weaverdyck, and B. Yanny. Chemical Analysis of the Brightest Star of the Cetus II Ultrafaint Dwarf Galaxy Candidate. *Astrophysical Journal*, 959(2):141, December 2023. doi:10.3847/1538-4357/ad0385.

Daniel R. Weisz and Michael Boylan-Kolchin. Local Group ultra-faint dwarf galaxies in the reionization era. *Monthly Notices of the Royal Astronomical Society*, 469 (1):L83–L88, July 2017. doi:10.1093/mnrasl/slx043.

M. Wenger, F. Ochsenbein, D. Egret, P. Dubois, F. Bonnarel, S. Borde, F. Genova, G. Jasniewicz, S. Laloë, S. Lesteven, and R. Monier. The SIMBAD astronomical database. The CDS reference database for astronomical objects. *Astronomy and Astrophysics, Supplement*, 143:9–22, April 2000. doi:10.1051/aas:2000332.

B. Willman and J. Strader. "Galaxy," Defined. *Astronomical Journal*, 144(3):76, September 2012. doi:10.1088/0004-6256/144/3/76.

C. C. Worley, V. Hill, J. Sobeck, and E. Carretta. Ba and Eu abundances in M 15 giant stars. *Astronomy and Astrophysics*, 553:A47, May 2013. doi:10.1051/0004-6361/201321097.

Yong Yang, Jing-Kun Zhao, Xin-Zhe Tang, Xian-Hao Ye, and Gang Zhao. The Spectacular Tidal Tails of Globular Cluster M3 (NGC 5272). *Astrophysical Journal*, 953(2):130, August 2023. doi:10.3847/1538-4357/acdee2.

Donald G. York, J. Adelman, Jr. Anderson, John E., Scott F. Anderson, James Annis, Neta A. Bahcall, J. A. Bakken, Robert Barkhouser, Steven Bastian, Eileen Berman, William N. Boroski, Steve Bracker, Charlie Briegel, John W. Briggs, J. Brinkmann, Robert Brunner, Scott Burles, Larry Carey, Michael A. Carr, Francisco J. Castander, Bing Chen, Patrick L. Colestock, A. J. Connolly, J. H. Crocker, István Csabai, Paul C. Czarapata, John Eric Davis, Mamoru Doi, Tom Dombeck, Daniel Eisenstein, Nancy Ellman, Brian R. Elms, Michael L. Evans, Xiaohui Fan, Glenn R. Federwitz, Larry Fiscelli, Scott Friedman, Joshua A. Frieman, Masataka

Fukugita, Bruce Gillespie, James E. Gunn, Vijay K. Gurbani, Ernst de Haas, Merle Haldeman, Frederick H. Harris, J. Hayes, Timothy M. Heckman, G. S. Hennessy, Robert B. Hindsley, Scott Holm, Donald J. Holmgren, Chi-hao Huang, Charles Hull, Don Husby, Shin-Ichi Ichikawa, Takashi Ichikawa, Željko Ivezić, Stephen Kent, Rita S. J. Kim, E. Kinney, Mark Klaene, A. N. Kleinman, S. Kleinman, G. R. Knapp, John Korienek, Richard G. Kron, Peter Z. Kunszt, D. Q. Lamb, B. Lee, R. French Leger, Siriluk Limmongkol, Carl Lindenmeyer, Daniel C. Long, Craig Loomis, Jon Loveday, Rich Lucinio, Robert H. Lupton, Bryan MacKinnon, Edward J. Mannery, P. M. Mantsch, Bruce Margon, Peregrine McGehee, Timothy A. McKay, Avery Meiksin, Aronne Merelli, David G. Monet, Jeffrey A. Munn, Vijay K. Narayanan, Thomas Nash, Eric Neilsen, Rich Neswold, Heidi Jo Newberg, R. C. Nichol, Tom Nicinski, Mario Nonino, Norio Okada, Sadanori Okamura, Jeremiah P. Ostriker, Russell Owen, A. George Pauls, John Peoples, R. L. Peterson, Donald Petravick, Jeffrey R. Pier, Adrian Pope, Ruth Pordes, Angela Prosapio, Ron Rechenmacher, Thomas R. Quinn, Gordon T. Richards, Michael W. Richmond, Claudio H. Rivetta, Constance M. Rockosi, Kurt Ruthmansdorfer, Dale Sandford, David J. Schlegel, Donald P. Schneider, Maki Sekiguchi, Gary Sergey, Kazuhiro Shimasaku, Walter A. Siegmund, Stephen Smee, J. Allyn Smith, S. Snedden, R. Stone, Chris Stoughton, Michael A. Strauss, Christopher Stubbs, Mark SubbaRao, Alexander S. Szalay, Istvan Szapudi, Gyula P. Szokoly, Anirudda R. Thakar, Christy Tremonti, Douglas L. Tucker, Alan Uomoto, Dan Vanden Berk, Michael S. Vogeley, Patrick Waddell, Shu-i. Wang, Masaru Watanabe, David H. Weinberg, Brian Yanny, Naoki Yasuda, and SDSS Collaboration. The Sloan Digital Sky Survey: Technical Summary. *Astronomical Journal*, 120(3):1579–1587, September 2000. doi:10.1086/301513.

Zhen Yuan, G. C. Myeong, Timothy C. Beers, N. W. Evans, Young Sun Lee, Projjwal Banerjee, Dmitrii Gudin, Kohei Hattori, Haining Li, Tadafumi Matsuno, Vinicius M. Placco, M. C. Smith, Devin D. Whitten, and Gang Zhao. Dynamical Relics of the Ancient Galactic Halo. *Astrophysical Journal*, 891(1):39, March 2020. doi:10.3847/1538-4357/ab6ef7.

Zhen Yuan, Khyati Malhan, Federico Sestito, Rodrigo A. Ibata, Nicolas F. Martin, Jiang Chang, Ting S. Li, Elisabetta Caffau, Piercarlo Bonifacio, Michele Bellazzini, Yang Huang, Karina Voggel, Nicolas Longeard, Anke Arentsen, Amandine Doliva-Dolinsky, Julio Navarro, Benoit Famaey, Else Starkenburg, and David S. Aguado. The Complexity of the Cetus Stream Unveiled from the Fusion of STREAMFINDER and StarGO. *Astrophysical Journal*, 930(2):103, May 2022a. doi:10.3847/1538-4357/ac616f.

Zhen Yuan, Nicolas F. Martin, Rodrigo A. Ibata, Elisabetta Caffau, Piercarlo Bonifacio, Lyudmila I. Mashonkina, Raphaël Errani, Amandine Doliva-Dolinsky, Else Starkenburg, Kim A. Venn, Anke Arentsen, David S. Aguado, Michele Bellazzini, Benoit Famaey, Morgan Fouesneau, Jonay I. González Hernández, Pascale Jablonka, Carmela Lardo, Khyati Malhan, Julio F. Navarro, Rubén Sánchez Janssen, Federico Sestito, Guillaume F. Thomas, Akshara Viswanathan, and Sara Vitali. The Pristine survey - XVII. The C-19 stream is dynamically hot and more extended than previously thought. *Monthly Notices of the Royal Astronomical Society*, 514(2):1664–1671, August 2022b. doi:10.1093/mnras/stac1399.

H. W. Zhang, T. Gehren, and G. Zhao. Scandium Abundance in Metal-poor Stars. In Sofia Feltzing, Gang Zhao, Nicholas A. Walton, and Patricia Whitelock, editors, *Setting the scene for Gaia and LAMOST*, volume 298 of *IAU Symposium*, pages 453–453, January 2014. doi:10.1017/S1743921313007187.

Hao Zhang, Richard de Grijs, Chengyuan Li, and Xiaohan Wu. No Evidence of Chemical Abundance Variations in the Intermediate-age Cluster NGC 1783. *Astrophysical Journal*, 853(2):186, February 2018. doi:10.3847/1538-4357/aaa428.